Chem Soc Rev

CORRECTION

View Article Online
View Journal | View Issue



Cite this: *Chem. Soc. Rev.*, 2025, **54**, 10845

DOI: 10.1039/d5cs90091c

rsc.li/chem-soc-rev

# Correction: Behavior, mechanisms, and applications of low-concentration $CO_2$ in energy media

Minghai Shen,[ac] Wei Guo,[a] Lige Tong,*[a] Li Wang,[a] Paul K. Chu,[b] Sibudjing Kawi[c] and Yulong Ding[d]

Correction for 'Behavior, mechanisms, and applications of low-concentration $CO_2$ in energy media' by Minghai Shen *et al.*, *Chem. Soc. Rev.*, 2025, **54**, 2762–2831, https://doi.org/10.1039/D4CS00574K.

The authors regret that there was an error in one of the affiliations in the original article. The correct affiliations are as shown here.

The Royal Society of Chemistry apologises for these errors and any consequent inconvenience to authors and readers.

[a] *Beijing Key Laboratory of Energy Saving and Emission Reduction for Metallurgical Industry, School of Energy and Environmental Engineering, University of Science and Technology Beijing, China. E-mail: tonglige@me.ustb.edu.cn*

[b] *Department of Physics, Department of Materials Science and Engineering, and Department of Biomedical Engineering, City University of Hong Kong, Hong Kong*

[c] *Department of Chemical and Biomolecular Engineering, National University of Singapore, Singapore. E-mail: chekawis@nus.edu.sg*

[d] *Birmingham Centre for Energy Storage & School of Chemical Engineering, University of Birmingham, UK. E-mail: Y.Ding@bham.ac.uk*

Chem Soc Rev

REVIEW ARTICLE

View Article Online
View Journal | View Issue



Cite this: *Chem. Soc. Rev.*, 2025, **54**, 2762

# Behavior, mechanisms, and applications of low-concentration $CO_2$ in energy media

Minghai Shen, †[ac] Wei Guo,†[a] Lige Tong,*[a] Li Wang,[a] Paul K. Chu,[b] Sibudjing Kawi[c] and Yulong Ding[d]

Received 17th October 2024

DOI: 10.1039/d4cs00574k

rsc.li/chem-soc-rev

This review explores the behavior of low-concentration $CO_2$ (LCC) in various energy media, such as solid adsorbents, liquid absorbents, and catalytic surfaces. It delves into the mechanisms of diffusion, adsorption, and catalytic reactions, while analyzing the potential applications and challenges of these properties in technologies like air separation, compressed gas energy storage, and $CO_2$ catalytic conversion. Given the current lack of comprehensive analyses, especially those encompassing multiscale studies of LCC behavior, this review aims to provide a theoretical foundation and data support for optimizing $CO_2$ capture, storage, and conversion technologies, as well as guidance for the development and application of new materials. By summarizing recent advancements in LCC separation techniques (*e.g.*, cryogenic air separation and direct air carbon capture) and catalytic conversion technologies (including thermal catalysis, electrochemical catalysis, photocatalysis, plasma catalysis, and biocatalysis), this review highlights their importance in achieving carbon neutrality. It also discusses the challenges and future directions of these technologies. The findings emphasize that advancing the efficient utilization of LCC not only enhances $CO_2$ reduction and resource utilization efficiency, promoting the development of clean energy technologies, but also provides an economically and environmentally viable solution for addressing global climate change.

## 1. Introduction

### 1.1 Sources of LCC

Fossil fuels such as coal, oil, and natural gas have supported the development of human society, but excessive reliance on these energy sources has led to numerous challenges.[1] With the rapid advancement of modern society, issues such as population growth, energy crises, and environmental pollution have become increasingly severe. $CO_2$ emissions from the burning of large amounts of fossil fuels are considered to be the main factor causing global warming.[2] According to the Fifth Assessment Report published by the Intergovernmental Panel on Climate Change (IPCC), global atmospheric $CO_2$ concentration has risen from pre-industrial levels of 280 ppm to over 400 ppm today. The U.S. National Oceanic and Atmospheric Administration (NOAA) reported in June 2023 that global $CO_2$ concentration has now reached 421 ppm,[3] marking a 50% increase since pre-industrial times.[4] Projections suggest that $CO_2$ concentrations could reach 500 ppm by 2050 and exceed 900 ppm by the end of the century.[5]

Since the Industrial Revolution (*circa* 1750), the rise in $CO_2$ concentration has led to an increase in global average surface temperatures by approximately 1.5–2 °C.[6] This warming trend triggers catastrophic events such as glacier melt and sea-level rise, posing a threat of submersion to coastal regions and island nations. Climate change also intensifies extreme weather events and disrupts ecosystems, jeopardizing the survival of humans and other species.[7,8] The 2015 Paris Agreement proposed to limit the global temperature rise to well below 2 °C above pre-industrial levels and to strive to limit it to 1.5 °C.[9]

Recent data (Fig. 1) shows that the primary sources of LCC include industrial emissions, transportation, and natural sources.[10] Industrial emissions constitute the largest share, accounting for approximately 50–60% and involving activities such as cement production, steel manufacturing, and fossil fuel combustion. LCC has different definitions and application ranges in different fields. Generally speaking, in atmospheric and environmental sciences, LCC usually refers to the natural atmospheric concentration of about 400–500 ppm. In industrial tail gas treatment and post-combustion flue gas capture, LCC refers to 1–15%, which is waste gas from combustion or industrial processes. In addition, in greenhouse gas emission reduction, carbon capture and catalytic conversion research,

[a] *Beijing Key Laboratory of Energy Saving and Emission Reduction for Metallurgical Industry, School of Energy and Environmental Engineering, China. E-mail: tonglige@me.ustb.edu.cn*
[b] *Department of Physics, Department of Materials Science and Engineering, and Department of Biomedical Engineering, City University of Hong Kong, Hong Kong*
[c] *Department of Chemical and Biomolecular Engineering, National University of Singapore, Singapore. E-mail: chekawis@nus.edu.sg*
[d] *Birmingham Centre for Energy Storage & School of Chemical Engineering, University of Birmingham, UK. E-mail: Y.Ding@bham.ac.uk*
† These authors contributed equally to this work.

the concentration of LCC can be as low as 1%. Emissions from transportation, including vehicles, airplanes, and ships, account for about 20–30%. Natural sources, such as biological respiration and soil decomposition, contribute 10–20%. Although both anthropogenic and natural environments produce $CO_2$, plants and other organisms also play a role in carbon sequestration, offsetting emissions.[11] $CO_2$ emission control measures include improving energy efficiency, adjusting energy structures, increasing the proportion of renewable energy, and employing various methods to capture and utilize emitted $CO_2$.[12]

To mitigate global warming, the primary strategy has been to implement carbon pricing for $CO_2$ emissions from energy production.[13] However, due to technological limitations, the transition from fossil fuels to clean energy remains a work in progress.[14] Some countries and sectors still face challenges in fully eliminating LCC emissions, leading to the release of $CO_2$ at various concentrations into the atmosphere.

### 1.2 Scope of the review

To achieve negative carbon emissions, direct capture of industrial stationary emission sources such as thermal power, steel, cement, and chemicals is an effective way and can save transportation costs. Current capture methods include pre-combustion capture, oxygen-enriched combustion, and post-combustion capture.[15,16] Pre-combustion capture converts the carbon-containing components in the fuel into water gas and then separates $CO_2$, which is suitable for integrated coal gasification combined cycle power plants.[17,18] Oxygen-enriched combustion can capture high-purity $CO_2$ by introducing pure oxygen into the combustion system and coordinating flue gas circulation, but the investment cost is high.[19,20] Post-combustion capture separates $CO_2$ from flue gas.

**Minghai Shen**

*Minghai Shen obtained his Master's degree in Inorganic Chemistry from China University of Mining and Technology (Beijing) in 2020, and is currently a PhD candidate in Power Engineering and Engineering Thermophysics at Beijing University of Science and Technology, as well as a visiting PhD student at the National University of Singapore. His research focuses on $CO_2$ capture and comprehensive utilization, direct air carbon capture, and cold plasma methane dry reforming technology.*

**Wei Guo**

*Wei Guo received the PhD degrees in power engineering and engineering thermophysics from University of Science and Technology Beijing, Beijing, China. He is currently a lecturer in the School of Energy and Environmental Engineering at the School of University of Science and Technology Beijing. He was selected for the Beijing Science and Technology Association's Young Talent Nurturing Program. His research interests include heat and mass transfer in multiphase flows, phase changes, and energy conversion and utilization. He has published ~30 international peer-reviewed journal papers in the last five years.*

**Lige Tong**

*Lige Tong is a professor at the School of Energy and Environmental Engineering at the University of Science and Technology Beijing. She mainly studies energy conversion and efficient utilization; energy storage; high-temperature flue gas dust removal and waste energy recovery and utilization; energy management and energy-saving strategies; refrigeration and low-temperature engineering; and industrial equipment service safety evaluation. She has published more than 160 papers, more than 10 authorized patents at home and abroad, participated in the compilation of 6 Chinese and English textbooks/books, and won many awards from Beijing, China Iron and Steel Association, and the Ministry of Education.*

**Li Wang**

*Li Wang received the PhD degree in metallurgical engineering from University of Science and Technology Beijing, Beijing, China, in 1990. Since 1996, he has been a Professor of Thermal Power Engineering in University of Science and Technology Beijing. His research interests include the energy storage, conversion and utilization, refrigeration/cryogenics, and gas separation. He has published 8 books, more than 330 international peer-reviewed journal papers, and more than 30 national patents. He has won eight scientific and technological progress awards at the provincial and ministerial levels.*

Although the energy consumption is high, the original system is less modified and is widely used.[21,22] In addition, for low-concentration carbon sources dispersed in the atmosphere, in addition to source control, negative emissions[12] can also be achieved through coastal blue carbon,[23] terrestrial carbon plant removal,[24] biomass capture and storage technology,[25] direct air capture technology,[26] and carbon mineralization technology[27] (Fig. 2).

LCC is a component of greenhouse gas emissions, and its effective capture and conversion are crucial for mitigating climate change.[28,29] However,[30] the enrichment cost of LCC is high, and the efficiency of direct adsorption or conversion is low.[31] Therefore, studying the behavior of LCC in different energy media is crucial to the development of efficient capture and conversion technologies to reduce the $CO_2$ content in the atmosphere and reduce the greenhouse effect. At present, the scale of clean energy supply cannot meet the needs of human activities, and a long transition period is still needed. The capture, storage and utilization of the generated $CO_2$ are also crucial. For high-concentration $CO_2$ tail gas, such as $CO_2$ generated during coal-fired power generation, the capture difficulty is relatively low and the cost is relatively low.[32] For low-concentration tail gas, such as coal-fired power plant flue gas and lime kiln gas, the separation and enrichment of $CO_2$ is difficult and the capture cost is high.[33] Table 1 shows that when using 30 wt% monoethanolamine (MEA) aqueous solution as the capture medium, the capture cost is closely related to the operating cost and capital cost of the plant, and the $CO_2$ concentration and scale have an important impact on the cost.[34,35]

LCC have had a major influence on the collection and conversion process during the development of CCUS (carbon collection, utilization and storage) technologies.[36–38] LCC undergoes complex behaviors such as diffusion,[39,40] adsorption[41,42] and catalysis[43–45] on the surface of solid adsorbents, liquid absorbents and catalysts. These behaviors are directly related to the optimization of material structure and performance, and affect capture. efficiency. In the transport process of LCC, physical processes such as diffusion and scattering play a key role. The performance of these processes in different media and conditions affects the distribution and migration efficiency of $CO_2$. Molecular diffusion and convective diffusion are the two main transport mechanisms. Molecular diffusion is based on the thermal motion of molecules and enables gas transport through concentration gradients. Convective diffusion relies on medium flow, allowing $CO_2$ to migrate with the fluid. In addition to the conventional molecular diffusion mechanism, Knudsen diffusion is particularly significant in porous materials whose pore size is close to or smaller than the molecular free path. Under such conditions, the collision of $CO_2$ molecules with the pore wall is better than the collision between molecules, thus affecting the transmission rate and direction. Moreover, during the transmission of $CO_2$ in porous materials

**Paul K. Chu**

*Paul K. Chu is Chair Professor of Materials Engineering in the Department of Physics, Department of Materials Science and Engineering, and Department of Biomedical Engineering at City University of Hong Kong. He obtained his PhD in chemistry from Cornell University in 1982. He is fellow of the APS, AVS, IEEE, MRS, Hong Kong Institution of Engineers, and the Hong Kong Academy of Engineering Sciences. His research interests are quite diverse spanning plasma surface engineering, materials science and engineering, surface science, and functional materials. He is a highly cited researcher and his papers have been cited more than 100 000 times.*

**Sibudjing Kawi**

*Professor Sibudjing Kawi is a productive researcher and has published more than 285 international peer-reviewed journal articles. He obtained his PhD in Delaware and has been attached to the Department of Chemical and Biomolecular Engineering at the National University of Singapore since 1994. In the past decade, his research has focused on the design and synthesis of nano-catalysts for green and sustainable development, such as $CO_2$ reforming with methane to bio-syngas and hydrogen, $CO_2$ hydrogenation, biomass gasification, and the water gas shift reactions. His expertise also includes the synthesis of novel inorganic membranes, as well as catalytic membrane reactors.*

**Yulong Ding**

*Professor Yulong Ding, founder of the Birmingham Energy Storage Centre and Professor of the School of Chemical Engineering at the University of Birmingham. His invention of liquid air energy storage technology won the 2011 'The Engineer' Energy and Environment Award and Comprehensive Award; his medium and high temperature composite phase change materials and heat storage technology won the 2019 IChemE Research Project Award, Global Energy Award and (the highest award) Outstanding Contribution Award. His main research is the span-scale multiphase transport phenomenon and its application in energy power, chemical metallurgy, building energy conservation, cold chain transportation and other fields.*

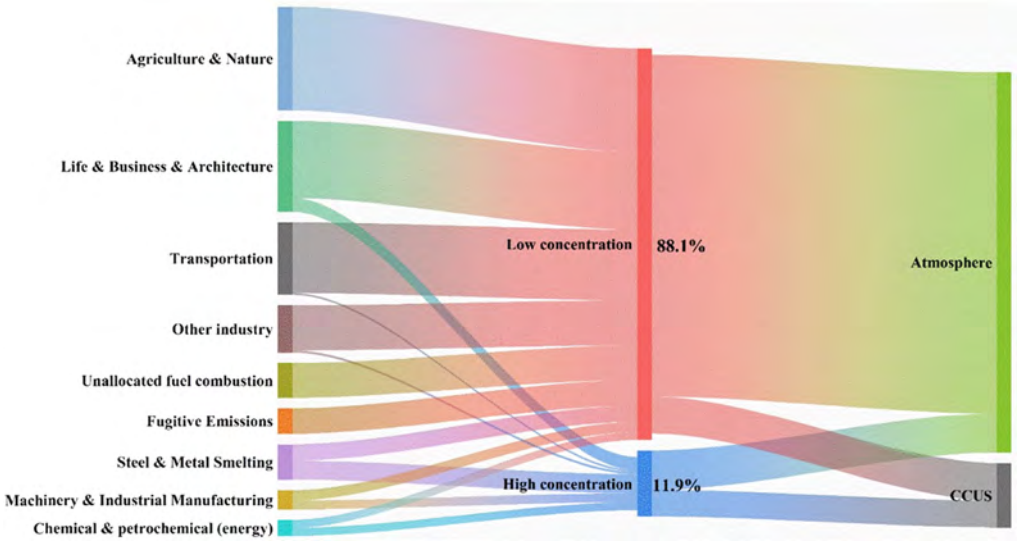


Fig. 1 Distribution of global greenhouse gas emissions by industry source. (Data from ref. 10 with permission from Our World in Data, copyright 2020.)

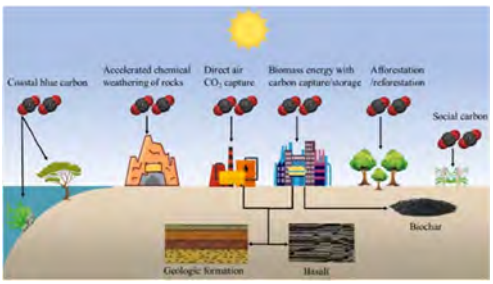


Fig. 2 Negative $CO_2$ emissions technology (adapted with permission from ref. 27 with permission from Springer Nature, copyright 2023).

and granular media, the scattering effect will change its movement path, thereby affecting the overall diffusion behavior.

The performance of these diffusion and scattering processes is affected by factors such as pressure, temperature and $CO_2$ concentration. Under high-pressure conditions, molecular diffusion is relatively rapid. Under low pressure conditions, Knudsen diffusion gradually dominates. The increase in temperature will enhance the thermal motion of molecules, thereby accelerating the rate of molecular diffusion and Knudsen diffusion. The diffusion behavior of $CO_2$ at low concentrations is relatively slow and susceptible to scattering. One of the main goals of current research is to determine how to harness these behavioral traits to efficiently capture LCC from industrial emission sources and so reduce its emissions.[26,31,46,47] By regulating the catalytic reaction characteristics of LCC on the catalyst surface, it can be converted into valuable chemicals and fuels, realizing the resource utilization of $CO_2$.[48–50]

Photocatalysis, as a green technology that utilizes renewable light energy to drive $CO_2$ reduction, has shown great potential. By gradually improving the efficiency and stability of photocatalysts, the photocatalytic reduction reaction of LCC has become more efficient.[51,52] The advantage of photocatalysis is to directly utilize solar energy for fuel production, which not only reduces the dependence on fossil energy but also provides a sustainable solution for $CO_2$ resource utilization.[53,54] And electrocatalytic technology has also received widespread attention. By regulating electrochemical reaction conditions, the selective reduction of LCC was achieved, and a variety of carbon-based fuels were successfully prepared.[55,56] Research focuses include catalyst selection, diffusion layer design and electrolyzer optimization, and breakthroughs have been

Table 1 Effects of $CO_2$ partial pressure and scale on carbon capture costs (reproduced from ref. 34 and 35 with permission from the International Energy Agency and Global CCS institute, copyright 2021)

| Scenario | $CO_2$ partial pressure (kPa) | Capture cost (USD per t) | Scale (Mtpa) |
|---|---|---|---|
| DAC | 0.04 | 134–342 | 1 |
| Aluminum smelting | 1.00 | 180–290 | 0.02–0.2 |
| Steel plant dust removal chimney | 2.00 | 110–180 | 0.04–0.4 |
| Natural gas combined power plant/steel sintering plant | 4.00 | 75–125 | 0.07–0.66 |
| Petroleum coke/natural gas power plant | 8.00 | 60–85 | 0.12–1.2 |
| Biomass power plant | 12.00 | 58–75 | 0.13–1.3 |
| Coal-fired power plant | 14.00 | 54–70 | 0.15–1.5 |
| Cement kiln | 18.00 | 50–60 | 0.18–1.8 |
| Steel metallurgy | 26.00 | 49–52 | 0.2–2 |
| Steel rotary kiln | 35.00 | 48–51 | 0.2–2 |

made in improving energy efficiency and reducing reaction overpotential.[57,58]

In terms of thermocatalysis, by developing new catalytic materials and optimizing reaction conditions, researchers have significantly improved $CO_2$ reduction efficiency, enabling LCC to be effectively converted into fuels such as methane and methanol.[59–61] Plasma catalysis generates high-energy electrons by stimulating low-temperature plasma, which activates and decomposes $CO_2$ molecules under non-equilibrium conditions. It can drive $CO_2$ reduction at lower temperatures and significantly reduce energy consumption.[62,63] In addition, the combination of plasma and catalyst further enhances the selectivity and efficiency of $CO_2$ reduction.[64] This technology has made significant progress in the preparation of fuels such as methane and ethylene, providing a new way for efficient utilization of $CO_2$. Biocatalysis uses microorganisms or enzymes as catalysts to convert LCC into organic compounds. With the development of synthetic biology, the modification of microbial metabolic pathways has improved $CO_2$ conversion efficiency.[65,66] Engineered strains designed through gene editing have achieved efficient conversion of $CO_2$ into chemicals such as methanol and ethanol under mild conditions.[67,68]

LCC can also be efficiently used by physical energy storage in addition to direct conversion.[69–71] $CO_2$ has high compressibility and can store a large amount of energy in a small volume. Its thermodynamic properties,[72] such as a higher critical point and lower compression power requirements, give it advantages in medium and high temperature energy storage and release processes.[73–77] By utilizing and recycling $CO_2$, compressed air energy storage (CAES) and compressed $CO_2$ energy storage (CCES) designs can reduce greenhouse gas emissions and help achieve carbon neutrality goals.[78] In CAES/CCES systems, the phase change process of $CO_2$ can effectively manage thermal energy and optimize system performance.[79] The phase change process involves a large amount of latent heat absorption or release, which can help manage thermal energy more effectively in CAES systems, thereby improving overall efficiency.[80] The phase change of $CO_2$ can also be used to cool compressed air or preheat expanded air to further optimize system performance.[81]

The presence of $CO_2$ has a significant impact on the efficiency and stability of compressed gas energy storage systems such as CAES/CCES. When moisture in compressed gases combines with $CO_2$, carbonic acid ($H_2CO_3$) may be formed.[82] Carbonic acid is corrosive, especially to iron, steel, aluminum and other metal materials. This corrosion can weaken the structural integrity of equipment, leading to increased wear on pipes, tanks, heat exchangers, and other equipment.[83] $CO_2$ is more corrosive and has a greater corrosion rate in high-temperature, high-pressure environments. This may lead to lower equipment life expectancy, more frequent equipment replacement and maintenance requirements, and higher operating expenses.[84] The presence and concentration changes of $CO_2$ in CAES systems may affect the efficiency of the compression and expansion processes and equipment operating time, and lead to thermal management complications.[85] Therefore, $CO_2$ may need to be processed or separated in the design of high-pressure and high-temperature CAES systems to ensure efficient and safe operation of the system.[86]

In the past few decades, CCUS technology for high-concentration $CO_2$ has been widely studied.[87–89] Although some reviews involve the direct capture and conversion of LCC, most of these reviews focus on purifying LCC to obtain high-purity $CO_2$ for industrial applications, or investigating single catalytic technologies (such as photocatalysis or electrocatalysis) to convert $CO_2$ into specific chemical products. Although valuable, these approaches often fail to address the comprehensive challenges of capturing LCC and converting it efficiently into useful products.[90–93] Yao *et al.*[93] reviewed the application of LCC in adsorption capture from the perspective of porous materials and discussed the chemical transformation of LCC diameter on porous catalysts. Yasuomi *et al.*[91] summarized the reported catalytic systems for the reduction of LCC. The system first performs a $CO_2$ capture reaction (or $CO_2$ adsorption) and then catalyzes $CO_2$ reduction. Hu *et al.*[94] reviewed LCC gas purification technology and analyzed methods for low-cost capture and electrocatalytic reduction using carbon-based materials.

To our knowledge, there is no comprehensive analysis of LCC, especially a cross-scale discussion of its behavioral characteristics. This review first analyzes the behavioral characteristics of LCC in different energy media, aiming to deeply understand its diffusion, adsorption and catalytic reaction mechanisms, so as to optimize $CO_2$ capture, storage and conversion technologies. It can provide theoretical basis and data support for scientific research in related fields and provide guidance for the development and application of new materials. This has important scientific value and practical significance for promoting the development and industrialization of related technologies. This will not only help improve the efficiency of $CO_2$ emission reduction and resource utilization, and promote the realization of carbon neutrality goals. It can also promote the development of clean energy technologies, provide economically and environmentally feasible solutions, and ultimately address global climate change. The separation technologies of LCC are summarized, including cryogenic air separation and direct air carbon capture. The research progress of LCC direct conversion technology in different catalytic fields is introduced, including thermal catalysis, electrochemical catalysis, photocatalysis, plasma catalysis and biocatalysis. In addition, the impact of low-concentration and pure $CO_2$ in compressed energy storage is also discussed. Finally, we emphasize the difficulties of these research directions and look forward to their development direction. The ultimate goal is to promote the efficient resource utilization of LCC through interdisciplinary and cross-industry forms to achieve the goal of carbon neutrality.

## 2. Behavior of LCC in different energy media

### 2.1 Diffusion characteristics

The diffusion characteristics of LCC in different energy media vary depending on factors such as temperature,[95,96]

 

pressure,[97,98] medium viscosity[99,100] and composition.[101,102] Increased temperature and pressure generally increase the diffusion coefficient of $CO_2$, while higher medium viscosity reduces the diffusion rate. Changes in medium composition affect the solubility and diffusion path of $CO_2$. In liquid phases, such as liquid fuels and electrolytes, the diffusion of $CO_2$ is affected by fluid dynamics and the diffusion rate is relatively fast. In solid phases, such as porous materials and solid adsorbents, the diffusion is affected by pore structure and surface interactions, and the diffusion rate is relatively slow.

Numerous sectors find considerable value and relevance in the study of LCC diffusion properties in liquid and solid phases. Recognizing the diffusion behavior of $CO_2$ in various mediums can help with carbon capture and storage (CCS) by increasing storage safety and capture efficiency.[39,40] Optimizing $CO_2$ diffusion properties in fuel cells can enhance battery stability and performance.[103,104] Determining the $CO_2$ diffusion properties in porous medium during enhanced oil and gas recovery (EOR/EGR) will assist increase oil and gas recovery.[105,106] In gas separation technology, studying the diffusion characteristics of $CO_2$ can help develop more efficient separation materials.[107,108] These studies can not only improve energy utilization efficiency, but also reduce carbon emissions and promote the development of sustainable energy, and have important scientific and practical application value.

**2.1.1 Diffusion in the liquid phase.** Reactive electrolytes and liquid adsorbents are frequently utilized in the conversion and adsorption of $CO_2$.[109–111] Compared with the diffusion mass transfer of high-purity $CO_2$ and pure $CO_2$, the diffusion mass transfer process of LCC is more complicated. Similar to molecular diffusion in the gas phase, $CO_2$ molecules in the liquid phase diffuse from high-concentration areas to low-concentration areas through random thermal motion.[112] Since the density and viscosity of liquids are greater than those of gases, the molecular diffusion rate is lower.[113] In liquids, liquid movement caused by density differences or external stirring (such as natural convection and forced convection) accelerates the diffusion of $CO_2$.[114,115]

In the process of $CO_2$ sequestration or enhanced oil recovery, its diffusion behavior will be affected by various factors in the actual reservoir.[116,117] In addition, existing research results have recognized that the process of $CO_2$ geological sequestration and $CO_2$ flooding is a process in which diffusion and dispersion occur simultaneously.[118,119] Convection diffusion is a combination of molecular diffusion and dispersion between particles of a substance in different phases of motion (or between phases). Molecular diffusion is the mass transfer between substances due to concentration differences, while dispersion is the mixing phenomenon caused by changes in velocity in or between flow channels.[120] In the continuous liquid phase of a porous medium, when the flow velocity is very small, molecular diffusion is usually the main mass transfer mechanism, while when the flow velocity increases to a certain value, hydraulic dispersion becomes the main mass transfer mechanism.[99]

For the diffusion of LCC in solution, when $CO_2$ gas comes into contact with the solution, mass transfer occurs between the gas and liquid, causing the composition of the fluid phase to change[121,122] (Fig. 3a). Due to the lower $CO_2$ concentration, the rate of diffusion may be slower and more susceptible to solution properties, solubility, and interfacial reaction kinetics.[113,123,124] In this case, the gas–liquid transition zone may be narrower and less miscible.[125] However, the composition of the solution will still gradually change due to factors such as molecular diffusion, viscosity, capillary forces, and gravity.[126,127] The injection of LCC drives the flow of the gas–liquid transition zone and liquid phase, and the diffusion process may show more obvious nonlinear characteristics[128] (Fig. 3b).

When multi-component fluids seep through porous media, the concentration changes of LCC usually do not completely follow Darcy's law (Fig. 3c). The velocity of fluid flow is not proportional to the pressure gradient of the fluid in the porous medium and is also significantly affected by dispersion phenomena.[129] In addition to the main molecular diffusion in the diffusion phenomenon, LCC may also produce convective diffusion or mechanical diffusion under changes in diffusion conditions.[130,131] Molecular diffusion is caused by the random motion of molecules, resulting in low concentrations of $CO_2$ tending to be evenly distributed in the solution.[132] Convective diffusion is mainly driven by the density difference caused by the inhomogeneity of the pore microstructure and the difference in $CO_2$ concentration at different locations in the solution, which accelerates the dissolution rate of LCC in the liquid phase.[114,133,134]

The diffusion coefficient is the most important parameter in the reaction–diffusion process. If the diffusion coefficient of $CO_2$ in the liquid phase is known, the various diffusion behaviors of $CO_2$ in the liquid phase can be obtained.[135–137] At present, there are two methods to determine the diffusion coefficient of $CO_2$ in the liquid phase, namely the direct method based on determining the concentration distribution and the indirect method based on measuring parameter changes. Among them, the most realistic diffusion coefficient value is obtained by the concentration of $CO_2$ in the liquid phase during the diffusion process, that is, the diffusion coefficient is calculated by the direct method.[138,139] However, how to measure the $CO_2$ concentration contained in different positions of the liquid phase during the diffusion process through indoor experiments is currently a difficulty. The advantages of the direct method for obtaining the diffusion coefficient are its simple theory and high experimental accuracy. However, its disadvantages are that the sampling operation will interrupt the continuity of the system diffusion process, affect the concentration distribution of $CO_2$ in the diffusion system, cause experimental errors, and its operation is relatively complicated and time-consuming, and requires component analysis instruments, resulting in high costs.[140,141] As a result, the direct approach is rarely employed during the actual measuring procedure.

The primary indirect technique used to determine the concentration of $CO_2$ in the liquid phase at the moment is Raman spectroscopy.[142–144] Because different substances correspond to a specific Raman peak, the concentration of $CO_2$ in the liquid phase can be indirectly calculated by

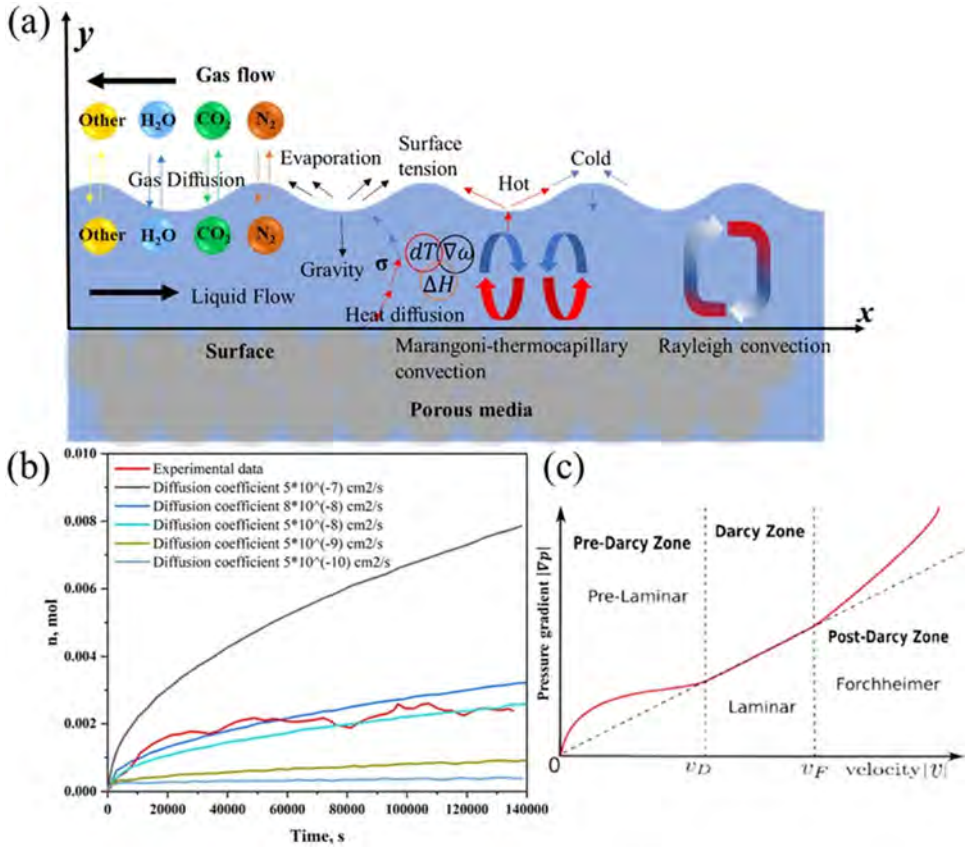


Fig. 3 (a) Diffusion model of $CO_2$-containing gas flow on the liquid surface; (b) change in mass of $CO_2$ during the diffusion process under different diffusion coefficients (reproduced with permission from ref. 128. Copyright 2022 Elsevier); (c) diffusion model of linear Darcy's law (reproduced with permission from ref. 129. Copyright 2017 Elsevier).

combining the Raman intensity. However, it is difficult for ordinary laboratories to carry out diffusion experiments using Raman spectrometers. On the one hand, the equipment is expensive, and on the other hand, professional technicians are required to operate it. Moreover, Raman spectroscopy can only measure the liquid phase in a transparent tube, and porous media conditions cannot be measured.[145,146] Computed tomography (CT) scanning calculations are similar to Raman spectroscopy measurement methods. Numerous approximations are utilized in the indirect calculation of the $CO_2$ concentration, and the measurement data is not as precise as that of Raman spectroscopy.[128,147,148] Another, more conventional approach is to estimate the $CO_2$ content in the liquid phase by measuring the pH of the liquid phase with a high-precision pH meter.[40,143,149] The method of measuring the pH value of the solution is relatively simple, but this method has a large error. A change in pH value will result in a change in $CO_2$ concentration by an order of magnitude, and it is impossible to determine whether all $CO_2$ exists in the pH standard solution in the form of ions.[110,150,151]

Combining theoretical computations with indoor tests is another way to get the $CO_2$ diffusion coefficient in liquid phase.[152–154] The correlation equation for the diffusion coefficient is then computed by combining the relevant diffusion mathematical model with the experimentally determined changes in pressure, liquid volume, and gas–liquid interface (Fig. 4a–c). This method's straightforward operation and inexpensive experimental equipment have made it a more popular way to compute the diffusion coefficient of $CO_2$, even if there is a slight discrepancy between the estimated and real diffusion.[100]

It is evident that gas flooding to improve oil recovery and the decrease of greenhouse gas emissions depend heavily on $CO_2$ diffusion. The average diffusion coefficient determined just by the change law of indirect physical variables in the diffusion process is insufficient to define the diffusion capacity of the entire process, since other factors will disrupt its real diffusion behavior.[155,156] The diffusion of LCC in the liquid phase is affected by factors such as temperature, liquid viscosity, stirring rate, solution composition, gas–liquid interface area and gas partial pressure. Increased temperature usually increases the diffusion coefficient, higher viscosity reduces the diffusion rate, stirring reduces the thickness of the boundary layer, and solution components such as ion concentration and other gas solubility also affect the diffusion behavior.[157–159] Compared with high-concentration $CO_2$, LCC has a smaller diffusion driving force, a relatively stable diffusion coefficient, a solution that has not reached a saturated state, weak intermolecular interactions, and less influence on the physical and chemical properties of the liquid phase.[160,161] High-concentration $CO_2$ has a larger concentration gradient, the diffusion coefficient

 

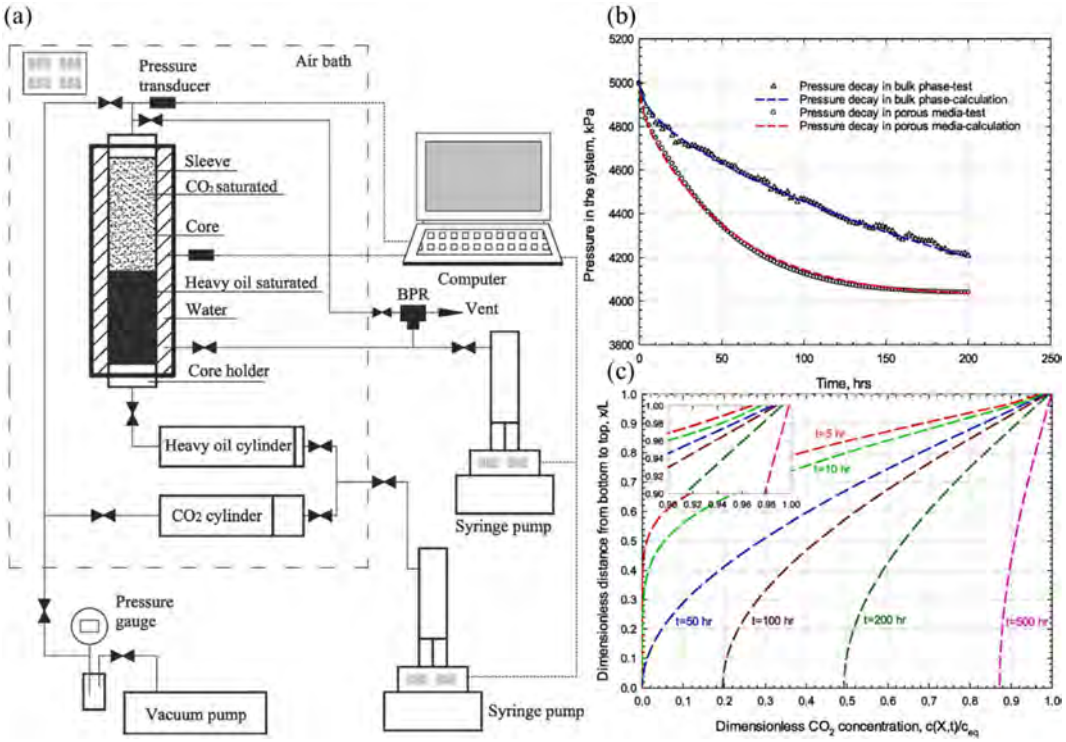


Fig. 4 (a) $CO_2$ gas–liquid diffusion coefficient test system in heavy oil; (b) pressure decay diagram of $CO_2$ diffusion coefficient in bulk phase and porous media in heavy oil under test and simulation comparison; (c) dimensionless $CO_2$ concentration distribution in bulk phase at different test times (reproduced with permission from ref. 100. Copyright 2020 Elsevier).

may show a nonlinear effect, and the solution is closer to a saturated state.[99,162,163] Enhanced intermolecular interactions may change the physicochemical properties of the liquid phase, such as pH[164,165] and viscosity,[166,167] thereby affecting the diffusion process.

In liquid fuels, $CO_2$ diffusion research mainly revolves around the determination of diffusion coefficient,[168,169] solubility,[170,171] study of dissolution mechanism[172,173] and kinetic simulation.[174,175] Experimental and simulation methods show that temperature, pressure and fuel composition significantly affect the diffusion behavior of $CO_2$, with higher temperatures and pressures generally increasing the diffusion coefficient.[176–178] Solubility studies have found that the chemical properties of different liquid systems will affect the dissolution and diffusion paths of $CO_2$.[179–181] Jeon *et al.*[182] studied the effect of surfactants (alkyl olefin sulfonates and cetyltrimethylammonium bromide) on $CO_2$-brine-clay under subcritical to supercritical $CO_2$ conditions (10–150 bar, 45 °C). Influence of chemical reactions of mineral systems (montmorillonite and sepiolite). Compared with the $CO_2$-brine-clay mineral system without surfactant, the introduction of surfactant increases the solubility of $CO_2$. Molecular dynamics simulation and computational fluid dynamics (CFD) methods reveal the microscopic diffusion process and molecular mechanism of $CO_2$ in liquid fuel.[183–185] Morgan *et al.*[186] analyzed in detail the catalytic mechanism of the gas–liquid–solid interface, especially the interaction between the electrolyte in the liquid phase and the $CO_2$ molecules in the gas phase. Through reasonable catalyst assembly, the researchers were able to achieve higher $CO_2$ adsorption and reduction efficiency at the interface, thereby increasing the methane yield. The gas–solid–liquid interface plays a vital role in electroreduction, accelerating the transfer of reactants and reducing the generation of side reactants. Marilia *et al.*[187] discussed the importance of the gas–liquid interface in the $CO_2$ capture process, especially in the application of MEA absorbents. The adsorption and reaction of MEA molecules at the gas–liquid interface not only increased the solubility of $CO_2$, but also accelerated the conversion process of $CO_2$. The study proposed that the reaction characteristics of MEA at the gas–liquid interface are closely related to the interface structure and surface properties, which provides a new direction for the optimization of gas–liquid interface catalysis. Lei *et al.*[188] proposed a $CO_2$-responsive gas valve. In the $CO_2$-responsive gas valve, the diameter of the liquid gating mechanism is associated with the gas–liquid interface. The introduction of $CO_2$ changes the physical state of the liquid by reacting with functional groups in the liquid phase, thereby affecting the opening and closing of the gas channel. By utilizing the interaction of the gas–liquid interface, the system can effectively respond to changes in $CO_2$ concentration in the gas environment. These studies provide important data support for optimizing CCS technology.

Optimizing $CO_2$ diffusion in fuel cells can raise stability and performance levels.[189–191] In electrolytes, $CO_2$ diffusion research mainly focuses on the determination of diffusion coefficient[192,193] and electrochemical properties,[194,195] the study of interfacial mass transfer processes[196,197] and the development of new electrolytes.[98,198] Studies have shown that electrolyte

composition and temperature have a significant impact on the $CO_2$ diffusion coefficient. Kenis *et al.*[192] found that carbonates formed in $K^+$-containing electrolytes formed concentrated deposition regions of different morphologies on the GDE surface. On the other hand, carbonates formed in $Cs^+$-containing electrolytes appear as small crystals dispersed on the electrode surface. The deposits blocking the surface of the catalyst layer and the deposits in the electrode microporous layer and carbon fiber substrate will reduce the diffusion of $CO_2$ and the performance of electroreduction reaction. Interfacial mass transfer rate has an important impact on battery electrochemical performance.[199] Lu *et al.*[110] found that the reduction in nominal overpotential caused by the use of alkaline electrolytes originated from the Nernst potential of the pH gradient layer at the cathode/electrolyte interface. The diffusion transport of $CO_2$ is greatly enhanced by forming a gas–liquid–solid three-phase interface, thereby significantly increasing the diffusion-limited current density. This has optimized the application of $CO_2$ electroreduction reaction ($CO_2$RR) by developing a variety of new electrolytes with high $CO_2$ solubility and good mass transfer properties.[200,201] These studies provide theoretical basis and technical support for improving energy conversion efficiency, reducing carbon emissions and developing efficient separation materials.

**2.1.2 Diffusion in the solid phase.** Surface diffusion and pore diffusion are the primary methods used in the solid phase to diffuse LCC.[202–204] Surface diffusion is the term used to describe the passage of $CO_2$ molecules over the solid surface on the surface of porous materials (such adsorbents).[97,205] The rate of surface diffusion is affected by surface energy, temperature and adsorbent properties.[206,207] In the internal pores of porous materials, $CO_2$ molecules are transported by diffusion through the pores.[208,209] The efficiency of pore diffusion depends on factors such as pore size, pore structure and molecular size.[210–212] Depending on the difference in pore size relative to molecular size, pore diffusion can be divided into two types: Knudsen diffusion[213,214] and ordinary diffusion.[215,216] When the pore size is close to or smaller than the mean free path of gas molecules, the frequency of collisions between molecules and pore walls is higher than the frequency of collisions between molecules. This diffusion mode is called Knudsen diffusion. When the pore size is larger, the frequency of intermolecular collisions is higher. The normal diffusion behavior at this time is similar to the molecular diffusion in the gas phase.

The diffusion law of LCC in the solid phase is mainly affected by the microstructure, porosity, temperature, pressure and surface interaction of the solid material. High temperature increases the molecular motion energy in the solid material, thereby accelerating the diffusion rate.[217] The surface energy and chemical properties of the solid material affect the surface diffusion rate.[218] High surface energy helps to increase the diffusion rate. The higher the density and crystallinity of the material, the more complex the molecular diffusion path and the lower the diffusion rate.[102,219] The adsorption capacity of the solid material for $CO_2$ affects its movement rate and diffusion efficiency on the material surface. Materials with stronger adsorption may slow down the diffusion of $CO_2$.[42,93]

In the solid-phase diffusion process of LCC, the classical diffusion model, molecular diffusion model, pore diffusion model and macroscopic mass transfer model each play an important role. The following are their applications and roles in the process:

*2.1.2.1 Classical diffusion model.* Adolf Fick established the diffusion equation to describe the migration of substances from high to low concentration areas, indicating that the flux of substances through a unit cross-sectional area is proportional to the concentration gradient. This is known as Fick's first law, expressed as:[220]

$$J = -D\frac{\partial C}{\partial x} \tag{1}$$

where $J$ is the diffusion flux (kg $(m^2\ s)^{-1}$), $D$ is the diffusion coefficient ($m^2\ s^{-1}$), and $C$ is the concentration (kg $m^{-3}$). For a three-dimensional diffusion system, eqn (2) becomes:[220]

$$J = -D\left(i\frac{\partial C}{\partial x} + j\frac{\partial C}{\partial y} + k\frac{\partial C}{\partial z}\right) = -D\nabla C \tag{2}$$

where $i, j, k$ are unit vectors in the $x, y, z$ directions, and $\nabla$ is the gradient operator. Fick's first law is applicable to steady-state diffusion, where the concentration gradient remains constant over time. However, in most diffusion processes, the concentration changes with time, and conservation of mass gives:[220]

$$\frac{\partial C}{\partial t} = \frac{\partial J}{\partial x} \tag{3}$$

Substituting eqn (1) into this, we obtain:[220]

$$\frac{\partial C}{\partial t} = \frac{\partial}{\partial x}\left(D\frac{\partial C}{\partial x}\right) = D\frac{\partial^2 C}{\partial x^2} + \frac{\partial D}{\partial x}\cdot\frac{\partial C}{\partial x} \tag{4}$$

If the diffusion coefficient $D$ is assumed constant with respect to $x$, the equation simplifies to:[221]

$$\frac{\partial C}{\partial t} = D\frac{\partial^2 C}{\partial x^2} \tag{5}$$

Eqn (5) is known as Fick's second law, describing the rate of change of concentration over time in non-steady-state diffusion.

In one-dimensional non-steady-state diffusion, we can use the Gaussian solution of eqn (4) to calculate the proportion $P(x,t)$ of diffusing species at any position $x$ and time $t$, assuming all molecules start at position $x = 0$ at $t = 0$:[221]

$$P(x,t) = \frac{e^{-\frac{x^2}{4Dt}}}{\sqrt{4\pi Dt}} \tag{6}$$

The mean square displacement (MSD) at time *ttt* is given by:[222]

$$\overline{x^2}(t) = \int_{-\infty}^{\infty} x^2 P(x,t)\mathrm{d}x = \int_{-\infty}^{\infty} x^2 \frac{e^{-\frac{x^2}{4Dt}}}{\sqrt{4\pi Dt}} = 2Dt \tag{7}$$

This relationship between MSD, diffusion coefficient, and time is known as Einstein's diffusion equation. From this, we can derive the self-diffusion coefficient $D_s$ in three

 

dimensions as:[222]

$$D_s = \frac{\mathrm{MSD}}{6t} \quad (8)$$

In larger spaces, molecular collisions dominate the diffusion coefficient, but as the pore size decreases, collisions between gas molecules and pore walls become more frequent, altering the diffusion mechanism. The average free path $\bar{\lambda}$ between two collisions is related to the gas molecular diameter $d$, temperature $T$, and pressure $p$ by:[223]

$$\bar{\lambda} = \frac{k_B T}{\sqrt{2} p \pi d^2} \quad (9)$$

Knudsen introduced a dimensionless number, the Knudsen number $K_n$, which compares the average free path to the pore size to assess the effect of pore dimensions on diffusion:[224]

$$K_n = \frac{\bar{\lambda}}{d_{pore}} \quad (10)$$

For $K_n \to 0$, diffusion is a free molecular flow, described by Euler's equations. For $K_n < 0.01$, it follows a viscous flow, described by the Navier–Stokes (N–S) equations. In the range $0.01 < K_n < 0.1$, boundary slip is considered in the N–S equations, and for $0.1 < K_n < 10$, the flow is in a transition region, no longer considered continuous. When $K_n > 10$, the Boltzmann equation governs molecular diffusion.

For small $K_n$, molecular diffusion is dominant, and the diffusion coefficient $D_{AB}$ for species A in background gas B can be estimated using Fuller's equation:[224]

$$D_{AB} = \frac{0.001858 T^{\frac{3}{2}} \left(\frac{1}{M_A} + \frac{1}{M_B}\right)^{\frac{1}{2}}}{p \sigma_{AB}^2 \Omega_D} \quad (11)$$

where $T$ is temperature (K), $M_A$ and $M_B$ are the molecular weights of A and B (kg kmol$^{-1}$), $p$ is pressure (atm), $\sigma_{AB}$ is the average collision diameter, and $\Omega_D$ is the molecular collision integral based on the Lennard-Jones potential.

For larger Knudsen numbers, Knudsen diffusion, governed by collisions between molecules and pore walls, can be modeled using the elastic ball model:[224]

$$D_{AK} = \frac{d_{pore}}{3} \sqrt{\frac{8RT}{\pi M_A}} \quad (12)$$

where $d_{pore}$ is the pore diameter (m), $R$ is the ideal gas constant (8.314 J (mol K)$^{-1}$), $T$ is temperature (K), and $M_A$ is the molecular weight of species A (kg kmol$^{-1}$).

For the transition region, where both molecular and Knudsen diffusion contribute, the effective diffusion coefficient $D_{AE}$ is given by:[225]

$$D_{AE} = \frac{1}{\frac{1}{D_{AB}} + \frac{1}{D_{AK}}} \quad (13)$$

This formulation covers both molecular and Knudsen diffusion and provides a comprehensive approach to understanding LCC diffusion in various media.

*2.1.2.2 Molecular diffusion model.* The diffusion coefficient obtained from Knudsen diffusion considers only collisions between gas molecules and pore walls, neglecting intermolecular interactions and forces such as van der Waals forces and electrostatic interactions.[226] This simplification is insufficient to fully reflect the effects of the physical and chemical properties of gas molecules and nanoporous materials on mass transfer.[227]

Recently, with advancements in computational power, molecular dynamics (MD) simulations have become an effective tool for predicting mass transfer properties in nanoporous materials.[97,228] MD simulates the motion of atoms or molecules under long-range and short-range interactions, and it serves as an important complement to experimental techniques, especially in cases where experiments at the nanoscale are difficult.[229]

In MD simulations, the position and velocity of each particle are governed by Newton's equations of motion.[230] Particles' initial velocities are typically assigned randomly according to the Maxwell–Boltzmann distribution.[231] The acceleration of each particle is determined by its mass and the net force applied to it, making the identification of the forces acting on particles critical for MD simulations.

The force field in MD simulations uses potential energy functions to describe interactions between particles, including bond stretching, bond angle bending, torsion, van der Waals forces, and electrostatic interactions.[232,233] A classical potential function used in MD simulations is the Lennard-Jones potential, proposed by John Lennard-Jones in 1924, which is still widely used today. The expression is:[234]

$$V(r_{ij}) = 4\varepsilon \left[ \left(\frac{\sigma}{r_{ij}}\right)^{12} + \left(\frac{\sigma}{r_{ij}}\right)^{6} \right], \quad r_{ij} \le R_c \quad (14)$$

where $V$ is the potential energy between particles $i$ and $j$, $r_{ij}$ is the distance between them, $\varepsilon$ is the depth of the potential well, $\sigma$ is the particle diameter, and $R_c$ is the cutoff radius beyond which interactions are negligible. The Lennard-Jones potential demonstrates that the repulsive force between two particles decays as the 12th power of the inverse distance, while the attractive force decays as the 6th power. This results in repulsion at short distances and attraction at longer distances, with both forces rapidly decreasing as the distance increases.

With the advancement of MD force fields, more accurate and specialized force fields have been developed, such as the CVFF force field for inorganic systems,[235] the COMPASS force field for polymer systems,[236] and the ReaxFF force field, which can model bond-breaking processes.[237]

*2.1.2.3 Pore diffusion model.* In porous media, mass transfer is also influenced by the complex pore structure. While pore dimensions, shape, and connectivity can be directly modeled based on structural images, this approach often results in large computational demands and is not practical for systems with many pores.[238,239] A common simplification is to replace the complex-shaped pores with a network of interconnected pore elements, creating a pore network model (PNM).[240]

In this model, the elements include pore bodies and the throats connecting them. The geometric shapes of the pores

and throats are idealized, but the model preserves important characteristics of the original porous medium, such as topology, pore position, spatial correlations, and pore volume.[241] This simplification significantly improves computational efficiency in large-scale pore flow calculations.

*2.1.2.4 Macroscopic mass transfer model.* In practical engineering applications, external mass transfer effects on adsorption and reaction processes in porous media often need to be considered. The governing equations used in computational fluid dynamics (CFD) simulations vary depending on the specific needs of the model.[242] For example, in the case of incompressible viscous flow without external forces, the governing equations are as follows:

Continuity equation:[243]

$$\frac{\partial \rho}{\partial t} + \rho \nabla \cdot V = 0 \tag{15}$$

Momentum conservation equation:[244]

$$\rho \frac{\partial V}{\partial t} + \rho (V \cdot \nabla) V = -\nabla p + \mu \nabla^2 V \tag{16}$$

Energy conservation equation:[245]

$$\frac{\partial \rho e}{\partial t} + \nabla \cdot (\rho V e) + p \nabla \cdot V - \nabla \cdot (K \nabla T) = 0 \tag{17}$$

where $\rho$ is fluid density, $V$ is the velocity vector, $\mu$ is fluid viscosity, $e$ is the internal energy per unit mass, $K$ is the thermal conductivity, and $T$ is temperature.

In macroscopic mass transfer modeling, it is also necessary to consider the effects of chemical reactions, in addition to simulating flow, mixing, and heat transfer processes. By introducing source terms related to chemical reactions into the governing equations, the concentration changes caused by chemical reactions can be accounted for in the transport equations for each species.[246,247]

For chemical reactions with clear mechanisms and fewer intermediate steps, the reaction rate can be computed using the overall reaction kinetics equation.[248] For reaction $j$ involving species $i$, the reaction rate can be expressed as:[249]

$$r_j = k_j \prod_{i=1}^{P} C_i^{n_{ij}} \tag{18}$$

where $k_j$ is the reaction rate constant for reaction $j$, $C_i$ is the concentration of species $i$, and $n_{ij}$ is the reaction order of species $i$ in reaction $j$.

The source terms in the mass and energy conservation equations are then given by:[250]

$$S_i = \sum_{j=1}^{Q} a_{ij} r_j \tag{19}$$

$$S_{\mathrm{H}} = \sum_{j=1}^{Q} -\Delta H_j r_j \tag{20}$$

where $a_{ij}$ is the stoichiometric coefficient of species $i$ in reaction $j$, and $\Delta H_j$ is the reaction heat for reaction $j$.

When a chemical mechanism involves many elementary reactions and species, directly coupling the reactions into fluid calculations can be resource-intensive and time-consuming.[251] In such cases, it is important to treat reactions and components based on their time scales. Similar reaction paths can be combined, and reactions that can be neglected should be removed, leaving only the core reactions to simplify the mechanism.

In the solid-phase diffusion process of LCC, various models provide a deep understanding of the diffusion mechanism from different levels. The classical diffusion model is mainly used to describe the diffusion process under steady-state conditions and calculate the diffusion rate.[252] The molecular diffusion model focuses on the interaction between molecules at the microscopic scale, and is particularly suitable for the diffusion of $CO_2$ in nanopores.[218] The pore diffusion model takes into account the influence of pore structure on diffusion and is suitable for transport behavior in porous media.[253] The macroscopic mass transfer model combines fluid dynamics and chemical reaction processes to simulate large-scale mass transfer phenomena, and is particularly suitable for reactive diffusion.[254] In practical applications, these models complement each other and jointly reveal the diffusion mechanism of LCC in the solid phase, providing an important theoretical basis for the optimization of $CO_2$ capture, storage and conversion technologies.

The pore structure of solid materials plays a key role in the diffusion of $CO_2$.[255–257] The pore size, pore distribution and pore connectivity affect the diffusion path and rate of $CO_2$. Smaller pore sizes lead to Knudsen diffusion, while larger pore sizes lead to ordinary diffusion.[258] Smaller pore sizes and complex pore structures increase diffusion resistance and reduce diffusion rate.[259] Different types of solid materials, such as porous carbon materials, metal organic frameworks (MOFs) and zeolites, have different pore characteristics and surface properties, so the diffusion behavior of $CO_2$ in them is different.[260–263] The adsorption process in porous media adsorbents includes the steps of molecules diffusing from the gas phase to the outer surface of the adsorbent, diffusing from the outer surface of the adsorbent through the internal pores to the inner surface of the adsorbent, and adsorption on the inner surface or site of the adsorbent, as shown in Fig. 5.

To effectively control and optimize this process, inorganic porous membranes have become an ideal choice. Their unique microscopic pore structure can not only significantly improve the diffusion efficiency of gases, but also achieve selective separation of specific gases.[264–267] Traditional inorganic porous membranes

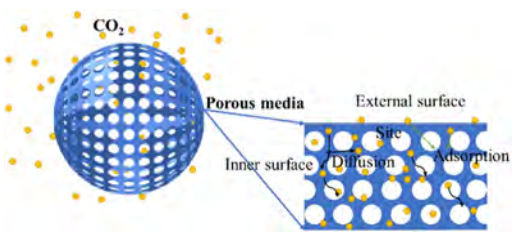


Fig. 5 Mass transfer and adsorption process of $CO_2$ molecules in porous media adsorbent.

mainly include ceramics,[268] zeolites,[269,270] carbon,[266,271] metal–organic framework materials (MOFs),[272,273] metal oxides[274,275] or metal inorganic membranes,[276,277] *etc.*

There is a regular pore structure inside the inorganic porous membrane, so it has a large specific surface area and forms a continuous gas transfer channel within the membrane. Inorganic membranes have acid, alkali, high temperature resistance and chemical stability that are unmatched by organic polymer membranes, ensuring their use under extreme working condition.[46,278] Although inorganic porous membranes have the advantages of high gas permeation flux and high gas separation selectivity.[279,280] However, its poor mechanical properties, technical problems with scale-up production, and its high cost have hindered the industrial production of inorganic porous membranes.[281,282]

The mechanism of gas permeation membranes can be roughly divided into several categories based on the differences in properties of the membrane materials. For inorganic membranes, the main mechanisms of micropore diffusion include Knudsen diffusion,[213,283] surface diffusion,[284,285] molecular sieving[286,287] and capillary condensation.[288,289] Knudsen diffusion dominates when the pore size is very small, and gas molecules mainly collide with the pore walls (Fig. 6a). Surface diffusion is the movement of molecules adsorbed on the pore wall along the surface, which is affected by the interaction between the molecules and the surface (Fig. 6b). Molecular sieving performs selective adsorption based on molecular size or shape (Fig. 6c), while capillary condensation is the condensation of gas in micropores under lower pressure due to capillary action to form a liquid phase (Fig. 6d). These mechanisms jointly determine the diffusion behavior of gas molecules in microporous materials.

For dense polymer membranes, the membrane surface is dense. Unlike porous membranes, there is no wide pore structure. Instead, the separation effect is achieved by relying on the gaps formed by the connection between polymer molecular chains and the difference in mass transfer rate of raw gas molecules in the membrane.[277,290,291] Therefore, the factors limiting the mass transfer rate are mainly the affinity of the molecular chain to the gas and its internal microporous structure. In contrast, the permeation mechanism of organic polymer membranes is usually a dissolution–diffusion mechanism[292,293] or a double adsorption model.[294,295]

The establishment of the dissolution–diffusion model is based on the mass transfer diffusion theory. The movement direction of gas molecules in the transmission process is random, but when there is a certain concentration gradient in the medium, the molecules show a macroscopic movement from the high concentration area to the low concentration area. This phenomenon is Fick's law of diffusion.[296] The dissolution–diffusion mechanism can be divided into three main processes:[220,224,297] (1) the raw gas to be tested passes from the feed side to the membrane surface, where it slowly dissolves and exerts a certain pressure on it. (2) The concentration pressure difference acts as a driving force, causing the gas to diffuse from the high concentration upstream to the low concentration downstream inside the membrane. (3) When the gas diffuses to the other surface of the membrane, the gas begins to desorb. The test gas molecules have different solubility and diffusivity during the process of transferring from the high concentration upstream to the low concentration downstream, thus forming different permeation fluxes.

The dual adsorption migration mechanism divides the transport of molecules in organic polymer membranes into two different adsorption types. One is that the gas molecules dissolve in the homogeneous structural region of the polymer,[298–300] and the other is that the gas molecules adsorb in the microcavities of the polymer membrane.[301,302] The two adsorption modes are based on Herry's law and Langmuir's law, respectively. The total adsorption of gas molecules is the sum of Herry dissolved $C_D$ and Langmuir adsorbed $C_H$, as shown in the following formula:[303]

$$C = C_D + C_H = k_D p + \frac{C_H b p}{1 + bp} \quad (21)$$

where $C_D$ is the Herry solubility concentration; $C_H$ is the Langmuir adsorption concentration; $k_D$ is the Henry coefficient; $p$ is the gas permeation pressure; $b$ is the Langmuir affinity parameter.

Evaluating the diffusion regulation of $CO_2$ at low concentrations in the solid phase has significant practical implications overall. Enhancement of industrial gas separation efficiency, optimization of gas separation and purification technology, and advancement of carbon capture and storage technology are all dependent on it. Optimizing the material performance of catalytic processes and energy storage (such as batteries and supercapacitors) also depends heavily on the investigation of these principles. In the SCR denitrification process, the diffusion behavior of $CO_2$ may affect the transmission efficiency of reactants and products on the catalyst surface.[304,305] Based on the diffusion law of LCC, it can help design more effective catalysts, optimize reaction conditions, improve the conversion efficiency of NOx, and thus reduce pollution emissions.[306,307] In reactions such as synthesis gas preparation and carbon dioxide hydrogenation, the diffusion characteristics of $CO_2$ directly affect the selection and optimization of catalysts.[308–310] The diffusion law of LCC can help researchers design catalysts with optimized pore size and surface properties to enhance $CO_2$ adsorption and reaction rate.[311,312]

In lithium-ion batteries, the performance of electrode materials is closely related to the diffusion of $CO_2$.[313–315] $CO_2$ may

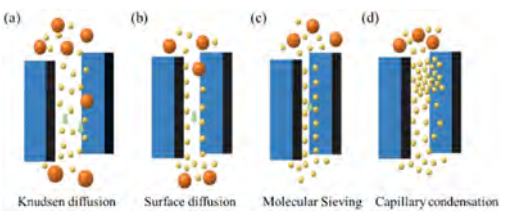


Fig. 6 Transfer mechanism of porous membranes: (a) Knudsen diffusion; (b) surface diffusion; (c) molecular sieving; (d) capillary condensation.

form in graphite electrodes, and controlling its diffusion behavior can help prevent the degradation of electrode materials and extend battery life.[316–318] In supercapacitors, the microporous structure of electrode materials has a significant impact on gas diffusion. The diffusion rules of LCC in these materials can help optimize electrode design and improve capacitance and cycle stability[319–321] In solid-state batteries, $CO_2$ may diffuse through the solid electrolyte. Exploration through their diffusion mechanisms can help develop more stable and efficient electrolyte materials, preventing gas-induced material degradation and performance loss.[322,323]

Some hydrogen storage materials may release $CO_2$ during storage or desorption. Carbon-based materials such as activated carbon and carbon nanotubes may adsorb $CO_2$ from the air while adsorbing hydrogen, and may also release $CO_2$ when releasing hydrogen.[324–326] MOFs may undergo hydrolysis during hydrogen storage, especially in the presence of water, resulting in decomposition of organic ligands and the production of $CO_2$.[327–329] Chemical hydrogen storage materials such as sodium borohydride ($NaBH_4$) may release byproducts such as sodium carbonate when reacting with water to produce hydrogen, which may decompose to produce $CO_2$ under certain conditions.[330,331] Formate compounds such as sodium formate also release $CO_2$ when catalytically decomposed to produce hydrogen.[332–334] Complex hydrides such as $LiBH_4$ and $Mg(BH_4)_2$ may react with $CO_2$ in the environment during hydrogen storage and desorption to produce carbonates and release some $CO_2$.[335–337] These phenomena are of great significance for material design, optimization of hydrogen storage efficiency and service life.

A variety of characterization and testing methods have been developed for the pore structure of $CO_2$ in porous media and the diffusion process therein.[338,339] These methods have different scopes of application, spatiotemporal resolution, and revelation of diffusion mechanisms, as shown in Table 2. Early porous media diffusion characterization methods mainly calculated the diffusion coefficient by measuring the rate of gas adsorption or desorption by porous media particles, usually under the condition of controlling the initial value and change rate of gas partial pressure.[340,341] This method is suitable for systems with slow adsorption and desorption rates and has high reliability. However, when the $CO_2$ adsorption and desorption rates are fast, the measurement results are easily affected by the external mass transfer rate and cannot accurately reflect the true situation of the diffusion process. With the deepening of research, new methods such as the zero-length column method have been proposed and widely used.[342,343] The zero-length column method can obtain key parameters such as the limiting diffusion rate, Henry constant, and surface resistance in one experiment by adjusting the $CO_2$ gas flow rate. Its advantage is that it can quickly obtain the mass transfer characteristics of porous media, especially suitable for large-scale screening of the diffusion properties of different materials. However, this method still conducts experiments at a macroscopic scale, and the overall diffusion coefficient of the gas in the porous medium particles is obtained, which cannot deeply study the local non-uniform pore structure or microscopic diffusion mechanism.[99,344]

To solve this problem, microscopic imaging techniques such as interference microscopy (IFM) and infrared microscopy (IRM) have been applied. These methods have become powerful tools for capturing the evolution of gas concentration during transient adsorption and desorption of porous media due to their high temporal and spatial resolution. IRM measures gas concentration by analyzing the infrared absorption spectrum at a specific position, with a spatial resolution of usually 5–10 μm and a minimum of 2.7 μm.[347,348] IFM determines gas concentration by the interference image of light transmitted through

Table 2 Comparison of the application scope, principle and technical characteristics of different gas–solid diffusion characterization methods

| Experimental methods | Scope of application | Principle | Technical features | Ref. |
|---|---|---|---|---|
| Frequency response method | Macro method | Impose disturbances on the diffusion system and characterize the diffusion by collecting response signals | Can simultaneously measure multiple kinetic processes in diffusion | 338 and 339 |
| Chromatography method | | Let the fluid flow through the chromatographic column containing the sample and characterize the diffusion by the change in the chromatographic signal | Applicable to diffusion tests of complex fluid components | 340 and 341 |
| Zero length column method | | Characterize the diffusion by the adsorption/desorption process of the gas in the sample | Applicable to tests of diffusion within sample lattices | 342 and 343 |
| Diffusion cell method | | Characterize the diffusion by measuring the change in concentration on both sides of the membrane | Applicable to tests of membrane diffusion | 99 and 344 |
| IFM | >0.5 μm | Characterize the structure and diffusion by the interference pattern generated by the coherent light beam in the sample | Track transient concentration change curves and lattice changes | 345 and 346 |
| IRM | >2.7 μm | Illuminate the sample with infrared light and characterize the diffusion by the spectral information | Simultaneously measure self-diffusion coefficients and transport diffusion coefficients | 347 and 348 |
| PFG-NMR | 100 nm–100 μm | Characterize the diffusion by the attenuation of the echo amplitude of the atom within the pulse time interval | Determine the diffusion coefficients of molecules in confined spaces | 349 and 350 |
| QENS | >10 nm | Characterize the diffusion by the small change in neutron energy before and after scattering | Measure molecular displacements in shorter times and smaller spaces | 351 and 352 |

 

the porous medium lattice and non-transmitted light, with a spatial resolution of up to 0.5 μm.[345,346] The combined use of IRM and IFM can directly observe the gas diffusion process at the micrometer scale, which is particularly suitable for studying the diffusion behavior of gas in molecular sieves or metal organic frameworks. However, the high cost of these technologies and the complexity of the equipment limit their popularity. At the nanoscale, pulsed gradient field nuclear magnetic resonance (PFG-NMR) technology has also been widely used.[349,350] This technology can track the self-diffusion coefficient of gas molecules in porous media through the attenuation of spin echo signals, and can track the smallest molecular displacement (as low as 100 nm). Quasi-elastic neutron scattering (QENS) technology has a high sensitivity to molecular nanoscale displacement and can accurately measure the diffusion coefficient in nanopores, which is particularly suitable for gas transport research in nanopores.[351,352] However, the experimental conditions of these technologies are harsh, high-end equipment is required, and sample preparation and data analysis are relatively complicated.

Compared with the diffusion test method in the solid phase, the diffusion study of $CO_2$ in the liquid phase focuses on the gas dissolution and diffusion process.[109,353] The diffusion coefficient in the liquid phase often depends on the properties of the liquid (such as viscosity, temperature, solubility, *etc.*) and the pore structure of the liquid.[137,354] The test methods for liquid phase diffusion include dew point method, dynamic light scattering (DLS) and conductivity method. The dew point method calculates the diffusion coefficient by measuring the concentration change of $CO_2$ dissolved in the liquid.[355] It is easy to operate, but it is only applicable to the study of low-concentration $CO_2$, and cannot directly obtain the microscopic distribution information of the diffusion coefficient.[356] DLS technology calculates the diffusion coefficient of $CO_2$ by analyzing the diffusion rate of particles in the liquid.[144] It can provide a higher spatiotemporal resolution, but the measurement of high-concentration $CO_2$ solutions may be interfered.[357] The conductivity method uses the change of liquid conductivity to measure the dissolution process of $CO_2$. It has the advantages of simplicity and low cost.[358] It is suitable for large-scale monitoring of $CO_2$ dissolution behavior, but the change of conductivity is more complicated and may be affected by other ions or dissolved substances in the solution.[359]

In the solid phase and liquid phase, the diffusion test methods of $CO_2$ have their own advantages and disadvantages. Methods in the solid phase, such as the zero-length column method and PFG-NMR technology, can analyze the diffusion behavior of gases in porous media at the macro and micro scales, but often cannot go deep into the details of the local pore structure.[149,360] Liquid phase methods, such as the dew point method and DLS, focus on the dissolution and diffusion processes, and can provide more direct dissolution rate and diffusion coefficient data, but are greatly affected by the properties of the liquid and cannot fully reveal the subtle diffusion process of gas molecules in the liquid phase.[100,361] The selection of an appropriate test method needs to be determined based on the research objectives, experimental environment, and the required spatiotemporal resolution. Usually in practical applications, a combination of different methods can provide more comprehensive diffusion characteristics information.

### 2.2 Adsorption characteristics

There are significant differences in the adsorption characteristics of LCC and high-concentration $CO_2$. The adsorption of LCC is usually dominated by weak interactions on the material surface, and the adsorption process is relatively mild.[41,42] This process generally relies on physical adsorption mechanisms such as van der Waals forces. In this case, the adsorption capacity and rate of $CO_2$ are low, but the requirements on the pore structure and surface properties of the material are relatively loose.[362,363] In contrast, the adsorption of high-concentration $CO_2$ may involve stronger chemical interactions or more complex adsorption mechanisms, such as chemical adsorption or multi-layer adsorption. At high concentrations, the adsorption capacity of $CO_2$ is usually larger because the concentration gradient is significant and saturation may occur on the material surface, resulting in accelerated adsorption rates and possibly stronger surface interactions.[218,259]

**2.2.1 Adsorption isotherm.** The adsorption isotherm describes the relationship between the amount of adsorbate (such as $CO_2$) adsorbed on the adsorbent surface and the equilibrium gas phase concentration under constant temperature conditions.[364–366] Researchers have widely used classic isotherm models such as Langmuir, Freundlich and Temkin to describe the adsorption characteristics of LCC (Table 3). These models help determine the adsorption capacity, adsorption energy and adsorption uniformity of $CO_2$ on the material surface. Among them, the Langmuir model is suitable for describing monolayer adsorption, indicating that $CO_2$ molecules form a monolayer adsorption on the material surface, which is suitable for descriptions under medium and low concentration conditions.[367–369] The Freundlich model is suitable for describing multilayer adsorption and heterogeneous surfaces, and is suitable for adsorption behavior under low concentration conditions.[370,371] The Temkin model takes into account the change in surface energy and is suitable for describing adsorption behavior under medium concentrations.[372,373]

The porosity and pore size of the material have a significant impact on the adsorption isotherm of LCC.[379,380] Materials with large pore sizes usually have higher adsorption capacity but exhibit slower adsorption rates at low concentrations. Wang *et al.*[381] found porous carbons with a bimodal pore size distribution of well-separated mesopores (3–7 nm) and micropores ($<2$ nm) to be most promising. The functional groups and chemical activity on the material surface significantly affect the shape of the adsorption isotherm and the adsorption capacity. Materials with higher surface affinity generally exhibit higher initial adsorption rates at low concentrations of $CO_2$. In the study of amine functionalized inorganic materials, focus is placed on the selection of organic amine species and the characteristics of inorganic carriers. According to the type and synthesis method of organic amines, this type of materials is roughly divided into three categories, as shown in Fig. 7.

Table 3 Common linear and nonlinear isotherm models applicable to low $CO_2$ concentrations

| Isothermal model | Linear | Nonlinear | $CO_2$ concentration range | Ref. |
|---|---|---|---|---|
| Langmuir | $\frac{C_e}{q_e} = Q_0 - \frac{q_e}{bC_e}$<br>$q_e = Q_0 - \frac{q_e}{bC_e}$<br>$\frac{1}{q_e} = \frac{1}{Q_0} + \frac{1}{bQ_0C_e}$<br>$\frac{q_e}{C_e} = bQ_0 - bq_e$ | $q_e = \frac{bQ_0C_e}{1+bC_e}$ | 0–1000 ppm | 374 |
| Henry | $q_e = K_{HE}C_e$ | — | 0–100 ppm | 375 |
| Freundlich | $\log q_e = \log K_F + \frac{1}{n}\log C_e$ | $q_e = \frac{1}{n}K_FC_e$ | 100 ppm to several thousand ppm | 376 |
| Temkin | $q_e = \frac{RT}{b_T}\ln A_T + \frac{RT}{b_T}\ln C_e$ | $q_e = \frac{RT}{b_T}\ln A_TC_e$ | 100 ppm to several thousand ppm | 377 |
| Toth | $\ln\left(\frac{q_e}{K_T}\right) = \ln C_e - \frac{1}{t}\ln(a_T + C_e)$ | $q_e = \frac{K_TC_e}{(a_T + C_e)^{\frac{1}{t}}}$ | 0 to several thousand ppm | 378 |

Studies have shown that primary amines have higher heat of adsorption than secondary and tertiary amines, and therefore exhibit higher $CO_2$ capture efficiency. Further research revealed that this phenomenon is mainly driven by entropy effects.

Temperature has a significant effect on the adsorption isotherm of LCC.[382,383] In general, higher temperatures reduce the adsorption capacity of $CO_2$. High temperatures increase the kinetic energy of $CO_2$ molecules and reduce their residence time on the surface of the material. At low concentrations, pressure has little effect on the adsorption isotherm. However, as pressure increases, the adsorption capacity of $CO_2$ gradually increases, which is reflected in the nonlinear change of the isotherm.[384,385]

**2.2.2 Adsorption kinetics.** Adsorption kinetics describes the changes in the adsorption process over time, and mainly studies the mass transfer process of the adsorbate from the gas phase or liquid phase to the surface of the solid phase adsorbent.[386–388] Pseudo-first-order, pseudo-second-order, and intraparticle diffusion models are examples of frequently used kinetic models. The adsorption rate, mechanism, and influencing variables are the primary components of the LCC adsorption kinetics. The adsorption of LCC is usually carried out through physical adsorption mechanisms, such as van der Waals force and hydrogen bonding, and the adsorption rate is slow.[389,390] Kinetic models such as pseudo-first-order and pseudo-second-order models are widely used to describe the adsorption process of $CO_2$ on solid materials.[42,391] Surface diffusion dominates the diffusion behavior of $CO_2$ under low concentration conditions because the coverage of $CO_2$ on the material surface is low. The increase in temperature affects the molecular motion energy of $CO_2$, thereby changing the adsorption rate. The pore structure and surface chemical properties of the material also have an important influence on the adsorption kinetics.[218,258,392,393]

When the adsorption rate of gas molecules on the inner surface or site of the adsorbent is fast, the internal and external diffusion steps of the molecules are the rate-controlling steps in the adsorption process. The adsorption rate under diffusion control can be described by the pseudo-first-order adsorption kinetic equation:[394,395]

$$\frac{dq_t}{dt} = k_1(q_e - q_t) \quad (22)$$

where $t$ is time; $q_t$ is the adsorption amount per unit mass of adsorbent; $q_e$ is the adsorption amount per unit mass of adsorbent at equilibrium; $k_1$ is the pseudo-first-order rate constant.

For the diffusion-controlled adsorption process, the adsorption rate can be increased and the adsorbent performance can be improved by strengthening the transmission of gas molecules in the adsorbent. Cao *et al.*[396] prepared CHA molecular sieves with a multi-level pore structure by combining the template method with the directional induced crystallization method. The rich pore structure improves the diffusion rate of $CO_2$ molecules in the molecular sieve, improves the adsorption and separation efficiency of $CO_2$, and reduces the regeneration energy consumption. Chen *et al.*[397] prepared carbon materials with multi-level pores for $CO_2$ adsorption. It was found that the introduction of macropores and mesopores ensures the rapid diffusion of $CO_2$ in the material, so that the adsorption rate of $CO_2$ reaches 0.5 mmol $g^{-1}$ $min^{-1}$. Liu *et al.*[398] synthesized nitrogen-doped multi-level porous carbon materials by a one-step method. It was found that the presence of mesopores can enhance diffusion and improve the accessibility of the inner surface of the material, so that the $CO_2$ adsorption capacity of the material reached 5.56 mmol $g^{-1}$, which is better than the same type of non-multi-level porous adsorbents.

When there are many adsorption sites on the surface of porous media, gas molecules are mainly adsorbed by chemical adsorption. The reaction between molecules and sites may become the rate-determining step of the adsorption process. In this case, a pseudo-second-order adsorption kinetic equation is needed to describe the adsorption rate under reaction control:[399,400]

$$\frac{dq_t}{dt} = k_2(q_e - q_t)^2 \quad (23)$$

where $k_2$ is the pseudo-second-order rate constant.

 

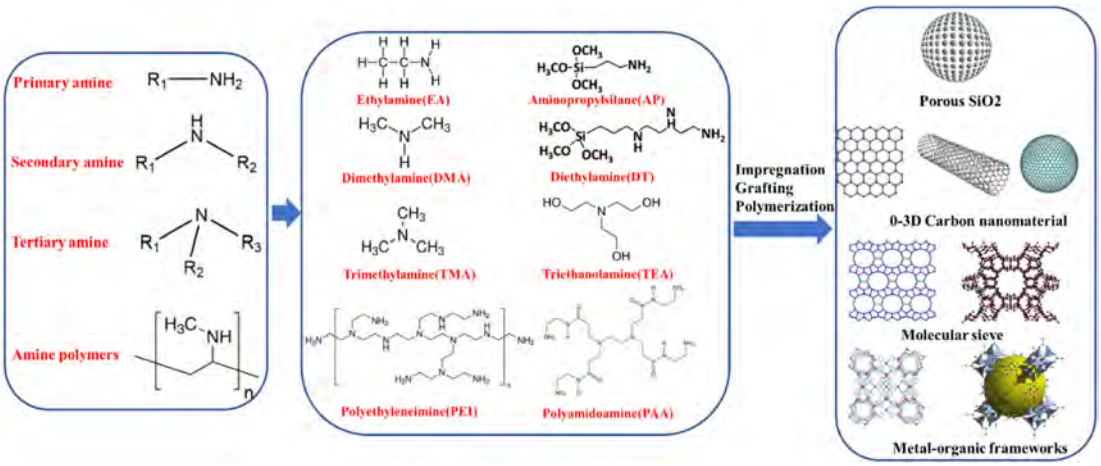


Fig. 7 Common amine-functionalized inorganic materials and their synthesis methods.

By introducing sites into the adsorbent material, the selectivity and adsorption capacity of the adsorbent material can be effectively improved. For example, amino-functionalized materials have become one of the research focuses of $CO_2$ adsorbent materials. Ma *et al.*[401] introduced PEI modification into the mesoporous molecular sieve and achieved an adsorption capacity of 140 mg $CO_2$ per g at a $CO_2$ partial pressure of 15 kPa. Martinez *et al.*[402] introduced TEPA modification into the ZIF-8 adsorbent material, so that its $CO_2$ adsorption capacity in the post-combustion water-containing flue gas reached 104 mg $CO_2$ per g. Lin *et al.*[403] prepared a 50%-PEI-modified SBA-15 adsorbent, which achieved large-capacity and rapid adsorption of $CO_2$, with an adsorption capacity of 182.1 mg $CO_2$ per g and an adsorption rate peak of 350 mg $g^{-1}$ $min^{-1}$ (Fig. 8a and b). Although the diffusion process is not the key step in determining the adsorption rate in the above materials, it still has an important influence on the adsorption performance of the material. Wu *et al.*[404] studied the mass transfer and adsorption process of $CO_2$ in amino-modified carbon materials. It was found that after the introduction of amino groups, a thin layer of about 23.7 nm was formed on the micropores and mesopores of the material, which reduced the specific surface area from 223 $m^2$ $g^{-1}$ to 21 $m^2$ $g^{-1}$. The diffusion of $CO_2$ was also reduced due to the reduction in pore size. In addition, the capillary condensation of $H_2O$ in the micropores increased the mass transfer resistance of $CO_2$. Goeppert *et al.*[405] found that under a relative humidity of 67%, a 33% PEI loading increased the $CO_2$ adsorption capacity of mesoporous silica by 50%. However, when the PEI loading was increased to 50%, the $CO_2$ adsorption capacity decreased due to the condensation of $H_2O$ and pore blockage.

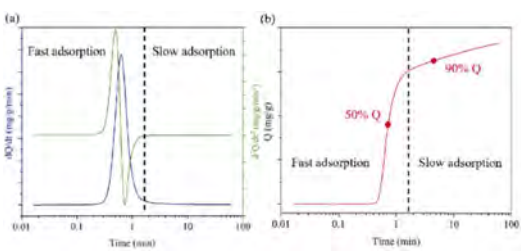


Fig. 8 (a) First-order (blue line) and second-order derivative (green line) curves and adsorption curve (b) of 50%-PEI-modified SBA-15 adsorbent (adapted with permission from ref. 403. Copyright 2023 Elsevier).

Although the capacity and selectivity of porous media adsorption materials can be improved by introducing adsorption sites, the loading amount and loading method of the sites need to be reasonably selected. Otherwise, it will cause clogging of the pore channels, hinder gas diffusion, and significantly reduce the adsorption efficiency.[406–408]

Compared with LCC, the adsorption kinetics of high-concentration $CO_2$ show significant differences. The adsorption process of high-concentration $CO_2$ involves more chemical adsorption and multi-layer adsorption mechanisms, the adsorption rate is usually faster, and saturation may occur on the material surface.[409,410] Pseudo-first-order and pseudo-second-order kinetic models may no longer be applicable under high concentration conditions, and more nonlinear models are needed to describe the complex adsorption process.[411–413] Temperature and pressure have a greater effect on the adsorption rate at high $CO_2$ concentrations. The rate and adsorption capacity of $CO_2$ will both be greatly increased by an increase in pressure.

The difference in adsorption kinetics between low and high concentrations of $CO_2$ is critical for optimizing gas separation, purification technology and CCS technology. The adsorption mechanism of LCC helps to improve the efficiency of low-concentration gas treatment,[92,389,414,415] while the adsorption mechanism of high-concentration $CO_2$ is of great significance in improving the efficiency of carbon capture, storage stability, and catalytic reaction processes.[387,416–418]

**2.2.3 LCC adsorption.** Current carbon capture technologies cover a variety of methods, each with its own unique advantages and limitations, as shown in Fig. 9. Chemical absorption (such as amines) is widely used in the industrial field due to its high adsorption performance and technical maturity.[418,419] However,

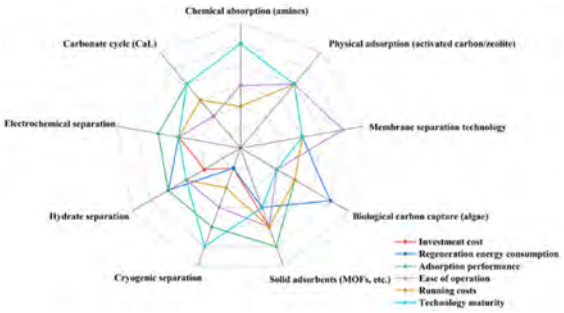


Fig. 9 Key indicator evaluation of carbon capture technology.

its regeneration energy consumption and operating costs are high. Physical adsorption (activated carbon, zeolite) and solid adsorbents (such as MOFs) are relatively superior in investment cost and energy consumption, and are suitable for the capture of medium and low concentrations of $CO_2$.[259,420,421] Membrane separation technology has attracted much attention due to its ease of operation and flexibility, but the separation efficiency and economy still need to be optimized.[46,291] Hydrate separation has certain advantages in energy consumption, but its high pressure and low temperature conditions limit its industrial application.[422,423] Electrochemical separation technology has shown good potential in LCC capture, but its current maturity needs to be improved.[424,425] Cryogenic separation technology is suitable for the separation of high-concentration $CO_2$, but its high energy consumption limits its scope of application.[36,426] Carbonate cycle (CaL) has outstanding performance in carbon capture capacity and long-term stability, but its operation complexity is relatively high.[427] In general, different technologies need to be selected in combination with application scenarios, and continuous improvement is needed to improve economic efficiency and feasibility, so as to achieve widespread promotion and application.

The adsorption technique makes advantage of a solid surface's ability to adsorb liquid or gas molecules. In carbon capture, high-concentration $CO_2$ is produced by desorption after directed $CO_2$ adsorption is achieved using porous solid adsorbents. It may be separated into pressure swing, electric swing, and temperature swing adsorption based on the variations in the adsorption process.[36–38] Commonly used adsorbents include carbon-based materials (activated carbon, activated carbon fiber, carbon nanotubes, *etc.*),[428,429] alkali metal-based materials[430,431] and solid amine materials.[432,433]

For LCC, it is necessary to improve the selectivity of the adsorbent to achieve directional adsorption of $CO_2$ in mixed gases.[419,434,435] In addition to selectivity, adsorption capacity, adsorption rate, desorption rate and regeneration performance are all important indicators for evaluating the quality of adsorbents.[21,406,436,437] Physical adsorbents have the advantages of fast adsorption and desorption rates, large adsorption capacity, and good recycling performance in capturing LCC, and are therefore considered a research hotspot.[92,259,408,438]

The above carbon capture methods have different scopes of application according to their own characteristics. For high-concentration $CO_2$, separation and purification are relatively easy.[87–89] However, for LCC, it is necessary to comprehensively consider factors such as gas composition, $CO_2$ concentration, operating conditions, operating costs, and material and energy consumption to determine the optimal carbon capture method.[26,31,46,47] Among them, the adsorption method is widely considered to be one of the most suitable technologies for LCC capture due to its advantages such as simple equipment, high degree of automation, many types of adsorbents, long service life and easy regeneration, no by-products, and low operating costs.[31,90,439]

*2.2.3.1 Common adsorbents based on LCC.* Chemical and physical adsorption are the two categories of adsorption techniques. Compared to chemical adsorption, physical adsorption is easier to implement. The adsorbent is extensively utilized, has a low energy consumption, and performs well in regeneration.[440–442] However, for the adsorption method, the core is the selection of adsorbents. High-efficiency and high-quality adsorbents need to have the advantages of large gas adsorption capacity, good selectivity, fast adsorption and desorption rate, and low preparation and regeneration cost.[443,444] The research and development of adsorbents has always been the focus of $CO_2$ capture using the adsorption method. At the moment, graphene, carbon nanotubes, zeolite molecular sieves, activated carbon, and activated carbon fibers are the most widely utilized adsorbents (Table 4).

Zeolites usually have a high specific surface area and pore volume, can provide a large number of adsorption sites, and have a certain selectivity for $CO_2$.[445–447] However, compared with MOFs and carbon-based materials, their selectivity is lower. Zeolites usually have good thermal stability and mechanical strength and are easy to regenerate.[448–450] Zeolites, as natural minerals or synthetic materials, have certain advantages in cost and preparability. X-type, A-type, Y-type, ZSM-type and some natural molecular sieves all have good $CO_2$ adsorption performance.[451,452] Harlick[453] studied the removal performance of 13 different types of zeolite molecular sieves for $CO_2$ in flue gas. The results showed that the low silicon–aluminum ratio of 13X molecular sieves led to its strong alkalinity, which enhanced the interaction with $CO_2$ and thus had the best adsorption performance. Another commonly used A (LTA) type molecular sieve in industry, such as 4A molecular sieve and 5A molecular sieve, has a larger cavity and a narrower pore. Because it contains a large amount of balanced charge, the pore size can be regulated by exchanging it with ions of larger radius. For example, the opening of NaA molecular sieve can be adjusted from 0.2 nm to 0.5 nm by using $Ca^{2+}$ exchange. A study reported[454] that NaKA molecular sieve after $K^+$ exchange can obtain an adsorption amount of 1.0 mmol $g^{-1}$ and a selectivity of nearly 1000 under the condition of about 400 mg per l $CO_2$. The adsorbed carbon dioxide presents two states: linear and curved. The curved one is carbonate, which is believed to be formed by the interaction between oxidizing ions next to the surface $K^+$ site and carbon dioxide (Fig. 10).

Currently, research on zeolite molecular sieves for $CO_2$ adsorption focuses on modifying them by adjusting the

 

Table 4 Comparison of properties of common adsorbents

| Adsorbent types | Performance characteristics | Advantages | Limitations |
|---|---|---|---|
| Activated carbon | High specific surface area (500–2000 $m^2 g^{-1}$), good thermal stability and mechanical properties | Low cost, adjustable pore structure, easy regeneration | Weak adsorption of polar water molecules, easily affected by moisture |
| Carbon nanomaterials | High conductivity, large specific surface area, good thermal stability | High conductivity suitable for electrochemical applications, can be combined with a variety of functional materials to improve adsorption performance | Expensive, low adsorption selectivity, high requirements for preparation and modification technology |
| Zeolite molecular sieves | High specific surface area (600–1200 $m^2 g^{-1}$), regular pore structure, strong polarity, good thermal stability | High selectivity for polar gases (such as $CO_2$, $H_2O$), good cycle stability | Low adsorption capacity for non-polar molecules, harsh synthesis conditions, some zeolites may be sensitive to water |
| Metal organic frameworks (MOFs) | Ultra-high specific surface area (1000–7000 $m^2 g^{-1}$), adjustable pore size and surface chemical properties | High selectivity, high specific surface area, strong design flexibility | Poor water and chemical stability, high synthesis cost, some materials are easily degraded at high temperature or in acidic environment |
| Covalent organic frameworks (COFs) | Ordered pore structure, high chemical stability, flexible functional design | High chemical stability, adjustable pore size and chemical properties, suitable for selective adsorption of specific target molecules | Complex synthesis process, low yield, some materials have weak mechanical properties |
| Polymer adsorbents | Usually hydrophobic or hydrophilic, molecular recognition can be achieved through functionalization | Low cost, flexible functional design, suitable for selective separation of specific molecules | Poor thermal stability and mechanical properties, adsorption capacity is usually lower than inorganic adsorbents |
| Silica gel | Medium specific surface area (300–800 $m^2 g^{-1}$), strong hydrophilicity, high thermal stability | Low cost, suitable for adsorption of water vapor and polar molecules | Easy to emit adsorption saturation under high temperature conditions, limited adsorption capacity |
| Alumina | Medium specific surface area (200–400 $m^2 g^{-1}$), high thermal stability | Low cost, suitable for adsorption of acidic gases (such as $H_2S$, $CO_2$) | Specific surface area and adsorption capacity are lower than activated carbon and MOFs |
| Biomass-based adsorbents | Renewable, environmentally friendly, high specific surface area and porous structure | Low cost, high sustainability, easy functionalization | Low mechanical strength, thermal stability and regeneration ability are usually insufficient |
| Ion exchange resins | Based on ion exchange mechanism, selective adsorption of specific ions | Good regeneration, high selectivity for ionic pollutants (such as heavy metals) | Usually only effective for specific molecules, limited adsorption range, poor mechanical properties |

silicon–aluminum ratio and exchanging cations in the molecular sieve structure.[382,455,456] However, zeolite molecular sieves are particularly sensitive to water vapor (strong water absorption and low selectivity). They are only suitable for carbon capture under anhydrous conditions, which limits their application areas.[457,458] In addition, zeolite molecular sieves have poor regeneration performance after adsorbing $CO_2$, high production costs and high energy consumption. Based on this, enhancing water resistance, broadening application areas and optimizing regeneration performance are the future development directions of zeolite molecular sieve adsorbents for carbon capture.[459,460]

MOFs are a type of crystalline porous coordination polymer formed by the self-assembly of metal ions or metal clusters and organic ligands. Their specific surface area can reach $1 \times 10^3$–$1 \times 10^4$ $m^2 g^{-1}$ and their adsorption capacity is strong.[420,461,462] The pore structure of MOFs is flexible in design, with adjustable pore size and pore capacity, so the adsorption capacity is usually high. Due to their adjustable pore structure and chemical functional groups, MOFs can achieve highly selective adsorption of $CO_2$.[463–465] The regeneration of MOFs depends on the stability of their structure and their stability to heat/humid environments. Millward *et al.*[466] studied the adsorption performance of 9 MOFs on $CO_2$. The results showed that the adsorption capacity of most MOFs materials for $CO_2$ is better than that of commonly used activated carbon and zeolite molecular sieves. Furukawa *et al.*[467] prepared MOF-210 materials with ultra-high porosity, and their $CO_2$ adsorption capacity can reach 54.5 mmol $g^{-1}$. MOF-177 has a $CO_2$ adsorption capacity of 1470 mg $g^{-1}$, which is twice that of 13X zeolite.[468] However, most studies have shown that MOF only exhibits high $CO_2$ adsorption capacity under high pressure conditions.[469,470] In addition, it has defects such as high production cost and poor chemical and hydrothermal stability.[471,472] The technology for industrial application is not yet mature. The adsorption performance can be further improved by loading functional groups, doping metal ions, *etc.*[402,473,474]

Carbon-based materials have rich pore structures and high surface areas, so they can also provide higher adsorption capacity.[475,476] Carbon-based materials usually have good chemical stability and selectivity, and can be designed as highly selective $CO_2$ adsorbents.[477] Carbon-based materials usually have good heat resistance and chemical stability and are easy to regenerate. Carbon-based materials are usually widely available, with relatively simple preparation processes and low costs.[478–480] As traditional adsorbents, carbon materials also have great development potential in $CO_2$ capture. For lower $CO_2$ concentrations, Coromina *et al.*[481] prepared activated carbon with high micropore content (84% of the pore volume comes from 5–7 Å) using giant fungus grass and camellia as raw materials, and the adsorption capacity can reach 1.5 mmol $g^{-1}$ at 298 K and 0.15 bar. In addition, relevant theoretical studies have shown that fulleric carbon also has good prospects for $CO_2$ capture.[482,483] However, it should be noted that a

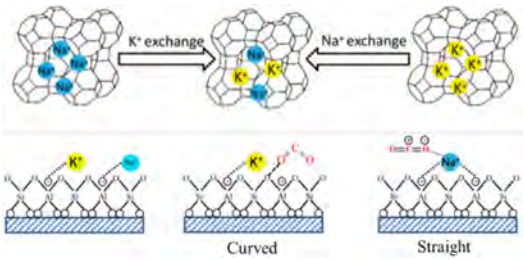


Fig. 10 Surface $CO_2$ adsorption form of NaKA molecular sieve after $K^+$ exchange (reproduced with permission from ref. 454. Copyright 1963 American Chemical Society).

considerable part of the current research on carbon material adsorption is focused on $CO_2$ capture at 1 bar pressure, while at low concentrations, it is mainly aimed at flue gas-like $CO_2$ conditions of 0.1–0.15 bar. There is a lack of systematic research on direct air capture (DAC) at lower concentrations, and some carbon materials have poor thermal stability.[484,485] Therefore, for the adsorption of lower concentrations of $CO_2$, in order to avoid the problem of low selectivity for $CO_2$ due to the non-polarity of carbon materials, it is a promising research direction to combine carbon materials with porous materials such as zeolites[486–488] and MOFs.[489–491]

Zeolites, MOFs and carbon-based materials each have their own advantages. The selection of a suitable adsorbent depends on the specific application requirements. When selecting an adsorbent, it is necessary to comprehensively consider factors such as its adsorption capacity, selectivity, regeneration, cost and preparability, and make a reasonable selection based on the actual situation.[47,492] The performance of the adsorbent can be further optimized to improve its adsorption efficiency and selectivity for LCC.

*2.2.3.2 Selective adsorption of LCC.* Selective adsorption of LCC refers to the adsorption priority of the adsorbent for $CO_2$ in a mixed gas with multiple gas components.[92,493,494] Selective adsorption is crucial in the process of $CO_2$ capture and separation. Because it can achieve high-efficiency $CO_2$ separation, reduce capture costs, and reduce energy consumption.[495,496]

Zeolites generally have pore sizes and surface chemistry that make their adsorption selectivity for $CO_2$ relatively low. The actual mechanism of $CO_2$ selective adsorption by medium-pore zeolites can change from cation-gated to cooperative cation-gated respiration to respiration, depending on the combination of their topological and compositional flexibility.[496] Decasilicon 3 R (DD3R) zeolites' flexibility was tuned *via* a template-regulated crystal transformation (TMCT) method by Du *et al.*,[497] who created superselective membranes with $CO_2/CH_4$ selectivities ranging from 157 to 1172. In addition to optimization through synthetic design of zeolites, their adsorption selectivity for $CO_2$ can also be enhanced through surface modification or modification. $CO_2$ molecules are generally highly polar and interact strongly with some adsorbents with hydrophilic or polar functional groups, resulting in highly selective adsorption. Kim *et al.*[498] improved $CO_2$ selectivity in low-$CO_2$ indoor environments by producing moisture resistance using a hydrophobic covering. Hydrophobic-coated zeolites showed a 4.1-fold improvement in $CO_2$ gas selectivity. With the use of this enhanced synthesis technique, there are more opportunities for utilizing adsorbents to absorb carbon dioxide inside. Shen *et al.*[499] found that the zeolite structure and cation distribution are related to the adsorption sites of $CO_2$ and $H_2O$, and the inhibition or co-capture of $CO_2$ and $H_2O$ can be achieved by regulating the pore structure. Subsequently, they proposed a simple and efficient technology,[500] which only requires 60 minutes of post-treatment to increase the adsorption capacity of commercial NaX zeolite by 11.5%. Through the synergistic effect of cold plasma and *in situ* $CO_2$, the co-regulation of cation distribution and pore structure is achieved (Fig. 11).

The flexibility in designing the pore structure and chemical functional groups of MOFs enables them to have good $CO_2$ selectivity. By adjusting the pore size and chemical structure of MOFs, highly selective adsorption of $CO_2$ can be achieved while excluding other gas components.[465,501,502] Qin *et al.*[503] prepared a new type of microporous two-dimensional cobalt-based MOF. It showed a more ideal selectivity for $CO_2$ adsorption than $C_2H_2$, $CH_4$, CO and $N_2$ at 298 K (1 bar) due to the pyridyl sites on the ligands and the open metal sites on the framework nodes. Cai *et al.*[504] developed an efficient photoinduced electron transfer (PIET) strategy to achieve efficient separation of $C_2H_2$, which is similar to $CO_2$ in size, shape and physical properties. Shi *et al.*[505] developed an ultramicroporous metal–organic framework

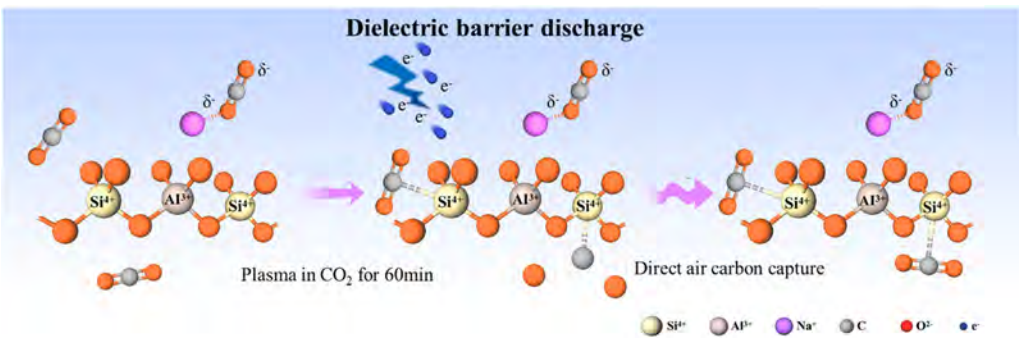


Fig. 11 Regulation of NaX based on the synergistic effect of cold plasma and *in situ* $CO_2$ (adapted with permission from ref. 500. Copyright 2024 John Wiley & Sons).

 

(Cu-F-pymo) composed of copper(II) and 5-fluoropyrimidine-2-olate and used it for the reverse separation of $CO_2$ from $C_2H_2$. Partially desolvated Cu-F-pymo can specifically capture $CO_2$ instead of $C_2H_2$. The separation ratio of over 105 is the highest value reported so far. The molecular sieving effect is attributed to the residual water molecules blocking the preferential sites of $C_2H_2$, thereby inhibiting the adsorption of $C_2H_2$.

Carbon-based materials usually have rich pore structures and surface functional groups, which can achieve selective adsorption of $CO_2$ by regulating pore size and surface chemical properties.[506,507] Some specific carbon-based materials have high $CO_2$ adsorption selectivity, such as graphene oxide and nitrogen-doped carbon nanotubes. Jin *et al.*[508] found that after Fe was inserted into rGO membrane, the increase in transmembrane pressure caused the $N_2$ diffusion mode to change from Maxwell-Stefan type to Knudsen type. It showed excellent and reproducible $N_2/CO_2$ selectivity ($\approx$97) at 110 mbar, which is an unprecedented value for graphene-based membranes. Guo *et al.*[509] enhanced the interaction with GO through silanol (Si-OH)-rich amorphous precursor particles, thereby forming a highly adhesive and stable SOD/GO membrane through strong bonds. It showed stable separation performance under water vapor (4 mol%) at high temperature (200 °C). The $H_2$ permeance was about 4900 GPU and the $H_2/CO_2$ selectivity was 56. The chemical functional groups on the adsorbent surface can interact specifically with $CO_2$ molecules, thereby achieving highly selective adsorption. Through surface modification or modification, the surface chemical properties of the adsorbent can be regulated to achieve selective adsorption of $CO_2$. Nitrogen and oxygen doped porous carbon have a significant impact on $CO_2/N_2$ selectivity due to the enhanced electrostatic interaction between the carbon surface and $CO_2$ molecules.[510] The contribution of N doping to $CO_2$ adsorption is often greater than the extremely high surface area value.[511]

Selective adsorption of LCC is a key link in $CO_2$ capture and separation technology. Adsorbents such as zeolites, MOFs and carbon-based materials achieve highly selective adsorption of $CO_2$ by regulating pore size, surface chemical properties and functional group design. The design and preparation of adsorbents can be further optimized to improve their selective adsorption performance to meet the needs of different $CO_2$ capture and separation applications.

### 2.3 Catalytic reaction characteristics

During the catalytic reaction, the characteristics of $CO_2$ molecules may change. This depends on the properties of the catalyst, the reaction conditions, and the interaction with other reactants.[512–514] $CO_2$ molecules may be adsorbed on the catalyst surface, and specific sites on the catalyst can adsorb $CO_2$ molecules and interact with other reactants.[515,516] The adsorption process may change the charge distribution and configuration of $CO_2$ molecules, affecting their activity and selectivity. Catalysts can reduce the activation energy required for $CO_2$ molecules to participate in the reaction, making it easier to react with other reactants.[43–45] Through the action of catalysts, the bond energy of $CO_2$ molecules may change, thereby lowering the energy threshold for $CO_2$ molecules to participate in the reaction. $CO_2$ molecules may form coordination bonds with catalysts on the catalyst surface to form $CO_2$-catalyst complexes. This change in coordination environment may affect the binding of $CO_2$ molecules with other reactants and the reaction path.[517,518]

In some catalytic reactions, $CO_2$ molecules may undergo redox reactions, thereby changing their oxidation state.[519–522] Catalysts can promote the redox reactions of $CO_2$ molecules, converting them into other hydrocarbons or oxides. Catalysts can adjust the selectivity of $CO_2$ molecules so that they react selectively with specific reactants to produce desired products.[523,524] By adjusting the structure and composition of the catalyst, the reaction path of $CO_2$ molecules can be controlled.[525–527] In summary, the characteristics of $CO_2$ molecules during catalytic reactions may undergo various changes, which are affected by catalysts. By adjusting the activity, selectivity and mechanism of participation of $CO_2$ molecules in the reaction, effective utilization and conversion of $CO_2$ can be achieved.

**2.3.1 Mechanism of $CO_2$ reduction reaction.** The key to $CO_2$ reduction reaction is that $CO_2$ molecules undergo chemical reactions to generate new compounds by accepting electrons and protons.[528,529] Since $CO_2$ has a low solubility in water, its adsorption state on the catalyst surface determines whether $CO_2$ reduction reaction ($CO_2$RR) or hydrogen evolution reaction (HER) will occur. Generally, $CO_2$ adsorption can be divided into physical adsorption and chemical adsorption, the latter of which is accompanied by electron transfer.[530] Typical surface coordination modes include: $CO_2$ provides electrons to the catalyst through the lone pair of electrons of oxygen atoms, carbon atoms accept electrons from the catalyst surface as electron acceptors, and oxygen and carbon act as electron donors and acceptors, respectively, to form a mixed coordination structure.[531] These adsorption modes can change the linear structure of the $CO_2$ molecule and bend it, thereby reducing the symmetry of the molecule and the LUMO (lowest unoccupied molecular orbital) energy level, making $CO_2$ more likely to accept electrons and form reactive species[532,533] (Fig. 12).

During the $CO_2$ reduction process, the reaction usually involves the stepwise transfer of multiple electrons, and the types of intermediates and final products generated vary depending on the catalyst surface properties and reaction conditions.[534] Common single-carbon products include carbon monoxide, formic acid, formaldehyde, methane, and methanol. Formic acid can be generated through various pathways, including the formation of coordinated intermediates on hydrogen-rich surfaces, or through the reaction of free radical $CO_2$ with external $H^+$, or through conversion after forming a carbonate configuration with surface OH groups.[535] CO can be generated by hydrogenation of COOH intermediates followed by the removal of water molecules, while formaldehyde, methanol, and methane are formed by the stepwise hydrogenation of CO* intermediates.[536] The pathways to $CH_4$ are also diverse, of which two are common: one is the breaking of the C–O bond through hydrogenation of $CH_3O$ intermediates, and the other is the stepwise hydrogenation and dehydration of CO on the surface to finally generate $CH_4$.[537,538] In addition, there is a more complex pathway that generates glyoxal intermediates

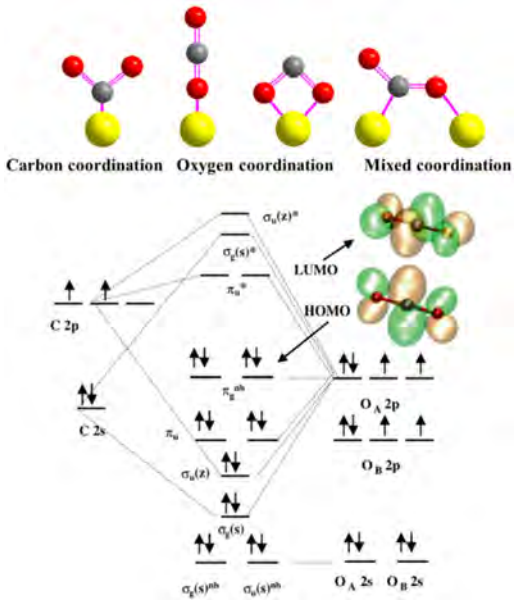


Fig. 12 Different coordination forms formed by $CO_2$ reduction and their LUMO energy level reduction process (reproduced with permission from ref. 533. Copyright 2022 Springer Nature).

through C–C coupling, which is then converted into $CH_4$ and acetaldehyde through multiple steps.[539]

For $C_{2+}$ products, such as ethylene and ethanol, CO is considered to be a key intermediate.[540,541] CO undergoes hydrogenation and C–C coupling on the catalyst surface to generate CHO* and COCHO*, and its subsequent reaction pathway determines the type of final product. In addition, COCHO* intermediates can also be hydrogenated to generate glyoxal, which is further converted into ethanol, ethylene glycol, or acetaldehyde.[542,543] Another pathway is to form acetaldehyde, acetic acid, or ethylene through the formation of COCHOH* intermediates.[544,545] Since the generation process of $C_{2+}$ products is relatively complex and involves multiple key intermediates, understanding the formation and conversion of these intermediates is crucial for regulating product selectivity and improving reaction efficiency. By precisely controlling these reaction pathways, the efficiency and selectivity of $CO_2$ reduction reactions can be achieved, thereby promoting the practical application and commercialization of $CO_2$ emission reduction.

**2.3.2 Effect of catalyst type and structure on the reaction.** In the $CO_2$ catalytic reaction, the type and structure of the catalyst have a crucial effect on the reaction.[546–548] First, different types of catalysts have different active centers and surface properties, which will affect the selectivity and activity of the reaction. For example, transition metal catalysts can usually promote the hydrogenation and reduction reactions of $CO_2$.[549,550] Acidic catalysts are more suitable for the carbonylation and cyclization reactions of $CO_2$.[551,552] Secondly, the crystal structure, pore size and surface chemical properties of the catalyst will also affect the reaction.[548,553,554] Catalysts with highly ordered crystal structures usually have better reaction selectivity.[555,556] Catalysts with large pore sizes and high specific surface areas are conducive to improving reaction activity and catalyst stability.[557,558] In addition, the carrier and support material of the catalyst may also be crucial to the reaction because they can regulate the dispersion and surface activity of the catalyst.[559,560] Therefore, designing and optimizing the type and structure of catalysts is an important research direction in the field of $CO_2$ catalytic conversion. Efficient and highly selective $CO_2$ conversion reactions can be achieved by rationally designing the structure and composition of the catalyst. Andreas *et al.*[561] reviewed examples of local chemical environmental effects in $CO_2$RR and classified them according to their potential physicochemical effects on reactivity and control of local concentrations of solution components. According to the classification shown in the figure, multiple effects may be present in real systems, which provides the opportunity to embed multiple functionalities into a single catalyst material.

When $CO_2$ is catalyzed at low concentrations as opposed to high concentrations, the reaction properties change significantly. The choice of catalyst is essential for $CO_2$ catalysis at low concentrations. under order to accelerate the pace of reaction, catalysts with increased surface activity and active sites are required since the supply of $CO_2$ is constrained under low concentration circumstances.[93,562] Catalyst design should focus on enhancing the adsorption capacity and activation efficiency for LCC, while maintaining high selectivity to increase the yield of target products.[563,564] Takuya *et al.*[51] developed a new molecular photocatalytic system using Ru(II)–Re(I) binuclear complex as a photocatalyst (Fig. 13a). This system not only has high $CO_2$ reduction capacity, but also has high $CO_2$ capture capacity. Using this photocatalytic system, 10% concentration of $CO_2$ can be selectively converted into CO, and its photocatalytic effect is almost the same as that in a pure $CO_2$ atmosphere (TONCO > 1000, $\Phi$CO > 0.4) (Fig. 13b). The reaction rate is sluggish at low concentration settings, thus it must be increased by improving the catalyst's efficiency or modifying the reaction environment.[48,49,565]

Due to the increased $CO_2$ concentration and enough reactant supply in high-concentration $CO_2$ catalysis, the reaction rate is often quicker than in LCC catalysis.[566,567] The catalyst is more active under high-concentration conditions, but attention should be paid to the selectivity of the catalyst to prevent the catalyst surface from being overloaded and causing an increase in side reactions.[568,569] The catalyst design for high-concentration $CO_2$ catalysis can focus more on improving the reaction rate and

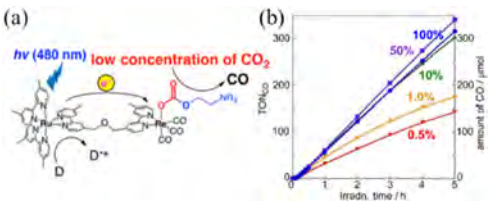


Fig. 13 (a) Photocatalyst based on Ru(II)–Re(I) binuclear complex; (b) photocatalytic CO production under different $CO_2$ concentrations (0.5–100%) (reproduced with permission from ref. 51. Copyright 2016 American Chemical Society).

optimizing the catalyst structure to cope with the needs of higher $CO_2$ concentrations and rapid reactions.[570,571]

In general, low-concentration and high-concentration $CO_2$ catalysis have different requirements in catalyst selection, reaction rate, selectivity, and reaction mechanism. Based on these differences, it is helpful to develop efficient catalysts for different $CO_2$ concentration conditions, optimize the catalytic reaction process, and improve the performance of catalytic technology in practical applications.

**2.3.3 Effect of reaction conditions on product distribution.** The effect of reaction conditions on product distribution is crucial, mainly including factors such as temperature, pressure, catalyst type, and reactant molar ratio.[572,573] Temperature is an important parameter in catalytic reactions and can affect reaction rate and product distribution. Generally, higher temperatures are beneficial to increase the reaction rate, but too high a temperature may lead to reduced product selectivity.[574] In the $CO_2$ hydrogenation reaction, higher temperatures are conducive to the production of hydrocarbon products such as methane, while lower temperatures may be more conducive to the production of liquid products such as methanol.[556,575,576] Pressure can affect the interaction and reaction rate of $CO_2$ with other reactants. Higher pressure often helps to boost product selectivity and reaction rate in the $CO_2$ hydrogenation reaction because it can make $CO_2$ and hydrogen more soluble and encourage their interaction with the catalyst surface.[577,578]

Different types of catalysts have different activities and selectivities, which will affect the distribution of products. For $CO_2$ hydrogenation reactions, transition metal catalysts such as nickel and iron are generally more inclined to produce hydrocarbon products such as methane.[578–580] Precious metal catalysts such as rhodium and ruthenium are more inclined to produce liquid products such as methanol.[581,582] The molar ratio of the reactants directly affects the distribution of products.[583,584] During the $CO_2$ hydrogenation reaction, the molar ratio of $CO_2$ and hydrogen affects the amount of methane and methanol produced because they are competing reactions for $CO_2$ and $H_2$.[585,586]

The mass transfer and reaction coupling in porous media has an important influence on the regulation mechanism of the catalytic process, especially when designing the catalyst pore structure and optimizing its performance, the influence of $CO_2$ concentration cannot be ignored. However, to deeply understand this process, it is necessary to consider the following key factors:

(a) The scale span is large. The mass transfer process of $CO_2$ spans different scales. From the macroscopic scale in which $CO_2$ diffuses to the catalyst surface through the gas phase in the reactor, to the mesoscopic scale in which $CO_2$ diffuses on the catalyst surface/interface and in the bulk phase micro–nano channels, and then to the $CO_2$ diffused to the active site where adsorption, reaction and desorption occur of microscopic scale[587–589] (Fig. 14a). When the $CO_2$ concentration changes, the Knudsen number may change from 0.01 to more than 10.[590,591] This makes it difficult to comprehensively study $CO_2$ mass transfer and reaction processes at different concentrations using a single method.

(b) Complex pore structure. Catalysts usually have complex multi-level pore systems (Fig. 14b). Factors such as the

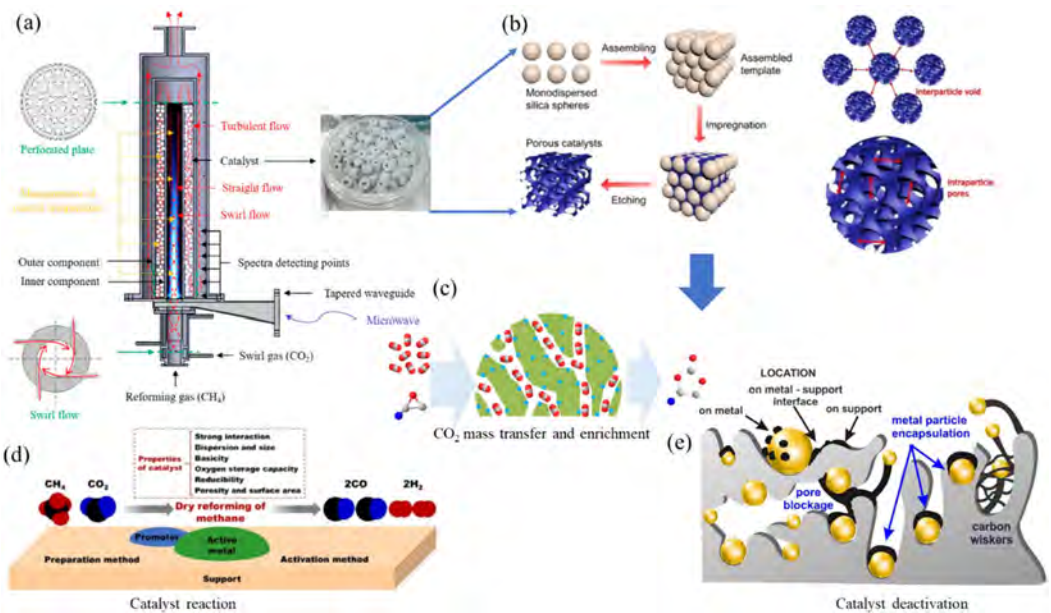


Fig. 14 Challenges faced by LCC catalytic processes: (a) the transfer process of gas flow in the reactor taking $CO_2$ methane dry reforming as an example (reproduced with permission from ref. 589. Copyright 2019 MDPI); (b) the porous structure of the catalyst (reproduced with permission from ref. 592. Copyright 2023 Elsevier); (c) diffusion mass transfer and enrichment of $CO_2$ in the pore structure of the catalyst (reproduced with permission from ref. 593. Copyright 2020 Elsevier); (d) the adsorption and reaction process of $CO_2$ at the active site (reproduced with permission from ref. 594. Copyright 2019 Elsevier); (e) after a long reaction time, the catalyst pores may experience structural collapse, sintering, product deposition or micropore blockage (reproduced with permission from ref. 595. Copyright 2021 MDPI).

connectivity, porosity, channel shape, tortuosity, and surface active sites of these pores will affect the diffusion and reaction efficiency of $CO_2$ molecules in them.[177,200,596] Especially when $CO_2$ concentration is high, these structural characteristics may significantly change the mass transfer path and reaction rate[592,597,598] (Fig. 14c). Therefore, it is necessary to study the behavior of $CO_2$ during the mass transfer process for catalyst pores with different structures, and to quantify the specific impact of these factors on the reaction.

(c) Dynamic coupling of mass transfer and reaction. Changes in $CO_2$ concentration have a significant impact on mass transfer and reaction coupling in catalytic reactions. As the $CO_2$ concentration increases, the spatiotemporal distribution, concentration gradient and reaction rate inside the catalyst will dynamically change[599] (Fig. 14d). During the reaction process, the concentration of $CO_2$ directly determines the rate of reaction and diffusion, and these processes in turn change the local concentration distribution of $CO_2$. High concentrations of $CO_2$ may lead to local accumulation of reactants, creating more pronounced concentration gradients, while diffusion processes attempt to balance these gradients.[593,594,600] Therefore, understanding the impact of $CO_2$ concentration on mass transfer and reaction coupling is crucial to optimizing catalytic effects.

(d) Pore channel changes caused by reaction. Although it is generally assumed that the pore structure of the catalyst remains stable during the reaction process, under high $CO_2$ concentrations, the catalyst pores may undergo changes such as structural collapse, sintering, product deposition, or micropore blocking[557,601,602] (Fig. 14e). For example, in denitration of coal-fired power plants, higher $CO_2$ concentrations may exacerbate ammonium bisulfate deposition.[603] In industrial catalytic dehydrogenation, $CO_2$ may promote carbon deposition.[595,604] These structural changes significantly affect the stability and durability of the catalyst. Therefore, when studying mass transfer and reaction in the actual catalytic process, the potential impact of $CO_2$ concentration on the catalyst pores must be considered.

# 3. LCC separation technology

## 3.1 Overview of air separation technology

Air separation technology refers to the technology of separating various gas components in the air, usually including oxygen, nitrogen, argon, *etc.* The main air separation technologies are divided into normal temperature separation and low temperature separation according to the reaction temperature.[605,606] Among them, normal vacuum adsorption (PSA), which is frequently used to create high-purity nitrogen and hydrogen,[607] is the method that separates gases in normal temperature separation primarily by the difference in adsorption properties of solid adsorbents. Membrane separation is often used to create high-purity oxygen or nitrogen.[608] It works by using the selective permeability of the membrane to separate various gases. Air separation, the primary technique for producing large-scale, high-purity oxygen, nitrogen, and argon, employs the liquefaction properties of gases at low temperatures for separation (cryogenic distillation). High-purity oxygen and nitrogen are frequently produced using cryogenic adsorption separation, which makes use of the differences in the adsorption properties of solid adsorbents for gas separation at low temperatures.[609,610]

These air separation technologies may be applied in producing high-purity products of different gases to fulfill the demands of diverse areas. They are extensively employed in scientific research as well as industrial production.[611,612] With the continuous development and innovation of technology, the efficiency and energy consumption of air separation technology are constantly improving, and it is becoming more and more important for applications in energy, chemical industry, medical and other fields. The presence of LCC will change the condensation temperature of various gases in the air, resulting in changes in the component distribution of the mixed gas during the condensation process.[36,613] In the low-temperature air separation process, the condensation temperature needs to be adjusted according to the $CO_2$ content in the mixed gas to ensure that high-purity oxygen, nitrogen and argon are effectively separated.

The energy consumption of low-temperature air separation equipment is huge. A typical 60 000 N $m^3$ $h^{-1}$ air separation equipment can consume up to 40 000 kW h $h^{-1}$.[614] In the coal chemical industry, the energy consumption of air separation equipment accounts for about 10% to 15% of the total energy consumption. In the metallurgical industry, the energy consumption required for air separation equipment accounts for about 15% to 20% of the total energy consumption.[615] A typical air separation equipment is shown in Fig. 15, and the purification system is the core component. According to statistics, the energy consumption of the air separation purification system accounts for about 11% of the total energy consumption of the air separation unit.[616]

Temperature swing adsorption towers frequently get employed by large air separation equipment to pre-purify air. Two or three mutually switchable adsorbers must be included in the TSA purification system in order to guarantee continuous purification of the processed air. The purifier is equipped with two layers of adsorbents, NaX 13X and activated alumina. The primary use of activated alumina is the adsorption of high-concentration water vapor due to its substantial equilibrium adsorption capacity and ability to be regenerated using waste heat. The NaX 13X is mainly utilized to adsorb and remove low-concentration water vapor, $CO_2$, and some hydrocarbons. It can also cause the processed air to reach an exceptionally low dew point. During the adsorption process, the air is cooled in the air humidification pressurized spray tower, the temperature reaches 12 °C, the humidity reaches saturation, and the pressure reaches 0.6 MPa, and then it enters the adsorption bed vertically. After the air enters the adsorption bed, moisture, $CO_2$ and sulfur-containing organic matter are basically removed, and then it enters the distillation tower for experimental oxygen and nitrogen separation.[617,618]

The regeneration operation is achieved by the dirty nitrogen gas from the low-pressure plate heat exchanger. These gases are heated to 175 °C in the steam heater and then enter the molecular sieve purifier to desorb under high temperature and low-pressure conditions to restore the adsorption capacity.

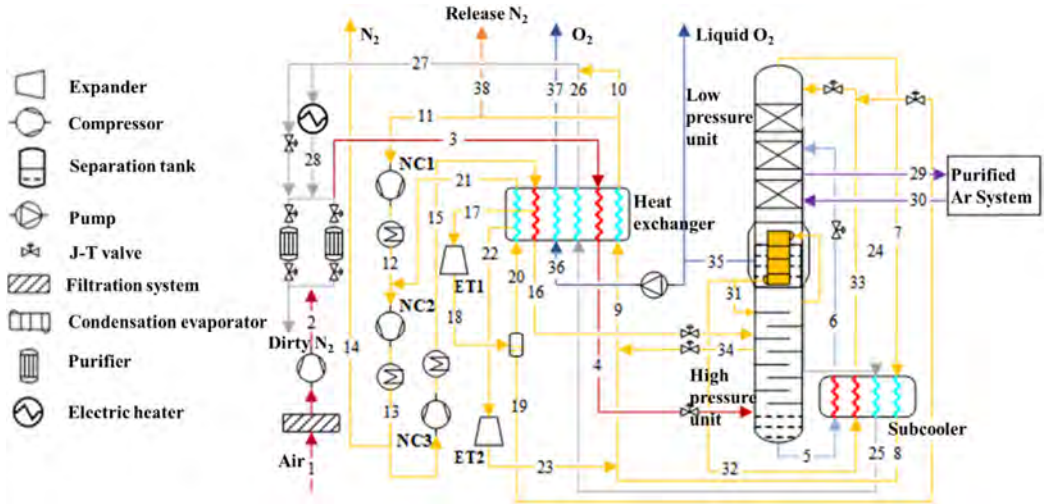


Fig. 15 Schematic diagram of the process flow of the cryogenic air separation and molecular sieve purification system.

The regeneration gas first enters the left heat exchange tube of the steam heater to exchange heat with condensed water, and then enters the right heat exchange tube to exchange heat with steam to heat the regeneration gas to the required temperature. Through the gas–liquid separator, the 80 °C condensed water produced by the process enters the condensed water network and is sent to the downstream process for recycling.[619,620]

When the $CO_2$ content in the air at the outlet of the molecular sieve purifier exceeds the standard (greater than 0.1–1 ppm), carbon dioxide plays a key negative role in the system, which directly reflects that the adsorption performance of the molecular sieve has dropped significantly.[621,622] This phenomenon indicates that carbon dioxide has broken through the adsorption capacity of the molecular sieve bed and began to enter the downstream plate-fin heat exchanger and distillation tower system in large quantities. Since these systems usually operate at extremely low temperatures (below −100 °C), carbon dioxide is very easy to freeze in these low-temperature equipment and form solids in the channels of the plate-fin heat exchanger.[623,624] Frozen carbon dioxide not only causes blockage of the channels of the heat exchanger, but also seriously affects the heat transfer efficiency of the equipment, and may eventually force the system to shut down and heat to clear the blockage, resulting in production interruption and overall efficiency reduction.[625]

Even more serious is the safety hazard caused by excessive carbon dioxide content. As carbon dioxide and hydrocarbons continue to accumulate in the main cooling system, especially under low temperature conditions, these accumulated substances have the potential risk of causing main cooling explosions, posing a great safety threat.[626,627] In addition, carbon dioxide freezes into solid on the liquid air side of the crude argon condenser, further blocking the heat exchange channel, resulting in a reduction in heat exchange area and reducing the load handling capacity of the argon tower.[628] This not only weakens the operating efficiency of the system, but also increases the safety risk of equipment operation, indicating that effective control of carbon dioxide is crucial to the safety and efficiency of the entire system.

Song *et al.*[629] studied the flue gas containing 13 vol% $CO_2$ at low temperature. The results showed that the frosted carbon dioxide layer significantly affected the heat transfer between the airflow and the cooling fins (Fig. 16). Over time (from 0 to 60 minutes), the frost layer thickness increased from 0 to 3.0 mm. The thermal conductivity increased from 0 to 0.4 W (m K)$^{-1}$. When the flow rate was 1 L min$^{-1}$, the SC cold head temperature changed from −105.2 °C to −102.1 °C; when the flow rate was 3 L min$^{-1}$, the temperature increased from −106.3 °C to −98.0 °C.

$CO_2$ is more soluble in liquid oxygen and liquid nitrogen at low temperatures.[631] Therefore, in the air separation process, the effect of $CO_2$ solubility on separation efficiency needs to be considered. It is usually necessary to reduce the dissolution of $CO_2$ by adjusting process parameters or adopting appropriate separation methods to improve the efficiency and purity of air separation.[632] For air separation technology based on the principle of adsorption separation, the presence of low concentrations of $CO_2$ may affect the selection and performance of adsorbents.[633] Some solid adsorbents, such as zeolites, activated carbons, and MOFs, have high selectivity for $CO_2$. This is because $CO_2$ molecules have a large adsorption capacity on the adsorbent due to their high polarity and ease of interaction with active sites on the adsorbent surface. These adsorbents' high selectivity

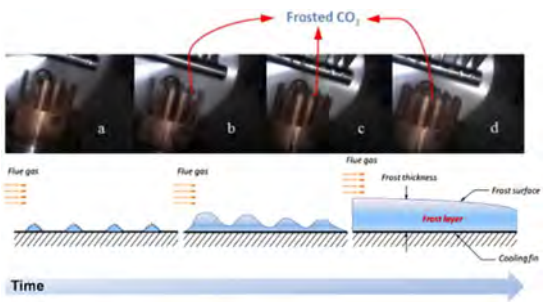


Fig. 16 $CO_2$ freezing process on the heat exchanger surface (reproduced from ref. 630 with permission from Elsevier, copyright 2013).

makes it possible for them to efficiently extract $CO_2$ from the air and separate it, increasing the effectiveness of the separation process.

In the separation process of oxygen or nitrogen, the presence of $CO_2$ may interfere with the separation of other target gases. $CO_2$ readily occupies adsorption sites due to its strong contact with the adsorbent surface, which reduces the target gas's adsorption capability. In this instance, the separation efficiency of other gases will be lowered if the adsorbent is overly selective for $CO_2$. Therefore, the adsorbent needs to be selected carefully to avoid excessive impact of $CO_2$ on the separation process.[621,630] Therefore, it is necessary to select the right adsorbent to achieve effective separation. In the air separation process, the choice of adsorbent needs to be weighed according to the specific application scenario. If the goal is to separate $CO_2$ efficiently, it is reasonable to choose an adsorbent with high selectivity for $CO_2$. However, if the main goal is to separate other gases, it may be necessary to choose an adsorbent with lower selectivity for $CO_2$ or higher selectivity for the target gas.

Since the presence of LCC will increase the process complexity and energy consumption in the separation process, it may increase the separation cost. Therefore, when designing the air separation process, it is necessary to comprehensively consider the impact of LCC on the process in order to achieve an efficient and economical air separation process.[634]

### 3.2 Capture and separation of LCC

The separation and capture of LCC in air separation mainly involves chemical absorption, adsorption, membrane separation and cryogenic separation. $CO_2$ is separated and taken in through membrane separation technology, which takes use of the varying permeabilities of gas molecules on the membrane.[635,636] For the separation of LCC in air, membrane materials with higher selectivity can be designed to more effectively separate $CO_2$ from the air. This technology is generally suitable for small-scale $CO_2$ capture and enrichment.[637] To separate $CO_2$ from other gases, adsorption separation technology employs solid adsorbents to selectively absorb $CO_2$. The separation and collection of LCC from the air can be accomplished by using adsorbents that are capable of adsorbing $CO_2$,[638–640] such as activated carbon, metal organic frameworks (MOFs), *etc.* $CO_2$ is adsorbed from the air and then desorbed, regenerated or converted. Chemical absorbents react with $CO_2$ to absorb $CO_2$ from the air *via* chemical absorption technology. There are typically two types of this technology: solid absorption and solution absorption. By choosing the right absorbents and modifying the reaction conditions, it can absorb and separate LCC.[641,642] Cryogenic technology condenses $CO_2$ in the air into liquid or solid by adjusting temperature and pressure conditions to achieve $CO_2$ separation and capture.[643] This technology is usually suitable for large-scale $CO_2$ capture and separation, including liquid air separation, cryogenic adsorption and other means.[644,645]

To combat climate change and reduce greenhouse gas emissions, LCC in the atmosphere may be captured, enhanced, and transformed into valuable products using these separation and capture methods. These technologies will become more significant in the areas of carbon use, carbon capture, and carbon neutrality as long as technology continues to advance. The following are the primary obstacles and bottlenecks that the LCC separation and capture technology must overcome, along with potential solutions.

**3.2.1 Separation efficiency of LCC.** The concentration of $CO_2$ in air is relatively low, usually about 0.04%, which increases the difficulty and energy consumption of the separation process.[646,647] This inefficient separation not only leads to higher energy consumption, but also directly drives up the capture cost, limiting the feasibility of this technology in large-scale commercial applications.[47] Therefore, improving the separation efficiency of LCC is crucial for the development of DAC technology.

To meet this challenge, researchers are working on developing a variety of solutions. First, by improving the $CO_2$ adsorption selectivity of adsorbents or membrane materials, $CO_2$ can be captured more efficiently under low-concentration conditions and reduce energy consumption.[648] Second, optimizing separation process parameters, such as operating temperature, pressure, and gas flow rate, can further improve separation efficiency.[649] In addition, the introduction of new and efficient separation technologies, such as the application of high-performance catalysts or innovative membrane separation technologies, also provides a new path to solve the problem of LCC separation.[650,651] Chae *et al.*[652] reported the combined DAC and methanation of $CO_2$ using a dual-functional material (DFM) consisting of an alkaline adsorbent and a catalytic metal. The feasibility of successful cyclic capture and methanation of 400 ppm $CO_2$ under isothermal conditions (320 °C) was demonstrated. Liu *et al.*[653] proposed an electrochemical process for the electrocatalytic regeneration of a hydroxide absorbent by circulating viologen, using renewable electricity to capture and convert $CO_2$ from air through an energy-efficient organic redox reaction. High-performance materials that take both thermodynamics and kinetics into account can also be designed and developed to increase adsorption capacity while enhancing mass transfer processes, which will facilitate low-cost, efficient and rapid capture.[654,655] These technical improvements can not only improve separation efficiency but also reduce operating costs.

**3.2.2 Energy consumption and cost.** Conventional air separation technologies usually require a lot of energy and cost.[31] The market demand for $CO_2$ is expected to grow exponentially to 6.1 Gt by 2050, while the cost of implementing DAC technology is expected to drop to less than \$\$125 per t $CO_2$ by 2030.[656] For example, low-temperature refrigeration and high-pressure compression in the air separation process consume a lot of energy. The creation of new, energy-efficient capture technologies, enhancements to current systems' processes to lower energy consumption, and the deployment of renewable energy sources to supply the energy needed for the separation process are among potential solutions.[657] The implementation of DAC technology relies on several key devices, including capture devices, adsorption or absorption devices, and desorption or regeneration devices. In terms of capture devices, the $CO_2$ concentration of stationary emission sources such as coal-fired power plants is

 

usually between 10% and 20%, while the $CO_2$ concentration in the atmosphere is much lower than this. The development of DAC in the industrial field is still in its early stages.

When there was no industrial data to support DAC, some researchers calculated the $CO_2$ capture efficiency based on the second law of thermodynamics and estimated that the cost of capturing 1 t of $CO_2$ was about \$\$1000.[658] The American Physical Society's 2011 technical report estimated that DAC would cost \$\$610 per ton of $CO_2$ captured. The largest DAC project is Climeworks' ''Mammoth'' plant in Iceland, which can capture up to 36 000 tons of $CO_2$ per year.[659] It is currently the largest operating DAC facility and has completed the demonstration phase, aiming to significantly scale up the technology. Climeworks is also involved in other large projects,[660,661] including upcoming DAC centers in the United States, such as the South Texas DAC Center and the Cypress Project in Louisiana, each of which aims to capture more than 1 million tons of $CO_2$ per year after it is put into operation. Jennifer *et al.*[662] evaluated the theoretical minimum work of separation under different concentrations of $CO_2$ sources. In the region where outlet $CO_2$ purity is less than 10% and capture efficiency is less than 60%, the minimum work of the DAC is 8–10 kJ $mol^{-1}$ $CO_2$. This is just the minimum work required to separate $CO_2$ from natural gas power plant exhaust to achieve a capture efficiency of 90% to a final $CO_2$ purity greater than 95% (Fig. 17).

Therefore, improving the $CO_2$ capture rate of air capture devices is a key link in reducing the cost of DAC. Efficient capture devices need to be able to effectively extract $CO_2$ from a rarefied gas environment, thereby improving the economic feasibility of the overall technology at the source.[664,665] The source of driving energy is very important. Combined with long-term life assessment, new technologies and new ways to couple DAC with renewable energy are sought and developed at different time and space scales. For example, new processes to drive adsorbent regeneration such as solar energy and wind energy are developed. Li *et al.*[663] extended the power-to-gas (P2G) and carbon capture and storage (CCS) technologies to a hybrid concentrated solar power and combined heat and power integrated energy system (IES). The proposed model reduced the total cost by 57.80%, achieved a carbon utilization rate of 24.38% and full wind energy absorption. Tom *et al.*[666] conducted a comprehensive life cycle assessment of different DACCS systems. The largest potential for removing greenhouse gases (up to 97%) is found in nations which generate waste heat and have low-carbon electrical supplies. Removing material with a high solar radiation efficiency ranges from 79% to 91%. It is possible to avoid consuming grid energy and heat that is derived from fossil fuels.

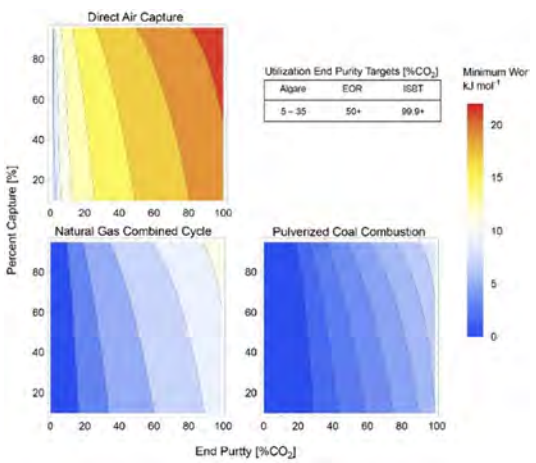


Fig. 17 Theoretical minimum work for separation under different $CO_2$ source concentrations. Ambient air (top), natural gas combined cycle (NGCC) flue gas (lower left) and pulverized coal combustion (PCC) flue gas (lower right). Ambient air is 0.04%, 4 mol% $CO_2$ (NGCC) and 12 mol% $CO_2$ (PCC) (adapted with permission from ref. 663 with permission from IOP Publishing Ltd, copyright 2017).

The design and optimization of adsorption and desorption devices are also crucial to the success of DAC technology. However, the research on DAC technology in industrial applications is still in its early stages, and there are relatively few reports on the corresponding equipment development and improvement.[31,440] Therefore, future development should focus on improving the overall efficiency of the system through process intensification and further reducing operating costs through integrated optimization of process systems.[667] In this way, DAC technology can not only become more economically viable, but also be more widely used in large-scale $CO_2$ capture and recycling.

**3.2.3 $CO_2$ capture and post-processing.** In the DAC process, the separation and capture of $CO_2$ is only the first step. The captured $CO_2$ often needs further post-processing to adapt to different application requirements.[668] The captured $CO_2$ needs to be separated from the impurities, filtered, and given additional necessary treatments since it typically includes impurities or does not match the purity criteria of some applications. Ensuring that $CO_2$ can be utilized for certain tasks, such as the manufacture of chemicals, the storage of $CO_2$, or industrial raw materials, depends on this process.[669–671] To guarantee stable long-term storage and efficient injection, $CO_2$ in geological storage typically has to be compressed to a supercritical level and be more than 95% pure.[672] Takeshi *et al.*[673] simulated the density of $CO_2$–$N_2$–$O_2$ mixtures and evaluated the cost of low-purity $CO_2$ storage. The evaluation shows that storing low-purity $CO_2$ in geological formations is environmentally acceptable. Low-purity carbon dioxide captured by advanced membrane-based DAC technology and appropriately stored in the geological state is also economically feasible (Fig. 18a–f). In the food and beverage industry, $CO_2$ purity requirements are higher, usually above 99.9%, to ensure the taste and safety of the product.[674] Different applications have different requirements for the state of $CO_2$. For example, geological storage and EOR usually require a supercritical state,[675] while chemical synthesis may use gaseous or supercritical $CO_2$.[676] As part of the CCS plan, the composition and transportation of $CO_2$ streams are also key. According to analysis, the relative cost/km of the pipeline network (in terms of pipeline inner diameter and length) will remain unchanged provided impurity addition is kept below 2 mol% when compared to the pure $CO_2$ equivalent.

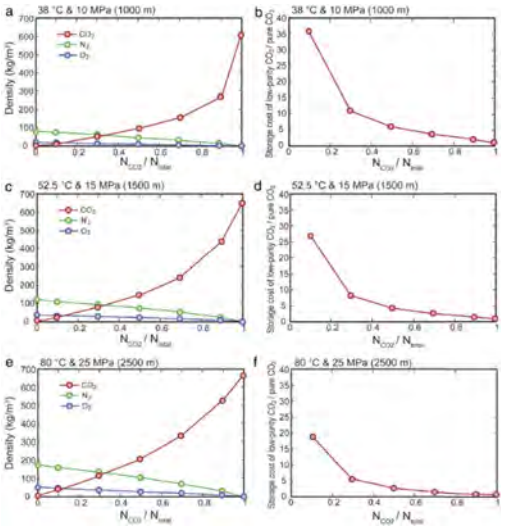


Fig. 18 Efficiency and cost of low-purity $CO_2$ storage. Geological storage density and storage cost of different proportions of $CO_2$, $N_2$, and $O_2$ at (a) 38 °C temperature and 10 MPa pressure (about 1000 m depth) (b); (c) 52.5 °C temperature and 15 MPa pressure (about 1500 m depth) (d); (e) 80 °C temperature and 25 MPa pressure (about 2500 m depth) (f) (adapted from ref. 676 with permission from John Wiley & Sons, copyright 2021).

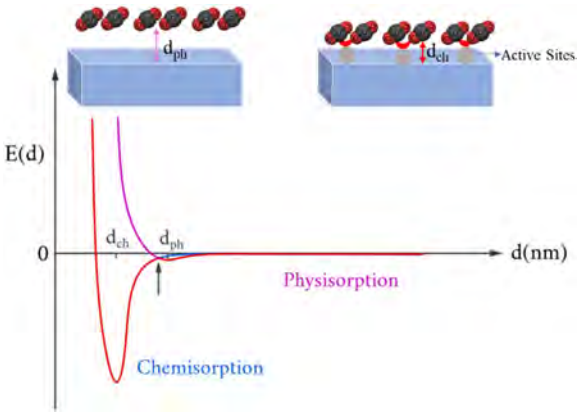


Fig. 19 Mechanisms of physical and chemical adsorption of $CO_2$ on the adsorbent surface.

These different purity and state requirements directly affect the choice of post-processing technology in DAC systems. To meet these requirements, DAC systems may need to be purified using technologies such as amine scrubbing[89] and PSA[677] to remove impurities and achieve the required purity. To meet state requirements, such as reaching a supercritical state, $CO_2$ must undergo energy-intensive compression and cooling processes.[678,679] These processes involve multiple areas such as power, operation scheduling, thermal management, and energy recovery.

Meanwhile, it is becoming increasingly important to integrate capture and post-processing processes for optimization. Through this systematic integration, the efficiency of the entire process chain can be improved, energy consumption and costs can be reduced, thereby promoting the widespread promotion and economic feasibility of DAC technology in practical applications.[680,681] Cheng *et al.*[682] proposed a design for the transformation of an existing NGCC to achieve negative $CO_2$ emissions power generation by utilizing post-combustion carbon capture and DAC. The DAC unit captures $CO_2$ directly from the atmosphere through low-grade heat from the NGCC. Adding flexibility to the NGCC system through heat integration and modular DAC design can still significantly extend the dispatch time and improve system profitability.

**3.2.4 Efficient, low-cost sustainable materials.** The core of DAC technology lies in the development of efficient, low-cost absorption/adsorption materials. Current research mainly focuses on the two mechanisms of physical adsorption and chemical adsorption,[443] as shown in Fig. 19. Physical adsorption relies on intermolecular van der Waals forces for $CO_2$ capture, usually occurring on the surface of the adsorbent. Therefore, material design needs to have high porosity or nano-sized structure to maximize surface area and enhance $CO_2$ capture capability.[683] Common physical and chemical adsorption solid adsorbents used for LCC capture are shown in Table 5. Lee *et al.*[684] prepared adsorbent-coated carbon fibers *via* a roll-to-roll process, which exhibited a 400 ppm $CO_2$ adsorption capacity of approximately 1.2 mmol $g^{-1}$ fiber. The advantage of physical adsorbents is that they are easy to regenerate and can maintain high efficiency over multiple cycles. However, since its adsorption performance and selectivity are usually low at room temperature, its application in LCC capture in the air is limited.[685]

Chemical adsorption, on the other hand, greatly improves both the adsorption capacity and selectivity by capturing $CO_2$ molecules through stronger chemical bonding forces.[695] Amine-functionalized metal–organic frameworks exhibit lower energy requirements,[649] with a minimum of 1000 kW h t $CO_2{}^{-1}$ and a minimum known cost of 60$$ t $CO_2{}^{-1}$. Liu *et al.*[696] found that the grafting process is a reaction between metal sites and secondary amines in AEEA, and MOFs with high specific surface area and low acidity can effectively promote amine grafting without destroying the active sites. In addition, the $CO_2$ adsorption capacity of MIL-100 (Cr) functionalized with *N*-(2-aminoethyl)-ethanolamine (AEEA) at 400 ppm was 1.91 mmol $g^{-1}$ at −25 °C and 2.42 mmol $g^{-1}$ at 0 °C, respectively. g. The structural decomposition temperature exceeds 400 °C, showing excellent thermal and cold stability. However, the high energy consumption and complex process steps of its desorption process limit the overall absorption efficiency.[697] Therefore, balancing adsorption intensity and desorption energy consumption is one of the key challenges facing DAC technology.

Future business applications of DAC technology will be contingent upon the creation of adsorbent materials possessing high selectivity and high adsorption capacity. To lower total energy consumption, these materials must have an effective and low-energy desorption mechanism in addition to demonstrating great capture capability at low $CO_2$ concentrations.[698,699] Based on the life cycle of the entire system, safe and scalable monolithic functionalized materials such as granular,[700] fiber,[701] film[702] or monolithic column[703] structures are developed to increase the number of sites per unit volume. Ali *et al.*[704] reported that the maximum adsorption

 

Table 5 Comparison of adsorption performance of solid materials for physical adsorption and chemical adsorption of LCC

| Solid adsorbent | Adsorption type/load | Ambience | Temperature (°C) | Desorption conditions | Adsorption capacity (mmol $g^{-1}$) | Ref. |
|---|---|---|---|---|---|---|
| Zeolite 13X | Physisorption | Dry $CO_2$ (0.15 atm $CO_2$, 0.85 atm $N_2$) | 30 | 200 | 0.034 | 686 |
| NaX | Physisorption | 400 ppm $CO_2/N_2$ | 25 | 200 | 0.41 | 687 |
| | Physisorption | 400 ppm $CO_2/N_2$ | | | 5.49 | |
| Mg-MOF-74 | Physisorption | Dry $CO_2$ (0.15 atm $CO_2$, 0.85 atm $N_2$) | 30 | 200 | 0.14 | 686 |
| HKUST-1 | Physisorption | Dry $CO_2$ (0.15 atm $CO_2$, 0.85 atm $N_2$) | 30 | 200 | 0.05 | 686 |
| Li-LSX | Physisorption | 400 ppm $CO_2/N_2$ | 25 | 200 | 1.34 | 687 |
| Na-LSX | Physisorption | 400 ppm $CO_2/N_2$ | 25 | 200 | 0.84 | 687 |
| SIFSIX-3-Cu | Physisorption | 400 ppm $CO_2/N_2$ | 25 | 200 | 1.24 | 688 |
| $SiO_2$ | Physisorption | 400 ppm $CO_2/N_2$ | 25 | 110 | 2.36 | 689 |
| Mesoporous silica foam | Chemisorption/PEI[a] | 400 ppm $CO_2/N_2$ | 25 | 110 | 1.74 | 690 |
| Silica | Chemisorption/PEI[a] | 400 ppm $CO_2/N_2$ | 25 | 100 | 2.34 | 691 |
| HP20/PEI-50 | Chemisorption/PEI[a] | 400 ppm $CO_2/N_2$ | 25 | 100 | 2.26 | 692 |
| SBA-15 | Chemisorption/APS[a] | 400 ppm $CO_2/N_2$ | 25 | 110 | 1.72 | 691 |
| MCM-41 | Chemisorption/DT[a] | 400 ppm $CO_2/N_2$ | 25 | 75 | 1.4 | 691 |
| TEPA-$Mg_{0.55}$Al-O | Chemisorption/TEPA[a] | 400 ppm $CO_2/N_2$ | 25 | 120 | 3.0 | 693 |
| TREN-MIL-101(Cr) | Chemisorption/TREN[a] | 400 ppm $CO_2/N_2$ | 25 | 110 | 2.76 | 694 |

[a] PEI: polyethyleneimine; APS: aminopropyltriethoxysilane; DT: diethylenetriamine; TEPA: tetraethylenepentamine; TREN: tris(2-aminoethyl)amine.

capacity of modified nanofibers with an ethanolamine grafting degree of 172.26% at a $CO_2$ concentration of 5% was 2.84 mmol $g^{-1}$. Sun *et al.*[705] studied the feasibility of ceramic membrane contactors for membrane absorption to remove $CO_2$ from the atmosphere. When NaOH was used as the absorbent, the NaOH utilization rate reached 75%, and it still had good absorption performance. In addition, the appropriate gas–liquid operating parameters in this study were 1000 mL $min^{-1}$ and 1 mL $min^{-1}$, respectively, and the corresponding mass transfer coefficient and $CO_2$ absorption flux were 2.6 mm $s^{-1}$ and 0.096 mol $m^{-2}$ $h^{-1}$, respectively. The good absorption stability indicates that ceramic membrane contactors have great potential in direct air capture applications. In addition, the stability and recycling performance of adsorbent materials are also key factors determining their economic feasibility.[461,706] Materials that continue to function well after several adsorption–desorption cycles can boost the effectiveness of DAC technology, encourage its widespread adoption, and guarantee the long-term financial gains.

**3.2.5 Coupling for industrial applications.** The deep integration of carbon dioxide removal and air separation technology can not only improve the overall efficiency of industrial processes, but also provide innovative and practical value in multiple fields. In the steel and cement industries, air separation technology is used to provide high-purity oxygen to support the oxygen-enriched combustion process. At the same time, combined with carbon dioxide capture devices, the low-concentration $CO_2$ in the exhaust gas is efficiently purified and reused, which can significantly reduce carbon emissions. In addition, combined with data-driven technology, artificial intelligence is used to optimize separation and capture process parameters and dynamically regulate the gas separation path, which can further improve the energy utilization efficiency of oxygen-rich combustion and $CO_2$ capture.

In the petrochemical and chemical industries, air separation devices can be used to supply oxygen-rich gas for hydrogen production. Through linkage with $CO_2$ capture devices, they can optimize the purification, storage or resource utilization of by-product $CO_2$. This technology integration can also achieve efficient separation of complex gas components through multi-functional adsorbents or selective separation membranes, and combine with intelligent control systems to adjust the process in real time to achieve collaborative production of nitrogen, oxygen, hydrogen and $CO_2$, improving Resource utilization efficiency and economy.

The synergy of carbon dioxide removal with air separation shows significant potential in energy systems. For example, using the cold energy of liquefied natural gas (LNG) to drive a low-temperature air separation device can not only improve the separation efficiency of oxygen and nitrogen, but also efficiently capture $CO_2$ through low-temperature condensation. Combined with membrane catalytic separation technology, the captured $CO_2$ can also be directly converted into high value-added chemicals such as methane or methanol. At the same time, recycling the captured $CO_2$ through supercritical $CO_2$ power generation can effectively expand the energy cycle path. Further innovation directions also include the development of non-equilibrium plasma coupling technology to achieve activation and conversion of $CO_2$ during separation, assisting technological upgrades in industrial emission reduction and resource utilization.

In summary, in response to the challenges faced by the separation and capture technology of LCC in air separation, solutions need to be sought through technological innovation, process optimization and material improvement, so as to improve separation efficiency, reduce energy consumption and cost, and achieve efficient capture and utilization of $CO_2$.

# 4. LCC direct conversion technology

## 4.1 Overview of $CO_2$ catalytic conversion technology

The chemical utilization of $CO_2$ as a carbon resource, especially the simultaneous utilization of carbon and oxygen resources, is one of the most promising and widely concerned directions in current large-scale applications. As a non-toxic, cheap and abundant raw material, $CO_2$ shows great industrial application prospects in the synthesis of high-value-added chemicals.[707]

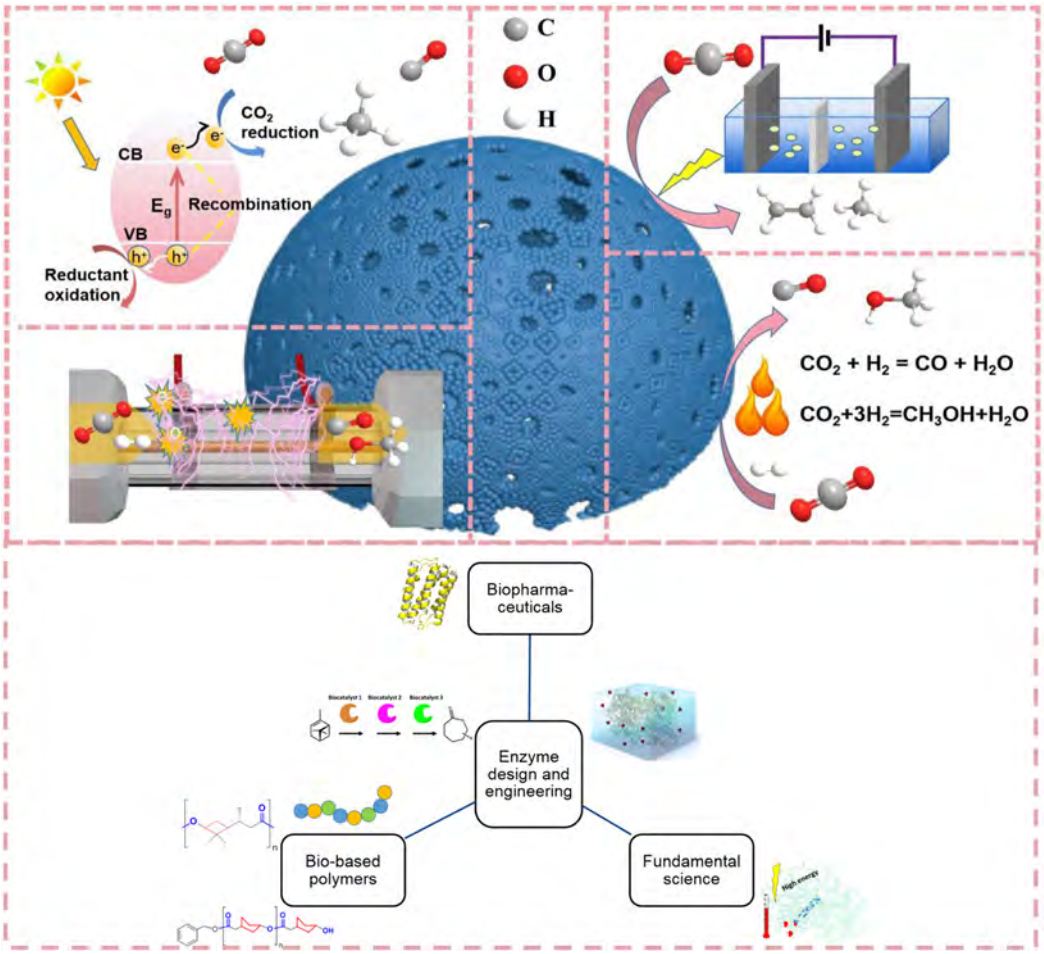


Fig. 20 Different utilization and conversion pathways of $CO_2$ through chemical technologies (reproduced from ref. 714 with permission from Elsevier, copyright 2023).

In order to prevent $CO_2$ formation in the atmosphere and to create fuels and industrial chemicals in place of conventional fossil resources, it is therefore possible to convert $CO_2$ into useful fuels or chemicals and thereby lessen reliance on fossil fuels. Through renewable energy to transform atmospheric $CO_2$ into tiny molecules with high energy density, such methane, methanol, carbon monoxide, and formic acid, is the best course of action.[708,709] To date, the main pathways for converting $CO_2$ into carbon-containing fuels include thermochemical, photochemical, biochemical and electrochemical catalytic conversions, as shown in Fig. 20.[710–713]

### 4.2 Potential application of LCC in new catalytic reactions

With the help of catalysts, LCC in the environment may be directly converted into beneficial chemicals or fuels *via* LCC direct catalytic conversion technology. Both economically and environmentally, this technology is significant. It can both actualize the resource utilization of $CO_2$ and lower greenhouse gas emissions.

**4.2.1 Photocatalytic $CO_2$ conversion.** Photocatalytic technology converts light energy into chemical energy through photocatalysts to drive the reduction reaction of $CO_2$. However, due to the chemical inertness of $CO_2$ molecules themselves, especially the difficulty of activation at room temperature, and the low concentration of $CO_2$ further reduces the probability of contact with the catalyst, the efficiency of photocatalytic reactions faces severe challenges.[51,52] Therefore, the photocatalytic conversion of LCC has extremely high requirements for photocatalysts. The catalyst not only needs to efficiently excite electron–hole pairs under visible light or sunlight, but also must have sufficient energy to drive the $CO_2$ reduction reaction.

The photocatalyst's quantum efficiency is crucial in LCC settings since without it, the reaction won't be able to efficiently use a significant quantity of light energy. Furthermore, the catalyst's effectiveness in transferring energy and absorbing light are also critical. One big difficulty is figuring out how to increase the light capturing capacity to speed up the reaction pace. Huang *et al.*[715] enhanced charge separation and transfer through the close interaction between 2D $Bi_2Se_3$ and 2D g-$C_3N_4$. In the 2D/2D $Bi_2Se_3$/g-$C_3N_4$ composite material, $Bi_2Se_3$ not only acts as a co-catalyst, but also provides additional heat energy for the photocatalytic reaction through photothermal conversion. The catalytic system generates CO with almost 100% selectivity, and the selectivity for CO is higher than 90%,

 

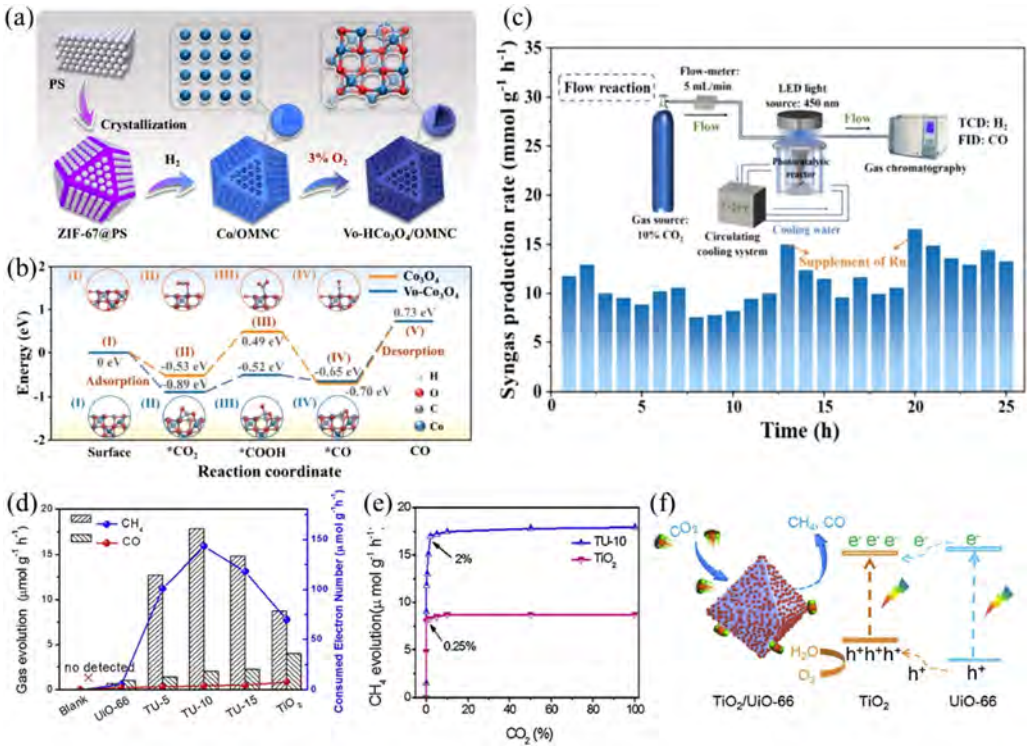


Fig. 21 (a) Preparation process of $Co_3O_4$ hollow nanoparticles containing oxygen vacancies; (b) $Co_3O_4$ hollow nanoparticles containing oxygen vacancies show lower surface adsorption energy and excellent photocatalytic performance (c) (reproduced from ref. 718 with permission from John Wiley & Sons, copyright 2023); (d) $CH_4$/CO generation rate of $TiO_2$/UiO-66 composites; (e) photocatalytic performance of $TiO_2$/UiO-66 composites in different $CO_2$ concentrations and their enrichment strategy (f) (reproduced from ref. 719 with permission from Elsevier, copyright 2020).

without the production of other carbon-based products. Huang *et al.*[716] developed a three-phase photocatalytic $CO_2$ reduction reaction system by loading Ag-modified $TiO_2$ nanoparticles on the gas–water interface to achieve efficient $CO_2$ conversion. The system exploits the wetting properties of the hydrophobic–hydrophilic interface to accelerate the transport of gas-phase $CO_2$ to the photocatalyst surface while maintaining water supply and open active sites. The $CO_2$ reduction rate of the three-phase system reached 305.7 μmol $g^{-1}$ $h^{-1}$ in a 10% $CO_2$ environment, which is about 8 times that of the traditional liquid-phase system without the use of hole scavengers. Lyu *et al.*[714] designed $Co_3O_4$ hollow nanoparticles with oxygen vacancies on an ordered macroporous N-doped carbon framework (Vo-$HCo_3O_4$/OMNC) for the photoreduction reaction of LCC. The catalyst showed unprecedented activity for the photocatalytic conversion of 10% $CO_2$/Ar under laboratory light source and natural light, with syngas production reaching 337.8 and 95.2 mmol $g^{-1}$ $h^{-1}$, respectively, and an apparent quantum yield of up to 4.2% (see Fig. 21a–c). Enhancing the separation of photogenerated charges, surface adsorption and catalytic processes is a key factor in overcoming the mass transfer limitations in the conversion of LCC. Guo *et al.*[717] prepared a highly crystalline $Ag_xNa_{1-x}TaO_3$–AgCl heterostructure composite material by a one-step flux method. A tight heterojunction was formed between $Ag_xNa_{1-x}TaO_3$–AgCl and AgCl in the catalyst, which effectively promoted the separation and transfer of photogenerated charges. In addition, the introduction of Ag cations and AgCl significantly enhanced the adsorption and activation of $CO_2$ on the catalyst surface.

There are several compounds produced during the photocatalytic reduction of $CO_2$, including methanol, carbon monoxide, formic acid, *etc.* One of the technological challenges is managing the selectivity of their products. Side reactions (such water photolysis) are frequently competitive when $CO_2$ concentrations are low, leading to complicated products that are challenging to precisely manage. Ma *et al.*[720] designed a $TiO_2$/UiO-66 composite material with a hierarchical porous structure through a two-step strategy, which effectively enhanced the enrichment ability of $CO_2$ on exposed active sites (Fig. 21d–f). The composite material demonstrated a high rate of $CH_4$ production (17.9 μmol $g^{-1}$ $h^{-1}$) and a high selectivity of 90.4% under $CO_2$ concentrations $<2\%$. In addition, Wang *et al.*[718] showed that basic OH groups and divalent cobalt play a key role in the generation of $CH_4$ in low-concentration atmospheric $CO_2$ and water environments. This result highlights even more how crucial it is to create sensible catalysts in order to increase LCC conversion efficiency.

Compared with traditional thermal catalysis technology, photocatalysis faces greater challenges in large-scale applications, especially when the $CO_2$ concentration is low, the reaction rate is slow, resulting in the photocatalytic system requiring a larger illumination area and longer reaction time.[53,54] And the long-term stability of the catalyst is also a key issue, especially in the continuous reaction process of LCC,

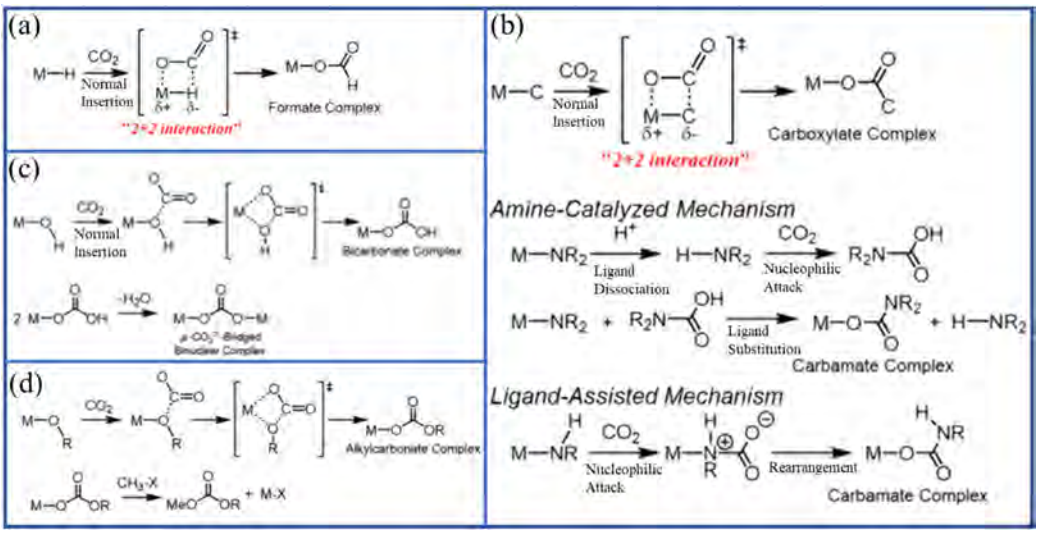


Fig. 22 M–X typing forms: (a) normal $CO_2$-Ins forms M–H bonds; (b) normal $CO_2$-Ins forms M–C bonds and M–N bonds; (c) normal $CO_2$-Ins forms M–OH bonds and subsequent possible dimerization reactions; (d) normal $CO_2$-Ins forms M–OR bonds and subsequent possible methylation reactions (reproduced from ref. 91 with permission from the Royal Society of Chemistry 2022).

the catalyst may fail due to photocorrosion or poisoning. Yamazaki *et al.*[91] summarized catalytic systems for LCC reduction (Fig. 22). These systems combine $CO_2$ reduction and capture reactions (or $CO_2$ adsorption), allowing $CO_2$ to significantly increase the binding rate constant and/or equilibrium constant of $CO_2$ to the catalyst by forming M–X bonds with the catalyst. In addition, these systems further stabilize the $CO_2$-bound catalyst by creating a second coordination layer. The unique properties of the photocatalytic reaction medium can also increase the concentration of $CO_2$ around the catalyst, thereby further improving reaction efficiency.

**4.2.2 Electrocatalytic $CO_2$ reduction.** The electrochemical reaction drives the electrocatalytic reduction reaction of $CO_2$ by converting electrical energy into chemical energy. This process is usually through the adsorption of $CO_2$ molecules on the electrode surface and their reduction to organic compounds or other hydrocarbons through electron transfer.[711,719,721] Nevertheless, the electrocatalytic reaction's kinetic rate is greatly slowed down under low $CO_2$ concentration circumstances. Due to the low contact probability between $CO_2$ molecules and the catalyst surface, electrochemical reactions often require higher overpotentials to drive, which not only increases energy consumption but also reduces conversion efficiency. In addition, low concentrations of $CO_2$ limit the supply of reactants, thereby reducing the overall reaction rate and product formation rate.[722] Samuel *et al.*[723] proposed a strategy to mimic cyanobacterial carboxysomes by utilizing microcompartments with nanozymes in porous electrodes. Carbonic anhydrase makes all dissolved carbon available and minimizes substrate consumption by accelerating $CO_2$ hydration kinetics, while efficient formate dehydrogenase reduces $CO_2$ to formate. The porous electrode structure helps facilitate rapid gas transport across the electrode–electrolyte interface at high current densities.[724]

Selectivity of the final product is impacted by the electrocatalytic process's increased susceptibility to side reactions (such the creation of hydrogen) at low concentrations. In the electrocatalytic $CO_2$ reduction process, for instance, the water electrolysis side reaction may speed up the synthesis of hydrogen rather than the $CO_2$ reduction product. To achieve this, extremely selective catalysts that can decrease $CO_2$ preferentially over water at low $CO_2$ concentrations must be developed. However, this goal is difficult to achieve. Masahiko *et al.*[725] found that early formation of carbonate complexes is crucial for efficient electrocatalytic reduction of LCC in ethanol. When the water concentration in the solution is as high as 2.8 M (5 vol%), it can still maintain high CO selectivity, faradaic efficiency and durability under 10% $CO_2$ conditions. By adjusting the hydrophobicity of the electrocatalyst using a polymer binder, the electrochemical reaction performance at the gas–solid–liquid interface can be optimized. The hydrophobic (aerophilic) nature of the polymer binder reduces the local concentration of HO and increases the concentration of reactants ($CO_2$) and reaction intermediates (CO).[55]

The electrochemical process is limited in low $CO_2$ conditions because it is more difficult for protons and electrons to transfer effectively. Therefore, the reaction is more dependent on the properties of the catalyst active sites and the optimization of the surface structure.[56] Hiromu *et al.*[722] achieved 94% CO selectivity and 85% faradaic efficiency at 1% $CO_2$ concentration by effectively inserting $CO_2$ into the Re(I)–O bond in 4,4′-dimethyl-2,2′-bipyridine (dmb), and the CO formation rate reached 67% (Fig. 23a and b). In addition, the low solubility of $CO_2$ leads to increased mass transfer resistance, further reducing the $CO_2$ concentration on the electrode surface and affecting the reaction efficiency (Fig. 23c). Due to the large intrinsic activation energy of the hydrogen evolution reaction (HER), the Ni single atom catalyst (Ni–N/C) shows high tolerance to low $CO_2$ partial pressure.[57]

The design of the electrode contact and the choice of electrolyte are especially important when the $CO_2$ concentration is low.

 

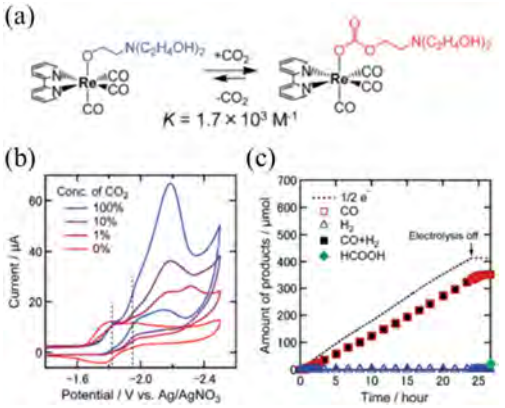


Fig. 23 (a) $CO_2$ capture pathway of Re(I) complex; (b) cyclic voltammograms (CVs) at different $CO_2$ concentrations; (c) yield at 1% $CO_2$ concentration (reproduced with permission from ref. 722. Copyright 2019 the Royal Society of Chemistry).

To enhance $CO_2$ enrichment on the electrode surface and for effective electrochemical reactions, certain electrolytes and electrode materials are needed.[726,727] However, optimizing these parameters to adapt to low concentration conditions is a complex process involving the balance of multiple factors such as conductivity, ionic conductivity and electrolyte stability. Kim *et al.*[57] studied the $CO_2$ reduction reaction at different $CO_2$ concentrations in a zero-gap membrane electrode assembly (MEA) electrolyzer and found that suppressing the hydrogen evolution reaction (HER) became more critical at low $CO_2$ concentrations (Fig. 24a). The electrocatalytic conversion of LCC usually requires higher electrical energy input (Fig. 24b and c), resulting in reduced energy efficiency.[58] This makes large-scale applications face cost challenges. In addition, how to combine the electrocatalytic process with renewable energy electricity to further improve the energy efficiency of the entire system is also an important direction of current research.[728,729]

**4.2.3 Thermal catalytic $CO_2$ conversion.** The thermal catalytic conversion technique for $CO_2$ is fueled by a thermal catalyst, which transforms thermal energy into chemical energy. To produce organic molecules or other chemicals, this process typically entails the adsorption and dissociation of $CO_2$ on the catalyst surface, followed by a reaction with other reactants.[730,731] Due to the chemical inertness of LCC, the thermal catalytic reduction process usually needs to be carried out at high temperatures above 600 °C, which not only increases the energy consumption of the system but also poses challenges to energy efficiency optimization.[732,733] In contrast, electrocatalysis and photocatalysis technologies drive reactions through electric fields or light energy and can proceed at lower temperatures, thus reducing reliance on high temperatures.[734]

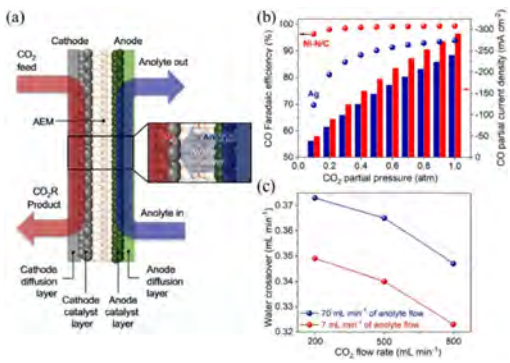


Fig. 24 (a) Schematic diagram of the MEA system and water crossover across the membrane shown in the inset; (b) simulated CO faradaic efficiency and CO partial current density at different $CO_2$ partial pressures; (c) plot of water crossover *versus* $CO_2$ feed rate for two anode electrolyte flow rates calculated by CFD simulation (reproduced with permission from ref. 57. Copyright 2021 American Chemical Society).

The selectivity of the $CO_2$ reduction process can be greatly impacted by the easy induction of a number of side reactions by thermal catalysis, including carbon deposition and catalyst sintering, at high temperatures.[735] The low concentration of $CO_2$ further reduces the frequency of contact between reactants and catalysts, thereby exacerbating the occurrence of side reactions.[736] This is in contrast to electrocatalytic technologies, which can precisely control reaction pathways and product selectivity by regulating potential.[737]

Thermal catalytic reduction of $CO_2$ requires extremely high catalyst activity, especially under LCC conditions. Catalysts need to remain active for long periods at high temperatures and prevent sintering or deactivation.[738] However, high temperatures can aggravate catalyst degradation, such as aggregation of metal particles and phase change of the support, leading to shortened catalyst life.[739,740] This situation occurs less frequently in low-temperature electrocatalysis and photocatalysis because these technologies operate at lower temperatures and have lower requirements for the thermal stability of the catalyst. Jiang *et al.*[741] synthesized a unique $Cu^{I}/Cu^{II}$ mixed valence copper-based framework with good solvent stability and thermal stability, as well as high density of uncoordinated amino groups evenly distributed in large nanopores. The triple synergistic catalytic effect between $Cu^{I}/Cu^{II}$ and uncoordinated amino groups significantly improves the green conversion efficiency of $CO_2$ (Fig. 25a and b). The yield can approach 99% at normal pressure, low temperature, and flue gas with a 25% $CO_2$ content.

Conditions with low $CO_2$ concentrations highlight mass transfer constraints in particular. Effective conversion is challenging because of the low concentration of $CO_2$ in the reactor, which limits its adsorption and reaction rate on the catalyst surface. One of the key strategies to increase the accessibility of catalyst active sites is to build multi-level catalyst pores.[742–744] The large pore structure helps the reactant molecules to diffuse more easily into the catalyst, while the small pores provide abundant specific surface area to accommodate more active sites.[745] In addition, the effect of mass transfer on the catalytic reaction is also reflected in the shape selectivity effect brought about by the matching relationship between the reactant molecules and the catalyst pore size.[746,747] Many researchers have improved catalyst performance by encapsulating active components in molecular sieve micropores to control the diffusion of reactant and product molecules.[59,60] Innovative

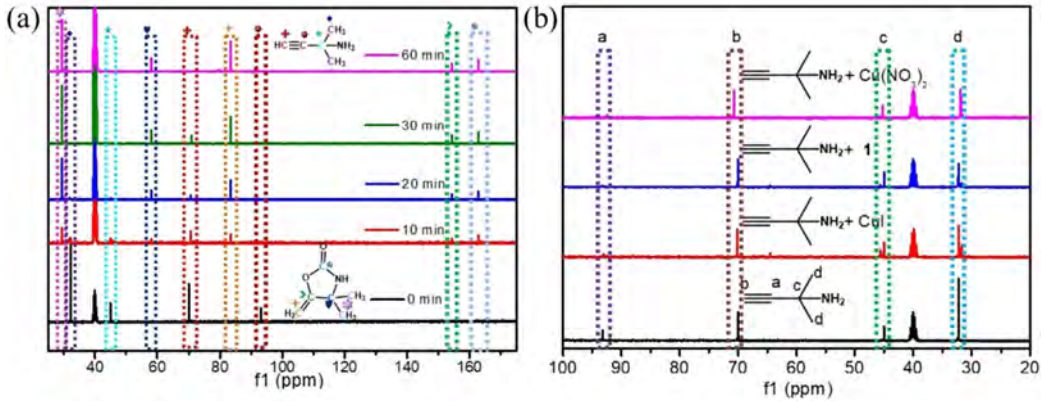


Fig. 25 (a) $^{13}C$ NMR ($D_6$-DMSO) monitoring of the cyclization reaction of $Cu^{I}/Cu^{II}$ mixed-valence copper-based framework and $CO_2$; (b) activation of propargylamine by different systems (reproduced with permission from ref. 742. Copyright 2021 John Wiley & Sons).

reactor design has also further improved the efficiency and rate of the reaction. GAO *et al.*[61] summarized the application of molecular sieve membrane catalytic reactors in methane/$CO_2$ dry catalytic reforming and achieved remarkable results, breaking through the limitations of thermodynamic equilibrium. The conversion rates of $CO_2$ and methane in the reaction can reach more than 70%.

Thermal catalytic reduction of LCC has low energy efficiency and requires a large amount of heat energy to maintain the reaction temperature, which makes large-scale application economically challenging. Even an ideal catalytic process requires electricity that emits less than 0.2 kg of $CO_2$ per kilowatt-hour to achieve a net reduction in $CO_2$.[748]

On the other hand, energy consumption can be better managed by electrocatalysis and photocatalysis, which employ electrical or light energy, particularly when powered by renewable energy. To increase the thermal conversion efficiency of LCC, it is now normal practice to combine photocatalysis with electrocatalysis.[749,750] Photothermal catalysis drives catalytic reactions through light energy, converts light energy into heat energy, and then enhances the catalytic reaction rate. Researchers have developed nanomaterials with broad spectrum absorption capabilities, such as metal nanoparticles and metal oxides,[751,752] which can efficiently absorb sunlight and convert it into heat energy, and show high conversion efficiency under low $CO_2$ concentration conditions. Photothermal catalysis can enhance the activation of $CO_2$ molecules through local thermal effects, thereby promoting its reaction efficiency at lower concentrations.[753,754] Combining the photothermal effect and the active sites on the catalyst surface can significantly improve the $CO_2$ conversion rate.

In photothermal catalysis, by optimizing reaction temperature, light intensity, and reaction time, higher product selectivity and yield can be achieved under LCC conditions.[755,756] Electrothermal catalysis combines electric field and thermal energy to promote catalytic reactions and is suitable for research on the conversion of LCC. Electrothermal catalytic materials usually have high electrical conductivity and high thermal stability, such as MOFs, metal oxides, and conductive polymers.[750] These materials can effectively promote the adsorption and conversion of LCC under the combined action of electric field and thermal energy.[757,758] Through the utilization of an external electric field to polarize $CO_2$, electrothermal catalysis also raises the temperature of the reaction and increases the surface reactivity of the catalyst *via* the Joule heat produced by an electric current.[759] This synergistic action can greatly increase conversion efficiency when $CO_2$ concentration is low. At low concentrations of $CO_2$, effective reaction kinetics may be accomplished while regulating the formation of byproducts by adjusting factors including current intensity, reaction temperature, and duration.[760] Catalytically activated open-cell foam was applied by Zheng *et al.*[761] It has the best mass transport and heat properties and acts as a Joule heating substrate for the catalytic conversion of $CO_2$ through interaction with hydrogen or methane (Fig. 26a). The proposed $Rh/Al_2O_3$-coated foam reactor system with Joule heating exhibits excellent catalytic and electrical stability with a duration of more than 75 hours and an operating temperature as high as 800 °C. Near equilibrium conversion at high space speeds, the volumetric space velocities of reverse water gas shift and electrified methane $CO_2$ reforming are 600 and 100 kN l $kgcat^{-1}$ $h^{-1}$ respectively (Fig. 26b–d). This reactor concept has the potential to significantly reduce the specific energy requirements required for $CO_2$ valorization. The energy consumption of reverse water gas shift is approximately 0.7 kW h $N^{-1}$ $m^{-3}$ $CO_2$.

**4.2.4 Plasma-catalyzed $CO_2$ conversion.** High-energy electrons in plasma serve in plasma catalysis to activate and excite $CO_2$ molecules, changing them into other chemicals or organic compounds.[762,763] In situations when $CO_2$ concentrations are minimal, the high-energy electrons in the plasma may not be sufficient to effectively and selectively activate $CO_2$. Further byproducts and non-selective side reactions, like carbon deposition, result.[764,765] In this instance, there is a hurdle in efficiently utilizing energy and maintaining product selectivity due to the vast and unpredictable energy distribution of the plasma.

The plasma environment has extremely high inhomogeneity, and the temperature, electron density and reactant

 

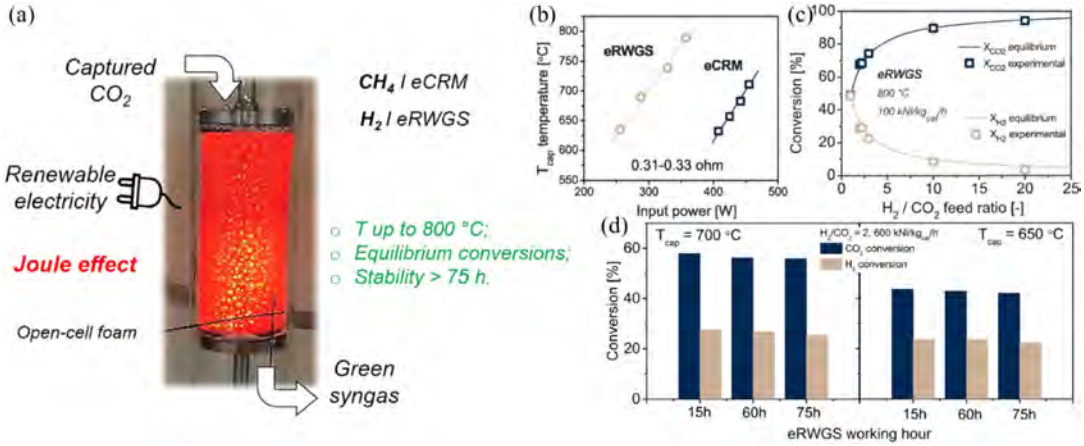


Fig. 26 (a) Electrothermal catalytic reaction system based on Joule heating; (b) $T_{cap}$ temperature *versus* input power measured during $CO_2$ methane reforming (eCRM) and reverse water gas shift (eRWGS) operations; (c) $CO_2$ and $H_2$ conversion during eRWGS operation at different $H_2/CO_2$ feed ratios; (d) stability of coated SiSiC foam in eRWGS experiments (reproduced with permission from ref. 761. Copyright 2023 Elsevier).

concentration are unevenly distributed in the reactor, making the reaction process difficult to accurately control.[766] This inhomogeneity is more pronounced at low $CO_2$ concentrations, which makes it more challenging to guarantee enough $CO_2$ molecule activation and consistent reduction processes.[767] In contrast, thermal catalysis and electrocatalysis reactions proceed under more uniform conditions, making the reaction process easier to control and optimize.[768,769]

The synergistic synergy between catalyst and plasma is crucial in plasma catalysis.[770] Nevertheless, the number of active species stimulated by the plasma is decreased at low $CO_2$ concentrations, which may lessen this synergistic impact and lower the reaction efficiency as a whole.[63] Brock *et al.*[64] found that low-concentration (2.5%) $CO_2$ dissociated in a helium flow, generating vibrationally excited $CO_2$+ intermediates through charge and energy transfer from excited helium species. The reactivity order of different metal catalyst coatings is Rh > Pt ≈ Cu > Pd > Au/Rh ≈ Rh/Au ≈ Au. When using a Rh-coated reactor, the $CO_2$ conversion rate can be as high as 30.5%, the reaction rate is $8.07 \times 10^{-4}$ mol $h^{-1}$, and the energy efficiency is 3.55% (Fig. 27). At low $CO_2$ concentrations, electrocatalysis and photocatalysis can enhance the interaction between reactants and catalysts by regulating electric fields or light fields, making it relatively easy to achieve efficient conversion.[771,772]

Plasma environments place higher demands on the stability of catalyst materials, mainly because the bombardment of high-energy particles can cause damage to the catalyst surface, structural changes, or metal migration.[773,774] This impact can accelerate the failure of the catalyst, especially at low $CO_2$ concentrations, where the catalyst is more vulnerable to damage when exposed to the plasma environment for a long time due to the low reaction rate.[775] According to Młotek *et al.*,[62] soot would develop after performing plasma-catalyzed biogas processes for an extended period of time. This might cause catalyst poisoning, which would hinder the reaction's ability to proceed, as well as discharge failure. Mohamed *et al.*'s[776] strategy for producing ethylene from $CO_2$ and $CH_4$ included direct current glow discharge; however, the process created carbon filaments, which led to electrical short circuits and plasma failures (Fig. 28). These carbon filaments not only affect the selectivity of $C_{2+}$ products, but also reduce the conversion of $CO_2$ and $CH_4$. In contrast, thermal catalysis and electrocatalysis have accumulated more experience in catalyst selection, stability optimization, *etc.*, and have better stability.[777,778] Therefore, in

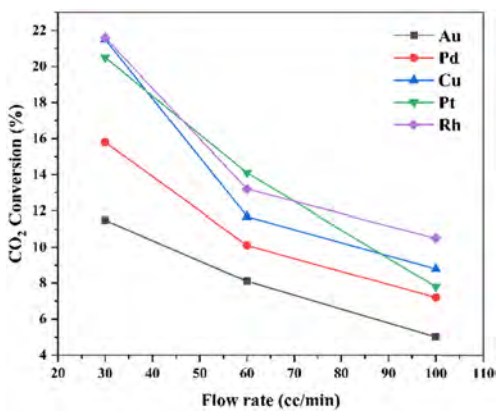


Fig. 27 $CO_2$ conversion of a 2.5% $CO_2$/He mixture as a function of reactant gas flow rate for various metal catalysts at 711 V rms (root-mean-square) input voltage (reproduced with permission from ref. 64. Copyright 1998 Elsevier).

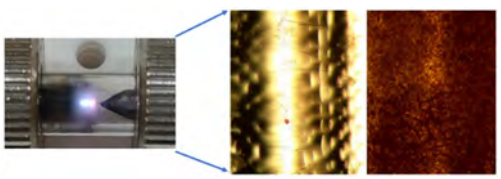

Fig. 28 Formation of a carbon filament between the electrodes of a plasma discharge. This filament short-circuits the reactive plasma, stopping all potential reactions and causing a critical reactor failure (reproduced with permission from ref. 776. Copyright 2021 Mohamed O M. All rights reserved).

plasma catalysis, the selection of highly durable catalyst materials and the development of strategies to reduce carbon deposition and structural degradation are key to improving the efficiency of catalytic reactions. In contrast, electrocatalysis and thermal catalysis technologies are more reliable in terms of material stability and long-term use.

The design of plasma catalytic reactors is relatively complex and requires the optimization of multiple parameters, such as plasma generation, maintenance, and contact between plasma and catalyst.[779,780] The design becomes more challenging when the $CO_2$ concentration is low because it must be made sure that the few $CO_2$ molecules can get enough plasma energy for a productive reaction. As a result, the reactor has to have a high energy density while minimizing unnecessary energy loss.

On the other hand, the design of reactors for thermal and electrocatalysis is more advanced, and these technologies have also operated on an industrial scale for a longer period of time.[781,782] Thermal catalysis usually relies on high temperature conditions, and high reaction efficiency can be achieved by optimizing the thermal management of the reactor and the distribution of the catalyst. Electrocatalysis controls the reaction by regulating the electric field and electrode materials, which allows it to operate effectively under low temperature conditions and is easier to combine with renewable energy to further improve energy efficiency. Therefore, although plasma catalysis has unique advantages in some cases, its complex reactor design and low energy efficiency limit its feasibility for large-scale application. Thermal catalysis and electrocatalysis have greater potential in industrial applications due to their more mature reactor design and easier large-scale operation.

**4.2.5 Biocatalytic $CO_2$ conversion.** Biocatalytic $CO_2$ conversion relies on specific enzymes or metabolic pathways, through which biological systems convert $CO_2$ into target compounds.[783,784] Multiple natural $CO_2$ fixation pathways have been discovered in nature, and there are currently 7 major $CO_2$ fixation pathways.[785] The response rate of biocatalysis is greatly decreased in low $CO_2$ concentration environments, which presents a considerable difficulty. Because biocatalysis often occurs in mild environments, biological systems find it challenging to sustain enough reactivity at low $CO_2$ concentrations.[786,787] In contrast, technologies such as photocatalysis or thermocatalysis can enhance the reaction rate through external energy fields, which is especially advantageous when the $CO_2$ concentration is low.

The effectiveness of biocatalysts is highly dependent on the capture and delivery of $CO_2$, but it is difficult for biological systems to achieve efficient $CO_2$ capture and delivery to reaction centers under low $CO_2$ concentration conditions.[788,789] This is in contrast to other catalytic technologies such as plasma catalysis, which can effectively improve the efficiency of $CO_2$ capture and reaction through the excitation of high-energy electrons.[790] Ismael *et al.*[65] compared the $CO_2$ capture capacity of porous zeolite adsorption and microalgae biomass and found that after numerical simulation, zeolite could capture 8 kg $CO_2$ per cubic meter of bed per hour with an energy consumption of 0.987 MJ $kg^{-1}$ $CO_2$. Scenedesmus almeriensis microalgae performed best in wastewater, with a capture rate of 0.1 kg $m^{-3}$ $h^{-1}$ and an energy consumption of 0.48 MJ $kg^{-1}$ $CO_2$, which is better than zeolite adsorption. Combining high specific surface area materials for $CO_2$ adsorption and bioconversion is an effective strategy. Li *et al.*[66] went on to show how MOFs may be utilized as $CO_2$ adsorbents and carriers of enzyme immobilization. They also showed how to accomplish effective $CO_2$ adsorption and conversion *via* a layer-by-layer self-assembly technique (Fig. 29a). In order to accomplish the conversion of $CO_2$ to formate, they employed amine-functionalized MIL-101(Cr) for initial $CO_2$ adsorption and built two layers of HKUST-1 on its surface, immobilizing carbonic anhydrase and formate dehydrogenase, respectively (Fig. 29b–e). The immobilized enzyme exhibited remarkable reusability and operational stability. 10 cycles of implementation resulted in a cumulative formate output of 1077.7%. The effective conversion

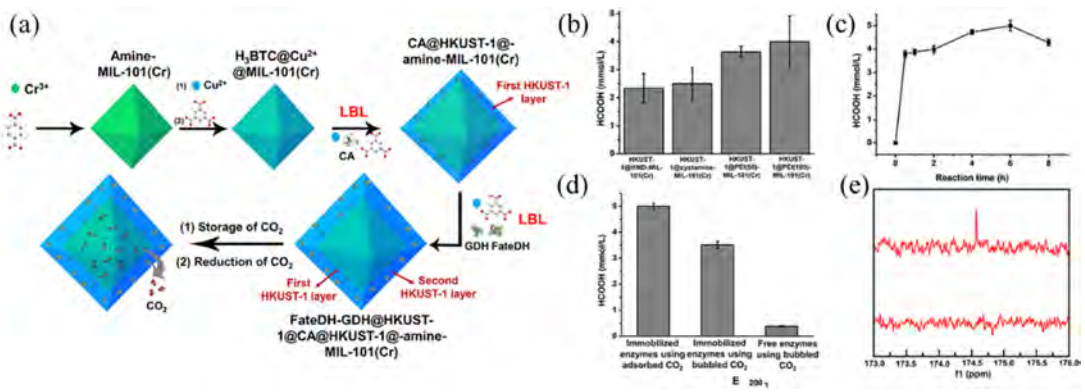


Fig. 29 (a) Amine-functionalized MIL-101(Cr) immobilized enzyme for $CO_2$ adsorption; (b) HCOOH production catalyzed by HKUST-1@HMD-MIL-101(Cr), HKUST-1@cystamine-MIL-101(Cr), HKUST-1@PEI(50)-MIL-101(Cr), and HKUST-1@PEI(100)-MIL-101(Cr) immobilized enzyme systems; (c) formic acid production at different reaction times; (d) HCOOH production catalyzed by HKUST-1@PEI(100)-MIL-101(Cr) immobilized enzyme with adsorbed $CO_2$ as substrate, HKUST-1@PEI(100)-MIL-101(Cr) immobilized enzyme with bubbled $CO_2$ as substrate, and free enzyme with bubbled $CO_2$ as substrate; (e) $^{13}C$ NMR spectrum of formic acid produced by HKUST-1@PEI(100)-MIL-101(Cr) immobilized enzyme using $CO_2$ as substrate (reproduced with permission from ref. 66. Copyright 2019, Frontiers Media S.A).

 

of LCC is made possible by this approach, which combines adsorption with biocatalysis.

The activity of biocatalysts is indeed severely limited by environmental conditions, such as temperature, pH, pressure, *etc.*[68] At low concentrations of $CO_2$, these limitations become more significant because subtle changes in reaction conditions can affect catalytic efficiency. Different microalgae species have different tolerances to $CO_2$. Some microalgae can maintain normal growth under low concentrations of $CO_2$, while other microalgae require high concentrations of $CO_2$ to achieve higher growth rates. Studies have shown that extremely high concentrations of $CO_2$ have an anesthetic effect on microalgae, inhibiting their cell growth and photosynthesis, resulting in a "lag phase" in growth.[67] The mass transfer process of $CO_2$ and $O_2$ is a key factor affecting the growth of microalgae and its carbon fixation efficiency. Due to the low mass transfer coefficient, the transfer rate of $CO_2$ required by microalgae at the air–liquid interface is limited.[791] $O_2$ produced by photosynthesis will inhibit the growth of microalgae as it accumulates.[792] To solve this problem, increasing the gas supply flow rate or creating turbulence is usually used to improve the gas mass transfer rate and liquid mixing efficiency. However, excessive turbulence and shear effects may damage microalgae cells, thereby affecting their normal growth.[793] To increase the $CO_2$ dissolution rate and extend the gas–liquid contact time, Xu *et al.*[794] designed a spiral $CO_2$ dissolver, aiming to enhance the $CO_2$ mass transfer efficiency in the horizontal tubular photobioreactor (Fig. 30a). By using spiral baffles, this dissolver shortens the bubble generation time by 30.6% and reduces the bubble diameter by 23.4%, thereby increasing the mass transfer coefficient by 69.2%. At the same time, the residence time of the bubbles increased by 190.2%, significantly extending the contact time between $CO_2$ and the liquid phase, thereby increasing the dissolved concentration of $CO_2$ (Fig. 30b and c). This optimization resulted in a 40.8% increase in the biomass accumulation of microalgae in the horizontal tubular photobioreactor under 15% $CO_2$ concentration.

However, biocatalysts are susceptible to deactivation in LCC environments, particularly when operating for an extended period of time. The catalyst's sustainability and stability present significant obstacles. Because they are more vulnerable to changes in the environment and byproducts than inorganic catalysts, biocatalysts have a shorter service life and are less reusable.

In addition to natural carbon sequestration pathways, various efficient artificial carbon sequestration methods have also been rapidly developed in recent years. For example, the Max Planck Institute of Terrestrial Microbiology in Germany developed the crotonyl–coenzyme A (CoA)/ethylmalonyl-CoA/hydroxybutyryl-CoA (CETCH) cycle, which converts $CO_2$ into glyoxylic acid through an enzymatic reaction, achieving $CO_2$ regeneration. Fixation and transformation.[795] The artificial starch anabolic pathway (ASAP) designed by the Tianjin Institute of Industrial Biotechnology, Chinese Academy of Sciences, can convert $CO_2$ into starch and hexoses, which provides a new strategy for sustainable biomass production.[796,797] In addition, the Institute of Microbiology of the Chinese Academy of Sciences created a POAP cycle by combining multiple enzymes (such as pyruvate carboxylase, oxaloacetate acetyl hydrolase, *etc.*) to convert $CO_2$ into oxalic acid through a four-step reaction.[798] Westlake University has also developed a chemical enzyme system that does not require ATP and NAD(P)H, and achieves carbon fixation by combining biological and chemical catalysis, using only dithiothreitol as a reducing agent.[799] Although these artificial carbon fixation pathways have shown significant potential *in vitro*, the large-scale application of biocatalysis under LCC conditions still faces many challenges. This includes

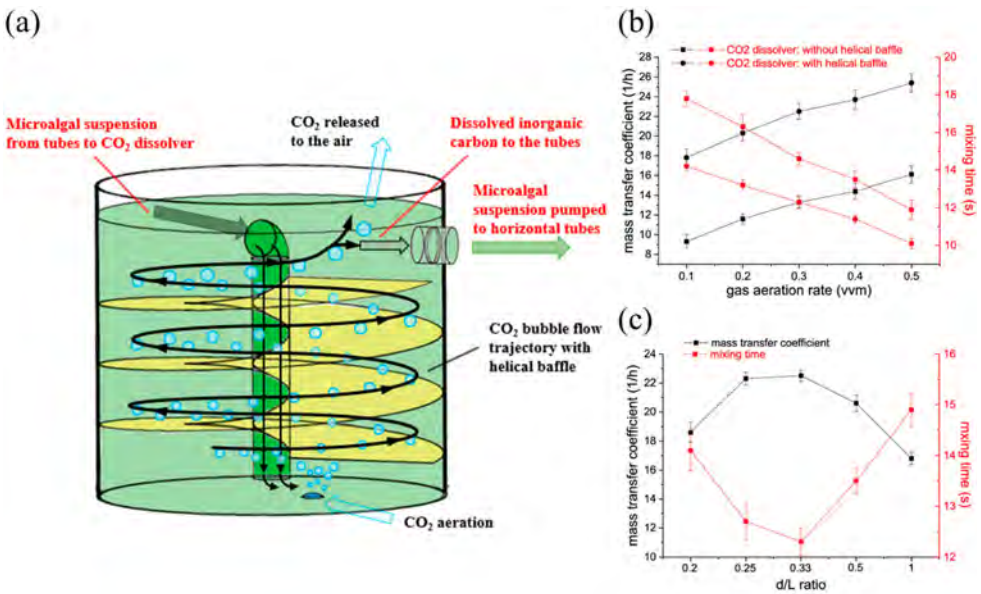


Fig. 30 (a) Schematic diagram of the $CO_2$ dissolver with spiral baffles; (b) mass transfer coefficient and mixing time with and without spiral baffles; (c) effect of the ratio of spiral baffle pitch to length ($d/L$) (reproduced with permission from ref. 794. Copyright 2020, American Chemical Society).

optimization of reaction conditions, system design complexity, and overall process scalability.[800,801]

It is currently challenging for biocatalysis technology to attain the industrial maturity of electrocatalysis and thermocatalysis. High manufacturing costs and low process energy efficiency are the key obstacles. These issues impede biocatalytic technology's progress toward industrialization. Despite this, biological carbon sequestration technology still has a lot of promise, particularly for the manufacture of protein meals and biofuels. It is also anticipated to make significant advancements in the future in the synthesis of fine compounds with high added value.

## 5. Application of $CO_2$ in compressed gas energy storage technology

Compressed gas energy storage (CGES) is an energy storage system with significant development potential, gaining attention for its efficiency and flexibility. The basic principle of CGES involves using surplus or low-cost electricity during off-peak periods to compress gas (typically air, $CO_2$, or other $CO_2$-based mixture) and store it in suitable storage media, such as natural salt caverns, underground rock formations, or man-made storage tanks. During peak demand periods, the high-pressure gas is released to drive an expander, generating electricity. This method allows for timely power adjustment and balancing, providing effective support for peak and frequency regulation in power systems.[802–804]

CGES not only alleviates the stress on the grid caused by the imbalance between power supply and demand but also addresses the intermittency and variability issues associated with renewable energy sources like wind and solar power. This enhances the stability and reliability of the power system, making CGES an innovative solution and a promising avenue for global energy transition, energy crisis mitigation, and environmental pollution reduction.

In this context, the application of $CO_2$ as a potential compressed medium in CGES has gained widespread attention. Unlike traditional air compression systems, $CO_2$ exhibits higher compressibility and a lower critical temperature under specific conditions, giving it unique thermodynamic properties during energy storage and release.[805,806] Exploring and utilizing these properties of $CO_2$ in CGES can not only improve the efficiency of storage systems but also integrate with LCC capture and conversion technologies. This integration forms a comprehensive carbon recycling system, achieving both energy and environmental benefits.

### 5.1 Application of $CO_2$ in compressed air energy storage

In CGES technology, air is a common working medium, and the corresponding system is usually called compressed air energy storage (CAES).[807,808] The corresponding schematic diagram is shown in Fig. 31.

Compressed air energy storage (CAES) is a well-established energy storage technology with a 50-year development history.[69–71] Early CAES systems mainly relied on fossil fuels, using high-pressure air directed into combustion chambers to drive turbines for power generation, which resulted in low efficiency. To enhance efficiency, researchers developed various CAES systems based on the traditional combustion-assisted CAES, including adiabatic CAES (A-CAES),[809] isothermal CAES (I-CAES),[810] liquid air energy storage (LA-CAES),[811] supercritical compressed air energy storage (SC-CAES), underwater CAES (UW-CAES),[812] compressed air energy storage in aquifers (CAESA),[813] and other second-generation technologies.[814,815] These advanced systems reduce reliance on fossil fuels and, under certain conditions, overcome geographical limitations.

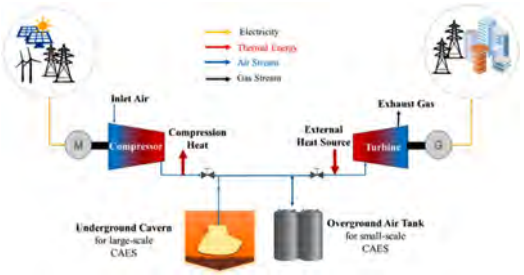


Fig. 31 Schematics of the operating principle of the CAES plant (reproduced with permission from ref. 808. Copyright 2022 Elsevier).

CAES stores energy by manipulating air states, as shown in the air phase diagram (Fig. 32),[805] with pressure and temperature ranges indicated for engineering applications. Due to atmospheric constraints, the pressure varies between 0.1 MPa and 20 MPa, while the temperature ranges from 273 K to 600 K. Additionally, for L-CAES and S-CAES, air is stored in liquid form, significantly reducing storage volume due to the high density of liquid air. During the charging process, air is typically compressed to a lower pressure before throttling and liquefaction, with liquid air pressure ranging from 0.5 to 4.5 MPa. In the discharge process, stored liquid air is first pressurized and then evaporated, absorbing heat to convert it into gaseous form, reaching up to 20 MPa to drive the expander for power generation.[805]

CAES can also be integrated with other power cycles, such as gas turbines,[816] coal-fired power plants,[817] and renewable

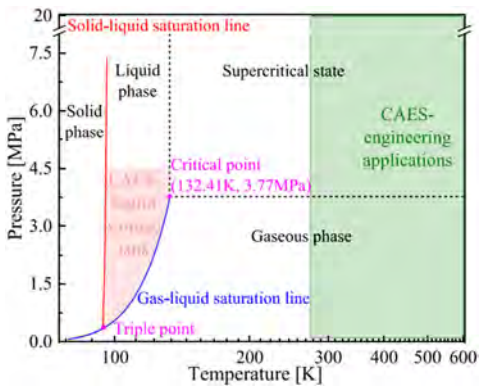


Fig. 32 Three-phase diagram of air (adapted with permission from ref. 805. Copyright 2024 Elsevier).


Fig. 33 The regional distribution and capacity of CAES projects (reproduced with permission from ref. 805. Copyright 2024 Elsevier).

energy sources. When combined with other power cycles, waste heat from these processes can be recovered through the CAES cycle to improve overall efficiency. When integrated with renewable energy sources like wind,[818] solar,[819] and biomass,[820] CAES enhances their availability and flexibility.[821]

In addition to theoretical work on A-CAES, demonstration systems have been established to verify its feasibility and promote the development of the CAES industry. With the widespread availability of air, as well as the advanced development of compressors and turbines, CAES technology has reached the stage of large-scale process validation and engineering demonstration worldwide. The regional distribution and scale of these systems are shown in Fig. 33.[805]

Currently, there are two operational CAES systems globally: the 290 MW Huntorf power station in Germany,[822] which was commissioned in 1978, and the 110 MW McIntosh power station in the United States, the second commercial CAES facility, which has been in operation since 1991. In China, there is a 1.5 MW A-CAES project in Langfang[823] and a 10 MW A-CAES project in Beijing.[815] In 2021, Chen *et al.*[824] built a 100 MW × 4 h A-CAES system in Zhangjiakou, Hebei Province. This system successfully integrated into the grid and began generating power in September 2022, achieving a round-trip efficiency (RTE) of 70.2%.

CAES offers large capacity, flexibility, high efficiency, long lifespan, and environmental benefits, providing a reliable and efficient energy storage and dispatch solution for power systems. It balances the difference in power supply and demand, enhancing the flexibility and stability of the grid.[825] Currently, CAES is mainly used for peak shaving, backup power, frequency regulation, and the storage and dispatch of renewable energy. Studies predict that CAES, with its substantial potential, is among the most economical alternatives for large-scale power plants.[826]

The way LCC behaves in CAES systems can have a big effect on how well the system works. $CO_2$ is compressed together with other gases during the air compression process and kept in the storage reservoir, despite the fact that the concentration of $CO_2$ in the air is normally low, at around 0.04%. Low concentrations of $CO_2$ in this atmosphere combine with other gases, including nitrogen ($N_2$) and oxygen ($O_2$), changing the compressed air's characteristics.[827] Especially in SC-CAES and LAES systems, where $CO_2$ may be compressed into a liquid state or even partially solidified, its presence might affect air stability. Additionally, $CO_2$ is somewhat soluble and can react with water molecules to create compounds like bicarbonates, which might result in solid $CO_2$ deposits that obstruct equipment and pipes.[802]

$CO_2$ can be utilized by CAES systems to assist in regulating the pressure inside storage chambers (Fig. 34). For CAES with artificial caverns, conventional salt caverns are no longer needed, and the site constraints of salt caverns can be lessen.[828] Since December 21, 2022, two 300 MW artificial CAES caverns are under construction in Chaoyang, Liaoning Province, and Jiuquan, Gansu Province, China, and their volume are approximately 210 000 cubic meters. However, the average construction cost for artificial caverns is around $500 per cubic meter, compared to just $100 per cubic meter for excavating salt caverns.[829] This high cost presents a significant challenge for artificial CAES caverns.[830] Within

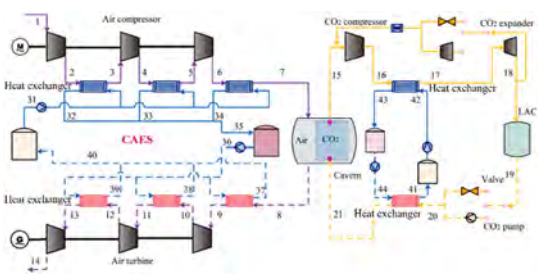


Fig. 34 Schematic diagram of isobaric CAES with artificial cavern (reproduced with permission from ref. 829. Copyright 2024 Elsevier).

artificial caverns, the pressure load is cyclic during the CAES charging and discharging operation. The expansion pressure must be less than the storage pressure during discharge process, and the air below expansion pressure does not do any work.

Maintaining isobaric conditions during discharge process not only reduces the amount of caverns needed and construction costs, but also improves cavern safety and reliability. Zhang *et al.*[829] designed a pressure-stabilizing unit utilizing the phase change of $CO_2$ to create an isobaric system. $CO_2$ balloons placed in storage caverns help balance the pressure, and their thermodynamic and economic performance was assessed numerically. The optimal design conditions were found to be 6.5 MPa for air storage, 6 MPa for $CO_2$ storage, and 9 MPa for $CO_2$ liquefaction, resulting in a system efficiency of 69.92%, a balanced storage cost of $0.1332 per kW h, a dynamic payback period of 7.26 years, and a return on investment of 1.58.[829] Compared to an isochoric system with equivalent efficiency, the storage pressure was reduced to 65% of its original value, and the system maintained constant pressure during operation, significantly improving reliability and safety of the system. Furthermore, the specific volume of saturated liquid is an order of magnitude smaller than that of saturated gas, enabling a 31.86% reduction in cavern scale.[829]

$CO_2$ can also be utilized as a cushion gas in CAES systems. Conventional CAES relies caverns to storage compressed air, however aquifers, which are widely dispersed, are thought to be efficient storage reservoirs for CAES in order to get over geological constraints. Reducing negative impacts on the reservoir during storage, such as oxygen loss from mineral oxidation, is essential to improve the reliability and effectiveness of energy recovery in CAESA systems.[831,832] One way to lessen these problems is to use $CO_2$ as the cushion gas in CAES (Fig. 35).[813]

$CO_2$ offers higher compressibility than air, making it an effective cushion gas for CAES. For a CAES using $CO_2$ as the cushion gas, the efficiency of gas storage operations can be improved, and the air storage capacity at the same reservoir pressure is enhanced.[833] Additionally, this approach provides a new carbon sequestration option, reducing the release of greenhouse gases into the atmosphere.[813] However, further research and experimentation are needed to evaluate the actual performance of CAES systems using $CO_2$ as a cushion gas, as well as to assess the economic and environmental costs and benefits of this approach.

Furthermore, the majority of the waste gases generated by CAES power plants are nitrogen oxides and carbon dioxide, both of which have an adverse effect on the environment and human health.[808] Moreover, noise levels during operation are also an issue, and prolonged operation of CAES would negatively impact the nearby residents. Nonetheless, CAES outperforms conventional energy technologies in terms of environmental preservation and is anticipated to emerge as a significant global energy alternative.[77]

### 5.2 Chemical effects of $CO_2$ in compressed $CO_2$ energy storage

**5.2.1 Technical overview.** The AA-CAES system relies on high-pressure containers or underground storage reservoirs, resulting in a relatively low energy storage density (typically ranging from 1.5 to 10 kW h $m^{-3}$) and large equipment size. SC-CAES and LAES systems involve the cryogenic liquefaction of supercritical air,[805] with the liquefaction temperature generally being −196 °C, leading to significant cold exergy losses that limit further performance improvements. Additionally, traditional CAES operates based on the Brayton cycle, but using a non-ideal gas (such as $CO_2$) instead of an ideal gas in the Brayton cycle can achieve better performance.[819] Utilizing the properties of non-ideal gases is a well-known method to enhance cycle efficiency.[834]

To further increase energy efficiency and energy density in storage systems, researchers have proposed a compressed carbon dioxide energy storage (CCES) system based on CAES technology, and $CO_2$ is used as the working fluid.[835] The layout of the CCES system (Fig. 36) is similar to that of CAES, with the primary difference being that CCES operates in a closed-loop configuration. Since $CO_2$ cannot be directly sourced from the environment, an additional low-pressure storage unit is required in the CCES system to store low-pressure $CO_2$.[69] By using $CO_2$, the CCES system can potentially achieve higher energy density and efficiency due to the favorable thermodynamic properties of $CO_2$, such as its high compressibility and lower liquefaction temperature compared to air. These characteristics allow for more efficient energy recovery and storage operations, making CCES a promising advancement in the field of energy storage technology.[829]

The superior thermophysical properties of $CO_2$ make it highly effective in energy storage systems.[836,837] As shown in the $CO_2$ phase diagram (Fig. 37a), its critical point is at 7.38 MPa and 31.3 °C, which is significantly easier to achieve

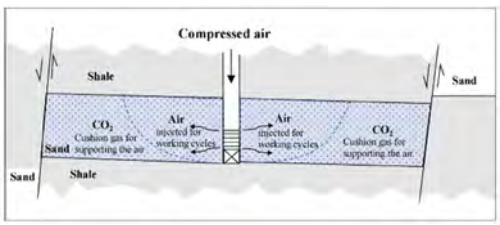


Fig. 35 An idealized single-well CAES reservoir using $CO_2$ as cushion gas (adapted with permission from ref. 813. Copyright 2021 Elsevier).

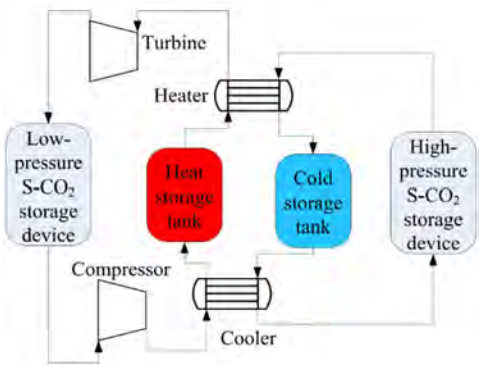


Fig. 36 The schematic diagram of SC-CCES system (adapted with permission from ref. 805. Copyright 2024 Elsevier).

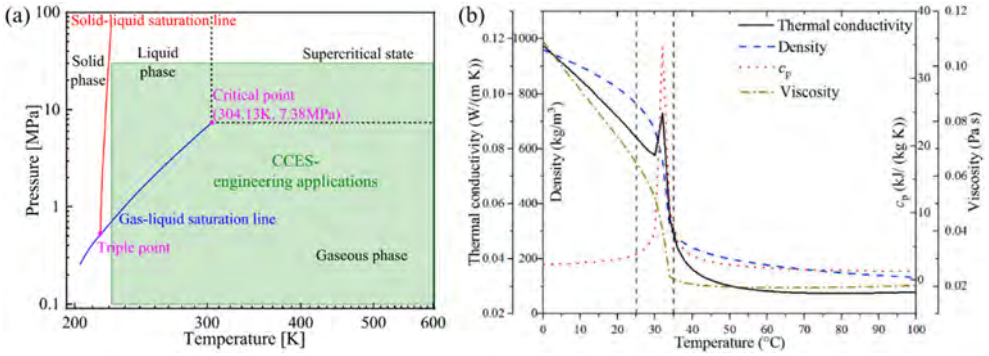


Fig. 37 (a) Three-phase diagram of $CO_2$ (adapted with permission from ref. 805. Copyright 2024 Elsevier); (b) rapid physical properties changes around the critical area of $CO_2$ (adapted with permission from ref. 806. Copyright 2022 Elsevier).

compared to air, with a critical point of 3.77 MPa and −140.5 °C.[805] This makes $CO_2$ more readily attainable in a supercritical state. Supercritical $CO_2$ ($sCO_2$) has low viscosity, high density, and excellent thermal conductivity,[806,838] which enhances efficient heat storage and heat exchange during system operations. As a result, compressed $CO_2$ energy storage systems are more compact than compressed air energy storage (CAES) systems at equivalent power levels.[839]

To increase the energy density of compressed gas storage technologies, the working fluid is often stored in a liquefied state. $CO_2$, with its higher dew point, liquefies more easily than air.[840] Unlike CAES, CCES operates as a closed-loop system, offering a scalable solution for $CO_2$ utilization,[841] which also contributes to reducing $CO_2$ emissions.[842] CCES technology offers several advantages: high cycle efficiency, lower construction complexity, long operational life, low system costs, and independence from geographical constraints. These features make it a promising option for large-scale energy storage and sustainable energy management.

The potential of CCES technology has been thoroughly investigated by researchers worldwide due to its many benefits. Depending on the temperature and pressure, $CO_2$ can exist in supercritical, liquid, gaseous, and solid forms. Fig. 37a also shows the usual working temperature and pressure ranges of CCES systems in engineering applications.[805] Presently, CCES systems operates in temperatures ranging from 220 K to 600 K and pressures between 0.1 MPa and 30 MPa. When $CO_2$ in the storage tank is in a supercritical state, the pressure and temperature must be above the critical point. If liquid $CO_2$ is present, the tank contains a two-phase state (liquid-gas), and the pressure corresponds to the saturation pressure at the given temperature. When $CO_2$ is in a gaseous state, the tank pressure must be lower than the saturation pressure corresponding to the storage temperature.

Despite the advantages of CCES, there are challenges due to $CO_2$'s properties. The significant variation in specific heat near the critical point (Fig. 37b) can worsen heat transfer processes, increasing exergy destruction in heat exchangers. Additionally, when an cold source at ambient temperature is used, the proximity of $CO_2$'s critical temperature to ambient conditions may lead to condensation issues.[843]

Up to now, various CCES systems have been developed. Based on the state of $CO_2$ in the low/high-pressure storage tanks, storage schemes can be categorized as follows: transcritical CCES (TC-CCES),[844] supercritical CCES (SC-CCES),[845] liquid CCES (L-CCES),[846] and vapor–liquid CCES (VL-CCES).[847] Moreover, CCES systems have been proposed for integration with other systems, such as Organic Rankine Cycle (ORC),[848] solar power,[849] Kalina cycle,[850] and wind turbine.[851,852]

Supercritical $CO_2$ ($sCO_2$) is kept in a high-pressure tank in TC-CCES, whilst liquid $CO_2$ is kept in a low-pressure tank. SC-CCES contains $sCO_2$ in both high-pressure and low-pressure tanks.[853] Both high-pressure and low-pressure tanks contain liquid $CO_2$ for L-CCES. $CO_2$ is normally stored in VL-CCES systems as a gas on the low-pressure side and as a liquid on the high-pressure side. The functioning of crucial components and the dynamic behavior of the system are greatly impacted by the dynamic changes in thermodynamic characteristics caused by the transformation of $CO_2$ between the states of gas, liquid, and supercritical during storage and discharge procedures.[854] VL-CCES is generally regarded as the best cost-effective and performance-balanced choice among these systems for engineering validation.[855] Zhang *et al.*[856] designed two energy storage systems to compare the performance differences between a transcritical $CO_2$ Brayton cycle and a supercritical $CO_2$ Brayton cycle. Their findings showed that the round-trip efficiency of the TC-CCES system is 11% lower than that of the SC-CCES system. Supercritical $CO_2$ ($sCO_2$), with its high fluid density and heat capacity, is an excellent working fluid for closed-loop power generation, allowing for highly compact turbine designs.[837] The compressibility factor of $sCO_2$ is lower than that of ideal gases, significantly reducing compression work. Compared to CAES, SC-CCES exhibits superior thermodynamic performance.[853]

Considering the above advantages of $sCO_2$, adopting $sCO_2$ instead of air as working medium in compressed gas energy storage systems reduces storage capacity and improves thermal efficiency. Despite being a relatively new technology, SC-CCES has drawn the interest of several academics worldwide because of its high efficiency and tiny footprint.[857] However, many aspects, including thermodynamic performance, system integration, and economic feasibility, need to be improved, making SC-CCES technology still in its infancy.[853]

For L-CCES, Zheng *et al.*[858] examined four different $CO_2$ storage configurations: low-pressure gas to high-pressure liquid, low-pressure gas to low-pressure liquid, low-pressure liquid to high-pressure liquid, and low-pressure liquid to low-pressure liquid. They conducted a detailed thermodynamic and economic performance comparison, showing that the low-pressure gas to high-pressure liquid configuration achieved storage efficiency above 68%. The low-pressure liquid to high-pressure liquid configuration demonstrated the best overall performance, indicating it as a key development direction for the future.

Currently, research on compressed $CO_2$ energy storage (CCES) technology mainly focuses on theoretical exploration,[835] and only a few demonstration projects are implemented, such as those by Dongfang Electric Corporation in China.[805] There are still significant challenges in developing key components for CCES systems, and their engineering applications remain in the early stages. The use of relatively high-pressure $CO_2$ poses safety and cost challenges regarding pressure capacity.[859]

Future efforts should aim to enhance theoretical research on $CO_2$ energy storage and strengthen experimental validation.[860] Additionally, exploring more system optimization strategies is essential.[861] The goal is to realize the transition from theoretical concepts to practical applications, and from concept development to project demonstration, ultimately promoting the widespread adoption of compressed $CO_2$ energy storage technology.

**5.2.2 $CO_2$ metal corrosion.** The corrosion problems brought on by $CO_2$ in CCES systems require particular consideration. A common electrochemical process is $CO_2$ corrosion, in which $CO_2$ dissolves in water to make carbonic acid that then splits into $H^+$, $HCO^{3-}$, and $CO^{3-}$ ions in two stages. By providing more $H^+$ ions, $CO_2$ speeds up the hydrogen evolution process, which in turn speeds up metal corrosion.[862] In this procedure, water is essential. According to studies, metal pipes do not corrode when supercritical $CO_2$ transport is conducted in completely dry or low-humidity (below the crucial moisture threshold) conditions.[863,864] However, under actual operating conditions, corrosion can happen quickly if the $CO_2$ gas is not completely dried and the moisture content becomes close to or over the critical threshold.[865]

Supercritical or dense-phase $CO_2$ has higher compressibility, diffusivity, and solubility, which can lead to corrosion rates in pipelines reaching up to 10 mm per year under certain conditions.[866] Hua *et al.*[867] studied the corrosion of X65 carbon steel at 50 °C and 8 MPa transport pressure under varying moisture levels in supercritical $CO_2$. They found that the corrosion rates of X65 steel in $CO_2$-saturated water, water-saturated $CO_2$, and partially water-saturated $CO_2$ were 10.0 mm per year, 1.4 mm per year, and 0.2 mm per year, respectively. In conditions where the water content was below 1600 μL $L^{-1}$ in partially saturated $CO_2$, no significant corrosion was observed.

Sun *et al.*[868] reported that the general corrosion rate was only 0.014 mm per year under 10 MPa and 50 °C after 120 hours. The corrosion process under these conditions is illustrated in Fig. 37.[84] Initially, water droplets condense locally as $CO_2$ saturates the droplets, forming $H_2CO_3$, which leads to localized corrosion of the steel. As the concentration of $Fe^{2+}$ increases in the water film, $FeCO_3$ forms, as shown in Fig. 38(a). With continued condensation, small water droplets merge, eventually forming a continuous water film that promotes uniform corrosion. This process leads to the development of a thick and protective $FeCO_3$ film on the steel surface (Fig. 38(b)). Notably, when the moisture content is low and exposure time is short, areas without water condensation do not experience corrosion.

Supercritical $CO_2$ may contain various impurity gases, such as $O_2$, $SO_2$, and $H_2S$. In the corrosion process of supercritical $CO_2$, $O_2$ can transform the corrosion product $FeCO_3$ into $Fe_2O_3$. The impact of $SO_2$ on pipeline corrosion is mainly due to its interaction with water and $O_2$, which promotes the formation of acidic media, lowering the system's pH and accelerating pipeline corrosion.[869] Research has shown that the corrosive effect of $SO_2$ on pipeline steel is more severe than that of $O_2$.[870,871] Moreover, when both $SO_2$ and $O_2$ are present, the corrosion rate of pipeline steel is higher than that under either gas alone.[870] $H_2S$ increases the pipeline's water adsorption capacity, and the amount of water condensing on the pipe walls is raised, which accelerates the formation of a thin liquid film on the surface and, consequently, speeds up the corrosion process. Wei *et al.*[872] found that

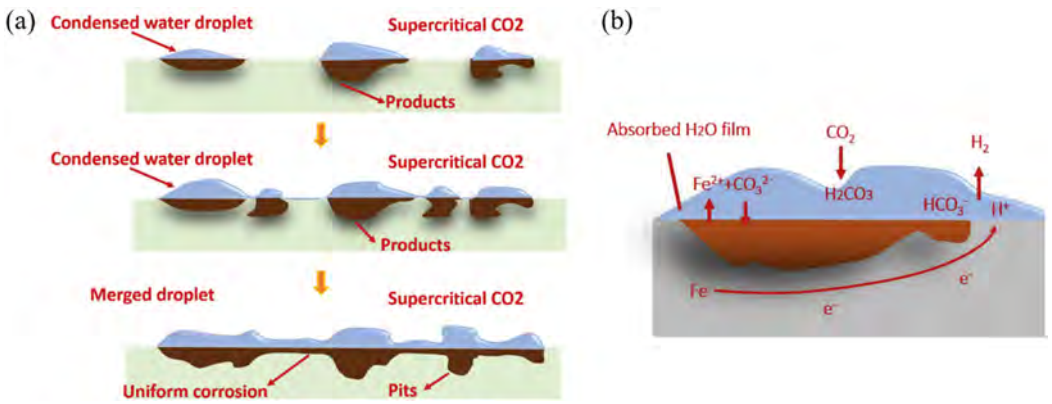


Fig. 38 (a) Corrosion process diagram under the water-saturated $CO_2$ phase; (b) corrosion mechanism diagram under the water-saturated $CO_2$ phase (reproduced with permission from ref. 84. Copyright 2019 Elsevier).

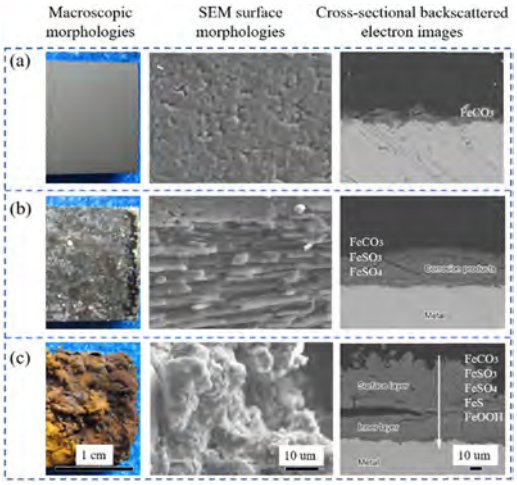


Fig. 39 Corrosion scales exposed to water-saturated supercritical $CO_2$ system containing (a) $CO_2$; (b) $CO_2$ + 1000 ppmv $SO_2$; (c) $CO_2$+ 1000 ppmv $O_2$ + 1000 ppmv $H_2S$ + 1000 ppmv $SO_2$ for 120 h at 10 MPa and 50 °C (reproduced with permission from ref. 870. Copyright 2016 Elsevier).

adding just 0.005% $H_2S$ to water-saturated supercritical $CO_2$ resulted in an increase of 40% in the average corrosion rate and 65% in the localized corrosion rate for X65 pipeline steel.

Sun *et al.*[870] investigated the effects of $O_2$, $H_2S$, and $SO_2$ impurities on the corrosion behavior of X65 steel in a water-saturated supercritical $CO_2$ system. Using SEM, EDS, and XRD to characterize the corrosion scale (Fig. 39), they found that even low concentrations of impurities significantly altered the characteristics of the corrosion scale. The interactions between $O_2$, $H_2S$, and $SO_2$ led to additional reactions, forming elemental sulfur, sulfuric acid, and water, thereby accelerating the corrosion of the steel.

In addition, strict control of temperature and pressure is required during the transportation of supercritical $CO_2$. At low temperatures and high pressures, $CO_2$ may solidify, causing pipeline blockages. In dense or supercritical states, the transportation temperature and pressure of $CO_2$ also influence pipeline corrosion. Hua *et al.*[873] compared the corrosion behavior of pipeline steel in dense-phase $CO_2$ (at 35 °C and 8 MPa) and supercritical $CO_2$ (at 50 °C and 8 MPa). Their results showed significant corrosion in the dense-phase $CO_2$, while no corrosion was observed in the supercritical state. Wei *et al.*[874] investigated the corrosion behavior of X70 steel in gaseous (1 MPa) and supercritical $CO_2$ (9.5 MPa) at 80 °C. The results indicated that the average corrosion rate of X70 steel in supercritical $CO_2$ was higher than in gaseous $CO_2$. The authors attributed this to the rapid formation of a dense $FeCO_3$ corrosion layer on the sample's surface in gaseous $CO_2$, which slows down the base material's corrosion. In contrast, in supercritical $CO_2$, an amorphous corrosion layer forms initially, which then gradually transforms into a dense $FeCO_3$ layer.

During the initial construction phase of salt caverns for compressed gas energy storage (CAES), water injection for cavity dissolution and gas injection for brine displacement are required to prevent impurities from accelerating $CO_2$ corrosion.[875,876] This process involves the injection and extraction of water containing high concentrations of halides and oxygen.

**5.2.3 $CO_2$ mineral reactions.** Storing compressed gas in porous formations, in addition to salt caverns, is a promising method for large-scale, long-term energy storage. Porous formations are widespread and offer high storage capacity.[877,878] However, due to their great depth, variable pressure, and brine saturation, the water-rock-$CO_2$ interactions during $CO_2$ injection must be carefully considered. In compressed energy storage in porous formations, $CO_2$ is injected into aquifers, where a portion dissolves into the formation's brine, lowering the pH and promoting the dissolution of carbonate and aluminosilicate minerals.[879] As these primary minerals dissolve, the pH is buffered, which facilitates the precipitation of carbonate minerals.[880–883]

These reactions lead to complex changes in the porosity and permeability of the formation, making predictions challenging. Black *et al.*[884] noted that mineral reaction rates vary with pH and $CO_2$ concentration, and impurities in the $CO_2$ or gas mixture can change the reaction extent and affect the properties of the resulting products. In recent studies, geochemical reactions, such as mineral replacement[885] and salt precipitation, have been observed in $CO_2$-saturated regions. Salt precipitation can occur near the wellbore area or in dry regions where the formation brine evaporates into the gas phase (Fig. 40). This may result in salt crystals precipitating within the formation[886–889] or in caprock fractures,[890] blocking or reducing flow pathways.[891] In water-bearing formations, residual water films may form on particle surfaces within $CO_2$-saturated regions.[892] These water films are reactive, causing mineral dissolution and precipitation reactions that often occur preferentially within small pores and pore throats where water films dominate.[892]

For the CGES system where $CO_2$ is stored in the formation, the reaction between $CO_2$ and minerals and the corresponding

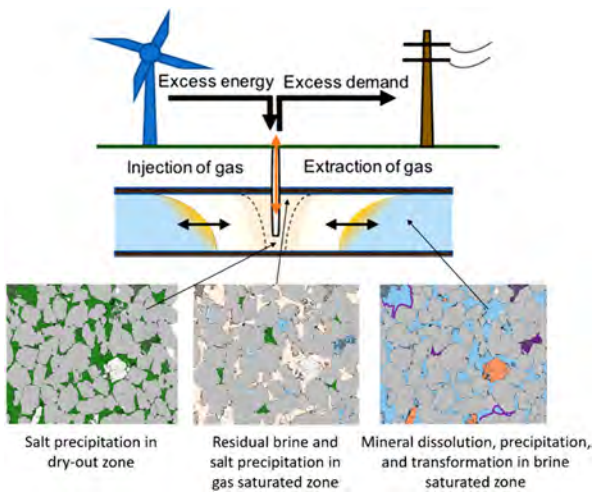


Fig. 40 Anticipated mineral reactions in reservoir formations including salt precipitation (green), mineral precipitation (purple), and mineral transformation (orange) (reproduced with permission from ref. 879. Copyright 2020 American Chemical Society).

negative consequences (flow blockages) should be noted and minimized.

### 5.3 Effect of $CO_2$ proportion on the performance of CGES

In order to improve the performance of the energy storage system, a binary mixture of $CO_2$ other than air and $CO_2$ can also be used as the working medium of CGES,[893] such as $CO_2/CH_4$, $CO_2/O_2$, $CO_2/N_2$,[894] $CO_2/H_2$, $CO_2$/R32,[895] $CO_2$/R161.[896] The molar fraction of $CO_2$ affects the thermophysical properties of the mixture, the compressor work input, the turbine output work, the storage density and round-trip efficiency, which are specifically stated below. This section focuses on the effect of the proportion of $CO_2$ in a binary mixture on a CGES system, and the molar fraction rather than the concentration is used to indicate the amount of $CO_2$.

**5.3.1 Thermophysical properties of the mixture.** The thermophysical properties of the gas affect the overall performance of the CGES system.[893] Thermophysical properties include thermodynamic properties (vapor–liquid equilibrium behavior and specific heat capacity) as well as transport properties (viscosity, thermal conductivity, and diffusion coefficient). The thermodynamic properties of the system can be significantly affected by the addition of other gases to the $CO_2$.[897,898]

The molar fraction of $CO_2$ affects the vapor–liquid equilibrium behavior, and critical point of the mixtures.[899–901] Li *et al.*[899] surveyed the available experimental data related to the vapor–liquid equilibrium properties of $CO_2$ mixtures as shown in Fig. 41. For $CO_2/CH_4$, $CO_2/O_2$, $CO_2/N_2$, and $CO_2/H_2$, the molar fraction of $CO_2$ affects the bubble point, dew point of the mixed gas. As the molar fraction of $CO_2$ increases, the bubble point pressure of the mixed gas gradually decreases, and the dew point pressure also shows a decreasing trend.[899] Therefore, a large mole fraction of $CO_2$ in the mixed gas is prone to gas–liquid phase change at lower pressure. The phase change point of the mixed gas is a parameter that needs to be focused on in the design of the CGES process.

Similarly, the critical point of the $CO_2$-based mixture depends on the type and ratio of the added gases.[71,895] Jeong *et al.*[902] and Wang *et al.*[806] investigated the critical temperatures and critical pressures of $CO_2$-based nonorganics (Fig. 42(a)) such as $CO_2$/Kr, $CO_2/O_2$, $CO_2/H_2S$, $CO_2$/CO, $CO_2/SO_2$, $CO_2/CH_4$. The critical temperature of the mixture becomes larger because of the addition of $SO_2$ and increases with its mole fraction, while the opposite is true for the addition of the other gases.[806] The critical pressure of the mixture increases and then decreases with the increase of the $CO_2$ mole fraction, except for $CO_2$/Kr (Fig. 42b).

In addition, organics such as R32, R161, and Propylene have also been used to form binary mixtures with $CO_2$ as the working medium of CGES. The results of Liu *et al.*,[895,903] Tang *et al.*[900] and Liu *et al.*[903] indicate that the critical temperatures of the $CO_2$-based binary mixtures are higher than that of pure $CO_2$, and generally increase monotonically with decreasing molar fraction of $CO_2$ (Fig. 42(c)). Therefore, mixing organics with suitable physical properties into $CO_2$ can increase the critical temperature, and the conventional cooling source in the energy

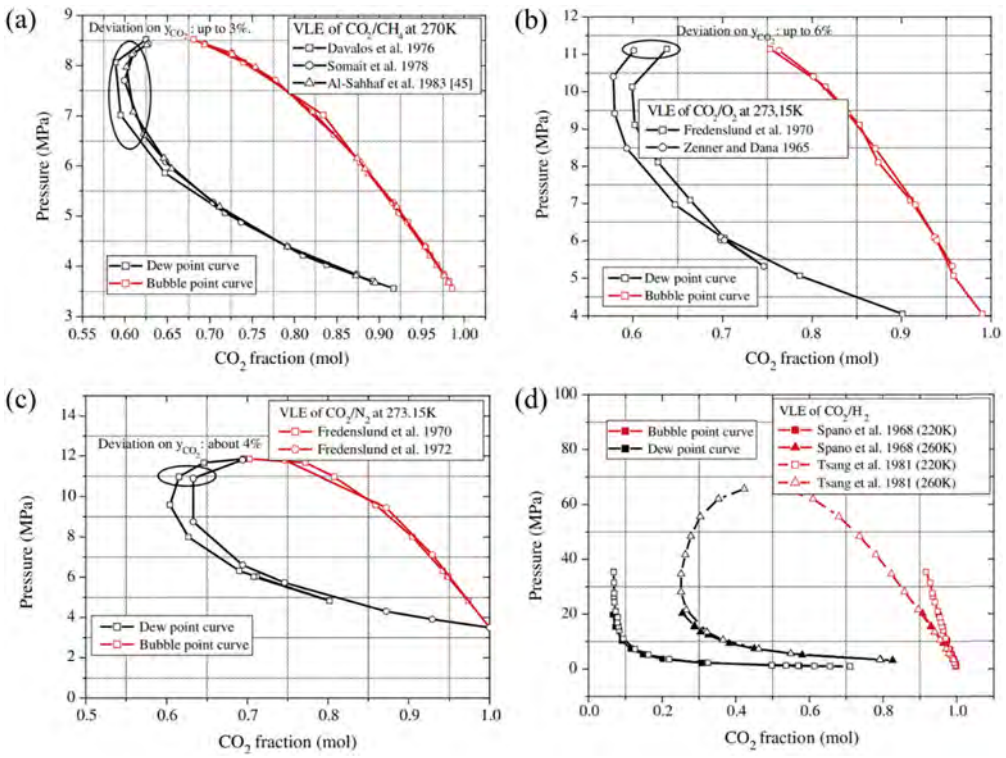


Fig. 41 Effect of $CO_2$ mole fraction on the vapor–liquid equilibrium behavior of mixtures: (a) $CO_2/CH_4$ mixture; (b) $CO_2/O_2$ mixture; (c) $CO_2/N_2$ mixture; (d) $CO_2/H_2$ mixture (reproduced with permission from ref. 899. Copyright 2011 Elsevier).

 

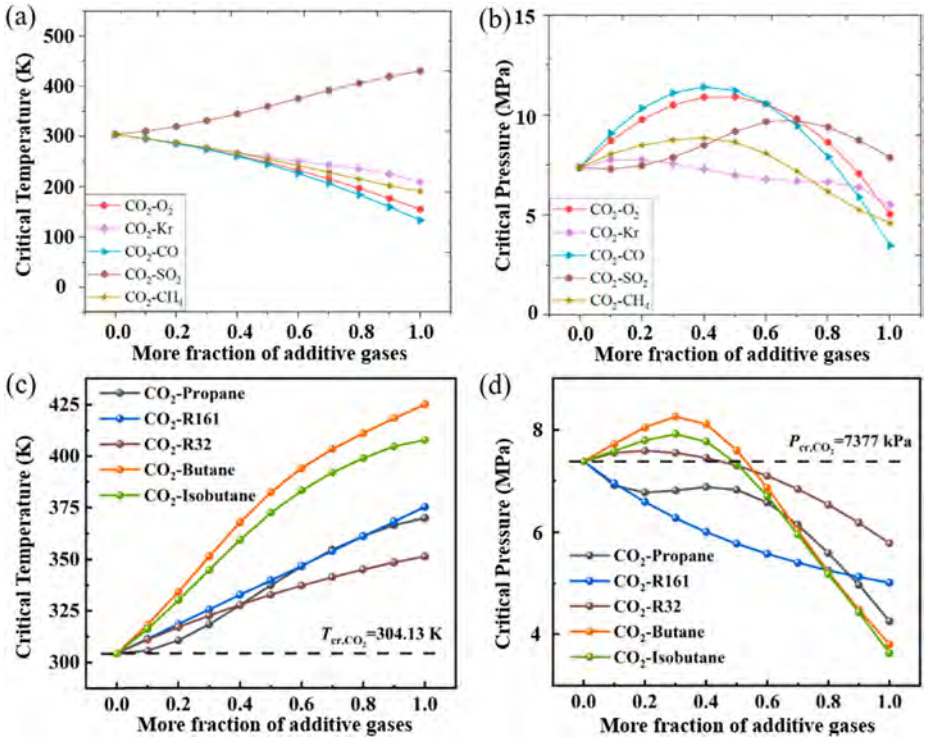


Fig. 42 The effects of addition gas molar fraction on (a) and (c) critical temperature and (b) and (d) critical pressure. (a) and (b) Reproduced with permission from ref. 806 and 902. Copyright 2022 Elsevier; (c) and (d) Reproduced with permission from ref. 900. Copyright 2012 Elsevier.

storage system can be effectively utilized to solve the problem of condensation of subcritical $CO_2$. Meanwhile, the $CO_2$ molar fraction affects the critical pressure of $CO_2$-based mixtures (Fig. 42(d)). The critical pressure of mixtures can be less than that of pure $CO_2$ by selecting a suitable additive gas,[900] which contributes to the reduction of operating pressure and equipment cost. Ma *et al.*[896] attempted to reduce the difficulty of liquefaction in a CGES system by using the $CO_2$ binary working fluids, and $CO_2$/R161 (0.7/0.3) and $CO_2$/R1270 (0.82/0.18) mixtures were found to had better system performance. Moreover, the flammability of the gas should be noted when considering the addition of organic gases. Propane, butane and isobutane are flammable, and $CO_2$ is an inert gas. The addition of 30% $CO_2$ can bring C3–C5 alkanes out of the flammability range.[904,905] Therefore, the mole fraction of the added organic gases should be lower than 70%.

For the CGES system, it is thermodynamically clear that the closer the main compressor inlet state is to the critical point, the better the performance. A lower compressor inlet temperature will allow the mass to be more easily compressed to the rated pressure level, while a lower compressor inlet pressure allows for higher compression ratios.[71]

Meanwhile, the critical line (*i.e.*, the trajectory of the critical point) is continuous or discontinuous between each critical point of the pure component.[906] In practice, for discontinuous critical lines, phase separations (gas–gas immiscibility, vapor–liquid equilibrium, and liquid–liquid equilibrium) can lead to instability of the working fluid.[902] However, it is almost impossible for a compressor to use mixtures with discontinuous critical lines as a working fluid near the critical point conditions of the fluid. Therefore, the critical phenomena of $CO_2$-based binary mixtures should be carefully considered.

The effect of the specific heat of the working medium on the CGES is mainly reflected in the energy consumption and efficiency of the compression process. The specific heat of gases increases with the increase of temperature, and $CO_2$ has a smaller specific heat capacity relative to CO, $H_2$, and $H_2O$ (Fig. 43(a)).[907] For $CO_2$-based mixtures, the results of Ning *et al.*[908] show that the specific heat of $CO_2/CH_4$ mixture is significantly affected by temperature. It increases with increasing temperature and is less affected by pressure. A large $CO_2$ mole fraction in the $CO_2/CH_4$ mixture corresponds to a small specific heat of the mixture.[908] Changes in the specific enthalpy and specific heat affect the performance of the system.[909] Zhang *et al.*[910] studied the specific heat of pure $CO_2$ and $CO_2$/propylene at different temperatures (Fig. 43(b)), and they pointed out that the specific heat of $CO_2$/Propylene mixture showed a decreasing trend with increasing temperature or decreasing $CO_2$ mole fraction. Meanwhile, the change in the specific heat of the mixtures became more drastic with increasing propylene content.[910] Moreover, as a working fluid with a small specific heat always carries less heat, the change in specific heat in turn affects the heat transfer of the $CO_2$ binary mixture: when the propylene mole fraction is high, the temperature difference is also high, and the heat exchanger performance deteriorates in the CGES system.[910]

The magnitude of the specific heat of a gas directly affects the amount of energy required for the compression process. Specific heat is the ability of a substance to absorb or release

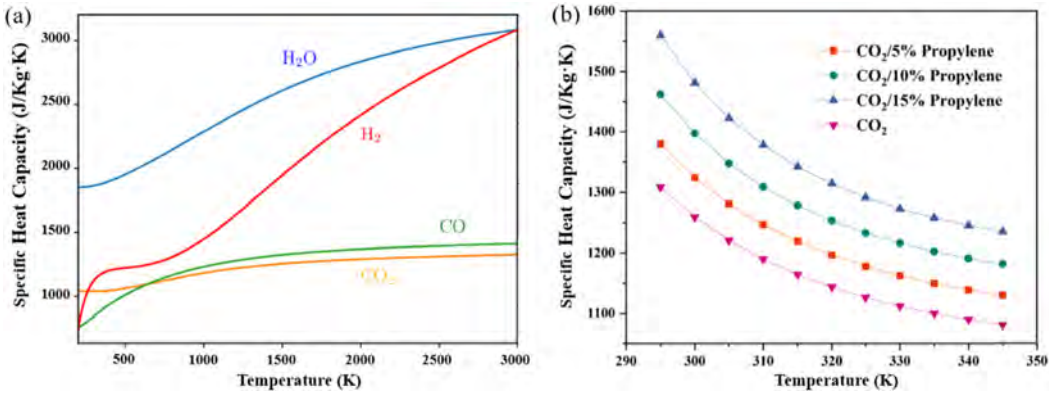


Fig. 43 (a) Variation of specific heat of different gases with increasing temperature (adapted with permission from ref. 907. Copyright 2020 EDP Sciences); (b) specific heat of $CO_2$ and $CO_2$/propylene mixture at different temperatures (reproduced with permission from ref. 910. Copyright 2023 Elsevier).

heat, and gases with a smaller specific heat require less energy input for compression, which is favorable to the efficiency of compression energy storage systems. However, this advantage may not be obvious in the practical application of energy storage systems, because the efficiency of compression energy storage systems is also affected by a variety of factors, including the performance of the compressor, the efficiency loss in the energy storage and release processes.

The molar fraction of $CO_2$ also affects the viscosity, thermal conductivity, and thermal diffusion coefficient of the mixtures. Li *et al.*[141] mathematically analyzed the viscosity, thermal conductivity, and diffusion coefficient of the $CO_2$ mixtures based on experimental data and theoretical modelling in the literature (Fig. 44). For mixtures composed of $CO_2/N_2$, $CO_2/CH_4$, $CO_2/H_2$, and $CO_2/SO_2$, the viscosity of the $CO_2$-based mixture all increases with the increase of the molar fraction of $CO_2$. However, for $CO_2/O_2$ mixture, the viscosity exhibits an downward trend with the increasing molar fraction of $CO_2$. Meanwhile, an increase in the molar fraction of $CO_2$ causes a decrease in the thermal conductivity of the $CO_2/H_2$ mixture, whereas for the $CO_2/H_2O$ mixture, the thermal conductivity increases and then decreases, with a maximum at a molar fraction of $CO_2$ of about 40%.[141] The viscosity of the working fluid directly affects the internal fluid flow in the compressor and the heat exchange process. Low viscosity helps to reduce friction losses inside the compressor and increase the energy conversion efficiency. In addition, the thermal conductivity of the working fluid affects the heat transfer process inside the storage tank, which in turn affects the temperature distribution and pressure changes inside the tank. Optimizing the gas thermal conductivity can better manage the heat transfer in the energy storage process and reduce the heat loss. Moreover, good thermal conductivity can help to control the temperature change in the energy storage process and avoid overheating or overcooling phenomenon, thus improving the safety and reliability of the energy storage system.

In summary, the thermophysical properties and transport properties of working fluid affect the along-track resistance loss in the pipeline, heat exchanger efficiency, and turbine efficiency, thus affecting the overall efficiency and economic

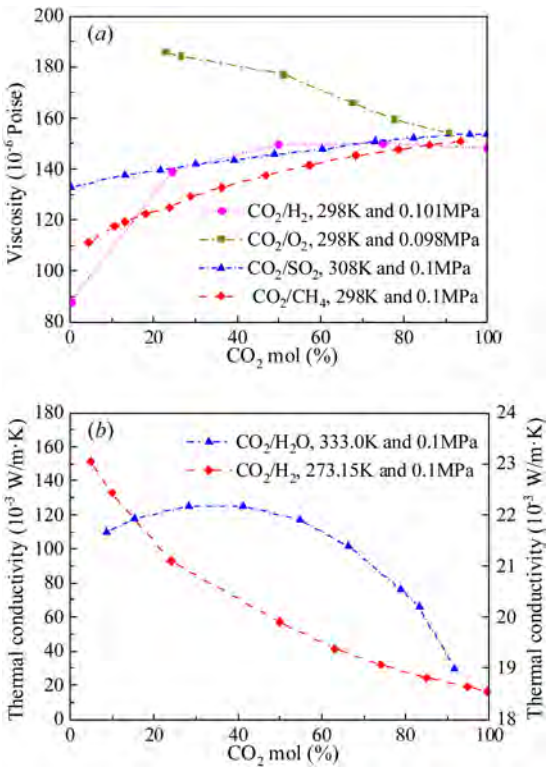


Fig. 44 Effect of $CO_2$ molar fraction on (a) viscosities and (b) thermal conductivities of binary gas mixtures. (Data extracted with permission from ref. 141. Copyright 2011 Elsevier.)

benefits of the CGES system. Therefore, the performance and efficiency of the compression energy storage system can be effectively improved by selecting a $CO_2$-based mixture with large specific heat, small viscosity, large thermal conductivity, and suitable dew point/bubble point/critical point.

**5.3.2 Compression power consumption and expansion power.** The increase in machine efficiency contributes to the improvement of CGES system efficiency, thus, attention should be paid to compressors and expanders.

 

The content of $CO_2$ in binary mixtures affects the power consumption of the compressor. For organics such as $CO_2$/R161, $CO_2$/R32, $CO_2$/propane, $CO_2$/propylene, and $CO_2$/DME, the compression ratios of the $CO_2$-based mixture are all less than that of pure $CO_2$, and the average isentropic efficiencies are all greater than that of pure $CO_2$ (86.20%), shown as Fig. 45(a).[910] The compression ratio decreases with the increase in the mass fraction of the added organic gas. Meanwhile, the isentropic efficiency of the compressor decreases with the increase of compression ratio, and the average isentropic efficiency of the compressor is high when the compression ratio is small. Therefore, the isentropic efficiency of the compressor increases with the increase in the mass fraction of the added organic gas (Fig. 45(b)).[910] At the same time, corresponding the power consumption of the compressor decreases, that is, the power consumption of the compressor decreases with the increasing mass fraction of the added organic gas.

The content of $CO_2$ in binary mixtures affects the expander output work. As shown in Fig. 45(c), the variation in the expansion ratio of the $CO_2$-based mixtures is always less than that of pure $CO_2$, and the average efficiency is always less than that of pure $CO_2$ (79.88%).[910] For the CGES system, the turbine pressure ratio at the beginning of the discharge process is determined by the pressure of the tank at the end of the charging process, thus, the initial turbine expansion ratio decreases with the increase in the mass fraction of the added R161 and R32. The uncertainty of the turbine performance increases because of the different initial expansion ratios at the beginning of the discharge process. The turbine output work and the average isentropic efficiency decrease with increasing mass fractions of DME, R161, R32, and propylene,[843,910] while the turbine isentropic efficiency of propylene decreases and then increases.[910] Moreover, the turbine output work decreases with increasing mass fraction of the added organic gas. The reason for this is similar to that of the compressor.

The exergy destruction of the system is mainly in the turbine and compressor, accounting for nearly 80% of the total exergy destruction.[910] The compression ratio should be maintained at no more than 1 : 3 during compression to prevent an increase in process irreversibility due to excessive energy consumption.[911] The system efficiency can also be effectively improved by reducing the temperature during compression or increasing the inlet temperature during expansion, shown as Fig. 45(d).

In addition, $CO_2$ has a large potential for phase change at high pressures. The gas temperature of gas may reduce to near the liquefaction point of $CO_2$ in the expansion progress in some CGES power generation systems. Even if the $CO_2$ content is low, this phase change can lead to condensation and phase separation. The phase change of $CO_2$ triggers additional energy loss, which affects the expansion work of the gas and reduces the efficiency of power generation. Moreover, $CO_2$ may be converted to dry ice in cryogenic equipment, and $CO_2$ freezing increases the pressure difference in the pipeline and even forces the turboexpander to stop working, which poses a significant threat to the safety, reliability, continuity, and stability of the system. Li *et al.*[912] investigated the expansion process of a turbine for recovering light hydrocarbons from natural gas, and simulated the freezing of $CO_2$ in a

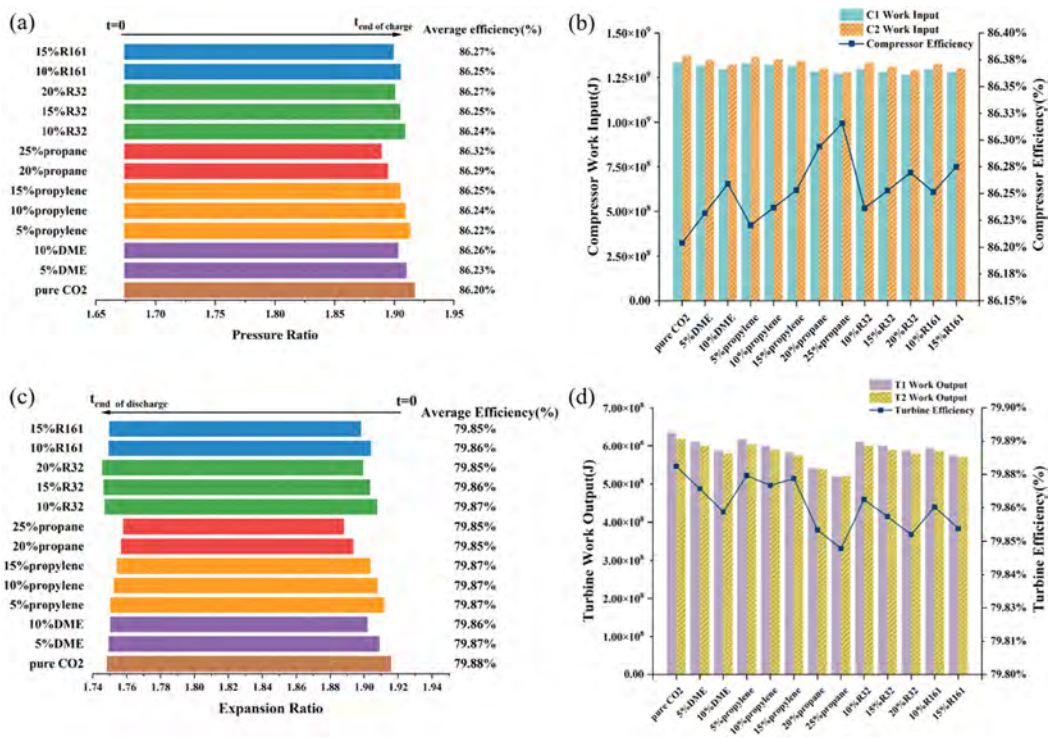


Fig. 45 (a) compression ratio variation, (b) compressor work input and isentropic efficiency, (c) expansion ratio change, (d) turbine output work and efficiency under different mixture pairs and mass fractions (reproduced with permission from ref. 910. Copyright 2023 Elsevier).

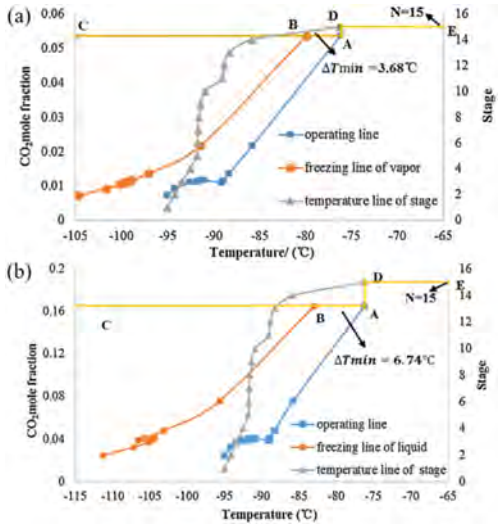


Fig. 46 (a) $CO_2$ freezing in vapor in demethanizer; (b) $CO_2$ freezing in liquid in demethanizer (reproduced with permission from ref. 912. Copyright 2017 Elsevier).

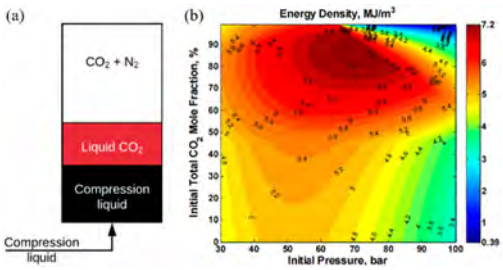


Fig. 47 (a) Schematic of the modeled system; (b) Contour plot of energy density *vs.* initial total pressure and initial total $CO_2$ mole fraction for $CO_2/N_2$ mixture (reproduced with permission from ref. 894. Copyright 2020 MDPI).

demethanizer using Aspen plus. The operating line of demethanizer, the freezing line of vapor and liquid phase (Fig. 46) were drawn based on the concentration and freezing temperature of $CO_2$ in the vapor and liquid phases. During operation process, it must be ensured that there is a safe boundary of at least 3–5 K in the vapor and liquid.[913]

In summary, the proportion of $CO_2$ in the binary mixture affects the thermal physical properties of working fluid, the power consumption of the compressor, the output work of the turbine, and the efficiency, and this need to be considered and adjusted in the design and operation of the CGES system. Meanwhile, attention should also be paid to preventing localized freezing of $CO_2$ in the operation process.

**5.3.3 Energy density and round-trip efficiency.** Low energy density is a common problem for all types of CGES that store air or $CO_2$ in gaseous form, and huge underground caverns are an indispensable. Geographic constraints have prompted researchers to use artificial tanks to store the working medium. As a result, the energy density of the system must be greatly improved to significantly reduce the volume of medium required for storage.[895] Energy density (EVR) is used to indicate the compactness characteristics of an energy storage system, and it is equal to the amount of energy that can be released per unit of storage volume in the energy storage system.

The molar fraction of $CO_2$ affects the energy density (EVR) of a CGES system. The composition of the gas in a compressed gas storage chamber is a key parameter to maximize the energy density, which can be increased by varying the type and proportion of the working medium in the energy storage system. Abuheiba *et al.*[894] proposed a new method to increase EVR of a compressed gas by adding a condensable component to it (Fig. 47). A mixture of $CO_2$ and $N_2$ is used as the working medium of the CGES. A liquid mineral oil, in which both $N_2$ and $CO_2$ are insoluble, is pumped into the vessel at a constant flow rate to compress the gas mixture, and the $CO_2$ begins to condense when its partial pressure exceeds the saturation pressure.[894] The compression process is stopped when the volume of the gas mixture is less than 5% of the total volume of the vessel or until the pressure reaches 140 bar.

As shown in Fig. 46,[894] for the case at any initial pressure, EVR gradually increases to a maximum value as the molar fraction of $CO_2$ increases and then decreases. A similar trend is observed for increasing initial pressure at any initial total molar fraction of $CO_2$. This is a manifestation of the competitive effect of higher pressure with larger utilized volume.[894] The storage density using a mixture of 88% $CO_2$ and 12% $N_2$ can be 7.33 MJ $m^{-3}$, that is, a 57% increase in energy storage density, compared to 4.67 MJ $m^{-3}$ using pure $N_2$.[894]

In addition to mixing with gases such as $N_2$, binary mixtures of $CO_2$ with organic fluids have recently been used as working medium for CGES to increase the energy density (EVR) and round-trip efficiency (RTE) of the system.[843,895,896,910,914] RTE, EVR, and charge pressure ($P_c$) of the system are closely related to the $CO_2$ mole fraction. RTE is a significant criterion for evaluating the efficiency of the energy conversion from energy input to energy output in the discharge process,[846,915] and is equal to the ratio of the system benefit (turbine power) to the cost (power consumption of the compressor and pumps).[843]

Liu *et al.*[895] mixed $CO_2$ with organic materials R32, propylene, R1234yf, DME, R1234ze, R161, R152a, isobutene and butane to form a binary mixture as the working fluid of the CGES, and investigated the RTE and EVR of the system with different $CO_2$ mass fractions. Zhang *et al.*[843,910] simulated the operating characteristics of a two-stage CGES system under dynamic operating conditions using a binary mixture of $CO_2$ as the working fluid. Energy and exergy methods were employed to analyze the effects of the type and mass fraction of added organics ($CO_2$/propane, $CO_2$/propylene, $CO_2$/R161, $CO_2$/R32, and $CO_2$/DME) to evaluate the RTE, EVR, and other performance parameters. Ma *et al.*[896] designed an energy storage system with high energy density and low-pressure storage by cycling a binary mixture of $CO_2$, and analyzed the thermodynamic performance of the system. In all of the above research, EVR always tends to increase with the increase of $CO_2$ molar fraction. In particular, the results of Liu *et al.*[895] are shown in Fig. 48(a)–(c): the EVR of $CO_2$/R32 is the largest among the various $CO_2$ binary mixtures (Fig. 48(a)). The system RTE and EVR can be significantly improved by increasing

 

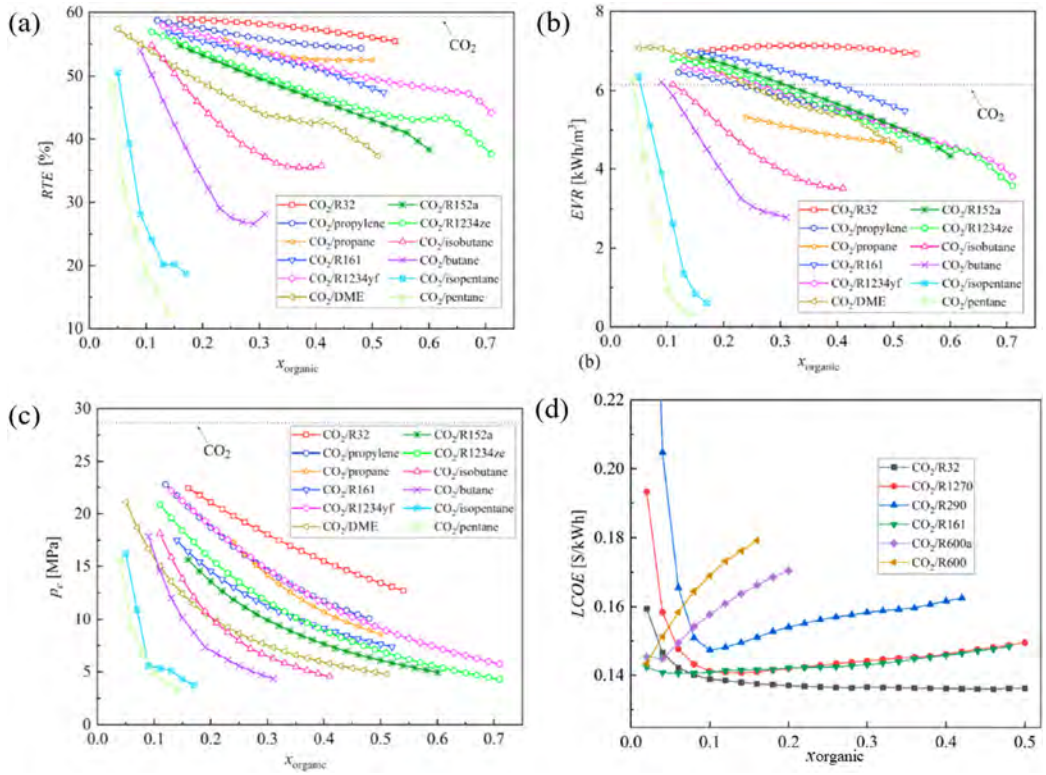


Fig. 48 Effect of organic fluid composition on: (a) round trip efficiency (RTE); (b) energy density (EVR); (c) charge pressure ($P_c$) (adapted with permission from ref. 895. Copyright 2022 Elsevier); (d) levelized cost of electricity (LCOE) (adapted with permission from ref. 914. Copyright 2023 Elsevier).

the $CO_2$ content of the $CO_2$-based mixtures, but at the cost of increasing the system charge pressure (Fig. 48(c)). The maximum EVR of the energy storage system can be higher than that of the pure $CO_2$ system, except for the system using $CO_2$/propane. For the $CO_2$/R32 system, the EVR is 16.16% higher than that of the $CO_2$ system, and at the same time the charge pressure is reduced from 28.65 MPa to 12.72 MPa,[895] which is beneficial to the safety and sealing performance of the system.

Meanwhile, Fu *et al.*[914] analyzed the effect of the mass fraction of organics added to $CO_2$ on levelized cost of electricity (LCOE) in addition to the effect of $CO_2$ mass fraction on system round trip efficiency (RTE). The LCOE curve for $CO_2$/R32 increases with increasing R32 mass fraction, while the corresponding curve for $CO_2$/R600 shows a decreasing trend (Fig. 47(d)). The addition of organic fluids to $CO_2$ reduces the corresponding critical pressure, and the more that is added, the lower the critical pressure of the mixture.[895] The corresponding operating pressure and the storage pressure in the tanks decrease, thus, the investment cost of the tanks tends to decrease. However, the required mass flow rate of the working fluid and the investment cost simultaneously increase with the increase of the mass fraction of additive organics.

In addition, for the system under the $CO_2$/R32 cycle, the compressor accounts for almost a quarter of the total exergy destruction according to the distribution of exergy destruction analyzed by Zhang *et al.*[843] (Fig. 49). As the mass fraction of R32 increases, the turbine's share of total exergy destruction decreases due to the decrease in turbine power generation, while the opposite trend is observed for the heat exchanger, preheater, and throttle shares.[843] In general, the increase in system exergy destruction is primarily a result of increased irreversibility of heat exchangers and preheaters, as well as increased differential pressures at throttling valves. Therefore, an increase in the performance of the heat exchanger needs to be considered when using working fluids with a high mass fraction of added organic fluids.

In summary, the behavior of $CO_2$ in the CGES system and its proportion have an significant impact on the stability,

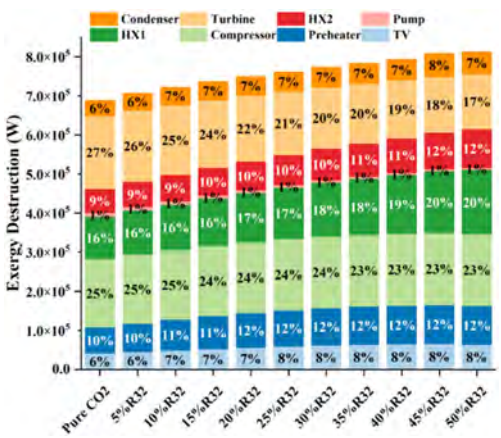


Fig. 49 Exergy destruction of $CO_2$/R32 mixture with varying mass fractions (adapted with permission from ref. 843. Copyright 2023 Elsevier).

operational efficiency, and safety of the system, which needs to be considered and dealt with in the system design, operation and management to ensure the safety and efficiency of the CGES system.

# 6. Outlook and summary

With the continuous development of CCUS technology and applications of high-concentration $CO_2$, the efficient recovery and direct conversion of LCC has become a key challenge in current research. LCC is widely present in various life and industrial scenarios. In-depth research on its behavior characteristics in different energy media will help improve its recovery and utilization efficiency and provide scientific basis and guidance for related production enterprises.

Compared to high-concentration $CO_2$, LCC faces greater resistance in diffusion, adsorption, dissolution, and catalytic processes on material surfaces. Changes in the composition of the medium can influence $CO_2$ solubility and diffusion paths. During liquid-phase diffusion, accurately determining the diffusion coefficient and understanding the dissolution–diffusion path are essential for optimizing solvent characteristics to drive the diffusion of LCC. This is important not only for solvent absorption-based DAC but also for applications in gas–liquid multiphase catalysis and gas–liquid conversion energy storage. $CO_2$ gas–solid diffusion is fundamental in carbon capture and multiphase catalysis. Adsorbents and catalysts for LCC should fully consider the relationships between pore structure, diffusion, transport, and active site distribution in solid materials to achieve efficient adsorption and conversion through effective $CO_2$ enrichment. Thus, selecting suitable adsorbent materials or carriers is necessary for the selective capture of $CO_2$ in low-concentration environments.

In the catalytic reduction process, $CO_2$ exhibits complex primary and side reactions depending on the products, pathways, and conditions. Even for high-concentration $CO_2$, there are still areas to explore, such as selectivity, catalytic efficiency, and catalyst selection. The direct conversion of LCC is even more challenging. Current strategies mainly focus on adjusting catalyst structure, environment, and active sites to enrich and convert $CO_2$, addressing issues like low reaction rates, poor selectivity, catalyst instability, and low energy efficiency. This includes using photocatalysis, electrocatalysis, thermocatalysis, plasma catalysis, biocatalysis, and various coupling methods.

In chemical production and energy storage, LCC can impact efficiency, safety, and overall performance. $CO_2$ is not typically targeted as a product in air separation processes, but due to its similar physicochemical properties to other air components, significant effort and cost are needed for its complete removal. In low-temperature air separation, residual $CO_2$ can reduce the lifespan of expensive projects. DAC technology targeting LCC still faces challenges in balancing cost, energy consumption, and efficiency. Therefore, researching both solid-phase and liquid-phase adsorption/absorption of LCC holds value for the development of air separation and DAC.

By reviewing the progress of LCC in catalytic reduction, different catalytic technologies' synergistic effects on $CO_2$ adsorption and conversion under low-concentration conditions are compared. Photocatalysis, electrocatalysis, and thermocatalysis theoretically have high potential for $CO_2$ conversion but often face issues like low reaction rates, poor selectivity, and catalyst deactivation under low-concentration conditions. Emerging technologies like plasma catalysis and adsorption-enhanced catalysis provide new approaches but also encounter bottlenecks such as low energy efficiency and difficulties in adsorbent regeneration. Biocatalysis, with its mild reaction conditions and high selectivity, has attracted attention, but improving stability and conversion efficiency remains challenging. Overall, future research should focus on innovative catalyst design and reaction condition optimization to overcome technological bottlenecks and achieve efficient, cost-effective $CO_2$ conversion.

In compressed gas energy storage (CGES) systems, using gas mixtures with different $CO_2$ concentrations/mole fraction as working media offers potential technical advantages and challenges. The molar fraction of $CO_2$ affects the thermophysical properties of the working medium, the compressor work input, the turbine output work, and the storage density and round-trip efficiency of the CGES system. Low molar fraction $CO_2$ can have high critical temperature and specific heat, low critical pressure and viscosity force, which is beneficial for CGES systems. The performance and efficiency of the CGES system can be effectively improved by selecting a suitable $CO_2$-based binary mixture. Meanwhile, attention should be paid to the corrosion of the pipeline and the mineral reaction with the subsurface reservoir of the $CO_2$ in the CGES system. CGES is attractive, especially when integrated with renewable energy generation and existing storage infrastructure. Additionally, achieving sustainability requires addressing the techno-economic challenges of $CO_2$ capture, separation, and reuse. Future development will depend on the advancement of new materials, optimization technologies, and integration with other energy storage systems. Therefore, developing high-efficiency catalytic technologies and new energy conversion and storage methods for LCC in energy media remains essential.

According to the technology maturity and the largest scale of industrial application, cryogenic air separation and thermal catalysis technologies are the most mature in the existing industry and suitable for large-scale applications, as shown in Table 6. In contrast, DAC, electrochemical catalysis, photocatalysis, plasma catalysis and biocatalysis technologies are at different stages of development. They are currently mainly used in small-scale demonstration and research projects. With the continuous development of technology, these technologies are expected to be more widely used in the future.

### 6.1 Efficient catalytic conversion technologies

For the catalytic reduction of LCC, the design of active sites is crucial. Low $CO_2$ concentrations mean that the collision frequency of molecules on the catalyst surface is low, requiring catalysts with highly efficient active sites to enhance $CO_2$

 

Table 6 Comparison of LCC capture and conversion technologies: technical characteristics, maturity and application scale

| Technology | Advantages | Limitations | Application adaptability | Technology maturity | Current largest scale of industrial applications |
|---|---|---|---|---|---|
| Cryogenic air separation | Can effectively treat LCC gas; mature technology; stable operation. | Low energy efficiency and high cost; requires lower temperature, increasing energy consumption. | Applicable to large-scale $CO_2$ capture, especially in industrial emissions. | Mature | Industrial emission sources, millions of tons of $CO_2$ per year. |
| DAC | Can capture $CO_2$ directly from the atmosphere; suitable for LCC sources. | High energy consumption; high equipment investment and operation and maintenance costs. | Applicable to the treatment of LCC from dispersed sources, especially the removal of atmospheric $CO_2$. | Developing | Demonstration projects, thousands of tons of $CO_2$ per year. |
| Thermal catalysis | Mature technology, widely used in industry; high reaction rate. | Requires higher temperature and energy input; may have catalyst deactivation problems. | Applicable to high-concentration $CO_2$ conversion and large-scale applications, especially in industrial processes. | Mature | Industrial scale, millions of tons of $CO_2$ per year. |
| Electrochemical catalysis | High energy efficiency, suitable for LCC conversion; can work at normal temperature and pressure. | Expensive electrode materials and poor stability; limited conversion efficiency. | Applicable to dispersed $CO_2$ sources, such as small-scale and local applications, such as homes or small factories. | Research stage/early development | Small demonstration facilities, several tons of $CO_2$ per year. |
| Photocatalysis | Can use solar energy to drive $CO_2$ conversion; environmentally friendly, low energy consumption. | Slow conversion efficiency; dependent on light source, large fluctuations in conversion efficiency. | Applicable to small-scale, LCC conversion, especially in areas with sufficient sunlight. | Research stage/ developing | Laboratory/demonstration scale, thousands of tons of $CO_2$ per year. |
| Plasma catalysis | Can carry out $CO_2$ conversion at normal temperature and pressure; suitable for low-concentration $CO_2$ conversion. | Low energy efficiency, large energy loss during catalysis; complex process. | Applicable to small, efficient conversion systems, such as household equipment or precision process applications. | Developing | Small demonstration facilities, several tons of $CO_2$ per year. |
| Biocatalysis | Carry out $CO_2$ conversion under mild conditions; can use the high selectivity of microorganisms or enzymes. | Slow conversion rate; poor stability of biocatalysts, may be affected by environmental changes. | Applicable to LCC conversion, especially in mild environments, such as agriculture and wastewater treatment. | Research stage/early development | Small-scale applications, hundreds of tons of $CO_2$ per year. |

adsorption and conversion. Increasing the surface area of the catalyst and optimizing its surface chemistry can improve $CO_2$ adsorption energy at active sites, promoting the reaction.[466,548,553,554] Utilizing materials like MOFs, porous carbon materials, or oxide composites, which offer high surface areas and multifunctional active sites, is a current research focus.[638–640] These materials can enhance $CO_2$ activation and reduction efficiency by tuning their electronic structure and surface energy states.

Effective diffusion and enrichment of $CO_2$ under low concentrations are key to ensuring reaction rates. Since gas-phase $CO_2$ is prone to mass transfer resistance during diffusion, designing an efficient gas diffusion layer (GDL) and enrichment strategy is essential.[101,102] In a gas diffusion electrode (GDE), the GDL must not only provide sufficient porosity and surface area but also be optimized for hydrophobicity to prevent electrolyte penetration while allowing gas-phase $CO_2$ to reach the catalyst surface. Additionally, using porous materials or designing nanostructured catalyst supports can enhance local $CO_2$ concentration, increasing enrichment on the catalyst surface and thereby improving reaction efficiency.[916]

In order to achieve efficient capture and conversion of LCC, future research should focus on the multifunctional design of catalysts, optimize gas diffusion and enrichment strategies, and explore effective integration with renewable energy. However, there are still many unresolved adjustments in these aspects of current research, and these gaps need to be filled through specific technical improvements and in-depth mechanism research.

First, the multifunctional design of catalysts is the key to improving the conversion efficiency of LCC. Although some progress has been made in catalyst optimization, most of the research focuses on the improvement of a single function, such as by outlining the adsorption performance of the catalyst or enhancing the activity of the reduction reaction. However, in the process of LCC conversion, the catalyst not only needs to efficiently adsorb $CO_2$, but also should have the ability to enhance the reaction rate and improve the product selectivity. To this end, further catalyst design strategies should integrate multiple functions. For example, designing a catalyst support material with a gradient pore structure can enrich and diffuse $CO_2$ step by step at different pore levels. Similar designs have been preliminarily applied in MOFs materials, where MOFs materials with different pore sizes can effectively enhance the diffusion and adsorption of gas molecules and improve the efficiency of catalytic reactions. However, further exploration of the synergistic effects between different catalytic components and structures is needed to improve the overall efficiency of the catalytic reaction.

Secondly, the optimization of gas diffusion and enrichment strategies is also another important direction to improve the conversion efficiency of LCC. During the conversion of LCC, the diffusion of gas and the contact efficiency of the reaction active sites directly determine the efficiency of the reaction. Current research often ignores the role of catalyst carriers in gas diffusion, resulting in limitations in catalyst performance.

How to integrate and optimize gas diffusion paths in the design of catalysts is the key. The use of microstructured catalyst carrier materials, such as nanoporous materials, carbon materials with multi-level pore structures, *etc.*, can promote the rapid diffusion and effective enrichment of $CO_2$ by adjusting the pore size and pore structure. This type of structure exhibits lower gas diffusion resistance and higher reaction efficiency in catalytic reactors. Similar design strategies have been successfully applied in catalytic combustion and hydrogen conversion reactions.[917]

However, single catalyst optimization and gas diffusion strategies are not sufficient to meet the needs of LCC conversion. In order to improve the energy efficiency of the reaction and achieve sustainable development, the integration of renewable energy and $CO_2$ conversion technology should be further explored. Renewable energy (such as solar energy and wind energy) can be used as input energy to power the $CO_2$ conversion process through electrochemistry or photocatalysis, which can not only reduce energy consumption but also promote energy self-sufficiency in the $CO_2$ conversion process. In the photocatalytic $CO_2$ reduction reaction, the light provided by solar energy can drive the electron transfer of the catalyst and reduce the demand for energy input. With the advancement of solar cells and photocatalytic technology, the LCC conversion process based on renewable energy is expected to be realized in the future. However, the volatility and intermittency of solar energy and wind energy make energy integration face great challenges. How to effectively regulate the $CO_2$ conversion efficiency under different time and space and conditions and reduce dependence on traditional energy is a task worth thinking about.[45,918]

Inevitably, the catalyst will also face the problem of deactivation and deactivation during the LCC conversion process. The stability and long-term durability of the catalyst are key factors determining its commercial application. During long-term use, the catalyst may lose active sites due to poisoning, sintering, surface structure changes, *etc.*, which in turn affects the reaction efficiency. To address this issue, the deactivation mechanism of the catalyst should be explored in depth. In the $CO_2$ reduction reaction, the metal active sites on the catalyst surface may sinter and oxidize due to long-term high-temperature reactions, resulting in a reduction in active sites. In order to improve the catalyst's ability to resist deactivation, it is necessary to develop catalytic materials with self-repairing functions or use high-temperature resistant and anti-poisoning materials. For example, doping with precious metals or using more stable solid acid catalysts can extend the service life of the catalyst.

### 6.2 Novel energy conversion and storage technologies

Utilizing LCC for novel energy conversion and storage can promote efficient energy use and sustainable development. This includes developing photocatalytic, electrocatalytic, and thermocatalytic technologies to convert LCC into high-energy-density chemicals or fuels, as well as exploring new energy storage technologies like $CO_2$ electrochemical storage and underground $CO_2$ sequestration.[710–713]

For LCC conversion, chemical carbon capture is currently a cost-effective option due to its high efficiency and energy conversion rate. However, because chemical carbon capture typically relies on non-renewable energy sources, integrating it with biological conversion offers an innovative approach for the high-value utilization of LCC.[799,919] For instance, converting LCC into methanol, formic acid, or acetic acid through electrochemical methods and further transforming these products into complex chemicals *via* biological pathways is a viable strategy.[711,719,721] Nevertheless, the energy efficiency of these inorganic–organic systems remains low due to limitations such as gas–liquid mass transfer and electrode-biointerface compatibility.[726,727] Future research should focus on designing efficient carbon capture components suitable for LCC and overcoming bottlenecks in the conversion of chemical, light, and electrical energy. Optimizing photo-enzyme and electro-enzyme synergistic catalysis can also help build more efficient photoelectrochemical-biochemical hybrid systems.[920] Moreover, developing three-phase mixed fermentation processes for LCC can enable artificial synthesis routes to high-value products, facilitating large-scale utilization and supporting global carbon neutrality goals.

To improve the energy conversion efficiency of LCC, exploring the conversion mechanisms and kinetics of LCC in multiphase reaction systems is essential. Understanding $CO_2$ interactions and conversion pathways in various media is necessary to optimize the conditions and characteristics that affect catalytic reaction efficiency and selectivity, enabling the engineering application of multiphase reactions.[512,921,922] Artificial intelligence, machine learning, and high-throughput experimental techniques can be used to accelerate the design and optimization of catalysts, improving efficiency, selectivity, and stability in catalytic reactions.[923,924]

In CCS, the long-term sequestration of $CO_2$ poses potential environmental risks. Improper handling of diffusion or dissolution behaviors may lead to $CO_2$ leakage, threatening the surface environment. Additionally, under high-pressure conditions, interactions between $CO_2$ and reservoir materials can cause unpredictable physical or chemical changes.[176–178] Addressing these risks requires integrating environmental science and engineering technology to establish comprehensive environmental impact assessment and monitoring systems, ensuring the long-term safety and sustainability of $CO_2$ storage.

Promoting the resource utilization of LCC and the carbon circular economy can ensure the effective use and recycling of carbon resources. This includes developing efficient capture, conversion, and utilization technologies for LCC, creating new carbon-neutral and carbon-negative technologies, and balancing carbon emissions and absorption.[925,926] DAC technology, as a method for recovering $CO_2$ from distributed sources such as transportation, agriculture, forestry, and construction, can handle various LCC emissions. Although DAC's feasibility remains debated, it can relieve the pressure on point-source carbon capture and reduce the costs associated with carbon storage transportation. The captured carbon can serve as an industrial feedstock or be used for soil enhancement, closing

the carbon cycle loop. DAC can generate negative carbon effects, effectively lowering atmospheric $CO_2$ levels.[664,665]

Data-driven technology is a key means to improve the efficiency of air separation and $CO_2$ capture. Optimizing process parameters through artificial intelligence (AI) can achieve dynamic control of separation paths, significantly reduce energy consumption and improve operating efficiency. For example, an intelligent optimization system based on machine learning algorithms can analyze gas components and equipment operating status in real time, and dynamically adjust process conditions such as adsorbent switching, pressure control, and flow rate distribution.

In addition, the development of real-time monitoring and adaptive control systems, through the integration of advanced sensor technology, can achieve seamless coupling of air separation and $CO_2$ capture processes, and accurately separate target gases. The system can also adjust separation ratios and gas purity according to industrial needs, optimizing overall process performance. This intelligent process management not only improves energy efficiency, but also enhances the flexibility and adaptability of the technology.

Energy consumption and cost are the main obstacles to the commercialization of air separation and $CO_2$ capture technologies. Research on low-energy-driven separation technologies, such as electrically driven gas separation based on electrochemical processes, can achieve selective migration of target molecules through potential gradients, thereby reducing the energy consumption of traditional thermodynamically driven separation processes.

And the development of modular integrated devices can meet the needs of large-scale deployment in different industrial scenarios. For example, the air separation and $CO_2$ capture unit is designed as an independent module and can be flexibly expanded through modular splicing to adapt to diverse industrial gas processing needs. This modular design not only reduces installation and maintenance costs, but also improves the scalability of the equipment and provides support for the application of distributed energy systems.

Material innovation is an important direction to improve air separation and $CO_2$ capture performance. For different gas component ratios in industrial processes, the development of intelligent adsorbents and functional separation membranes can adapt to complex gas conditions. For example, porous MOFs (metal organic frameworks) and modified zeolites enable efficient and selective separations based on different molecular sizes and polarities. At the same time, surface functionalization design is introduced to enable the adsorbent to maintain efficient performance under different temperature, humidity and pressure conditions.

Exploring new non-equilibrium plasma coupling technology provides new ways for process innovation. While air is separated, non-equilibrium plasma can effectively promote the activation and conversion of $CO_2$, converting it into high value-added chemicals such as methane and synthesis gas. This technology can be integrated with the traditional physical separation process to build a separation-conversion integrated system, greatly improving the comprehensive economic benefits of the technology.

To advance CGES technologies, understanding $CO_2$ diffusion, dissolution, corrosion, phase change, and expansion behaviors under varying conditions, including temperature, pressure, and storage medium properties like porosity and chemical composition, is critical. Researching these behaviors requires high-precision experimental equipment and powerful computational resources for numerical simulation. Accurately simulating and predicting these processes demands complex fluid dynamics models, necessitating the development of precise simulation tools and experimental methods to better understand and forecast behaviors such as diffusion, dissolution, and expansion of $CO_2$ under different conditions.[183–185] This will help optimize the design of the storage system and the CGES operation strategy to improve the system efficiency.

Future research could explore the development of advanced storage media with tailored properties, such as high porosity and chemical stability, to minimize corrosion and improve $CO_2$ retention and phase behavior management. Additionally, the integration of AI-driven predictive models and real-time monitoring systems could provide more accurate control over storage conditions, ensuring optimal energy storage and release cycles. By combining experimental insights with advanced simulation techniques, researchers can refine CGES designs and operational strategies, paving the way for more efficient and sustainable energy storage solutions that effectively utilize $CO_2$ under various conditions.

In summary, the frontier of LCC research spans multiple fields, including efficient catalytic conversion technologies, novel energy conversion and storage technologies, carbon resource utilization and circular economy, intelligent catalysis and reaction engineering, and multidisciplinary research and collaboration. Research in these areas will provide essential support for addressing climate change, promoting sustainable development, and building a carbon-neutral society.

## Author contributions

Writing – original draft: M. H. S. and W. G. Writing – review & editing: M. H. S, W. G., L. G. T., S. K. and Y. L. D. Conceptualization: P. K. C. and Y. L. D. Project administration: L. G. T. and S. K. Funding acquisition: L. G. T. and Y. L. D.

## Data availability

This review article contains no new data. All presented data are reproduced from other published sources, which are cited within the article.

## Conflicts of interest

There are no conflicts to declare.

## Acknowledgements

This work was supported by the National Key Research and Development Program of China (No. 2022YFC3800401), the China Scholarship Council (Grant No. 202306460067), Beijing Natural Science Foundation (Grant No. 3232043).

## References

1 D. Welsby, J. Price, S. Pye and P. Ekins, *Nature*, 2021, **597**, 230–234.
2 M. Romanello, C. Di Napoli, P. Drummond, C. Green, H. Kennard, P. Lampard, D. Scamman, N. Arnell, S. Ayeb-Karlsson and L. B. Ford, *Lancet*, 2022, **400**, 1619–1654.
3 M. Nelson and D. B. Nelson, *Int. J. Geosci.*, 2024, **15**, 246–269.
4 H. F. Franzen and S. Franzen, *A physical demonstration of the increase in global surface energy due to increasing $PCO_2$*, 2024, DOI: **10.21203/rs.3.rs-3674188/v1**.
5 T. F. Valone, *J. Geosci. Environ. Prot.*, 2021, **9**, 84.
6 G.-W. Zhang, Z. Gang, V. Iyakaremye and Y. Qing-Long, *Adv. Clim. Change Res.*, 2020, **11**, 198–209.
7 T. M. Lenton, C. Xu, J. F. Abrams, A. Ghadiali, S. Loriani, B. Sakschewski, C. Zimm, K. L. Ebi, R. R. Dunn and J.-C. Svenning, *Nat. Sustainability*, 2023, **6**, 1237–1247.
8 C. Tebaldi, R. Ranasinghe, M. Vousdoukas, D. Rasmussen, B. Vega-Westhoff, E. Kirezci, R. E. Kopp, R. Sriver and L. Mentaschi, *Nat. Clim. Change*, 2021, **11**, 746–751.
9 P. Agreement, *report of the conference of the parties to the United Nations framework convention on climate change (21st session, 2015: Paris)*, 2015, vol. 4, p. 2.
10 H. Ritchie, OurWorldInData.org[Online Resource], 2020, **https://ourworldindata.org/ghg-emissions-by-sector**.
11 T. Zhao, Y. Li and Y. Zhang, *Green Chem.*, 2021, **23**, 7852–7864.
12 M. Shen, Z. Hu, F. Kong, L. Tong, S. Yin, C. Liu, P. Zhang, L. Wang and Y. Ding, *Rev. Environ. Sci. Bio/Technol.*, 2023, **22**, 823–885.
13 M. Shen, F. Kong, L. Tong, Y. Luo, S. Yin, C. Liu, P. Zhang, L. Wang, P. K. Chu and Y. Ding, *Carbon Neutrality*, 2022, **1**, 37.
14 J. E. G. Baquero and D. B. Monsalve, *Int. J. Hydrogen Energy*, 2024, **54**, 574–585.
15 M. Safaei-Farouji, D. Misch and R. F. Sachsenhofer, *Int. J. Coal Geol.*, 2023, **277**, 104351.
16 M. Kheirinik, S. Ahmed and N. Rahmanian, *Sustainability*, 2021, **13**, 13567.
17 K. Talus and R. Maddahi, *J. World Energy Law Bus.*, 2024, **17**, 295–308.
18 Z. Chen, *Proceedings of the 2022 7th International Conference on Social Sciences and Economic Development (ICSSED 2022)*, 2022, pp. 524–528.
19 C. Feng, T. Lin, R. Zhu, G. Wei and K. Dong, *J. Cleaner Prod.*, 2022, **380**, 135128.
20 S. García-Luna, C. Ortiz, R. Chacartegui and L. Pérez-Maqueda, *Energy*, 2023, **268**, 126697.
21 C. Chao, Y. Deng, R. Dewil, J. Baeyens and X. Fan, *Renewable Sustainable Energy Rev.*, 2021, **138**, 110490.
22 F. Raganati and P. Ammendola, *Energy Fuels*, 2024, **38**, 13858–13905.
23 C. E. Lovelock and R. Reef, *One Earth*, 2020, **3**, 195–211.
24 C. J. Nolan, C. B. Field and K. J. Mach, *Nat. Rev. Earth Environ.*, 2021, **2**, 436–446.
25 L. Rosa and M. Mazzotti, *Renewable Sustainable Energy Rev.*, 2022, **157**, 112123.
26 M. Erans, E. S. Sanz-Pérez, D. P. Hanak, Z. Clulow, D. M. Reiner and G. A. Mutch, *Energy Environ. Sci.*, 2022, **15**, 1360–1405.
27 S.-Y. Pan, Y.-H. Chen, L.-S. Fan, H. Kim, X. Gao, T.-C. Ling, P.-C. Chiang, S.-L. Pei and G. Gu, *Nat. Sustainability*, 2020, **3**, 399–405.
28 R. Hanna, A. Abdulla, Y. Xu and D. G. Victor, *Nat. Commun.*, 2021, **12**, 368.
29 K. Madhu, S. Pauliuk, S. Dhathri and F. Creutzig, *Nat. Energy*, 2021, **6**, 1035–1044.
30 Y. Hu, J. Liao, Z. Su, Z. Wang and T. Wu, *Int. J. Technol. Manage.*, 2024, **96**, 192–227.
31 F. Sabatino, A. Grimm, F. Gallucci, M. van Sint Annaland, G. J. Kramer and M. Gazzani, *Joule*, 2021, **5**, 2047–2076.
32 M. N. Dods, E. J. Kim, J. R. Long and S. C. Weston, *Environ. Sci. Technol.*, 2021, **55**, 8524–8534.
33 M. Fang, N. Yi, W. Di, T. Wang and Q. Wang, *Int. J. Greenhouse Gas Control*, 2020, **93**, 102904.
34 D. Kearns, H. Liu and C. Consoli, *Technology readiness and costs of CCS*, Global CCS institute, 2021, vol. 3.
35 A. Baylin-Stern and N. Berghout, 2021, **https://www.iea.org/commentaries/is-carbon-capture-too-expensive**.
36 M. Shen, L. Tong, S. Yin, C. Liu, L. Wang, W. Feng and Y. Ding, *Sep. Purif. Technol.*, 2022, **299**, 121734.
37 L. Fu, Z. Ren, W. Si, Q. Ma, W. Huang, K. Liao, Z. Huang, Y. Wang, J. Li and P. Xu, *J. $CO_2$ Util.*, 2022, **66**, 102260.
38 M. Hanifa, R. Agarwal, U. Sharma, P. Thapliyal and L. Singh, *J. $CO_2$ Util.*, 2023, **67**, 102292.
39 S. Omrani, S. Mahmoodpour, B. Rostami, M. Salehi Sedeh and I. Sass, *Greenhouse Gases: Sci. Technol.*, 2021, **11**, 764–779.
40 M. Chen, Y. Zhang, S. Liu, C. Zhao, S. Dong and Y. Song, *Fuel*, 2023, **334**, 126805.
41 L. Keshavarz, M. R. Ghaani, J. D. MacElroy and N. J. English, *Chem. Eng. J.*, 2021, **412**, 128604.
42 Y. Mu, M. Zhang and M. Guo, *Sep. Purif. Technol.*, 2025, **352**, 128268.
43 W. Y. Guo Xiao, C. Jie, L. Gongqiang and X. Ji-Bao, *Chin. J. Org. Chem.*, 2020, **40**, 2208–2220.
44 H. S. Shafaat and J. Y. Yang, *Nat. Catal.*, 2021, **4**, 928–933.
45 I. Sullivan, A. Goryachev, I. A. Digdaya, X. Li, H. A. Atwater, D. A. Vermaas and C. Xiang, *Nat. Catal.*, 2021, **4**, 952–958.
46 R. Castro-Munoz, M. Z. Ahmad, M. Malankowska and J. Coronas, *Chem. Eng. J.*, 2022, **446**, 137047.
47 N. McQueen, K. V. Gomes, C. McCormick, K. Blumanthal, M. Pisciotta and J. Wilcox, *Prog. Energy*, 2021, **3**, 032001.
48 J. Liu, *ChemSusChem*, 2018, **11**, 2340–2347.
49 H. Koizumi, *J. Org. Chem.*, 2023, **88**, 5015–5024.

 

50 P. Hou, W. Song and X. Wang, *et al.*, Well–defined single–atom cobalt catalyst for electrocatalytic flue gas $CO_2$ reduction, *Small*, 2020, **16**(24), 2001896.
51 T. Nakajima, Y. Tamaki, K. Ueno, E. Kato, T. Nishikawa, K. Ohkubo, Y. Yamazaki, T. Morimoto and O. Ishitani, *J. Am. Chem. Soc.*, 2016, **138**, 13818–13821.
52 Y. Wang, E. Chen and J. Tang, *ACS Catal.*, 2022, **12**, 7300–7316.
53 K. Li, B. Peng and T. Peng, *ACS Catal.*, 2016, **6**, 7485–7527.
54 M. Dong, J.-X. Gu, C.-Y. Sun, X.-L. Wang and Z.-M. Su, *Chem. Commun.*, 2022, **58**, 10114–10126.
55 T. H. M. Pham, J. Zhang, M. Li, T.-H. Shen, Y. Ko, V. Tileli, W. Luo and A. Züttel, *Adv. Energy Mater.*, 2022, **12**, 2103663.
56 W. Lai, Y. Qiao, J. Zhang, Z. Lin and H. Huang, *Energy Environ. Sci.*, 2022, **15**, 3603–3629.
57 D. Kim, W. Choi, H. W. Lee, S. Y. Lee, Y. Choi, D. K. Lee, W. Kim, J. Na, U. Lee, Y. J. Hwang and D. H. Won, *ACS Energy Lett.*, 2021, **6**, 3488–3495.
58 G. O. Larrazábal, M. Ma and B. Seger, *Acc. Mater. Res.*, 2021, **2**, 220–229.
59 T. Xie, J. Ding, X. Shang, X. Zhang and Q. Zhong, *J. Colloid Interface Sci.*, 2023, **635**, 148–158.
60 Y. Huang, X. Zhang, X. Luo, H. Gao, Z. A. S. Bairq, P. Tontiwachwuthikul and Z. Liang, *Ind. Eng. Chem. Res.*, 2021, **60**, 2698–2709.
61 X. Gao, S. Deng and S. Kawi, *iScience*, 2022, **25**(12), 105343.
62 M. Młotek, M. Perron, K. Tutaj and K. Krawczyk, *ACS Omega*, 2021, **6**, 34805–34811.
63 D. Mei, X. Zhu, C. Wu, B. Ashford, P. T. Williams and X. Tu, *Appl. Catal., B*, 2016, **182**, 525–532.
64 S. L. Brock, M. Marquez, S. L. Suib, Y. Hayashi and H. Matsumoto, *J. Catal.*, 1998, **180**, 225–233.
65 I. Matito-Martos, C. Sepúlveda, C. Gómez, G. Acién, J. Perez-Carbajo, J. A. Delgado, V. I. Águeda, C. Ania, J. B. Parra, S. Calero and J. A. Anta, *Chem. Eng. J.*, 2021, **417**, 128020.
66 Y. Li, L. Wen, T. Tan and Y. Lv, *Front. Bioeng. Biotechnol.*, 2019, **7**, 394.
67 M. Morales, L. Sánchez and S. Revah, *FEMS Microbiol. Lett.*, 2018, **365**, fnx262.
68 M. Irfan, Y. Bai, L. Zhou, M. Kazmi, S. Yuan, S. M. Mbadinga, S.-Z. Yang, J. F. Liu, W. Sand and J.-D. Gu, *Bioresour. Technol.*, 2019, **288**, 121401.
69 Z. Liu, X. Yang, W. Jia, H. Li and X. Yang, *J. Energy Storage*, 2020, **27**, 101132.
70 S. y Obara, *Renewable Sustainable Energy Rev.*, 2023, **179**, 113290.
71 L. Chen, L. Zhang, Y. Wang, M. Xie, H. Yang, K. Ye and S. Mohtaram, *Energy Convers. Manage.*, 2023, **276**, 116583.
72 J. Wang, *ACS Omega*, 2019, **4**, 19193–19198.
73 X. Zhang and Y. Ge, Power Generation with Renewable Energy and Advanced Supercritical $CO_2$ Thermodynamic Power Cycles: A Review, *Energies*, 2023, **16**(23), 7781.
74 A. R. Razmi and M. Janbaz, Exergoeconomic assessment with reliability consideration of a green cogeneration system based on compressed air energy storage (CAES), *Energy Convers. Manage.*, 2020, **204**, 112320.
75 S. Sadeghi and P. Ahmadi, *Sustainable Energy Technol. Assess.*, 2021, **45**, 101112.
76 S. Obara, *Renewable Sustainable Energy Rev.*, 2023, **179**, 113290.
77 L. Chen, Y. Wang, M. Xie, K. Ye and S. Mohtaram, *J. Energy Storage*, 2021, **42**, 103009.
78 T. Liang, T. Zhang and X. Lin, *et al.*, *Prog. Energy*, 2023, **5**(1), 012002.
79 Y. Zhang, *Renewable Energy*, 2016, **99**, 682–697.
80 S. B. Mousavi, M. Adib and M. Soltani, *et al.*, Transient thermodynamic modeling and economic analysis of an adiabatic compressed air energy storage (A-CAES) based on cascade packed bed thermal energy storage with encapsulated phase change materials, *Energy Convers. Manage.*, 2021, **243**, 114379.
81 T. X. Phuoc and M. Massoudi, *Recent Advances in Mechanics and Fluid-Structure Interaction with Applications*, The Bong Jae Chung Memorial Volume, 2022, pp. 345–356.
82 D. Hünert, W. Schulz and A. Kranzmann, *C. ICPWS XV*, Berlin, 2008, pp. 8–11.
83 R. K. Vagapov, *Metallurgist*, 2021, **65**, 50–61.
84 G. Cui, Z. Yang and J. Liu, *et al.*, A comprehensive review of metal corrosion in a supercritical $CO_2$ environment, *Int. J. Greenhouse Gas Control*, 2019, **90**, 102814.
85 M. Farzaneh-Gord, A. Niazmand, M. Deymi-Dashtebayaz and H. R. Rahbari, *Energy*, 2015, **90**, 1152–1162.
86 A. Lockley and T. von Hippel, *Front. Eng. Manage.*, 2021, **8**, 456–464.
87 P. Bains, P. Psarras and J. Wilcox, *Prog. Energy Combust. Sci.*, 2017, **63**, 146–172.
88 K. de Kleijne, S. V. Hanssen, L. van Dinteren, M. A. Huijbregts, R. van Zelm and H. de Coninck, *One Earth*, 2022, **5**, 168–185.
89 F. Meng, Y. Meng, T. Ju, S. Han, L. Lin and J. Jiang, *Renewable Sustainable Energy Rev.*, 2022, **168**, 112902.
90 X. Zhu, W. Xie, J. Wu, Y. Miao, C. Xiang, C. Chen, B. Ge, Z. Gan, F. Yang and M. Zhang, *Chem. Soc. Rev.*, 2022, **51**, 6574–6651.
91 Y. Yamazaki, M. Miyaji and O. Ishitani, *J. Am. Chem. Soc.*, 2022, **144**, 6640–6660.
92 Y. Belmabkhout, V. Guillerm and M. Eddaoudi, *Chem. Eng. J.*, 2016, **296**, 386–397.
93 M. Ding, X. Liu, P. Ma and J. Yao, *Coord. Chem. Rev.*, 2022, **465**, 214576.
94 Y. Hu, Y. Ding, L. Xie, H. Li, Y. Jiang, K. Gong, A. Zhang, W. Zhu and Y. Wang, *Carbon*, 2024, **230**, 119574.
95 D. Wakerley, S. Lamaison, J. Wicks, A. Clemens, J. Feaster, D. Corral, S. A. Jaffer, A. Sarkar, M. Fontecave and E. B. Duoss, *Nat. Energy*, 2022, **7**, 130–143.
96 R. Küngas, *J. Electrochem. Soc.*, 2020, **167**, 044508.
97 H. Long, H.-f Lin, M. Yan, Y. Bai, X. Tong, X.-g Kong and S.-g Li, *Fuel*, 2021, **292**, 120268.
98 M. Ma, E. L. Clark, K. T. Therkildsen, S. Dalsgaard, I. Chorkendorff and B. Seger, *Energy Environ. Sci.*, 2020, **13**, 977–985.
99 M. G. Rezk, J. Foroozesh, A. Abdulrahman and J. Gholinezhad, *Energy Fuels*, 2021, **36**, 133–155.

100 X. Zhou, Q. Jiang, Q. Yuan, L. Zhang, J. Feng, B. Chu, F. Zeng and G. Zhu, *Fuel*, 2020, **263**, 116205.
101 T. N. Nguyen and C.-T. Dinh, *Chem. Soc. Rev.*, 2020, **49**, 7488–7504.
102 H. Rabiee, L. Ge, X. Zhang, S. Hu, M. Li and Z. Yuan, *Energy Environ. Sci.*, 2021, **14**, 1959–2008.
103 E. W. Lees, B. A. Mowbray, F. G. Parlane and C. P. Berlinguette, *Nat. Rev. Mater.*, 2022, **7**, 55–64.
104 Z. Xing, L. Hu, D. S. Ripatti, X. Hu and X. Feng, *Nat. Commun.*, 2021, **12**, 136.
105 M. S. Santos, M. Hamza, L. F. Franco, M. Castier and I. G. Economou, *Energy Fuels*, 2022, **36**, 8301–8310.
106 S. K. Prasad, J. S. Sangwai and H.-S. Byun, *J. $CO_2$* Util., 2023, **72**, 102479.
107 M. Sandru, E. M. Sandru, W. F. Ingram, J. Deng, P. M. Stenstad, L. Deng and R. J. Spontak, *Science*, 2022, **376**, 90–94.
108 L. Cheng, G. Liu, J. Zhao and W. Jin, *Acc. Mater. Res.*, 2021, **2**, 114–128.
109 Y. Zhang, S. Wang, D. Feng, J. Gao, L. Dong, Y. Zhao, S. Sun, Y. Huang and Y. Qin, *Energy Fuels*, 2022, **36**, 2945–2970.
110 X. Lu, C. Zhu, Z. Wu, J. Xuan, J. S. Francisco and H. Wang, *J. Am. Chem. Soc.*, 2020, **142**, 15438–15444.
111 W. Jiang, F. Wu, G. Gao, X. Li, L. Zhang and C. Luo, *Chem. Eng. J.*, 2021, **420**, 129897.
112 Z. Xing, X. Hu and X. Feng, *ACS Energy Lett.*, 2021, **6**, 1694–1702.
113 S. Kim, C. A. Scholes, D. E. Heath and S. E. Kentish, *Chem. Eng. J.*, 2021, **411**, 128468.
114 M. H. Doranehgard and H. Dehghanpour, *Phys. Fluids*, 2020, **32**(8), 085110.
115 C. Brouzet, Y. Méheust and P. Meunier, *Phys. Rev. Fluids*, 2022, **7**, 033802.
116 G. Hu, K. Jiang, R. Wang and K. G. Li, *Green Finance, Sustainable Development and the Belt and Road Initiative*, Routledge, 2020, pp. 177–215.
117 C. Temizel, C. Canbaz, H. Aydin and Z. Wijaya, IOR, 2021, vol. 1, pp. 1–27.
118 V. K. Kudapa, T. Dora and P. Swaninathan, *Unconventional Shale Gas Exploration and Exploitation: Current Trends in Shale Gas Exploitation*, Springer, 2024, pp. 77–91.
119 H. Samara, M. Al-Eryani and P. Jaeger, *Fuel*, 2022, **323**, 124271.
120 X. Zhao, H. Jin, Y. Chen and Z. Ge, *Comput. Math. App.*, 2021, **81**, 759–771.
121 M. Mehdipour, P. Keshavarz and M. R. Rahimpour, *Chem. Eng. Process. Process Intensif.*, 2021, **165**, 108447.
122 K. Xue, H. Fu, H. Chen, H. Zhang and D. Gao, *Sep. Purif. Technol.*, 2023, **304**, 122309.
123 M. Mutailipu, Y. Song, Q. Yao, Y. Liu and J. M. Trusler, *Fuel*, 2024, **357**, 129712.
124 J. Zhang, A. R. Teixeira, H. Zhang and K. F. Jensen, *React. Chem. Eng.*, 2020, **5**, 51–57.
125 Z.-Y. Liu, L. Chen and H. Chen, *Phys. Fluids*, 2022, **34**, 6.
126 C. Zhang and M. Wang, *J. Pet. Sci. Eng.*, 2023, **220**, 111154.
127 M. Bahari Moghaddam and S. A. Kamani, *Ira. J. Oil Gas Sci. Technol.*, 2022, **11**, 27–50.
128 H. Chen, M. Yang, C. Huang, Y. Wang, Y. Zhang and M. Zuo, *Chem. Eng. J.*, 2022, **428**, 131151.
129 L. Bloshanskaya, A. Ibragimov and F. Siddiqui, *et al.*, *J. Porous Media*, 2017, **20**(9), 769–786.
130 S. Wang, Y. Liu, Y. Zhao, Y. Zhang, L. Jiang, B. Yu, Y. Yin and Y. Song, *Ind. Eng. Chem. Res.*, 2020, **59**, 9300–9309.
131 V. Kossov, O. Fedorenko, A. Kalimov and A. Zhussanbayeva, *Fluids*, 2021, **6**, 177.
132 R. E. Zeebe, *Geochim. Cosmochim. Acta*, 2011, **75**, 2483–2498.
133 D. Li and X. Jiang, *Int. J. Greenhouse Gas Control*, 2020, **96**, 103015.
134 W. Amarasinghe, I. Fjelde, J.-Å. Rydland and Y. Guo, *Int. J. Greenhouse Gas Control*, 2020, **99**, 103082.
135 D. Bellaire, O. Großmann, K. Münnemann and H. Hasse, *J. Chem. Thermodyn.*, 2022, **166**, 106691.
136 H. W. Jang, D. Yang and H. Li, *J. Energy Resour. Technol.*, 2018, **140**, 052904.
137 H. Ahmadi, M. Jamialahmadi, B. S. Soulgani, N. Dinarvand and M. S. Sharafi, *Fluid Phase Equilib.*, 2020, **523**, 112584.
138 K. Namoulniara, P. Turcry and A. Aït-Mokhtar, *Eur. J. Environ. Civ. Eng.*, 2016, **20**, 1183–1196.
139 C. Moya, J. Palomar, M. Gonzalez-Miquel, J. Bedia and F. Rodriguez, *Ind. Eng. Chem. Res.*, 2014, **53**, 13782–13789.
140 S. R. Upreti and A. K. Mehrotra, *Ind. Eng. Chem. Res.*, 2000, **39**, 1080–1087.
141 H. Li, Ø. Wilhelmsen, Y. Lv, W. Wang and J. Yan, *Int. J. Greenhouse Gas Control*, 2011, **5**, 1119–1139.
142 C. Belgodere, J. Dubessy, D. Vautrin, M. C. Caumon, J. Sterpenich, J. Pironon, P. Robert, A. Randi and J. P. Birat, *J. Raman Spectrosc.*, 2015, **46**, 1025–1032.
143 P. N. Perera, H. Deng, P. J. Schuck and B. Gilbert, *J. Phys. Chem. B*, 2018, **122**, 4566–4572.
144 T. Klein, M. Piszko, C. J. Kankanamge, G. Kasapis and A. P. Fröba, *J. Phys. Chem. B*, 2021, **125**, 5100–5113.
145 T. Deleau, M. Fechter, J.-J. Letourneau, S. Camy, J. Aubin, A. S. Braeuer and F. Espitalier, *Chem. Eng. Sci.*, 2020, **228**, 115960.
146 L. Truche, E. F. Bazarkina, G. Berger, M.-C. Caumon, G. Bessaque and J. Dubessy, *Geochim. Cosmochim. Acta*, 2016, **177**, 238–253.
147 Y. Zhang, W. Geng, M. Chen, X. Xu, L. Jiang and Y. Song, *Energy Fuels*, 2023, **37**, 19695–19703.
148 Y. Liu, Y. Teng, G. Lu, L. Jiang, J. Zhao, Y. Zhang and Y. Song, *Fluid Phase Equilib.*, 2016, **417**, 212–219.
149 Y. Hou, J. Lux, P.-Y. Mahieux, P. Turcry and A. Aït-Mokhtar, *Constr. Build. Mater.*, 2023, **372**, 130715.
150 M. C. Monteiro, A. Mirabal, L. Jacobse, K. Doblhoff-Dier, S. C. Barton and M. T. Koper, *JACS Au*, 2021, **1**, 1915–1924.
151 W. Li, Y. Nan, Q. You and Z. Jin, *Chem. Eng. J.*, 2021, **411**, 127626.
152 F. Melzer, R. Breuer, R. Dahlmann and C. Hopmann, *J. Cell. Plast.*, 2022, **58**, 603–622.
153 A. C. D'Alicandro and A. Mauro, *J. Build. Perform. Simul.*, 2023, **16**, 434–459.

 

154 A. Bulińska, Z. Popiołek and Z. Buliński, *Build. Sci.*, 2014, **72**, 319–331.
155 A. Dehlouz, J.-N. Jaubert, G. Galliero, M. Bonnissel and R. Privat, *Ind. Eng. Chem. Res.*, 2022, **61**, 14033–14050.
156 S. Omrani, M. Ghasemi, S. Mahmoodpour, A. Shafiei and B. Rostami, *J. Mol. Liq.*, 2022, **345**, 117868.
157 B. Li, C. Wang, Y. Zhang and Y. Wang, *Green Energy Environ.*, 2021, **6**, 253–260.
158 Q. Sohaib, A. Muhammad, M. Younas and M. Rezakazemi, *Sep. Purif. Technol.*, 2020, **241**, 116677.
159 K. E. Ringstad, Y. Allouche, P. Gullo, Å. Ervik, K. Banasiak and A. Hafner, *Therm. Sci. Eng. Prog.*, 2020, **20**, 100647.
160 T. Klein, M. Piszko, M. Lang, J. Mehler, P. S. Schulz, M. H. Rausch, C. D. Giraudet, T. M. Koller and A. P. Fröba, *J. Chem. Eng. Data*, 2020, **65**, 4116–4129.
161 M. N. Amar, M. A. Ghriga, H. Ouaer, M. E. A. B. Seghier, B. T. Pham and P. Ø. Andersen, *J. Nat. Gas Sci. Eng.*, 2020, **77**, 103271.
162 R. S. Chatwell, G. Guevara-Carrion, Y. Gaponenko, V. Shevtsova and J. Vrabec, *Phys. Chem. Chem. Phys.*, 2021, **23**, 3106–3115.
163 H. W. Jang and D. Yang, *Ind. Eng. Chem. Res.*, 2020, **59**, 15028–15047.
164 S. Balchandani, B. Mandal and S. Dharaskar, *Fluid Phase Equilib.*, 2020, **521**, 112643.
165 R. Kas, A. G. Star, K. Yang, T. Van Cleve, K. C. Neyerlin and W. A. Smith, *ACS Sustainable Chem. Eng.*, 2021, **9**, 1286–1296.
166 W. Wu, T. Klein, M. Kerscher, M. H. Rausch, T. M. Koller, C. D. Giraudet and A. P. Fröba, *J. Phys. Chem. B*, 2020, **124**, 2482–2494.
167 K. Li, W. Wu, L. Peng and H. Zhang, *J. Mol. Liq.*, 2021, **337**, 116240.
168 Y. Zhao, Y. Feng and X. Zhang, *Fuel*, 2016, **165**, 19–27.
169 Y. Luo, H. Xiao, X. Liu, T. Zheng and Z. Wu, *J. Mol. Liq.*, 2023, **382**, 121943.
170 Z. Ma, U. Legrand, E. Pahija, J. R. Tavares and D. C. Boffito, *Ind. Eng. Chem. Res.*, 2020, **60**, 803–815.
171 D. Ma, T. Jin, K. Xie and H. Huang, *J. Mater. Chem. A*, 2021, **9**, 20897–20918.
172 P. Zhu and H. Wang, *Nat. Catal.*, 2021, **4**, 943–951.
173 C. W. Anson and S. S. Stahl, *Chem. Rev.*, 2020, **120**, 3749–3786.
174 J. Zhao, X. Li, C. Shum and J. McPhee, *Energy AI*, 2021, **6**, 100114.
175 P. Zhu, J. Yao, Z. Wu, S.-M. Huang, M. R. A. Mansor, F. Yang and Z. Zhang, *Chem. Eng. J.*, 2022, **442**, 136159.
176 K. Yang, R. Kas, W. A. Smith and T. Burdyny, *ACS Energy Lett.*, 2020, **6**, 33–40.
177 K. Junge Puring, D. Siegmund, J. Timm, F. Möllenbruck, S. Schemme, R. Marschall and U. P. Apfel, *Adv. Sustainable Syst.*, 2021, **5**, 2000088.
178 S. Hernandez-Aldave and E. Andreoli, *Catalysts*, 2020, **10**, 713.
179 Y.-S. Jun, L. Zhang, Y. Min and Q. Li, *Acc. Chem. Res.*, 2017, **50**, 1521–1529.
180 A. Mustafa, B. G. Lougou, Y. Shuai, Z. Wang and H. Tan, *J. Energy Chem.*, 2020, **49**, 96–123.
181 D. Corral, J. T. Feaster, S. Sobhani, J. R. DeOtte, D. U. Lee, A. A. Wong, J. Hamilton, V. A. Beck, A. Sarkar and C. Hahn, *Energy Environ. Sci.*, 2021, **14**, 3064–3074.
182 P. R. Jeon and C.-H. Lee, *Chem. Eng. J.*, 2020, **382**, 123014.
183 T. R. Reina, J. A. Odriozola and H. Arellano-Garcia, *Engineering solutions for $CO_2$ conversion*, Wiley Online Library, 2021.
184 I. Mehdipour, G. Falzone, D. Prentice, N. Neithalath, D. Simonetti and G. Sant, *React. Chem. Eng.*, 2021, **6**, 494–504.
185 W. Li, M. Zhang, Y. Nan, W. Pang and Z. Jin, *Langmuir*, 2020, **37**, 542–552.
186 M. McKee, M. Kutter, Y. Wu, H. Williams, M.-A. Vaudreuil, M. Carta, A. K. Yadav, H. Singh, J.-F. Masson and D. Lentz, *Nat. Chem.*, 2024, 1–9.
187 M. T. Martins-Costa and M. F. Ruiz-López, *J. Phys. Chem. B*, 2024, **128**, 1289–1297.
188 J. Lei, Y. Hou, H. Wang, Y. Fan, Y. Zhang, B. Chen, S. Yu and X. Hou, *Angew. Chem., Int. Ed.*, 2022, **61**, e202201109.
189 A. A. Samu, I. Szenti, Á. Kukovecz, B. Endrődi and C. Janáky, *Commun. Chem.*, 2023, **6**, 41.
190 C. Ampelli, F. Tavella, D. Giusi, A. M. Ronsisvalle, S. Perathoner and G. Centi, *Catal. Today*, 2023, **421**, 114217.
191 Z. Zhang, X. Huang, Z. Chen, J. Zhu, B. Endrődi, C. Janáky and D. Deng, *Angew. Chem.*, 2023, **135**, e202302789.
192 E. R. Cofell, U. O. Nwabara, S. S. Bhargava, D. E. Henckel and P. J. Kenis, *ACS Appl. Mater. Interfaces*, 2021, **13**, 15132–15142.
193 A. Rieder, J. Lorenzetti, I. Zelocualtecatl Montiel, A. Dutta, A. Iarchuk, M. Mirolo, J. Drnec, F. Lorenzutti, S. Haussener and N. Kovács, *Small Methods*, 2024, 2400200.
194 Y. Wu, S. Garg, M. Li, M. N. Idros, Z. Li, R. Lin, J. Chen, G. Wang and T. E. Rufford, *J. Power Sources*, 2022, **522**, 230998.
195 A. Löwe, M. Schmidt, F. Bienen, D. Kopljar, N. Wagner and E. Klemm, *ACS Sustainable Chem. Eng.*, 2021, **9**, 4213–4223.
196 S. Lu, Y. Wang, H. Xiang, H. Lei, B. B. Xu, L. Xing, E. H. Yu and T. X. Liu, *J. Energy Storage*, 2022, **52**, 104764.
197 M. Ma, S. Kim, I. Chorkendorff and B. Seger, *Chem. Sci.*, 2020, **11**, 8854–8861.
198 Y. Zhong, Y. Xu, J. Ma, C. Wang, S. Sheng, C. Cheng, M. Li, L. Han, L. Zhou and Z. Cai, *Angew. Chem.*, 2020, **132**, 19257–19263.
199 Y. Chen, N. S. Lewis and C. Xiang, *J. Electrochem. Soc.*, 2020, **167**, 114503.
200 C. Chen, X. Yan, Y. Wu, S. Liu, X. Zhang, X. Sun, Q. Zhu, H. Wu and B. Han, *Angew. Chem., Int. Ed.*, 2022, **61**, e202202607.
201 M. Sun, J. Cheng and M. Yamauchi, *Nat. Commun.*, 2024, **15**, 491.
202 H. Dashtian, S. Bakhshian, S. Hajirezaie, J.-P. Nicot and S. A. Hosseini, *Comput. Geosci.*, 2019, **125**, 19–29.
203 D. Pereira, R. Fonseca, I. Marin-Montesinos, M. Sardo and L. Mafra, *Curr. Opin. Colloid Interface Sci.*, 2023, **64**, 101690.
204 S. C. Reyes, J. H. Sinfelt and G. J. DeMartin, *J. Phys. Chem. B*, 2000, **104**, 5750–5761.
205 C. Zhao, Y. Wang, Z. Li, W. Chen, Q. Xu, D. He, D. Xi, Q. Zhang, T. Yuan and Y. Qu, *Joule*, 2019, **3**, 584–594.

206 K. Ge, Q. Yu, S. Chen, X. Shi and J. Wang, *Chem. Eng. J.*, 2019, **364**, 328–339.
207 H. Chen, S. Dong, Y. Zhang and P. He, *Energy*, 2022, **239**, 122348.
208 H. Penman, *J. Agric. Sci.*, 1940, **30**, 570–581.
209 S. Li, C. Qiao, Z. Li and Y. Hui, *J. $CO_2$* Util., 2018, **28**, 1–14.
210 D. Benavente and C. Pla, *Mater. Struct.*, 2018, **51**, 21.
211 J. Liu, H. Xie, Q. Wang, S. Chen and Z. Hu, *Energy Fuels*, 2019, **34**, 1240–1250.
212 H. Sharifigaliuk, S. M. Mahmood, R. Rezaee, F. Ayobami Afolabi and I. Ul Haq, *Energy Fuels*, 2022, **36**, 6167–6186.
213 T. Wang, K. Zhang, S.-W. Du, L.-G. Wu, C.-J. Li, H.-L. Chen and H.-C. Guo, *Chem. Eng. J.*, 2023, **477**, 147280.
214 R. Krishna, *Ind. Eng. Chem. Res.*, 2016, **55**, 4749–4759.
215 Y. Tang, C. Hou, Y. He, Y. Wang, Y. Chen and Z. Rui, *Energy Technol.*, 2021, **9**, 2000787.
216 B. C. Bukowski, F. J. Keil, P. I. Ravikovitch, G. Sastre, R. Q. Snurr and M.-O. Coppens, *Adsorption*, 2021, **27**, 683–760.
217 M. Seggiani, M. Puccini and S. Vitolo, *Int. J. Greenhouse Gas Control*, 2011, **5**, 741–748.
218 B. Petrovic, M. Gorbounov and S. M. Soltani, *Microporous Mesoporous Mater.*, 2021, **312**, 110751.
219 B. Zhu, X. Jiang, S. He, X. Yang, J. Long, Y. Zhang and L. Shao, *J. Mater. Chem. A*, 2020, **8**, 24233–24252.
220 F. A. Hashim, R. R. Mostafa, A. G. Hussien, S. Mirjalili and K. M. Sallam, *Knowl. Based Syst.*, 2023, **260**, 110146.
221 R. Gama and R. Gama, *WSEAS Trans. Heat Mass Transfer*, 2021, **16**, 59–67.
222 R. Marquardt, *Mol. Phys.*, 2021, **119**, e1971315.
223 V. Domazetoski, A. Masó-Puigdellosas, T. Sandev, V. Méndez, A. Iomin and L. Kocarev, *Phys. Rev. Res.*, 2020, **2**, 033027.
224 J. Li, C. Cai and Z. H. Li, *Phys. Fluids*, 2021, **33**(4), 042009.
225 M. Mourkou, H. Yu, S. Baltussen, N. Snead, N. Kapil and M.-O. Coppens, *React. Chem. Eng.*, 2024, **9**, 3047–3059.
226 L. Yang, Z. Zhang, Y. Song, S. Hong, R. Xu, Y. Zhao, W. Zhang, B. Cui and M.-H. Yang, *ACM Comput. Surv.*, 2023, **56**, 1–39.
227 K. Wang, C. Liu, X. Chen, C. Fang, Y. Wang, C. Lian, L. Lei and Z. Xu, *J. Membr. Sci.*, 2024, **708**, 123029.
228 H. Jin, Y. Zhang, H. Dong, Y. Zhang, Y. Sun, J. Shi and R. Li, *Fuel*, 2022, **320**, 123951.
229 Š. Svoboda, M. Lebeda, P. Vlčák, Z. Budinská and J. Drahokoupil, *Results Phys.*, 2024, **64**, 107943.
230 Q. Mao, M. Feng, X. Z. Jiang, Y. Ren, K. H. Luo and A. C. van Duin, *Prog. Energy Combust. Sci.*, 2023, **97**, 101084.
231 Y. Munei, Y. Shigeta and R. Harada, *Chem. Lett.*, 2023, **52**, 385–388.
232 P. Gkeka, G. Stoltz, A. Barati Farimani, Z. Belkacemi, M. Ceriotti, J. D. Chodera, A. R. Dinner, A. L. Ferguson, J.-B. Maillet and H. Minoux, *J. Chem. Theory Comput.*, 2020, **16**, 4757–4775.
233 J. J. Winetrout, K. Kanhaiya, J. Kemppainen, P. J. in't Veld, G. Sachdeva, R. Pandey, B. Damirchi, A. van Duin, G. M. Odegard and H. Heinz, *Nat. Commun.*, 2024, **15**, 7945.
234 X. Wang, S. Ramírez-Hinestrosa, J. Dobnikar and D. Frenkel, *Phys. Chem. Chem. Phys.*, 2020, **22**, 10624–10633.
235 K. Kanhaiya, M. Nathanson, P. J. in't Veld, C. Zhu, I. Nikiforov, E. B. Tadmor, Y. K. Choi, W. Im, R. K. Mishra and H. Heinz, *J. Chem. Theory Comput.*, 2023, **19**, 8293–8322.
236 R. L. Akkermans, N. A. Spenley and S. H. Robertson, *Mol. Simul.*, 2021, **47**, 540–551.
237 A. Rahnamoun, M. C. Kaymak, M. Manathunga, A. W. Götz, A. C. Van Duin, K. M. Merz Jr and H. M. Aktulga, *J. Chem. Theory Comput.*, 2020, **16**, 7645–7654.
238 A. Miyagawa, S. Nagatomo, H. Kuno, T. Terada and K. Nakatani, *Langmuir*, 2023, **39**, 11329–11336.
239 L. Chen, A. He, J. Zhao, Q. Kang, Z.-Y. Li, J. Carmeliet, N. Shikazono and W.-Q. Tao, *Prog. Energy Combust. Sci.*, 2022, **88**, 100968.
240 L. Yu, W.-L. Hsu, J. A. Shamim and H. Daiguji, *Int. J. Heat Mass Transfer*, 2022, **186**, 122456.
241 F. Ahmad, M. Talbi, M. Prat, E. Tsotsas and A. Kharaghani, *Chem. Eng. Sci.*, 2020, **228**, 115957.
242 M. M. Bhatti, M. Marin, A. Zeeshan and S. I. Abdelsalam, *Front. Phys.*, 2020, **8**, 593111.
243 E. Martínez-Moreno, G. Garcia-Ros and I. Alhama, *Eng. Comput.*, 2020, **37**, 3269–3291.
244 S. Mirjalili and A. Mani, *J. Comput. Phys.*, 2021, **426**, 109918.
245 Z. Cheng, Z. Guo, P. Fu, J. Yang and Q. Wang, *Int. Commun. Heat Mass Transfer*, 2021, **129**, 105652.
246 S. Stephan and H. Hasse, *Int. Rev. Phys. Chem.*, 2020, **39**, 319–349.
247 K. Yuan, Y. Liu, H. Feng, Y. Liu, J. Cheng, B. Luo, Q. Wu, X. Zhang, Y. Wang and X. Bao, *Chin. Chem. Lett.*, 2024, **35**, 109022.
248 Y. He, S. Liu, M. Wang, H. Ji, L. Zhang, Q. Cheng, T. Qian and C. Yan, *Adv. Funct. Mater.*, 2022, **32**, 2208474.
249 K. R. Wilson, A. M. Prophet, G. Rovelli, M. D. Willis, R. J. Rapf and M. I. Jacobs, *Chem. Sci.*, 2020, **11**, 8533–8545.
250 J. E. C. Lerner, M. B. Del Sole, F. I. Dubois, J. Sambeth, A. A. Porta, M. A. Peluso and E. Y. Sanchez, *Chem. Eng. Res. Des.*, 2024, **207**, 257–267.
251 S. M. M. Alghazali, K. Polshchykov and A. M. Hailan, *et al.*, *Int. J. Adv. Comput. Sci. App.*, 2021, **12**(7), 32–36.
252 Z. Li, J. Peng, L. Li, L. Qi and W. Li, *Energy Fuels*, 2021, **35**, 7844–7857.
253 K. O. Yoro, M. K. Amosa, P. T. Sekoai, J. Mulopo and M. O. Daramola, *Int. J. Sustainable Eng.*, 2020, **13**, 54–67.
254 L. Li and Y. T. Kang, *Int. J. Heat Mass Transfer*, 2021, **164**, 120444.
255 G. Singh, J. Lee, A. Karakoti, R. Bahadur, J. Yi, D. Zhao, K. AlBahily and A. Vinu, *Chem. Soc. Rev.*, 2020, **49**, 4360–4404.
256 M. S. B. Reddy, D. Ponnamma, K. K. Sadasivuni, B. Kumar and A. M. Abdullah, *RSC Adv.*, 2021, **11**, 12658–12681.
257 W. Tian, H. Zhang, X. Duan, H. Sun, G. Shao and S. Wang, *Adv. Funct. Mater.*, 2020, **30**, 1909265.

 

258 F. Lou, A. Zhang, G. Zhang, L. Ren, X. Guo and C. Song, *Appl. Energy*, 2020, **264**, 114637.
259 R. S. Liu, X. D. Shi, C. T. Wang, Y. Z. Gao, S. Xu, G. P. Hao, S. Chen and A. H. Lu, *ChemSusChem*, 2021, **14**, 1428–1471.
260 S. Krause, N. Hosono and S. Kitagawa, *Angew. Chem., Int. Ed.*, 2020, **59**, 15325–15341.
261 R.-B. Lin, Z. Zhang and B. Chen, *Acc. Chem. Res.*, 2021, **54**, 3362–3376.
262 M. A. Little and A. I. Cooper, *Adv. Funct. Mater.*, 2020, **30**, 1909842.
263 M. T. Dunstan, F. Donat, A. H. Bork, C. P. Grey and C. R. Müller, *Chem. Rev.*, 2021, **121**, 12681–12745.
264 H. Wen, L. Zhang, Y. Du, Z. Wang, Y. Jiang, H. Bian, J. Cui and S. Jia, *J. $CO_2$* Util., 2020, **39**, 101171.
265 Y. Fan, W. Yu, A. Wu, W. Shu and Y. Zhang, *RSC Adv.*, 2024, **14**, 20714–20734.
266 L. Lei, L. Bai, A. Lindbråthen, F. Pan, X. Zhang and X. He, *Chem. Eng. J.*, 2020, **401**, 126084.
267 M. Chawla, H. Saulat, M. Masood Khan, M. Mahmood Khan, S. Rafiq, L. Cheng, T. Iqbal, M. I. Rasheed, M. Z. Farooq and M. Saeed, *Chem. Eng. Technol.*, 2020, **43**, 184–199.
268 T. Arumugham, N. J. Kaleekkal, S. Gopal, J. Nambikkattu, K. Rambabu, A. M. Aboulella, S. R. Wickramasinghe and F. Banat, *J. Environ. Manage.*, 2021, **293**, 112925.
269 C. Algieri and E. Drioli, *Sep. Purif. Technol.*, 2021, **278**, 119295.
270 R. Mahdavi Far, B. Van der Bruggen, A. Verliefde and E. Cornelissen, *J. Chem. Technol. Biotechnol.*, 2022, **97**, 575–596.
271 Y. Xiang, L. Lu, A. G. P. Kottapalli and Y. Pei, *Carbon Energy*, 2022, **4**, 346–398.
272 B. Hosseini Monjezi, K. Kutonova, M. Tsotsalas, S. Henke and A. Knebel, *Angew. Chem., Int. Ed.*, 2021, **60**, 15153–15164.
273 Y. Cheng, S. J. Datta, S. Zhou, J. Jia, O. Shekhah and M. Eddaoudi, *Chem. Soc. Rev.*, 2022, **51**, 8300–8350.
274 M. Safarpour, S. Arefi-Oskoui and A. Khataee, *J. Ind. Eng. Chem.*, 2020, **82**, 31–41.
275 K. A. Adegoke and N. W. Maxakato, *Coord. Chem. Rev.*, 2022, **457**, 214389.
276 Z. Zhang, G. Huang, Y. Li, X. Chen, Y. Yao, S. Ren, M. Li, Y. Wu and C. An, *Chem. Eng. J.*, 2022, **427**, 131987.
277 Y. Shi, B. Liang, R.-B. Lin, C. Zhang and B. Chen, *Trends Chem.*, 2020, **2**, 254–269.
278 N. H. Solangi, A. Anjum, F. A. Tanjung, S. A. Mazari and N. M. Mubarak, *J. Environ. Chem. Eng.*, 2021, **9**, 105860.
279 A. S. Embaye, L. Martínez-Izquierdo, M. Malankowska, C. Téllez and J. Coronas, *Energy Fuels*, 2021, **35**, 17085–17102.
280 M. Mohsenpour Tehrani and E. Chehrazi, *ACS Appl. Mater. Interfaces*, 2024, **16**, 32906–32929.
281 M. H. Zeeshan, Y. F. Yeong and T. L. Chew, *ChemBioEng Rev.*, 2024, **11**, 513–542.
282 F. Russo, F. Galiano, A. Iulianelli, A. Basile and A. Figoli, *Fuel Process. Technol.*, 2021, **213**, 106643.
283 M.-Y. Wey, H.-H. Chen, Y.-T. Lin and H.-H. Tseng, *Int. J. Hydrogen Energy*, 2020, **45**, 7290–7302.
284 V. Zhdanov and A. Stepanenko, *J. Eng. Phys. Thermophys.*, 2021, **94**, 623–632.
285 C. Gao, J. Liao, J. Lu, J. Ma and E. Kianfar, *Rev. Inorg. Chem.*, 2021, **41**, 1–20.
286 M. A. Carreon, *ACS Mater. Lett.*, 2022, **4**, 868–873.
287 Z. Xu, Z. Fan, C. Shen, Q. Meng, G. Zhang and C. Gao, *Adv. Membr.*, 2022, **2**, 100027.
288 N. Pal and M. Agarwal, *Int. J. Hydrogen Energy*, 2021, **46**, 27062–27087.
289 X. Li, H. Chen, Z. Li and H. Zhang, *J. Membr. Sci.*, 2023, **680**, 121762.
290 R. S. K. Valappil, N. Ghasem and M. Al-Marzouqi, *J. Ind. Eng. Chem.*, 2021, **98**, 103–129.
291 Y. Han and W. W. Ho, *J. Membr. Sci.*, 2021, **628**, 119244.
292 C. Chen, X. Wu, J. Zhang, J. Chen, X. Cui, W. Li, W. Wu and J. Wang, *AIChE J.*, 2022, **68**, e17795.
293 I. Beckman, D. Syrtsova, M. Shalygin, P. Kandasamy and V. Teplyakov, *J. Membr. Sci.*, 2020, **601**, 117737.
294 L. Rodríguez-Jardón, M. López-González, M. Iglesias and E. M. Maya, *J. Membr. Sci.*, 2021, **619**, 118795.
295 C. Wu, K. Zhang, H. Wang, Y. Fan, S. Zhang, S. He, F. Wang, Y. Tao, X. Zhao and Y.-B. Zhang, *J. Am. Chem. Soc.*, 2020, **142**, 18503–18512.
296 A. Paul, T. Laurila, V. Vuorinen, S. V. Divinski, A. Paul, T. Laurila, V. Vuorinen and S. V. Divinski, *Thermodynamics, diffusion and the Kirkendall effect in solids*, 2014, pp. 115–139.
297 T. J. dos Santos, F. W. Tavares and C. R. Abreu, *J. Mol. Liq.*, 2021, **329**, 115460.
298 Z. Liu, L. Qin, X. Cao, J. Zhou, A. Pan, G. Fang, S. Wang and S. Liang, *Prog. Mater. Sci.*, 2022, **125**, 100911.
299 X. You, S. Liu, C. Dai, Y. Guo, G. Zhong and Y. Duan, *Sci. Total Environ.*, 2020, **743**, 140703.
300 X.-d Qi, J.-h Yang, N. Zhang, T. Huang, Z.-w Zhou, I. Kühnert, P. Pötschke and Y. Wang, *Prog. Polym. Sci.*, 2021, **123**, 101471.
301 S. Luo, T. Han, C. Wang, Y. Sun, H. Zhang, R. Guo and S. Zhang, *Ind. Chem. Mater.*, 2023, **1**, 376–387.
302 C. A. Scholes, J. Jin, G. W. Stevens and S. E. Kentish, *J. Polym. Sci., Part B: Polym. Phys.*, 2015, **53**, 719–728.
303 J. Zhu, S. Yuan, J. Wang, Y. Zhang, M. Tian and B. Van der Bruggen, *Prog. Polym. Sci.*, 2020, **110**, 101308.
304 J. G. Brandin, C. P. Hulteberg and C. I. Odenbrand, *Chem. Eng. J.*, 2012, **191**, 218–227.
305 Q. Xin, Y. Yang, S. Liu, X. Zhang, C. Zheng, Q. Lin and X. Gao, *Appl. Energy*, 2023, **331**, 120450.
306 Y. J. Kim, K. M. Min, J. K. Lee, S. B. Hong, B. K. Cho and I. S. Nam, *ChemCatChem*, 2014, **6**, 1186–1189.
307 T. Maunula, M. Tuikka and T. Wolff, *Emiss. Control Sci. Technol.*, 2020, **6**, 390–401.
308 Y. Xu, H. Liang, R. Li, Z. Zhang, C. Qin, D. Xu, H. Fan, B. Hou, J. Wang and X. K. Gu, *Angew. Chem.*, 2023, **135**, e202306786.
309 T. Piemsinlapakunchon and M. C. Paul, *Int. J. Hydrogen Energy*, 2021, **46**, 7573–7588.

310 Y. H. Chan, S. N. F. S. A. Rahman, H. M. Lahuri and A. Khalid, *Environ. Pollut.*, 2021, **278**, 116843.
311 L. Delafontaine, T. Asset and P. Atanassov, *ChemSusChem*, 2020, **13**, 1688–1698.
312 Y. C. Xiao, C. M. Gabardo, S. Liu, G. Lee, Y. Zhao, C. P. O'Brien, R. K. Miao, Y. Xu, J. P. Edwards and M. Fan, *EES Catal.*, 2023, **1**, 54–61.
313 F. Qiu, S. Ren, X. Mu, Y. Liu, X. Zhang, P. He and H. Zhou, *Energy Storage Mater.*, 2020, **26**, 443–447.
314 Y. Jiao, J. Qin, H. M. K. Sari, D. Li, X. Li and X. Sun, *Energy Storage Mater.*, 2021, **34**, 148–170.
315 E. R. Ezeigwe, L. Dong, R. Manjunatha, Y. Zuo, S.-Q. Deng, M. Tan, W. Yan, J. Zhang and D. P. Wilkinson, *Nano Energy*, 2022, **95**, 106964.
316 X. Yu and A. Manthiram, *Small Struct.*, 2020, **1**, 2000027.
317 Y. Zheng, Z. Shi, D. Ren, J. Chen, X. Liu, X. Feng, L. Wang, X. Han, L. Lu and X. He, *J. Energy Chem.*, 2022, **69**, 593–600.
318 X. Liu, L. Yin, D. Ren, L. Wang, Y. Ren, W. Xu, S. Lapidus, H. Wang, X. He and Z. Chen, *Nat. Commun.*, 2021, **12**, 4235.
319 G. Nazir, A. Rehman and S.-J. Park, *J. $CO_2$* Util., 2020, **42**, 101326.
320 C. Jiang, G. A. Yakaboylu, T. Yumak, J. W. Zondlo, E. M. Sabolsky and J. Wang, *Renewable Energy*, 2020, **155**, 38–52.
321 L. Wang, F. Sun, F. Hao, Z. Qu, J. Gao, M. Liu, K. Wang, G. Zhao and Y. Qin, *Chem. Eng. J.*, 2020, **383**, 123205.
322 S. Zhao, D. Xia, M. Li, D. Cheng, K. Wang, Y. S. Meng, Z. Chen and J. Bae, *ACS Appl. Mater. Interfaces*, 2021, **13**, 12033–12041.
323 A. Banerjee, X. Wang, C. Fang, E. A. Wu and Y. S. Meng, *Chem. Rev.*, 2020, **120**, 6878–6933.
324 A. Salehabadi, M. F. Umar, A. Ahmad, M. I. Ahmad, N. Ismail and M. Rafatullah, *Int. J. Energy Res.*, 2020, **44**, 11044–11058.
325 N. Sazali, *J. Mater. Sci.*, 2020, **55**, 11052–11070.
326 A. Zaker, S. ben Hammouda, J. Sun, X. Wang, X. Li and Z. Chen, *J. Environ. Chem. Eng.*, 2023, **11**, 109741.
327 S. P. Shet, S. S. Priya, K. Sudhakar and M. Tahir, *Int. J. Hydrogen Energy*, 2021, **46**, 11782–11803.
328 J. Ren, H. W. Langmi, B. C. North and M. Mathe, *Int. J. Energy Res.*, 2015, **39**, 607–620.
329 P. Kumar, B. Anand, Y. F. Tsang, K.-H. Kim, S. Khullar and B. Wang, *Environ. Res.*, 2019, **176**, 108488.
330 H. N. Abdelhamid, *Macromol. Chem. Phys.*, 2020, **221**, 2000031.
331 Y. Zhu, L. Ouyang, H. Zhong, J. Liu, H. Wang, H. Shao, Z. Huang and M. Zhu, *Angew. Chem.*, 2020, **132**, 8701–8707.
332 M. H. Masood, N. Haleem, I. Shakeel and Y. Jamal, *Res. Chem. Intermed.*, 2020, **46**, 5165–5180.
333 L. Yang, X. Hua, J. Su, W. Luo, S. Chen and G. Cheng, *Appl. Catal., B*, 2015, **168**, 423–428.
334 F. Xu, W. Huang, Y. Wang, D. Astruc and X. Liu, *Inorg. Chem. Front.*, 2022, **9**, 3514–3521.
335 P. Javadian, D. A. Sheppard, C. E. Buckley and T. R. Jensen, *Nano Energy*, 2015, **11**, 96–103.
336 Z. Ding, S. Li, Y. Zhou, Z. Chen, W. Yang, W. Ma and L. Shaw, *Nano Mater. Sci.*, 2020, **2**, 109–119.
337 X. Wang, X. Xiao, J. Zheng, X. Huang, M. Chen and L. Chen, *Int. J. Hydrogen Energy*, 2020, **45**, 2044–2053.
338 M. Nori, R. Venegas and R. Raspet, *Chem. Eng. Sci.*, 2017, **164**, 1–16.
339 R. Grün, A. S. Hashim, C. Grau Turuelo and C. Breitkopf, *Chem. Methods*, 2024, **4**, e202400006.
340 V. R. Maynard and E. Grushka, *Adv. Chromatogr.*, 2021, 99–140.
341 S. Garg, Q. Xu, A. B. Moss, M. Mirolo, W. Deng, I. Chorkendorff, J. Drnec and B. Seger, *Energy Environ. Sci.*, 2023, **16**, 1631–1643.
342 S. Brandani and E. Mangano, *Adsorption*, 2021, **27**, 319–351.
343 X. Hu, S. Brandani, A. I. Benin and R. R. Willis, *Ind. Eng. Chem. Res.*, 2015, **54**, 5777–5783.
344 I.-S. Park, D. D. Do and A. E. Rodrigues, *Catal. Rev.*, 1996, **38**, 189–247.
345 R. Shi, J. Guo, X. Zhang, G. I. Waterhouse, Z. Han, Y. Zhao, L. Shang, C. Zhou, L. Jiang and T. Zhang, *Nat. Commun.*, 2020, **11**, 3028.
346 Y. Guo, F. Liu, J. Qiu, Z. Xu and B. Bao, *Energy*, 2022, **256**, 124524.
347 S. Hwang, R. Semino, B. Seoane, M. Zahan, C. Chmelik, R. Valiullin, M. Bertmer, J. Haase, F. Kapteijn and J. Gascon, *Angew. Chem., Int. Ed.*, 2018, **57**, 5156–5160.
348 C. Chmelik, J. van Baten and R. Krishna, *J. Membr. Sci.*, 2012, **397**, 87–91.
349 A. Baniani, S. J. Berens, M. P. Rivera, R. P. Lively and S. Vasenkov, *Adsorption*, 2021, **27**, 485–501.
350 B.-T. L. Bleken, K. P. Lillerud, T. Splith, A.-K. Pusch and F. Stallmach, *Microporous Mesoporous Mater.*, 2013, **182**, 25–31.
351 M. Prakash, H. Jobic, N. Ramsahye, F. Nouar, D. Damasceno Borges, C. Serre and G. Maurin, *J. Phys. Chem. C*, 2015, **119**, 23978–23989.
352 H. J. Moon, J. M. Y. Carrillo and C. W. Jones, *Acc. Chem. Res.*, 2023, **56**, 2620–2630.
353 J. Barrett, P. Girr and L. C. Mackinder, *Biochim. Biophys. Acta, Mol. Cell. Res.*, 2021, **1868**, 118949.
354 A. Tavakoli, K. Rahimi, F. Saghandali, J. Scott and E. Lovell, *J. Environ. Manage.*, 2022, **313**, 114955.
355 M. S. Sharafi, M. Ghasemi, M. Ahmadi and A. Kazemi, *Chin. J. Chem. Eng.*, 2021, **34**, 160–170.
356 Y. Shi, S. Zheng and D. Yang, *Int. J. Heat Mass Transfer*, 2017, **107**, 572–585.
357 M. Piszko, K. Batz, M. H. Rausch, C. Giraudet and A. P. Fröba, *J. Chem. Eng. Data*, 2019, **65**, 1068–1082.
358 M. Garcia-Rates, J.-C. de Hemptinne, J. B. Avalos and C. Nieto-Draghi, *J. Phys. Chem. B*, 2012, **116**, 2787–2800.
359 A. Zhadan, V. Sarou-Kanian, L. Del Campo, L. Cosson, M. Malki and C. Bessada, *Int. J. Hydrogen Energy*, 2021, **46**, 15059–15065.
360 J. He, P. C. Pérez Rickert, T. Suhasaria, O. Sohier, T. Bäcker, D. Demertzi, G. Vidali and T. K. Henning, *Mol. Phys.*, 2024, **122**, e2176181.
361 P. Goyal, M. J. Purdue and S. Farooq, *Ind. Eng. Chem. Res.*, 2019, **58**, 19611–19622.

 

362 C. Goel, S. Mohan and P. Dinesha, *Sci. Total Environ.*, 2021, **798**, 149296.
363 C. Dhoke, A. Zaabout, S. Cloete and S. Amini, *Ind. Eng. Chem. Res.*, 2021, **60**, 3779–3798.
364 M. M. Majd, V. Kordzadeh-Kermani, V. Ghalandari, A. Askari and M. Sillanpää, *Sci. Total Environ.*, 2022, **812**, 151334.
365 M. A. Al-Ghouti and D. A. Da'ana, *J. Hazard. Mater.*, 2020, **393**, 122383.
366 V. K. Singh and E. A. Kumar, *Appl. Therm. Eng.*, 2016, **97**, 77–86.
367 A. Sarwar, M. Ali, A. H. Khoja, A. Nawar, A. Waqas, R. Liaquat, S. R. Naqvi and M. Asjid, *J. $CO_2$* Util., 2021, **46**, 101476.
368 R. Melouki, A. Ouadah and P. L. Llewellyn, *J. $CO_2$* Util., 2020, **42**, 101292.
369 H. Jedli, M. Almoneef, M. Mbarek, A. Jbara and K. Slimi, *Fuel*, 2022, **321**, 124097.
370 M. M. Almoneef, H. Jedli and M. Mbarek, *Mater. Res. Express*, 2021, **8**, 065602.
371 J. Serafin and B. Dziejarski, *Microporous Mesoporous Mater.*, 2023, **354**, 112513.
372 D. C. Fernandez, D. S. Morales, J. R. Jiménez and J. M. Fernández-Rodriguez, *Chem. Eng. J.*, 2022, **431**, 134324.
373 A. Chegeni, V. Babaeipour, M. Fathollahi and S. G. Hosseini, *J. Cluster Sci.*, 2022, **33**, 2167–2178.
374 W. Thompson, E. S. Fernandez and M. Maroto-Valer, *Chem. Eng. J.*, 2020, **384**, 123356.
375 P. Faravar, Z. Zarei and M. G. Monjezi, *J. Environ. Chem. Eng.*, 2020, **8**, 103946.
376 S. Wang, Y.-R. Lee, Y. Won, H. Kim, S.-E. Jeong, B. W. Hwang, A. R. Cho, J.-Y. Kim, Y. C. Park and H. Nam, *Chem. Eng. J.*, 2022, **437**, 135378.
377 G. Mohamed, A. Ashraf and A. Mohamed, *Biointerface Res. Appl. Chem.*, 2022, **12**, 6252–6268.
378 K. Kiełbasa, A. Kamińska, O. Niedoba and B. Michalkiewicz, *Materials*, 2021, **14**, 7458.
379 A. Mukhtar, N. Mellon, S. Saqib, S.-P. Lee and M. A. Bustam, *SN Appl. Sci.*, 2020, **2**, 1–4.
380 H. Chen, Y. Guo, Y. Du, X. Xu, C. Su, Z. Zeng and L. Li, *Chem. Eng. J.*, 2021, **415**, 128824.
381 S. Wang, Y. Li, S. Dai and D. E. Jiang, *Angew. Chem., Int. Ed.*, 2020, **59**, 19645–19648.
382 E. Davarpanah, M. Armandi, S. Hernández, D. Fino, R. Arletti, S. Bensaid and M. Piumetti, *J. Environ. Manage.*, 2020, **275**, 111229.
383 F. Raganati, R. Chirone and P. Ammendola, *Ind. Eng. Chem. Res.*, 2020, **59**, 3593–3605.
384 H. Tun and C.-C. Chen, *Adsorption*, 2021, **27**, 979–989.
385 J. Young, E. García-Díez, S. Garcia and M. Van Der Spek, *Energy Environ. Sci.*, 2021, **14**, 5377–5394.
386 J. M. Kolle, M. Fayaz and A. Sayari, *Chem. Rev.*, 2021, **121**, 7280–7345.
387 S. Loganathan, M. Tikmani, S. Edubilli, A. Mishra and A. K. Ghoshal, *Chem. Eng. J.*, 2014, **256**, 1–8.
388 G. Song, X. Zhu, R. Chen, Q. Liao, Y.-D. Ding and L. Chen, *Chem. Eng. J.*, 2016, **283**, 175–183.
389 Y. Guo, C. Zhao and C. Li, *Chem. Eng. Technol.*, 2015, **38**, 891–899.
390 S. I. Garcés-Polo, J. Villarroel-Rocha, K. Sapag, S. Korili and A. Gil, *Chem. Eng. J.*, 2016, **302**, 278–286.
391 Z. Cai, C. E. Bien, Q. Liu and C. R. Wade, *Chem. Mater.*, 2020, **32**, 4257–4264.
392 W. A. Thompson, E. Sanchez Fernandez and M. M. Maroto-Valer, *ACS Sustainable Chem. Eng.*, 2020, **8**, 4677–4692.
393 C. Ma, T. Lu, J. Shao, J. Huang, X. Hu and L. Wang, *Sep. Purif. Technol.*, 2022, **281**, 119899.
394 E. D. Revellame, D. L. Fortela, W. Sharp, R. Hernandez and M. E. Zappi, *Cleaner Eng. Technol.*, 2020, **1**, 100032.
395 R. Ezzati, *Chem. Eng. J.*, 2020, **392**, 123705.
396 S. Cao, L. Li, M. Guo, W. Xu, T. Liu, T. Xing, Z. Li, M. Wang, M. Wang and M. Wu, *Chem. Mater.*, 2023, **35**, 10119–10128.
397 W. Chen, X. Wang, Z. Hashisho, M. Feizbakhshan, P. Shariaty, S. Niknaddaf and X. Zhou, *Microporous Mesoporous Mater.*, 2019, **280**, 57–65.
398 Y. Liu, Y. Chen, L. Tian and R. Hu, *J. Porous Mater.*, 2017, **24**, 583–589.
399 B. Guo, J. Zhang, Y. Wang, X. Qiao, J. Xiang and Y. Jin, *Energy*, 2023, **263**, 125764.
400 M. Abunowara, M. A. Bustam, S. Sufian, M. Babar, U. Eldemerdash, A. Mukhtar, S. Ullah, M. A. Assiri, A. G. Al-Sehemi and S. S. Lam, *Environ. Res.*, 2023, **218**, 114905.
401 X. Ma, X. Wang and C. Song, *J. Am. Chem. Soc.*, 2009, **131**, 5777–5783.
402 F. Martínez, R. Sanz, G. Orcajo, D. Briones and V. Yángüez, *Chem. Eng. Sci.*, 2016, **142**, 55–61.
403 L. Lin, T. Ju, S. Han, F. Meng, J. Li and J. Jiang, *Sep. Purif. Technol.*, 2023, **322**, 124346.
404 D. Wu, F. Xu, B. Sun, R. Fu, H. He and K. Matyjaszewski, *Chem. Rev.*, 2012, **112**, 3959–4015.
405 A. Goeppert, M. Czaun, R. B. May, G. S. Prakash, G. A. Olah and S. Narayanan, *J. Am. Chem. Soc.*, 2011, **133**, 20164–20167.
406 P. Madejski, K. Chmiel, N. Subramanian and T. Kuś, *Energies*, 2022, **15**, 887.
407 M. Karimi, M. Shirzad, J. A. Silva and A. E. Rodrigues, *J. $CO_2$* Util., 2022, **57**, 101890.
408 A. A. Abd, S. Z. Naji, A. S. Hashim and M. R. Othman, *J. Environ. Chem. Eng.*, 2020, **8**, 104142.
409 F. Raganati, F. Miccio and P. Ammendola, *Energy Fuels*, 2021, **35**, 12845–12868.
410 V. K. Singh and E. A. Kumar, *Energy Procedia*, 2016, **90**, 316–325.
411 J. A. H. Lalinde, P. Roongruangsree, J. Ilsemann, M. Baeumer and J. Kopyscinski, *Chem. Eng. J.*, 2020, **390**, 124629.
412 V. Tartaglione, C. Farges and J. Sabatier, *Phys. Rev. E*, 2020, **102**, 052102.
413 Q. Liu, J. Shi, S. Zheng, M. Tao, Y. He and Y. Shi, *Ind. Eng. Chem. Res.*, 2014, **53**, 11677–11683.

414 Z. Gu, X. Wang, P. Huang, Y. Huang, X. He, X. Wei, J. Yue, J. Jiang and C. Zhao, *Process Saf. Environ. Prot.*, 2022, **160**, 573–583.
415 J. Wang, H. Huang, M. Wang, L. Yao, W. Qiao, D. Long and L. Ling, *Ind. Eng. Chem. Res.*, 2015, **54**, 5319–5327.
416 J. Ma, N. Sun, X. Zhang, N. Zhao, F. Xiao, W. Wei and Y. Sun, *Catal. Today*, 2009, **148**, 221–231.
417 C. Costentin, S. Drouet, M. Robert and J.-M. Savéant, *Science*, 2012, **338**, 90–94.
418 F. Vega, F. Baena-Moreno, L. M. G. Fernández, E. Portillo, B. Navarrete and Z. Zhang, *Appl. Energy*, 2020, **260**, 114313.
419 B. Aghel, S. Janati, S. Wongwises and M. S. Shadloo, *Int. J. Greenhouse Gas Control*, 2022, **119**, 103715.
420 M. Younas, M. Rezakazemi, M. Daud, M. B. Wazir, S. Ahmad, N. Ullah and S. Ramakrishna, *Prog. Energy Combust. Sci.*, 2020, **80**, 100849.
421 Z. Zhang, Q. Ding, J. Cui, X. Cui and H. Xing, *Sci. China Mater.*, 2020, **64**, 691–697.
422 Z. Cheng, S. Li, Y. Liu, Y. Zhang, Z. Ling, M. Yang, L. Jiang and Y. Song, *Renewable Sustainable Energy Rev.*, 2022, **154**, 111806.
423 S. Sinehbaghizadeh, A. Saptoro and A. H. Mohammadi, *Prog. Energy Combust. Sci.*, 2022, **93**, 101026.
424 K. M. Diederichsen, R. Sharifian, J. S. Kang, Y. Liu, S. Kim, B. M. Gallant, D. Vermaas and T. A. Hatton, *Nat. Rev. Methods Primers*, 2022, **2**, 68.
425 M. Rahimi, A. Khurram, T. A. Hatton and B. Gallant, *Chem. Soc. Rev.*, 2022, **51**, 8676–8695.
426 Y. Bi and Y. Ju, *Front. Energy*, 2022, **16**, 793–811.
427 Z. Wang, S. Su, Z. Yin, X. An, Z. Zhao, Y. Chen, T. Liu, Y. Wang, S. Hu and J. Xiang, *Chem. Ind. Eng. Prog.*, 2021, **40**, 2318.
428 A. Sharma, J. Jindal, A. Mittal, K. Kumari, S. Maken and N. Kumar, *Environ. Chem. Lett.*, 2021, **19**, 875–910.
429 J. H. Park, J. Yang, D. Kim, H. Gim, W. Y. Choi and J. W. Lee, *Chem. Eng. J.*, 2022, **427**, 130980.
430 O. Akeeb, L. Wang, W. Xie, R. Davis, M. Alkasrawi and S. Toan, *J. Environ. Manage.*, 2022, **313**, 115026.
431 J. Chen, Y. Xu, P. Liao, H. Wang and H. Zhou, *Carbon Capture Sci. Technol.*, 2022, **4**, 100052.
432 B. Dziejarski, J. Serafin, K. Andersson and R. Krzyżyńska, *Mater. Today Sustainability*, 2023, 100483.
433 L. B. Hamdy, C. Goel, J. A. Rudd, A. R. Barron and E. Andreoli, *Mater. Adv.*, 2021, **2**, 5843–5880.
434 O. Gutiérrez-Sánchez, B. Bohlen, N. Daems, M. Bulut, D. Pant and T. Breugelmans, *ChemElectroChem*, 2022, **9**, e202101540.
435 S. E. Renfrew, D. E. Starr and P. Strasser, *ACS Catal.*, 2020, **10**, 13058–13074.
436 X. Wang and C. Song, *Front. Energy Res.*, 2020, **8**, 560849.
437 W. Y. Hong, *Carbon Capture Sci. Technol.*, 2022, **3**, 100044.
438 M. Mirzaei, B. Mokhtarani, A. Badiei and A. Sharifi, *Chem. Eng. Technol.*, 2018, **41**, 1272–1281.
439 S. Deutz and A. Bardow, *Nat. Energy*, 2021, **6**, 203–213.
440 M. Ozka, S. P. Nayak and A. D. Ruiz, *et al.*, *iScience*, 2022, **25**(4), 103990.
441 G. Rim, F. Kong, M. Song, C. Rosu, P. Priyadarshini, R. P. Lively and C. W. Jones, *JACS Au*, 2022, **2**, 380–393.
442 X. Xu, M. B. Myers, F. G. Versteeg, B. Pejcic, C. Heath and C. D. Wood, *Chem. Commun.*, 2020, **56**, 7151–7154.
443 H. E. Holmes, S. Banerjee, A. Vallace, R. P. Lively, C. W. Jones and M. J. Realff, *Energy Environ. Sci.*, 2024, **17**, 4544–4559.
444 N. McQueen, P. Psarras, H. Pilorgé, S. Liguori, J. He, M. Yuan, C. M. Woodall, K. Kian, L. Pierpoint and J. Jurewicz, *Environ. Sci. Technol.*, 2020, **54**, 7542–7551.
445 S. M. Wilson and F. H. Tezel, *Ind. Eng. Chem. Res.*, 2020, **59**, 8783–8794.
446 S. M. Wilson, *Sep. Purif. Technol.*, 2022, **294**, 121186.
447 L. Jiang, W. Liu, R. Wang, A. Gonzalez-Diaz, M. Rojas-Michaga, S. Michailos, M. Pourkashanian, X. Zhang and C. Font-Palma, *Prog. Energy Combust. Sci.*, 2023, **95**, 101069.
448 J. M. Findley and D. S. Sholl, *J. Phys. Chem. C*, 2021, **125**, 24630–24639.
449 S. Kumar, R. Srivastava and J. Koh, *J. $CO_2$* Util., 2020, **41**, 101251.
450 X. Shi, H. Xiao, H. Azarabadi, J. Song, X. Wu, X. Chen and K. S. Lackner, *Angew. Chem., Int. Ed.*, 2020, **59**, 6984–7006.
451 W. Rahmah, G. Kadja, M. Mahyuddin, A. Saputro, H. Dipojono and I. Wenten, *J. Environ. Chem. Eng.*, 2022, **10**, 108707.
452 D. Fu and M. E. Davis, *Chem. Soc. Rev.*, 2022, **51**, 9340–9370.
453 P. Harlick, PhD thesis, Université d'Ottawa/University of Ottawa, 2015.
454 L. Bertsch and H. Habgood, *J. Phys. Chem.*, 1963, **67**, 1621–1628.
455 P. Murge, S. Dinda and S. Roy, *Langmuir*, 2019, **35**, 14751–14760.
456 M. Debost, P. B. Klar, N. Barrier, E. B. Clatworthy, J. Grand, F. Laine, P. Brázda, L. Palatinus, N. Nesterenko and P. Boullay, *Angew. Chem., Int. Ed.*, 2020, **59**, 23491–23495.
457 M. Shen, F. Kong, W. Guo, Z. Zuo, T. Gao, S. Chen, L. Tong, P. Zhang, L. Wang and P. K. Chu, *Chem. Eng. J.*, 2024, **479**, 147923.
458 H. Lee, D. Xie, S. I. Zones and A. Katz, *J. Am. Chem. Soc.*, 2023, **146**, 68–72.
459 G. Deng, K. Cheng, B. Meng, X. Shi, X. Liu, Y. Zhou and J. Wang, *Sep. Purif. Technol.*, 2024, **340**, 126764.
460 C.-H. Ho and F. Paesani, *ACS Appl. Mater. Interfaces*, 2023, **15**, 48287–48295.
461 X. Shi, G. A. Lee, S. Liu, D. Kim, A. Alahmed, A. Jamal, L. Wang and A.-H. A. Park, *Mater. Today*, 2023, **65**, 207–226.
462 L. Li, H. S. Jung, J. W. Lee and Y. T. Kang, *Renewable Sustainable Energy Rev.*, 2022, **162**, 112441.
463 Z. Du, X. Nie, S. Deng, L. Zhao, S. Li, Y. Zhang and J. Zhao, *Microporous Mesoporous Mater.*, 2020, **298**, 110053.
464 A. S. Palakkal and R. S. Pillai, *J. Phys. Chem. C*, 2020, **124**, 16975–16989.
465 L. Lei, Y. Cheng, C. Chen, M. Kosari, Z. Jiang and C. He, *J. Colloid Interface Sci.*, 2022, **612**, 132–145.

 

466 A. R. Millward and O. M. Yaghi, *J. Am. Chem. Soc.*, 2005, **127**, 17998–17999.
467 H. Furukawa, N. Ko, Y. B. Go, N. Aratani, S. B. Choi, E. Choi, A. Ö. Yazaydin, R. Q. Snurr, M. O'Keeffe and J. Kim, *Science*, 2010, **329**, 424–428.
468 S. Gaikwad, Y. Kim, R. Gaikwad and S. Han, *J. Environ. Chem. Eng.*, 2021, **9**, 105523.
469 J. Y. Jung, F. Karadas, S. Zulfiqar, E. Deniz, S. Aparicio, M. Atilhan, C. T. Yavuz and S. M. Han, *Phys. Chem. Chem. Phys.*, 2013, **15**, 14319–14327.
470 K. M. C. Santos, R. J. O. Santos, M. M. D. A. Alves, J. F. De Conto, G. R. Borges, C. Dariva, S. M. Egues, C. C. Santana and E. Franceschi, *J. Solid State Chem.*, 2019, **269**, 320–327.
471 J. A. Coelho, A. M. Ribeiro, A. F. Ferreira, S. M. Lucena, A. E. Rodrigues and D. C. D. Azevedo, *Ind. Eng. Chem. Res.*, 2016, **55**, 2134–2143.
472 S. Nandi, S. Collins, D. Chakraborty, D. Banerjee, P. K. Thallapally, T. K. Woo and R. Vaidhyanathan, *J. Am. Chem. Soc.*, 2017, **139**, 1734–1737.
473 Z. Zhang, B. Jin, J. Liao, X. Luo and Z. Liang, *Chem. Eng. J.*, 2022, **431**, 133855.
474 B. Ghalei, K. Sakurai, Y. Kinoshita, K. Wakimoto, A. P. Isfahani, Q. Song, K. Doitomi, S. Furukawa, H. Hirao and H. Kusuda, *Nat. Energy*, 2017, **2**, 1–9.
475 M.-M. Titirici, R. J. White, N. Brun, V. L. Budarin, D. S. Su, F. Del Monte, J. H. Clark and M. J. MacLachlan, *Chem. Soc. Rev.*, 2015, **44**, 250–290.
476 Y. Fang, Y. Liu, L. Qi, Y. Xue and Y. Li, *Chem. Soc. Rev.*, 2022, **51**, 2681–2709.
477 S. N. Talapaneni, G. Singh, I. Y. Kim, K. AlBahily, A. A. H. Al-Muhtaseb, A. S. Karakoti, E. Tavakkoli and A. Vinu, *Adv. Mater.*, 2020, **32**, 1904635.
478 U. Kamran and S.-J. Park, *J. Cleaner Prod.*, 2021, **290**, 125776.
479 S. He, G. Chen, H. Xiao, G. Shi, C. Ruan, Y. Ma, H. Dai, B. Yuan, X. Chen and X. Yang, *J. Colloid Interface Sci.*, 2021, **582**, 90–101.
480 M. E. Casco, M. Martínez-Escandell, J. Silvestre-Albero and F. Rodríguez-Reinoso, *Carbon*, 2014, **67**, 230–235.
481 H. M. Coromina, D. A. Walsh and R. Mokaya, *J. Mater. Chem. A*, 2016, **4**, 280–289.
482 M. D. Esrafili and P. Mousavian, *J. Mol. Graphics Modell.*, 2022, **111**, 108112.
483 M. D. Esrafili and S. Abolghasemzadeh, *Comput. Theor. Chem.*, 2022, **1208**, 113557.
484 C. P. Dineen, Direct air capture (DAC): capturing $CO_2$ from the air–design of a lab-scale PVSA system and the development of a carbon-based adsorbent material for atmospheric $CO_2$ capture, 2020, **https://hdl.handle.net/10468/10012**.
485 T. Tang, Z. Wang and J. Guan, *Coord. Chem. Rev.*, 2023, **492**, 215288.
486 C. Xiao, Q. Song, Q. Shen, T. Wang and W. Xie, *Composites, Part B*, 2022, **239**, 109946.
487 S. Candamano, A. Policicchio, G. Conte, R. Abarca, C. Algieri, S. Chakraborty, S. Curcio, V. Calabro, F. Crea and R. Agostino, *J. Cleaner Prod.*, 2022, **330**, 129843.
488 H. Li, F. Zheng, J. Wang, J. Zhou, X. Huang, L. Chen, P. Hu, J.-M. Gao, Q. Zhen and S. Bashir, *Chem. Eng. J.*, 2020, **390**, 124513.
489 J. Chen, G. Xiao, G. Duan, Y. Wu, X. Zhao and X. Gong, *Chem. Eng. J.*, 2021, **421**, 127743.
490 Y. Qiu, H. Yang, Y. Cheng and Y. Lin, *Composites, Part A*, 2022, **154**, 106772.
491 W. Xiao, M. Cheng, Y. Liu, J. Wang, G. Zhang, Z. Wei, L. Li, L. Du, G. Wang and H. Liu, *ACS Catal.*, 2023, **13**, 1759–1790.
492 X. Shi, Y. Lin and X. Chen, *MRS Bull.*, 2022, **47**, 405–415.
493 Y. Wei, T. Zhao, J. Wang, Y. Chen, Q. Wang, X. Liu and Y. Zhao, *Ind. Eng. Chem. Res.*, 2023, **62**, 7635–7641.
494 H. Li, Y. Qi, J. Chen, J. Wang, M. Yang and H. Qiu, *Chin. Chem. Lett.*, 2024, **35**, 109659.
495 J.-R. Li, J. Yu, W. Lu, L.-B. Sun, J. Sculley, P. B. Balbuena and H.-C. Zhou, *Nat. Commun.*, 2013, **4**, 1538.
496 H. J. Choi, D. Jo, J. G. Min and S. B. Hong, *Angew. Chem., Int. Ed.*, 2021, **60**, 4307–4314.
497 P. Du, Y. Zhang, X. Wang, S. Canossa, Z. Hong, G. Nénert, W. Jin and X. Gu, *Nat. Commun.*, 2022, **13**, 1427.
498 M. Kim, J. W. Lee, S. Kim and Y. T. Kang, *J. Cleaner Prod.*, 2022, **337**, 130597.
499 M. Shen, F. Kong, W. Guo, Z. Zuo, T. Gao, S. Chen, L. Tong, P. Zhang, L. Wang, P. K. Chu and Y. Ding, *Chem. Eng. J.*, 2024, **479**, 147923.
500 M. Shen, F. Kong, W. Guo, Z. Zuo, C. Guo, L. Tong, S. Yin, L. Wang, S. Kawi, P. K. Chu and Y. Ding, *Adv. Funct. Mater.*, 2024, **34**(49), 2408922.
501 T. Ghanbari, F. Abnisa and W. M. A. W. Daud, *Sci. Total Environ.*, 2020, **707**, 135090.
502 S. Ullah, M. A. Bustam, A. G. Al-Sehemi, M. A. Assiri, F. A. A. Kareem, A. Mukhtar, M. Ayoub and G. Gonfa, *Microporous Mesoporous Mater.*, 2020, **296**, 110002.
503 L. Qin, Y. Li, F. Liang, L. Li, Y. Lan, Z. Li, X. Lu, M. Yang and D. Ma, *Microporous Mesoporous Mater.*, 2022, **341**, 112098.
504 L. Z. Cai, Z. Z. Yao, S. J. Lin, M. S. Wang and G. C. Guo, *Angew. Chem., Int. Ed.*, 2021, **60**, 18223–18230.
505 Y. Shi, Y. Xie, H. Cui, Y. Ye, H. Wu, W. Zhou, H. Arman, R. B. Lin and B. Chen, *Adv. Mater.*, 2021, **33**, 2105880.
506 R. Ahmed, G. Liu, B. Yousaf, Q. Abbas, H. Ullah and M. U. Ali, *J. Cleaner Prod.*, 2020, **242**, 118409.
507 M. M. Sabzehmeidani, S. Mahnaee, M. Ghaedi, H. Heidari and V. A. Roy, *Mater. Adv.*, 2021, **2**, 598–627.
508 X. Jin, T. Foller, X. Wen, M. B. Ghasemian, F. Wang, M. Zhang, H. Bustamante, V. Sahajwalla, P. Kumar and H. Kim, *Adv. Mater.*, 2020, **32**, 1907580.
509 H. Guo, G. Kong, G. Yang, J. Pang, Z. Kang, S. Feng, L. Zhao, L. Fan, L. Zhu and A. Vicente, *Angew. Chem.*, 2020, **132**, 6343–6347.
510 X. Ma, C. Su, B. Liu, Q. Wu, K. Zhou, Z. Zeng and L. Li, *Sep. Purif. Technol.*, 2021, **259**, 118065.
511 L. Spessato, V. A. Duarte, J. M. Fonseca, P. A. Arroyo and V. C. Almeida, *J. $CO_2$ Util.*, 2022, **61**, 102013.
512 J. Zhong, X. Yang, Z. Wu, B. Liang, Y. Huang and T. Zhang, *Chem. Soc. Rev.*, 2020, **49**, 1385–1413.

513 E. Boutin, L. Merakeb, B. Ma, B. Boudy, M. Wang, J. Bonin, E. Anxolabéhère-Mallart and M. Robert, *Chem. Soc. Rev.*, 2020, **49**, 5772–5809.
514 D.-H. Nam, P. De Luna, A. Rosas-Hernández, A. Thevenon, F. Li, T. Agapie, J. C. Peters, O. Shekhah, M. Eddaoudi and E. H. Sargent, *Nat. Mater.*, 2020, **19**, 266–276.
515 S. Zhang, Q. Fan, R. Xia and T. J. Meyer, *Acc. Chem. Res.*, 2020, **53**, 255–264.
516 J. Ashok, S. Pati, P. Hongmanorom, Z. Tianxi, C. Junmei and S. Kawi, *Catal. Today*, 2020, **356**, 471–489.
517 X. Jiang, X. Nie, X. Guo, C. Song and J. G. Chen, *Chem. Rev.*, 2020, **120**, 7984–8034.
518 Y. Liu, D. Deng and X. Bao, *Chem*, 2020, **6**, 2497–2514.
519 Z.-Z. Wu, F.-Y. Gao and M.-R. Gao, *Energy Environ. Sci.*, 2021, **14**, 1121–1139.
520 P.-P. Yang, X.-L. Zhang, F.-Y. Gao, Y.-R. Zheng, Z.-Z. Niu, X. Yu, R. Liu, Z.-Z. Wu, S. Qin, L.-P. Chi, Y. Duan, T. Ma, X.-S. Zheng, J.-F. Zhu, H.-J. Wang, M.-R. Gao and S.-H. Yu, *J. Am. Chem. Soc.*, 2020, **142**, 6400–6408.
521 S. H. Lee, J. C. Lin, M. Farmand, A. T. Landers, J. T. Feaster, J. E. Avilés Acosta, J. W. Beeman, Y. Ye, J. Yano, A. Mehta, R. C. Davis, T. F. Jaramillo, C. Hahn and W. S. Drisdell, *J. Am. Chem. Soc.*, 2021, **143**, 588–592.
522 T.-C. Chou, C.-C. Chang, H.-L. Yu, W.-Y. Yu, C.-L. Dong, J.-J. Velasco-Vélez, C.-H. Chuang, L.-C. Chen, J.-F. Lee, J.-M. Chen and H.-L. Wu, *J. Am. Chem. Soc.*, 2020, **142**, 2857–2867.
523 F. Dattila, R. García-Muelas and N. López, *ACS Energy Lett.*, 2020, **5**, 3176–3184.
524 H. Jeong, *Angew. Chem.*, 2020, **132**, 20872–20877.
525 J. Timoshenko, *Nat. Catal.*, 2022, **5**, 259–267.
526 A. C. Deacy, *Nat. Chem.*, 2020, **12**, 372–380.
527 J. Zhu, P. Wang, X. Zhang, G. Zhang, R. Li, W. Li, T. P. Senftle, W. Liu, J. Wang, Y. Wang, A. Zhang, Q. Fu, C. Song and X. Guo, *Sci. Adv.*, 2022, **8**, eabm3629.
528 Q. Lu, *Nano Energy*, 2016, **29**, 439–456.
529 L. Zhang, *Angew. Chem., Int. Ed.*, 2017, **56**, 11326–11353.
530 S. A. Ali, I. Sadiq and T. Ahmad, *Mater. Today Sustainability*, 2023, **24**, 100587.
531 Y. Li, S. Li and H. Huang, *Chem. Eng. J.*, 2023, **457**, 141179.
532 L. Xie, Y. Jiang, W. Zhu, S. Ding, Y. Zhou and J.-J. Zhu, *Chem. Sci.*, 2023, **14**, 13629–13660.
533 H. Sabet-Sarvestani, M. Izadyar, H. Eshghi and N. Noroozi-Shad, in *Carbon Dioxide Utilization to Sustainable Energy and Fuels*, ed. Inamuddin, R. Boddula, M. I. Ahamed and A. Khan, Springer International Publishing, Cham, 2022, pp. 153–220, DOI: **10.1007/978-3-030-72877-9_8**.
534 K. Rossi, *Acc. Chem. Res.*, 2022, **55**, 629–637.
535 L. Fan, C. Xia, P. Zhu, Y. Lu and H. Wang, *Nat. Commun.*, 2020, **11**, 3633.
536 J. Tian, Y. Ren, L. Liu, Q. Guo, N. Sha and Z. Zhao, *Mater. Res. Express*, 2020, **7**, 085504.
537 X. Jiang, J. Huang, Z. Bi, W. Ni, G. Gurzadyan, Y. Zhu and Z. Zhang, *Adv. Mater.*, 2022, **34**, 2109330.
538 W. Zou, Y. Cheng, Y. X. Ye, X. Wei, Q. Tong, L. Dong and G. Ouyang, *Angew. Chem., Int. Ed.*, 2023, **62**, e202313392.
539 E. P. Delmo, *J. Phys. Chem. C*, 2023, **127**, 4496–4510.
540 X. Zhi, *Energy Environ. Sci.*, 2021, **14**, 3912–3930.
541 H. An, *Angew. Chem., Int. Ed.*, 2021, **60**, 16576–16584.
542 C. Ren, *J. Am. Chem. Soc.*, 2023, **145**, 28276–28283.
543 E. P. Delmo, *J. Am. Chem. Soc.*, 2024, **146**, 1935–1945.
544 C. Xiao, *ACS Nano*, 2021, **15**, 7975–8000.
545 B. Zhang and J. Jiang, *Energy Environ. Mater.*, 2024, **7**(6), e12738.
546 T. Möller, *Angew. Chem.*, 2020, **132**, 18130–18139.
547 T. Otroshchenko, *Chem. Soc. Rev.*, 2021, **50**, 473–527.
548 H. Liu, Y. Zhu, J. Ma, Z. Zhang and W. Hu, *Adv. Funct. Mater.*, 2020, **30**, 1910534.
549 N. W. Kinzel, *Angew. Chem., Int. Ed.*, 2021, **60**, 11628–11686.
550 F. Franco, *Chem. Soc. Rev.*, 2020, **49**, 6884–6946.
551 Y. Xie, *Nat. Catal.*, 2022, **5**, 564–570.
552 J. Gu, *Nat. Catal.*, 2022, **5**, 268–276.
553 D. Gao, *ACS Energy Lett.*, 2021, **6**, 713–727.
554 S. Zhu, E. P. Delmo, T. Li, X. Qin, J. Tian, L. Zhang and M. Shao, *Adv. Mater.*, 2021, **33**, 2005484.
555 F. Scholten, *Angew. Chem., Int. Ed.*, 2021, **60**, 19169–19175.
556 Y. Zhang, L.-Z. Dong, S. Li, X. Huang, J.-N. Chang, J.-H. Wang, J. Zhou, S.-L. Li and Y.-Q. Lan, *Nat. Commun.*, 2021, **12**, 6390.
557 F. Naseem, *ACS Nano*, 2020, **14**, 7734–7759.
558 Y. H. Zou, *Angew. Chem.*, 2021, **133**, 21083–21088.
559 I. Hussain, *J. Energy Chem.*, 2021, **62**, 377–407.
560 G. I. Siakavelas, N. D. Charisiou, S. AlKhoori, A. A. AlKhoori, V. Sebastian, S. J. Hinder, M. A. Baker, I. Yentekakis, K. Polychronopoulou and M. A. Goula, *Appl. Catal., B*, 2021, **282**, 119562.
561 A. Wagner, C. D. Sahm and E. Reisner, *Nat. Catal.*, 2020, **3**, 775–786.
562 M. Miyaji, *ACS Catal.*, 2024, **14**, 10403–10411.
563 T. Kajiwara, *Angew. Chem., Int. Ed.*, 2016, **55**, 2697–2700.
564 T. Nakajima, *J. Am. Chem. Soc.*, 2016, **138**, 13818–13821.
565 P. Hou, W. Song, X. Wang, Z. Hu and P. Kang, *Small*, 2020, **16**, 2001896.
566 A. Jangam, *Catal. Today*, 2020, **358**, 3–29.
567 P. Zhu, *Nat. Catal.*, 2021, **4**, 943–951.
568 Y. J. Sa, *Chem. Soc. Rev.*, 2020, **49**, 6632–6665.
569 J. E. Huang, *Science*, 2021, **372**, 1074–1078.
570 Y. C. Tan, K. B. Lee, H. Song and J. Oh, *Joule*, 2020, **4**, 1104–1120.
571 A. S. Malkani, *ACS Catal.*, 2020, **10**, 14871–14876.
572 Z. Li, Q. Lin, M. Li, J. Cao, F. Liu, H. Pan, Z. Wang and S. Kawi, *Renewable Sustainable Energy Rev.*, 2020, **134**, 110312.
573 A. M. Bahmanpour, M. Signorile and O. Kröcher, *Appl. Catal., B*, 2021, **295**, 120319.
574 R. I. Masel, *Nat. Nanotechnol.*, 2021, **16**, 118–128.
575 R. E. Vos, K. E. Kolmeijer, T. S. Jacobs, W. van der Stam, B. M. Weckhuysen and M. T. Koper, *ACS Catal.*, 2023, **13**, 8080–8091.
576 Y. Chen, X. Mu, X. Luo, K. Shi, G. Yang and T. Wu, *Energy Technol.*, 2020, **8**, 1900750.
577 R. C. Rabelo-Neto, M. P. Almeida, E. B. Silveira, M. Ayala, C. D. Watson, J. Villarreal, D. C. Cronauer, A. J. Kropf,

 

M. Martinelli and F. B. Noronha, *Appl. Catal., B*, 2022, **315**, 121533.
578 A. Cherevotan, B. Ray, S. R. Churipard, K. Kaur, U. K. Gautam, C. P. Vinod and S. C. Peter, *Appl. Catal., B*, 2022, **317**, 121692.
579 F. Yuan, *Catal. Today*, 2021, **371**, 142–149.
580 C. Song, *ACS Catal.*, 2020, **10**, 10364–10374.
581 J. Wang, *Catal. Today*, 2021, **365**, 341–347.
582 B. G. Schieweck, *ACS Catal.*, 2020, **10**, 3890–3894.
583 H. Li, *Angew. Chem.*, 2021, **133**, 14450–14454.
584 Y. Xue, Y. Guo, H. Cui and Z. Zhou, *Small Methods*, 2021, **5**, 2100736.
585 T. Fan, *J. Phys. Chem. Lett.*, 2021, **12**, 10486–10496.
586 S. Saeidi, S. Najari, V. Hessel, K. Wilson, F. J. Keil, P. Concepción, S. L. Suib and A. E. Rodrigues, *Prog. Energy Combust. Sci.*, 2021, **85**, 100905.
587 T. Yan, *Chem. Rev.*, 2023, **123**, 10530–10583.
588 G. Gadikota, *Nat. Rev. Chem.*, 2020, **4**, 78–89.
589 S. M. Chun, D. H. Shin, S. H. Ma, G. W. Yang and Y. C. Hong, *Catalysts*, 2019, **9**, 292.
590 B. Jung, S. Park, C. Lim, W. H. Lee, Y. Lim, J. Na, C.-J. Lee, H.-S. Oh and U. Lee, *Chem. Eng. J.*, 2021, **424**, 130265.
591 Y. R. Lu, D. Pashchenko and P. A. Nikrityuk, *Chem. Eng. Sci.*, 2021, **238**, 116565.
592 D. Jia, L. Ma, Y. Wang, W. Zhang, J. Li, Y. Zhou and J. Wang, *Chem. Eng. J.*, 2020, **390**, 124652.
593 M. S. Kodaimati, R. Gao, S. E. Root and G. M. Whitesides, *Chem. Catal.*, 2022, **2**, 797–815.
594 B. A. Zhang, *ACS Cent. Sci.*, 2019, **5**, 1097–1105.
595 K. Nakagawa, *J. Catal.*, 2001, **203**, 87–93.
596 J. Wang, K. Zhang, A. Bogaerts and V. Meynen, *Chem. Eng. J.*, 2023, **464**, 142574.
597 Z. Xing, *ACS Energy Lett.*, 2021, **6**, 1694–1702.
598 T. Wang, X. Sang, W. Zheng, B. Yang, S. Yao, C. Lei, Z. Li, Q. He, J. Lu and L. Lei, *Adv. Mater.*, 2020, **32**, 2002430.
599 W.-J. Jang, J.-O. Shim, H.-M. Kim, S.-Y. Yoo and H.-S. Roh, *Catal. Today*, 2019, **324**, 15–26.
600 A. Pavlišič, M. Huš, A. Prašnikar and B. Likozar, *J. Cleaner Prod.*, 2020, **275**, 122958.
601 J. Grams and A. M. Ruppert, *Catalysts*, 2021, **11**, 265.
602 J. Chen and L. Wang, *Adv. Mater.*, 2022, **34**, 2103900.
603 M. Qing, S. Lei, F. Kong, L. Liu, W. Zhang, L. Wang, T. Guo, S. Su, S. Hu and Y. Wang, *Fuel*, 2022, **313**, 122790.
604 S. A. Theofanidis, *J. Catal.*, 2020, **388**, 52–65.
605 M. W. Ackley, *Adsorption*, 2019, **25**, 1437–1474.
606 D. Xiang, P. Li, X. Yuan, P. Cui and W. Huang, *J. Cleaner Prod.*, 2020, **258**, 120910.
607 S.-J. Chen, *J. Taiwan Inst. Chem. Eng.*, 2021, **127**, 56–68.
608 R. Sidhikku Kandath Valappil, *J. Ind. Eng. Chem.*, 2021, **98**, 103–129.
609 J. Xu, T. Wang, Q. Chen, S. Zhang and J. Tan, *Front. Mech. Eng.*, 2020, **15**, 24–42.
610 A. F. Young, *Ind. Eng. Chem. Res.*, 2021, **60**, 14830–14844.
611 M. H. Hamayun, N. Ramzan, M. Hussain and M. Faheem, *Energies*, 2020, **13**, 6361.
612 Y. Tao, W. Tian, L. Kong, S. Sun and C. Fan, *Energy*, 2022, **261**, 125365.
613 M. Cheng, P. Verma, Z. Yang and R. L. Axelbaum, *Sep. Purif. Technol.*, 2022, **302**, 122086.
614 K. Wang, L. Tong, S. Yin, Y. Yang, P. Zhang, C. Liu, Z. Zuo, L. Wang and Y. Ding, *Energy*, 2024, **288**, 129720.
615 F. Kong, Y. Liu and L. Tong, *et al.*, Optimization of co-production air separation unit based on MILP under multi-product deterministic demand, *Appl. Energy*, 2022, **325**, 119850.
616 P. Zhang, Z. Wang and L. Wang, Performance study on an energy-efficient TSA air-purification process utilizing compression heat regeneration, *Sep. Purif. Technol.*, 2024, **349**, 127854.
617 Y. Yang, Y. Chen and Z. Xu, *et al.*, A three-bed six-step TSA cycle with heat carrier gas recycling and its model-based performance assessment for gas drying, *Sep. Purif. Technol.*, 2020, **237**, 116335.
618 P. Zhang, J. Liang and Y. Yang, *et al.*, A new heating system for the air pre-purification of air separation units, *Appl. Therm. Eng.*, 2023, **226**, 120194.
619 P. Zhang, *Ind. Eng. Chem. Res.*, 2013, **52**, 15912–15922.
620 G. V. Brigagão, L. de Oliveira Arinelli and J. L. de Medeiros, *et al.*, *Sep. Purif. Technol.*, 2020, **248**, 116969.
621 S. U. Rege, *Chem. Eng. Sci.*, 2000, **55**, 4827–4838.
622 S. U. Rege, *Chem. Eng. Sci.*, 2001, **56**, 2745–2759.
623 J. Wu, *Cryogenics*, 2018, **91**, 128–135.
624 C.-F. Song, *Int. J. Greenhouse Gas Control*, 2013, **13**, 26–33.
625 A. M. Yousef, W. M. El-Maghlany and Y. A. Eldrainy, *et al.*, Low-temperature distillation process for $CO_2$/$CH_4$ separation: a study for avoiding $CO_2$ freeze-out, *J. Heat Transfer*, 2018, **140**(4), 042001.
626 X. Pan, *Greenhouse Gases: Sci. Technol.*, 2013, **3**, 8–20.
627 Council, Safety British Cryogenics, *Cryogenics safety manual: a guide to good practice*, Elsevier, 2013.
628 D. Clodic and M. Younes, *Greenhouse gas control technologies-6th international conference*, 2003, pp. 155–160.
629 C.-F. Song, Y. Kitamura, S.-H. Li and W.-Z. Jiang, *Int. J. Greenhouse Gas Control*, 2013, **13**, 26–33.
630 A. Majchrzak and W. Nowak, *J. $CO_2$ Util.*, 2017, **17**, 69–79.
631 A. J. Rest, *Chem. Eng. J.*, 1990, **43**, 25–31.
632 C. Song, *Renewable Sustainable Energy Rev.*, 2019, **101**, 265–278.
633 Y. Wang, *ACS Sustainable Chem. Eng.*, 2019, **7**, 3301–3308.
634 X. He, W. Guo, Z. Zuo, Y. Liu and L. Wang, *Appl. Therm. Eng.*, 2024, **250**, 123476.
635 R. Castro-Muñoz, M. Zamidi Ahmad, M. Malankowska and J. Coronas, *Chem. Eng. J.*, 2022, **446**, 137047.
636 S. Fujikawa, *Polym. J.*, 2021, **53**, 111–119.
637 C. Castel, R. Bounaceur and E. Favre, Membrane processes for direct carbon dioxide capture from air: possibilities and limitations, *Fron. Chem. Eng.*, 2021, **3**, 668867.
638 X. Zhu, *Chem. Soc. Rev.*, 2022, **51**, 6574–6651.
639 L. Jiang, W. Liu and R. Q. Wang, *et al.*, Sorption direct air capture with $CO_2$ utilization, *Prog. Energy Combust. Sci.*, 2023, **95**, 101069.
640 Y. Deng, J. Li, Y. Miao and D. Izikowitz, *Energy Rep.*, 2021, **7**, 3506–3516.
641 F. Barzagli, *ACS Sustainable Chem. Eng.*, 2020, **8**, 14013–14021.

642 F. O. Ochedi, *Environ. Chem. Lett.*, 2021, **19**, 77–109.
643 M. Shen, L. Tong and S. Yin, *et al.*, Cryogenic technology progress for $CO_2$ capture under carbon neutrality goals: A review, *Sep. Purif. Technol.*, 2022, **299**, 121734.
644 X. He, W. Guo and Y. Liu, *et al.*, Utmost substance recovery and utilization for integrated technology of air separation unit and liquid air energy storage and its saving benefits, *Renewable Energy*, 2024, **225**, 120278.
645 M. Younas, *Int. J. Environ. Sci. Technol.*, 2016, **13**, 1839–1860.
646 M. Erans, *Energy Environ. Sci.*, 2022, **15**, 1360–1405.
647 R. Hanna, A. Abdulla and Y. Xu, *et al.*, Emergency deployment of direct air capture as a response to the climate crisis, *Nat. Commun.*, 2021, **12**(1), 368.
648 G. Rim, *JACS Au*, 2022, **2**, 380–393.
649 D. Marinič and B. Likozar, Direct air capture multiscale modelling: From capture material optimization to process simulations, *J. Cleaner Prod.*, 2023, **408**, 137185.
650 C. Jeong-Potter and R. Farrauto, Feasibility study of combining direct air capture of $CO_2$ and methanation at isothermal conditions with dual function materials, *Appl. Catal., B*, 2021, **282**, 119416.
651 S. Liu, *Energy Environ. Sci.*, 2024, **17**, 1266–1278.
652 C. Jeong-Potter and R. Farrauto, *Appl. Catal., B*, 2021, **282**, 119416.
653 S. Liu, J. Zhang, F. Li, J. P. Edwards, Y. C. Xiao, D. Kim, P. Papangelakis, J. Kim, D. Elder, P. De Luna, M. Fan, G. Lee, R. K. Miao, T. Ghosh, Y. Yan, Y. Chen, Y. Zhao, Z. Guo, C. Tian, P. Li, Y. Xu, E. H. Sargent and D. Sinton, *Energy Environ. Sci.*, 2024, **17**, 1266–1278.
654 G. Rim, T. G. Feric, T. Moore and A. H. A. Park, *Adv. Funct. Mater.*, 2021, **31**, 2010047.
655 F. Liu, Y. Shen, L. Shen, Y. Zhang, W. Chen, X. Wang, Q. Wang, S. Li, S. Zhang and W. Li, *Sep. Purif. Technol.*, 2022, **286**, 120457.
656 C. Ortiz, S. García-Luna, A. Carro, R. Chacartegui and L. Pérez-Maqueda, *Renewable Sustainable Energy Rev.*, 2023, **185**, 113614.
657 S. Deutz, *Nat. Energy*, 2021, **6**, 203–213.
658 K. Z. House, A. C. Baclig, M. Ranjan, E. A. Van Nierop, J. Wilcox and H. J. Herzog, *Proc. Natl. Acad. Sci. U. S. A.*, 2011, **108**, 20428–20433.
659 M. Nilsson, *ADVANCING CARBON NEUTRALITY: Techno-economic analysis of Direct Air Capture at commercial scale*, 2024, p. 52.
660 B. Wright, *J. Pet. Technol.*, 2023, **75**, 32–37.
661 W. Jones, G. Bower and N. Pastorek, *The Landscape of Carbon Dioxide Removal and US Policies to Scale Solutions*, 2024.
662 J. Wilcox, P. C. Psarras and S. Liguori, *Environ. Res. Lett.*, 2017, **12**, 065001.
663 X. Li, T. Li, L. Liu, Z. Wang, X. Li, J. Huang, J. Huang, P. Guo and W. Xiong, *J. Cleaner Prod.*, 2023, **391**, 136119.
664 X. Wu, *Annu. Rev. Chem. Biomol. Eng.*, 2022, **13**, 279–300.
665 J. Young, N. McQueen, C. Charalambous, S. Foteinis, O. Hawrot, M. Ojeda, H. Pilorgé, J. Andresen, P. Psarras, P. Renforth, S. Garcia and M. van der Spek, *One Earth*, 2023, **6**, 899–917.
666 T. Terlouw, K. Treyer, C. Bauer and M. Mazzotti, *Environ. Sci. Technol.*, 2021, **55**, 11397–11411.
667 B. Lux, N. Schneck, B. Pfluger, W. Männer and F. Sensfuß, *Energy Strategy Rev.*, 2023, **45**, 101012.
668 S. Chowdhury, *Energy Fuels*, 2023, **37**, 10733–10757.
669 L. Sala, S. A. Zaryab, P. Chiesa and E. Martelli, *Int. J. Greenhouse Gas Control*, 2024, **136**, 104193.
670 T. Zheng, C. Liu, C. Guo, M. Zhang, X. Li, Q. Jiang, W. Xue, H. Li, A. Li and C.-W. Pao, *Nat. Nanotechnol.*, 2021, **16**, 1386–1393.
671 S. Sun, Z. Lv, Y. Qiao, C. Qin, S. Xu and C. Wu, *Carbon Capture Sci. Technol.*, 2021, **1**, 100001.
672 S. Li, P. Wang, Z. Wang, H. Cheng and K. Zhang, *Geophys. Res. Lett.*, 2023, **50**, e2022GL101431.
673 T. Tsuji, M. Sorai, M. Shiga, S. Fujikawa and T. Kunitake, *Greenhouse Gases: Sci. Technol.*, 2021, **11**, 610–618.
674 S. M. Hosseini, A. Aslani and A. Kasaeian, *Energy Rep.*, 2023, **9**, 414–436.
675 M. Aresta, A. Dibenedetto, M. Aresta and A. Dibenedetto, *The Carbon Dioxide Revolution: Challenges and Perspectives for a Global Society*, 2021, pp. 123–138.
676 Q. Niu, Q. Wang, W. Wang, J. Chang, M. Chen, H. Wang, N. Cai and L. Fan, *Energy*, 2022, **238**, 121727.
677 J. Du, H. Cao, Y. Li, Z. Yang, A. Eslamimanesh, M. Fakhroleslam, S. S. Mansouri and W. Shen, *Chem. Eng. Sci.*, 2024, **283**, 119379.
678 L. M. Romeo, I. Bolea, Y. Lara and J. M. Escosa, *Appl. Therm. Eng.*, 2009, **29**, 1744–1751.
679 S. Dilshad, A. R. Kalair and N. Khan, *Int. J. Energy Res.*, 2020, **44**, 1408–1463.
680 Y. Ma, H. Wang, F. Hong, J. Yang, Z. Chen, H. Cui and J. Feng, *Energy*, 2021, **236**, 121392.
681 S. S. Iyer, I. Bajaj, P. Balasubramanian and M. F. Hasan, *Ind. Eng. Chem. Res.*, 2017, **56**, 8622–8648.
682 P. Cheng, D. M. Thierry, H. Hendrix, K. D. Dombrowski, D. J. Sachde, M. J. Realff and J. K. Scott, *Appl. Energy*, 2023, **341**, 121076.
683 J. Young, F. Mcilwaine, B. Smit, S. Garcia and M. Van der Spek, *Chem. Eng. J.*, 2023, **456**, 141035.
684 W. H. Lee, X. Zhang, S. Banerjee, C. W. Jones, M. J. Realff and R. P. Lively, *Joule*, 2023, **7**, 1241–1259.
685 A. Rajendran, G. K. Shimizu and T. K. Woo, *Adv. Mater.*, 2024, **36**, 2301730.
686 A. Kumar, D. G. Madden, M. Lusi, K. J. Chen, E. A. Daniels, T. Curtin, J. J. Perry IV and M. J. Zaworotko, *Angew. Chem., Int. Ed.*, 2015, **54**, 14372–14377.
687 A. N. Stuckert and R. T. Yang, *Environ. Sci. Technol.*, 2011, **45**, 10257–10264.
688 O. Shekhah, Y. Belmabkhout, Z. Chen, V. Guillerm, A. Cairns, K. Adil and M. Eddaoudi, *Nat. Commun.*, 2014, **5**, 4228.
689 S. Choi, M. L. Gray and C. W. Jones, *ChemSusChem*, 2011, **4**, 628–635.
690 W. Chaikittisilp, R. Khunsupat, T. T. Chen and C. W. Jones, *Ind. Eng. Chem. Res.*, 2011, **50**, 14203–14210.
691 A. Goeppert, H. Zhang, M. Czaun, R. B. May, G. S. Prakash, G. A. Olah and S. Narayanan, *ChemSusChem*, 2014, **7**, 1386–1397.

 

692 Z. Chen, S. Deng, H. Wei, B. Wang, J. Huang and G. Yu, *ACS Appl. Mater. Interfaces*, 2013, **5**, 6937–6945.
693 M. Zhao, J. Xiao, W. Gao and Q. Wang, *J. Energy Chem.*, 2022, **68**, 401–410.
694 L. A. Darunte, A. D. Oetomo, K. S. Walton, D. S. Sholl and C. W. Jones, *ACS Sustainable Chem. Eng.*, 2016, **4**, 5761–5768.
695 P. Priyadarshini, G. Rim, C. Rosu, M. Song and C. W. Jones, *ACS Environ. Au*, 2023, **3**, 295–307.
696 F. Liu, T. Wang, H. Dong and W. Liu, *Chem. Eng. J.*, 2023, **454**, 140431.
697 Y. Ji, R. Xie, C. Wu, X. Liu, X. Zhang and L. Jiang, *J. $CO_2$* Util., 2023, **69**, 102422.
698 M. R. Ketabchi, S. Babamohammadi, W. G. Davies, M. Gorbounov and S. M. Soltani, *Carbon Capture Sci. Technol.*, 2023, **6**, 100087.
699 J. W. Lee, H. Ahn, S. Kim and Y. T. Kang, *J. Cleaner Prod.*, 2023, **390**, 136141.
700 M. Goldman, S. Kota, X. Gao, L. Katzman and R. Farrauto, *Carbon Capture Sci. Technol.*, 2023, **6**, 100094.
701 L.-a Xing, F. Yang, X. Zhong, Y. Liu, H. Lu, Z. Guo, G. Lv, J. Yang, A. Yuan and J. Pan, *Sep. Purif. Technol.*, 2023, **324**, 124470.
702 M. Zhang, T. Xu, Q. Zhao, K. Liu, D. Liang and C. Si, *Carbon Capture Sci. Technol.*, 2024, **10**, 100157.
703 Q. Grossmann, V. Stampi-Bombelli, A. Yakimov, S. Docherty, C. Copéret and M. Mazzotti, *Ind. Eng. Chem. Res.*, 2023, **62**, 13594–13611.
704 A. A. Tourzani, F. Hormozi, M. Asadollahzadeh and R. Torkaman, *Sci. Rep.*, 2023, **13**, 6173.
705 J. Sun, P. Xu, D. Gong, X. Kong, K. Fu, X. Chen, M. Qiu and Y. Fan, *Sep. Purif. Technol.*, 2023, **309**, 122978.
706 C. Kim, S. N. Talapaneni and L. Dai, *Mater. Rep.: Energy*, 2023, **3**, 100199.
707 R. Santiago, J. Lemus, C. Moya, D. Moreno, N. Alonso-Morales and J. Palomar, *ACS Sustainable Chem. Eng.*, 2018, **6**, 14178–14187.
708 R. Banerjee, A. Phan, B. Wang, C. Knobler, H. Furukawa, M. O'Keeffe and O. M. Yaghi, *Science*, 2008, **319**, 939–943.
709 Y. Y. Birdja, E. Pérez-Gallent, M. C. Figueiredo, A. J. Göttle, F. Calle-Vallejo and M. Koper, *Nat. Energy*, 2019, **4**, 732–745.
710 L.-S. Fan, L. Zeng, W. Wang and S. Luo, *Energy Environ. Sci.*, 2012, **5**, 7254–7280.
711 W. Zhang, Y. Hu, L. Ma, G. Zhu, Y. Wang, X. Xue, R. Chen, S. Yang and Z. Jin, *Adv. Sci.*, 2018, **5**, 1700275.
712 A. Raza, H. Shen and A. A. Haidry, *Appl. Catal., B*, 2020, **277**, 119239.
713 Y. Sun, Y. Zhao, Y. Zhou, L. Wang, Z. Wang, J. Qi, D. Fu, P. Zhang and K. Zhao, *Mater. Today Energy*, 2023, **37**, 101397.
714 W. Lyu, Y. Liu, J. Zhou, D. Chen, X. Zhao, R. Fang, F. Wang and Y. Li, *Angew. Chem., Int. Ed.*, 2023, **62**, e202310733.
715 Y. Huang, K. Wang, T. Guo, J. Li, X. Wu and G. Zhang, *Appl. Catal., B*, 2020, **277**, 119232.
716 H. Huang, R. Shi, Z. Li, J. Zhao, C. Su and T. Zhang, *Angew. Chem.*, 2022, **134**, e202200802.
717 Q. Guo, Y. Luo, J. Xu, L. Deng, Z. Wang and H. He, *Appl. Catal., B*, 2023, **324**, 122253.
718 K. Wang, L. Zhang, Y. Su, D. Shao, S. Zeng and W. Wang, *J. Mater. Chem. A*, 2018, **6**, 8366–8373.
719 G. Wang, J. Chen, Y. Ding, P. Cai, L. Yi, Y. Li, C. Tu, Y. Hou, Z. Wen and L. Dai, *Chem. Soc. Rev.*, 2021, **50**, 4993–5061.
720 Y. Ma, Q. Tang, W.-Y. Sun, Z.-Y. Yao, W. Zhu, T. Li and J. Wang, *Appl. Catal., B*, 2020, **270**, 118856.
721 D. Raciti and C. Wang, *ACS Energy Lett.*, 2018, **3**, 1545–1556.
722 H. Kumagai, T. Nishikawa, H. Koizumi, T. Yatsu, G. Sahara, Y. Yamazaki, Y. Tamaki and O. Ishitani, *Chem. Sci.*, 2019, **10**, 1597–1606.
723 S. J. Cobb, A. M. Dharani, A. R. Oliveira, I. A. C. Pereira and E. Reisner, *Angew. Chem., Int. Ed.*, 2023, **62**, e202218782.
724 J.-J. Lv, M. Jouny, W. Luc, W. Zhu, J.-J. Zhu and F. Jiao, *Adv. Mater.*, 2018, **30**, 1803111.
725 M. Miyaji, Y. Tamaki, K. Kamogawa, Y. Abiru, M. Abe and O. Ishitani, *ACS Catal.*, 2024, **14**, 10403–10411.
726 J. J. Lv, R. Yin, L. Zhou, J. Li, R. Kikas, T. Xu, Z. J. Wang, H. Jin, X. Wang and S. Wang, *Angew. Chem.*, 2022, **134**, e202207252.
727 Y. Pei, H. Zhong and F. Jin, *Energy Sci. Eng.*, 2021, **9**, 1012–1032.
728 D. Xu, K. Li, B. Jia, W. Sun, W. Zhang, X. Liu and T. Ma, *Carbon Energy*, 2023, **5**, e230.
729 M. G. Kibria, J. P. Edwards, C. M. Gabardo, C. T. Dinh, A. Seifitokaldani, D. Sinton and E. H. Sargent, *Adv. Mater.*, 2019, **31**, 1807166.
730 W. J. Lee, C. Li, H. Prajitno, J. Yoo, J. Patel, Y. Yang and S. Lim, *Catal. Today*, 2021, **368**, 2–19.
731 E. P. Komarala, A. A. Alkhoori, X. Zhang, H.-M. Cheng and K. Polychronopoulou, *J. Energy Chem.*, 2023, **86**, 246–262.
732 W. Mo, X.-Q. Tan and W.-J. Ong, *ACS Sustainable Chem. Eng.*, 2023, **11**, 5782–5799.
733 X.-Y. Wu and A. F. Ghoniem, *Prog. Energy Combust. Sci.*, 2019, **74**, 1–30.
734 W. Zhang, D. Ma, J. Pérez-Ramírez and Z. Chen, *Adv. Energy Sustainability Res.*, 2022, **3**, 2100169.
735 S. De, A. Dokania, A. Ramirez and J. Gascon, *ACS Catal.*, 2020, **10**, 14147–14185.
736 K. Stangeland, D. Y. Kalai, H. Li and Z. Yu, *Appl. Energy*, 2018, **227**, 206–212.
737 F. Hussin and M. K. Aroua, *Rev. Chem. Eng.*, 2021, **37**, 863–884.
738 S. Das, J. Pérez-Ramírez, J. Gong, N. Dewangan, K. Hidajat, B. C. Gates and S. Kawi, *Chem. Soc. Rev.*, 2020, **49**, 2937–3004.
739 Y. Xie, J. Wen, Z. Li, J. Chen, Q. Zhang, P. Ning, Y. Chen and J. Hao, *Green Chem.*, 2023, **25**, 130–152.
740 P. Tyagi, D. Singh, N. Malik, S. Kumar and R. S. Malik, *Mater. Today*, 2023, **65**, 133–165.
741 X.-L. Jiang, Y.-E. Jiao, S.-L. Hou, L.-C. Geng, H.-Z. Wang and B. Zhao, *Angew. Chem., Int. Ed.*, 2021, **60**, 20417–20423.
742 J. Liu, J. Zhang, H. Sun, C. Gao, Y. Chen, R. Cui and Y. Tian, *Fuel*, 2024, **357**, 129801.
743 J. Wang, M. Yang and D. Wang, *Chin. J. Chem.*, 2022, **40**, 1190–1203.

744 C. Dai, A. Zhang, M. Liu, J. Li, F. Song, C. Song and X. Guo, *RSC Adv.*, 2016, **6**, 10831–10836.
745 C. Catlow, S. French, A. Sokol and J. Thomas, *Philos. Trans. R. Soc., A*, 2005, **363**, 913–936.
746 J. Zhong, J. Han, Y. Wei and Z. Liu, *J. Catal.*, 2021, **396**, 23–31.
747 N. Chen and W. Garwood, *Catal. Rev.: Sci. Eng.*, 1986, **28**, 185–264.
748 B. M. Tackett, E. Gomez and J. G. Chen, *Nat. Catal.*, 2019, **2**, 381–386.
749 F. Zhang, Y.-H. Li, M.-Y. Qi, Y. M. Yamada, M. Anpo, Z.-R. Tang and Y.-J. Xu, *Chem Catal.*, 2021, **1**, 272–297.
750 W. Wang, S. Zhao, X. Tang, C. Chen and H. Yi, *Chem. Eng. J.*, 2023, **455**, 140272.
751 B. Xie, E. Lovell, T. H. Tan, S. Jantarang, M. Yu, J. Scott and R. Amal, *J. Energy Chem.*, 2021, **59**, 108–125.
752 B. Deng, H. Song, K. Peng, Q. Li and J. Ye, *Appl. Catal., B*, 2021, **298**, 120519.
753 Z. Wang, Z. Yang, R. Fang, Y. Yan, J. Ran and L. Zhang, *Chem. Eng. J.*, 2022, **429**, 132322.
754 S. Wang, A. A. Tountas, W. Pan, J. Zhao, L. He, W. Sun, D. Yang and G. A. Ozin, *Small*, 2021, **17**, 2007025.
755 Z. Chen, X. Dong and Z. X. Sun, *et al.*, Hierarchical Carbon Nanocages as Superior Supports for Photothermal $CO_2$ Catalysis, *ACS Nano*, 2024, **18**(30), 19672–19681.
756 Y. Guo, T. Li, D. Li and J. Cheng, *Renewable Sustainable Energy Rev.*, 2024, **189**, 114053.
757 L. Chen, J. T. Ren and Z. Y. Yuan, *Adv. Energy Mater.*, 2023, **13**, 2203720.
758 Y. Tang, T. Zhao, H. Han, Z. Yang, J. Liu, X. Wen and F. Wang, *Adv. Sci.*, 2023, **10**, 2300122.
759 J. Chang, M. J. Hülsey, S. Wang, M. Li, X. Ma and N. Yan, *Angew. Chem.*, 2023, **135**, e202218265.
760 G. Mei, Y. Lu, X. Yang, S. Chen, X. Yang, L. M. Yang, C. Tang, Y. Sun, B. Y. Xia and B. You, *Angew. Chem., Int. Ed.*, 2024, **63**, e202314708.
761 L. Zheng, M. Ambrosetti, A. Beretta, G. Groppi and E. Tronconi, *Chem. Eng. J.*, 2023, **466**, 143154.
762 A. George, B. Shen, M. Craven, Y. Wang, D. Kang, C. Wu and X. Tu, *Renewable Sustainable Energy Rev.*, 2021, **135**, 109702.
763 A. Bogaerts and G. Centi, *Front. Energy Res.*, 2020, **8**, 111.
764 D. Ray, P. Chawdhury, K. Bhargavi, S. Thatikonda, N. Lingaiah and C. Subrahmanyam, *J. $CO_2$* Util., 2021, **44**, 101400.
765 D. Li, V. Rohani, F. Fabry, A. P. Ramaswamy, M. Sennour and L. Fulcheri, *Appl. Catal., B*, 2020, **261**, 118228.
766 S. Liu, L. R. Winter and J. G. Chen, *ACS Catal.*, 2020, **10**, 2855–2871.
767 G. Trenchev and A. Bogaerts, *J. $CO_2$* Util., 2020, **39**, 101152.
768 W. Cai, Q. Zhong and Y. Zhao, *Catal. Commun.*, 2013, **39**, 30–34.
769 K. Lei and B. Yu Xia, *Chem. – Eur. J.*, 2022, **28**, e202200141.
770 G. Chen, R. Snyders and N. Britun, *J. $CO_2$* Util., 2021, **49**, 101557.
771 M. L. Clark, A. Ge, P. E. Videla, B. Rudshteyn, C. J. Miller, J. Song, V. S. Batista, T. Lian and C. P. Kubiak, *J. Am. Chem. Soc.*, 2018, **140**, 17643–17655.
772 Y. Xu, Z. Zhou, M. Zou, Y. Liu, Y. Zheng, Y. Yang, S. Lan, J. Lan, C.-W. Nan and Y.-H. Lin, *Mater. Today*, 2022, **54**, 225–246.
773 Z. Wang, Y. Zhang, E. C. Neyts, X. Cao, X. Zhang, B. W.-L. Jang and C.-J. Liu, *ACS Catal.*, 2018, **8**, 2093–2110.
774 L. Di, J. Zhang and X. Zhang, *Plasma Processes Polym.*, 2018, **15**, 1700234.
775 J. C. Whitehead, *J. Phys. D: Appl. Phys.*, 2016, **49**, 243001.
776 O. M. Mohamed, *Production of C4–C10 Hydrocarbons from $CO_2$, $H_2O$, CO, $H_2$ and $CH_4$ Utilizing DC Glow Discharges, Catalytic Rapid Temperature Pulsing in Micro-Scale Reactors, 2021, https://ir.library.oregonstate.edu/concern/graduate_thesis_or_dissertations/1z40m162p.*
777 J. C. Bui, C. Kim, A. J. King, O. Romiluyi, A. Kusoglu, A. Z. Weber and A. T. Bell, *Acc. Chem. Res.*, 2022, **55**, 484–494.
778 P. Saha, S. Amanullah and A. Dey, *Acc. Chem. Res.*, 2022, **55**, 134–144.
779 M. Biset-Peiró, R. Mey, J. Guilera and T. Andreu, *Chem. Eng. J.*, 2020, **393**, 124786.
780 Y. Wang, Y. Chen, J. Harding, H. He, A. Bogaerts and X. Tu, *Chem. Eng. J.*, 2022, **450**, 137860.
781 R. Lin, J. Guo, X. Li, P. Patel and A. Seifitokaldani, *Catalysts*, 2020, **10**, 473.
782 H. L. Huynh and Z. Yu, *Energy Technol.*, 2020, **8**, 1901475.
783 R. Villa, S. Nieto, A. Donaire and P. Lozano, *Molecules*, 2023, **28**, 5520.
784 L. Luan, X. Ji, B. Guo, J. Cai, W. Dong, Y. Huang and S. Zhang, *Biotechnol. Adv.*, 2023, **63**, 108098.
785 I. A. Figueroa, T. P. Barnum, P. Y. Somasekhar, C. I. Carlström, A. L. Engelbrektson and J. D. Coates, *Proc. Natl. Acad. Sci. U. S. A.*, 2018, **115**, E92–E101.
786 P. Bakonyi, L. Koók, T. Rózsenberszki, V. Kalauz-Simon, K. Bélafi-Bakó and N. Nemestóthy, *J. $CO_2$* Util., 2023, **67**, 102348.
787 M. E. Russo, C. Capasso, A. Marzocchella and P. Salatino, *Appl. Microbiol. Biotechnol.*, 2022, **106**, 3419–3430.
788 E. Daneshvar, R. J. Wicker, P.-L. Show and A. Bhatnagar, *Chem. Eng. J.*, 2022, **427**, 130884.
789 H. Onyeaka, T. Miri, K. Obileke, A. Hart, C. Anumudu and Z. T. Al-Sharify, *Carbon Capture Sci. Technol.*, 2021, **1**, 100007.
790 S. Li, M. Ongis, G. Manzolini and F. Gallucci, *Chem. Eng. J.*, 2021, **410**, 128335.
791 H. J. Ryu, K. K. Oh and Y. S. Kim, *J. Ind. Eng. Chem.*, 2009, **15**, 471–475.
792 N. Hajinajaf, A. Fallahi, E. Eustance, A. Sarnaik, A. Askari, M. Najafi, R. W. Davis, B. E. Rittmann and A. M. Varman, *Algal Res.*, 2024, **80**, 103506.
793 J. Pires, M. Alvim-Ferraz, F. Martins and M. Simões, *Renewable Sustainable Energy Rev.*, 2012, **16**, 3043–3053.
794 J. Xu, J. Cheng, K. Xin, J. Xu and W. Yang, *ACS Sustainable Chem. Eng.*, 2020, **8**, 18926–18935.
795 T. Schwander, L. Schada von Borzyskowski, S. Burgener, N. S. Cortina and T. J. Erb, *Science*, 2016, **354**, 900–904.
796 T. Cai, H. Sun, J. Qiao, L. Zhu, F. Zhang, J. Zhang, Z. Tang, X. Wei, J. Yang and Q. Yuan, *Science*, 2021, **373**, 1523–1527.

 

797 J. Yang, W. Song, T. Cai, Y. Wang, X. Zhang, W. Wang, P. Chen, Y. Zeng, C. Li and Y. Sun, *Sci. Bull.*, 2023, **68**, 2370–2381.
798 L. Xiao, G. Liu, F. Gong, H. Zhu, Y. Zhang, Z. Cai and Y. Li, *ACS Catal.*, 2021, **12**, 799–808.
799 J. Liu, H. Zhang, Y. Xu, H. Meng and A.-P. Zeng, *Nat. Commun.*, 2023, **14**, 2772.
800 R. Gupta, A. Mishra, Y. Thirupathaiah and A. K. Chandel, *Biomass Convers. Biorefin.*, 2024, **14**, 3007–3030.
801 S. Bajracharya, S. Srikanth, G. Mohanakrishna, R. Zacharia, D. P. Strik and D. Pant, *J. Power Sources*, 2017, **356**, 256–273.
802 P. Valdivia, R. Barraza, D. Saldivia, L. Gacitúa, A. Barrueto and D. Estay, *Renewable Energy*, 2020, **147**, 1251–1265.
803 A. Arabkoohsar, M. Dremark-Larsen, R. Lorentzen and G. B. Andresen, *Appl. Energy*, 2017, **205**, 602–614.
804 A. Arabkoohsar, L. Machado, M. Farzaneh-Gord and R. N. N. Koury, *Renewable Energy*, 2015, **83**, 491–509.
805 Y. Liang, P. Li, L. Xing, W. Su, W. Li and W. Xu, *J. Energy Storage*, 2024, **80**, 110347.
806 L. Wang, L.-m Pan, J. Wang, D. Chen, Y. Huang, W. Sun and L. Hu, *Prog. Nucl. Energy*, 2022, **143**, 104049.
807 Y. Zhang, E. Yao and T. Wang, *J. Energy Storage*, 2021, **35**, 102274.
808 E. Bazdar, M. Sameti, F. Nasiri and F. Haghighat, *Renewable Sustainable Energy Rev.*, 2022, **167**, 112701.
809 E. Barbour and D. L. Pottie, *Joule*, 2021, **5**, 1914–1920.
810 Z. Gao, X. Zhang, X. Li, Y. Xu and H. Chen, *Energy*, 2023, **284**, 129304.
811 Z. Liu, H. Yu and T. Gundersen, *Computer Aided Chemical Engineering*, Elsevier, 2020, vol. 48, pp. 967–972.
812 Z. Liu, J. Ding, X. Huang, Z. Liu, X. Yan, X. Liu and X. Yang, *Appl. Energy*, 2024, **354**, 122142.
813 C. Guo, C. Li, K. Zhang, Z. Cai, T. Ma, F. Maggi, Y. Gan, A. El-Zein, Z. Pan and L. Shen, *Appl. Energy*, 2021, **286**, 116513.
814 M. Budt, D. Wolf, R. Span and J. Yan, *Appl. Energy*, 2016, **170**, 250–268.
815 Z. Tong, Z. Cheng and S. Tong, *Renewable Sustainable Energy Rev.*, 2021, **135**, 110178.
816 M. Nakhamkin, R. H. Wolk, S. van der Linden, *et al.*, New compressed air energy storage concept improves the profitability of existing simple cycle, combined cycle, wind energy, and landfill gas power plants//Turbo Expo: Power for Land, Sea, and Air, 2004, 41707, pp. 103–110.
817 X. Wang, H. Guo, H. Zhang, Y. Xu, Y. Liu and H. Chen, *Energy Storage Sci. Technol.*, 2021, **10**, 598–610.
818 J. A. Bennett, J. G. Simpson, C. Qin, R. Fittro, G. M. Koenig, A. F. Clarens and E. Loth, *Appl. Energy*, 2021, **303**, 117587.
819 S. van der Linden, Integrating wind turbine generators (WTG′s) with GT-CAES (compressed air energy storage) stabilizes power delivery with the inherent benefits of bulk energy storage//ASME International Mechanical Engineering Congress and Exposition, 2007, 43009, pp. 379–386.
820 M. Heidari, D. Parra and M. K. Patel, *J. Energy Storage*, 2021, **35**, 102268.
821 X. Zhang, Z. Gao, B. Zhou, H. Guo, Y. Xu, Y. Ding and H. Chen, *Engineering*, 2024, **34**, 246–269.
822 B. Zakeri and S. Syri, *Renewable Sustainable Energy Rev.*, 2015, **42**, 569–596.
823 Y. Li, F. Yao, S. Zhang, Y. Liu and S. Miao, *J. Energy Storage*, 2022, **51**, 104366.
824 X. Zhang, Y. Li, Z. Gao, S. Chen, Y. Xu and H. Chen, *J. Energy Storage*, 2023, **66**, 107408.
825 L. Chen, T. Zheng, S. Mei, X. Xue, B. Liu and Q. Lu, *J. Modern Power Syst. Clean Energy*, 2016, **4**, 529–541.
826 M. Beaudin, H. Zareipour, A. Schellenberg and W. Rosehart, *Energy Storage for Smart Grids: Planning and Operation for Renewable and Variable Energy Resources*, 2014, vol. 14, pp. 1–33.
827 Y. Liu, D. Yu and L. Tong, *et al.*, Improved liquid air energy storage process considering air purification: Continuous and flexible energy storage and power generation, *Renewable Energy*, 2024, **231**, 120951.
828 X. Liu, J. Yang, C. Yang, Z. Zhang and W. Chen, *Energy*, 2023, **282**, 128916.
829 W. Zhang, J. Ding, S. Yin, F. Zhang, Y. Zhang and Z. Liu, *Energy*, 2024, **294**, 130821.
830 W. Guo, Z. Zhang, H. Wu, L. Ge, X. Liang and R. Mao, *Int. Commun. Heat Mass Transfer*, 2023, **146**, 106930.
831 M. Medeiros, R. Booth, J. Fairchild, D. Imperato, C. Stinson, M. Ausburn, M. Tietze, S. Irani, A. Burzlaff and H. Moore, *Technical Feasibility of Compressed Air Energy Storage (CAES) Utilizing a Porous Rock Reservoir*, Pacific Gas and Electric Company, San Francisco, CA (United States), 2018.
832 H. Liu, Q. He, A. Borgia, L. Pan and C. M. Oldenburg, *Energy Convers. Manage.*, 2016, **127**, 149–159.
833 C. M. Oldenburg and L. Pan, *Greenhouse Gases: Sci. Technol.*, 2013, **3**, 124–135.
834 Z. Ma and C. S. Turchi, *Advanced supercritical carbon dioxide power cycle configurations for use in concentrating solar power systems*, National Renewable Energy Lab. (NREL), Golden, CO (United States), 2011.
835 H. Li, R. Ding, W. Su, X. Lin, S. Guan, Q. Ye, Z. Zheng and J. Wang, *Energy Convers. Manage.*, 2024, **319**, 118972.
836 Ł. Bartela, A. Skorek-Osikowska, S. Dykas and B. Stanek, *Energy Convers. Manage.*, 2021, **241**, 114297.
837 Y. Ahn, S. J. Bae, M. Kim, S. K. Cho, S. Baik, J. I. Lee and J. E. Cha, *Nucl. Eng. Technol.*, 2015, **47**, 647–661.
838 Y. J. Chae and J. I. Lee, *Energy Convers. Manage.*, 2022, **256**, 115374.
839 W. Xu, P. Zhao, F. Gou, W. Wu, A. Liu and J. Wang, *Energy Convers. Manage.*, 2022, **260**, 115610.
840 J. Liu, H. Chen, Y. Xu, L. Wang and C. Tan, *Renewable Energy*, 2014, **64**, 43–51.
841 H. Fu, J. Shi, J. Yuan and L. Sun, *J. Energy Storage*, 2023, **66**, 107415.
842 S. Liu, S. Wu, Y. Hu and H. Li, *Energy Convers. Manage.*, 2019, **181**, 608–620.
843 Y. Zhang, X. Shen, Z. Tian, C. Yang, W. Gao and K. Yang, *Energy Convers. Manage.*, 2023, **292**, 117399.
844 Y. Hao, Q. He and D. Du, *Renewable Energy*, 2020, **152**, 1099–1108.

845 Y. Hao, Q. He, Q. Zhou and D. Du, *J. Energy Storage*, 2020, **28**, 101273.
846 Z. Liu, Z. Liu, X. Xin and X. Yang, *Appl. Energy*, 2020, **269**, 115067.
847 R. Zhao and Z. Liu, *J. Energy Storage*, 2023, **60**, 106675.
848 Y. Zhang, T. Liang and K. Yang, *Energy*, 2022, **247**, 123566.
849 J. Meng, M. Wei, P. Song, R. Tian, L. Hao and S. Zheng, *Energy Convers. Manage.*, 2020, **215**, 112931.
850 Y. Zhang, F. Lin, Z. Liu, Y. Lin and K. Yang, *J. Energy Storage*, 2023, **60**, 106605.
851 Y. Zhang, Y. Lin, F. Lin and K. Yang, *Energy Convers. Manage.*, 2022, **260**, 115609.
852 F. Chaychizadeh, H. Dehghandorost, A. Aliabadi and A. Taklifi, *Energy Convers. Manage.*, 2018, **166**, 500–511.
853 Q. He, H. Liu, Y. Hao, Y. Liu and W. Liu, *Renewable Energy*, 2018, **127**, 835–849.
854 W. Sun, X. Liu, X. Yang, X. Yang and Z. Liu, *Energy Convers. Manage.*, 2021, **239**, 114227.
855 Z. Liu, Z. Liu, X. Yang, H. Zhai and X. Yang, *Energy Convers. Manage.*, 2020, **205**, 112391.
856 X. R. Zhang and G. B. Wang, *Int. J. Energy Res.*, 2017, **41**, 1487–1503.
857 H. Ma, Y. Tong and X. Wang, *et al.*, Advancements and assessment of compressed carbon dioxide energy storage technologies: a comprehensive review, *RSC Sustainability*, 2024, **2**(10), 2731–2750.
858 P. Zheng, Z. Zhang, J. Yang, J. Hao, Y. Li, Y. Yue and H. Chang, *Appl. Therm. Eng.*, 2024, **243**, 122669.
859 M. Qi, Y. Liu, R. S. Landon, Y. Liu and I. Moon, *Process Saf. Environ. Prot.*, 2021, **149**, 994–1016.
860 Y. Li, H. Yu, Y. Liu, G. Zhang, D. Tang and Z. Jiang, *Renewable Energy*, 2020, **151**, 1318–1338.
861 L. Sun, B. Tang and Y. Xie, *Energy*, 2022, **256**, 124648.
862 W. Li, B. Brown, D. Young and S. Nešić, *Corrosion*, 2014, **70**, 294–302.
863 F. Schremp and G. Roberson, *Soc. Pet. Eng. J.*, 1975, **15**, 227–233.
864 A. Dugstad, B. Morland and S. Clausen, *Energy Procedia*, 2011, **4**, 3063–3070.
865 A. Q. Liu, C. Bian, Z. M. Wang, X. Han and J. Zhang, *Corros. Sci.*, 2018, **134**, 149–161.
866 J. Gale and J. Davison, *Energy*, 2004, **29**, 1319–1328.
867 Y. Hua, R. Barker and A. Neville, *Int. J. Greenhouse Gas Control*, 2015, **37**, 412–423.
868 C. Sun, J. Sun, S. Liu and Y. Wang, *Corros. Sci.*, 2018, **137**, 151–162.
869 Y. Xiang, Z. Wang, C. Xu, C. Zhou, Z. Li and W. Ni, *J. Supercrit. Fluids*, 2011, **58**, 286–294.
870 C. Sun, J. Sun, Y. Wang, X. Lin, X. Li, X. Cheng and H. Liu, *Corros. Sci.*, 2016, **107**, 193–203.
871 W. Wang, K. Shen, S. Tang, R. Shen, T. Parker and Q. Wang, *Process Saf. Environ. Prot.*, 2019, **130**, 57–66.
872 L. Wei, X. Pang and K. Gao, *Corros. Sci.*, 2016, **103**, 132–144.
873 Y. Hua, R. Barker and A. Neville, *Int. J. Greenhouse Gas Control*, 2014, **31**, 48–60.
874 L. Wei and K. Gao, *J. Alloys Compd.*, 2019, **792**, 328–340.
875 W. Liu, Q. Li, C. Yang, X. Shi, J. Wan, M. J. Jurado, Y. Li, D. Jiang, J. Chen and W. Qiao, *Energy Storage Mater.*, 2023, **63**, 103045.
876 H. Li, H. Ma, J. Liu, S. Zhu, K. Zhao, Z. Zheng, Z. Zeng and C. Yang, *Energy*, 2023, **281**, 128271.
877 Y. Shi, Y. Lu, Y. Rong, Z. Bai, H. Bai, M. Li and Q. Zhang, *Alexandria Eng. J.*, 2023, **64**, 679–689.
878 Y. Li, J. Cui, H. Yu, D. Tang, G. Zhang and Y. Liu, *Renewable Energy*, 2024, **231**, 120954.
879 L. E. Beckingham and L. Winningham, *ACS Sustainable Chem. Eng.*, 2019, **8**, 2–11.
880 S. Bachu, W. Gunter and E. Perkins, *Energy Convers. Manage.*, 1994, **35**, 269–279.
881 I. Gaus, P. Audigane, L. André, J. Lions, N. Jacquemet, P. Durst, I. Czernichowski-Lauriol and M. Azaroual, *Int. J. Greenhouse Gas Control*, 2008, **2**, 605–625.
882 B. M. Tutolo, A. J. Luhmann, X.-Z. Kong, M. O. Saar and W. E. Seyfried Jr, *Geochim. Cosmochim. Acta*, 2015, **160**, 132–154.
883 C. Noiriel and D. Daval, *Acc. Chem. Res.*, 2017, **50**, 759–768.
884 J. R. Black, S. A. Carroll and R. R. Haese, *Chem. Geol.*, 2015, **399**, 134–144.
885 J. H. Kwak, J. Z. Hu, R. V. Turcu, K. M. Rosso, E. S. Ilton, C. Wang, J. A. Sears, M. H. Engelhard, A. R. Felmy and D. W. Hoyt, *Int. J. Greenhouse Gas Control*, 2011, **5**, 1081–1092.
886 G. Cui, Y. Wang, Z. Rui, B. Chen, S. Ren and L. Zhang, *Energy*, 2018, **155**, 281–296.
887 G. Cui, S. Ren, Z. Rui, J. Ezekiel, L. Zhang and H. Wang, *Appl. Energy*, 2018, **227**, 49–63.
888 M. Kim, A. Sell and D. Sinton, *Lab Chip*, 2013, **13**, 2508–2518.
889 M. Zeidouni, M. Pooladi-Darvish and D. Keith, *Int. J. Greenhouse Gas Control*, 2009, **3**, 600–611.
890 M. Nooraiepour, H. Fazeli, R. Miri and H. Hellevang, *Environ. Sci. Technol.*, 2018, **52**, 6050–6060.
891 S. Zhang and H.-H. Liu, *Int. J. Greenhouse Gas Control*, 2016, **52**, 24–31.
892 C. R. Bryan, T. A. Dewers, J. E. Heath, Y. Wang, E. N. Matteo, S. P. Meserole and D. R. Tallant, *Fundamental study of $CO_2$–$H_2O$-mineral interactions for carbon sequestration, with emphasis on the nature of the supercritical fluid-mineral interface,* Sandia National Lab. (SNL-NM), Albuquerque, NM (United States), 2013.
893 M. Zarnoush, P. P. Golaki, M. Soltani, E. Yamini, F. Esmaeilion and J. Nathwani, *J. Energy Storage*, 2023, **73**, 108831.
894 A. Abuheiba, M. R. Ally, B. Smith and A. Momen, *Energies*, 2020, **13**, 2431.
895 Z. Liu, X. Liu, W. Zhang, S. Yang, H. Li and X. Yang, *Energy*, 2022, **238**, 121759.
896 H. Ma and Z. Liu, *Energy*, 2022, **246**, 123346.
897 S. T. Blanco, C. Rivas and J. Fernandez, *et al.*, Influence of methane in $CO_2$ transport and storage for CCS technology, *Environ. Sci. Technol.*, 2012, **46**(23), 13016–13023.

 

898 H. Li and J. Yan, *Appl. Energy*, 2009, **86**, 826–836.
899 H. Li, J. P. Jakobsen, Ø. Wilhelmsen and J. Yan, *Appl. Energy*, 2011, **88**, 3567–3579.
900 B. Tang, L. Sun and Y. Xie, *Energy Convers. Manage.*, 2022, **268**, 116043.
901 J. Wang, D. Ryan, E. J. Anthony, N. Wildgust and T. Aiken, *Energy Procedia*, 2011, **4**, 3071–3078.
902 W. S. Jeong and Y. H. Jeong, *Nucl. Eng. Des.*, 2013, **262**, 12–20.
903 X. Liu, Z. Xu, Y. Xie and H. Yang, *Appl. Therm. Eng.*, 2019, **162**, 114226.
904 J. Xia, J. Wang, G. Zhang, J. Lou, P. Zhao and Y. Dai, *Appl. Therm. Eng.*, 2018, **144**, 31–44.
905 M. G. Zebetakis, Flammability Characteristics of Combustible Gases and Vapors, US Bureau Mines, Bulletin, 1965, 627.
906 Y. S. Wei, *Prediction of the fluid phase equilibria of binary and ternary mixtures*, Swinburne University of Technology, 1998.
907 N. Katyal, G. Ortenzi, J. L. Grenfell, L. Noack, F. Sohl, M. Godolt, A. G. Muñoz, F. Schreier, F. Wunderlich and H. Rauer, *Astron. Astrophys.*, 2020, **643**, A81.
908 F. Ning, K. Glavatskiy, Z. Ji, S. Kjelstrup and T. H. Vlugt, *Phys. Chem. Chem. Phys.*, 2015, **17**, 2869–2883.
909 C. Li and L. Laloui, *Int. J. Greenhouse Gas Control*, 2016, **51**, 394–408.
910 Y. Zhang, X. Shen, Z. Tian, A. Kan, W. Gao and K. Yang, *Energy*, 2023, **282**, 128415.
911 M. S. Khan, S. Lee and M. Lee, *Asia-Pac. J. Chem. Eng.*, 2012, **7**, S62–S70.
912 Y. Li, F. Xu and C. Gong, *Chem. Eng. Res. Des.*, 2017, **124**, 159–169.
913 H. Jiang, Y. He and C. Zhu, *Nat. Gas Ind.*, 2011, **31**, 112–115.
914 X. Fu, X. Yan and Z. Liu, *Energy*, 2023, **284**, 128642.
915 M. Xu, P. Zhao, Y. Huo, J. Han, J. Wang and Y. Dai, *J. Cleaner Prod.*, 2020, **242**, 118437.
916 P. Prabhu, V. Jose and J. M. Lee, *Adv. Funct. Mater.*, 2020, **30**, 1910768.
917 P. H. Ho, G. S. de Luna, S. Angelucci, A. Canciani, W. Jones, D. Decarolis, F. Ospitali, E. R. Aguado, E. Rodríguez-Castellón and G. Fornasari, *Appl. Catal., B*, 2020, **278**, 119256.
918 M. Cai, Z. Wu, Z. Li, L. Wang, W. Sun, A. A. Tountas, C. Li, S. Wang, K. Feng and A.-B. Xu, *Nat. Energy*, 2021, **6**, 807–814.
919 T. Wu, Q. Shen, M. Xu, T. Peng and X. Ou, *Energy*, 2018, **154**, 298–307.
920 J. Wang, H. Shirvani, H. Zhao, M. G. Kibria and J. Hu, *Biotechnol. Adv.*, 2023, **66**, 108157.
921 A. Mazheika, Y.-G. Wang, R. Valero, F. Viñes, F. Illas, L. M. Ghiringhelli, S. V. Levchenko and M. Scheffler, *Nat. Commun.*, 2022, **13**, 419.
922 Y. Li, B. Zeng, T. Wu and H. Hao, *J. Cleaner Prod.*, 2019, **215**, 600–610.
923 M. Erdem Günay and R. Yıldırım, *Catal. Rev.*, 2021, **63**, 120–164.
924 J. Benavides-Hernández, *ACS Catal.*, 2024, **14**, 11749–11779.
925 D. V. Quang, D. Milani and M. A. Zahra, A review of potential routes to zero and negative emission technologies via the integration of renewable energies with $CO_2$ capture processes, *Int. J. Greenhouse Gas Control*, 2023, **124**, 103862.
926 I. Ioannou, *Energy Environ. Sci.*, 2023, **16**, 113–124.